



HAL
open science

Electronic and optical devices integrating thin films of the spin crossover complex [Fe(HB(1,2,4-triazol-1-yl)3)2]

Yuteng Zhang

► To cite this version:

Yuteng Zhang. Electronic and optical devices integrating thin films of the spin crossover complex [Fe(HB(1,2,4-triazol-1-yl)3)2]. Coordination chemistry. Université Paul Sabatier - Toulouse III, 2021. English. NNT : 2021TOU30226 . tel-03693637

HAL Id: tel-03693637

<https://theses.hal.science/tel-03693637>

Submitted on 10 Jun 2022

HAL is a multi-disciplinary open access archive for the deposit and dissemination of scientific research documents, whether they are published or not. The documents may come from teaching and research institutions in France or abroad, or from public or private research centers.

L'archive ouverte pluridisciplinaire **HAL**, est destinée au dépôt et à la diffusion de documents scientifiques de niveau recherche, publiés ou non, émanant des établissements d'enseignement et de recherche français ou étrangers, des laboratoires publics ou privés.



THÈSE

En vue de l'obtention du
DOCTORAT DE L'UNIVERSITÉ DE TOULOUSE

Délivré par l'Université Toulouse 3 - Paul Sabatier

Présentée et soutenue par

Yuteng ZHANG

Le 14 décembre 2021

Dispositifs électroniques et optiques à base de complexe à transition de spin [Fe(HB(1,2,4-triazol-1-yl)3)2]

Ecole doctorale : **SDM - SCIENCES DE LA MATIERE - Toulouse**

Spécialité : **Chimie Organométallique et de Coordination**

Unité de recherche :

LCC - Laboratoire de Chimie de Coordination

Thèse dirigée par

Gabor MOLNAR et Azzedine BOUSSEKSOU

Jury

M. Rodrigue LESCOUEZEC, Rapporteur

M. José SANCHEZ COSTA, Rapporteur

M. Emmanuel FLAHAUT, Examinateur

Mme Isabelle SÉGUY, Examinatrice

Mme Amandine BELLEC, Examinatrice

M. Gabor MOLNAR, Directeur de thèse

Do not go gentle into that good night

Acknowledgements

Firstly, I would like to thank the Laboratory of Coordination Chemistry (LCC), the Laboratory of Analysis and Architecture of Systems (LAAS) and the China Scholarship Council (CSC) for hosting me and funding the thesis. This work won't be accomplished without anyone of you.

Most of my gratitude goes to my supervisors Azzedine Bousseksou and Gabor Molnar for their huge wisdom, great humanity and abounding scientific knowledge that helped me finish this work in a proper way. The same to Isabelle Séguy, although you are not officially my supervisor, we shared lot of experimental time and nearly all the chapters were done with your help. I appreciate all the efforts that you have made to get the truth.

I warmly thank my jury members for having accepted to attend my defense. I want to send my sincere grateful to all of you, either my reporter Rodrigue Lescouezec and José Sanchez Costa, or the examiners Emmanuel Flahaut, Isabelle Séguy, Amandine Bellec and Gabor Molnar, or the inviters Azzedine Bousseksou and Aurelian Rotaru. Some of you we have already worked together and I have to mention that I really enjoyed it. Some of you we will cooperate in a not-far future, and I want to thank for this opportunity to enrich my scientific knowledge.

Large thanks to all the team members in LCC. I know I was not a people who is easy to go with, especially when he hardly join the common activities. Although I was autistic and social phobia during the most time of my thesis due to some personal reasons, you still helped me in many aspects and I am quite moved about that. Lionel, William, Karl, Lucie, Victoria, Alin, Barbora, Amalia, Alejandro, Baptiste, Mario, Elias, Alaa, Yue, Shiteng, Lijun, Oleksandr, Livia, Ion, Onkar, Fayan, Xinyu, Yonjian... This won't be an exhausted list and I want to thank all of you.

Additionally, I want to thank some friends in Toulouse, who makes this corner a bit more genial. I would like to thank Xudong, Xue and Xing for their accommodating and Tao as well as Xiaoning for some discussions in-depth, this becomes more and more rare with time going and I really appreciate this kind of friendship. I would also like to thank all the friends that we met/talked online/in real life, especially half time of my thesis was during the covid pandemic. There are surely some fascinating moments when I looked back.

Many thanks to my family, especially my parents, who are always present and having supported me all along those years. It's very lucky that I can assuredly know I have a robust connection to this world since you are here. This really saves my life when some dark moment comes. Special thanks also to my cat, I appreciate for your accompanying for past few years. We shared many precious memories and it's great to have you that we can discover this world together in the following years :)

I would like also to thank Yuteng, for not ever totally abandoned himself, especially when he hits rock bottom in the past years. To be honest, I am glad that I can suffer and go through those as they took place in the early time of my life. Apparently, it helps me to think it over and to build a system for myself, which incorporated my world view, life's perspectives and personal values. This added some philosophical reflections, to my poor PhD life, and it is one of the most satisfying thing for the past three years.

'Have the lamps stopped screaming?' It can be a good question to scrutinize after this thesis. As for the answer, I think it was well given in the book.

Electronic and optical devices integrating thin films of the spin crossover complex [Fe(HB(1,2,4-triazol-1-yl)₃)₂]

Table of contents

General introduction.....	1
Chapter 1 Introduction	3
1.1 Introduction to the spin crossover phenomenon.....	3
1.1.1 Molecular aspects of the spin crossover phenomenon.....	3
1.1.2 Spin crossover induced by different stimuli	5
1.1.3 Experimental techniques to characterize the SCO phenomenon	7
1.2. From bulk to thin film applications: vacuum thermal evaporation	9
1.2.1 [Fe(phen) ₂ (NCS) ₂] thin films	11
1.2.2 [Fe(H ₂ B(pz) ₂) ₂ (phen)] thin films	12
1.2.3 [Fe(H ₂ B(pz) ₂) ₂ (bipy)] thin films	13
1.2.4 [Fe(HB(pz) ₃) ₂] thin films	14
1.2.5 [Fe(H ₂ B(pz) ₂) ₂ L ³] thin films	15
1.2.6 [Fe(HB(3,5-(CH ₃) ₂ (pz) ₃) ₂] thin films.....	16
1.2.7 [Fe(qnal) ₂] thin films.....	17
1.2.8 [Fe(HB(tz) ₃) ₂] thin films	18
1.3 State of art in SCO-based electronic devices.....	20
1.3.1 Two-terminal SCO-based electronic devices.....	20
1.3.2 Three-terminal SCO-based electronic devices.....	31
1.4 Conclusions and perspectives for further work	35
Chapter 2 Integration of the spin crossover complex [Fe(HB(tz) ₃) ₂] into two-terminal resistance switching devices.....	38
2.1 Resistance switching devices.....	38
2.2 Synthesis and characterization of the bulk [Fe(HB(tz) ₃) ₂] complex	40
2.3 Fabrication and characterization of [Fe(HB(tz) ₃) ₂] thin films.....	42

2.3.1 Deposition of [Fe(HB(tz) ₃) ₂] thin films by vacuum thermal evaporation	42
2.3.2 Crystallinity of the films	44
2.3.3 SCO properties of the [Fe(HB(tz) ₃) ₂] thin films	45
2.3.4 Surface morphology of [Fe(HB(tz) ₃) ₂] thin films	47
2.4 SCO-based resistance switching devices.....	48
2.4.1 Fabrication and characterization of ITO/[Fe(HB(tz) ₃) ₂]/Al junctions	49
2.4.2 Resistance switching properties of ITO/[Fe(HB(tz) ₃) ₂]/Al junctions.....	51
2.4.3 Stability of ITO/[Fe(HB(tz) ₃) ₂]/Al junctions	55
2.4.4 Charge transport mechanism underlying the resistance-switching phenomenon	60
2.5 Fabrication and characterization of NiFe/SCO/Co junctions	67
2.6 Conclusions and perspectives	71
Chapter 3 Integration of the spin crossover complex [Fe(HB(tz) ₃) ₂] into three-terminal electronic devices	73
3.1 General considerations	73
3.2 Introduction to OFETs.....	75
3.2.1 Basic structure of OFETs.....	75
3.2.2 Operation mechanism of OFETs	77
3.2.3 Basic parameters of OFETs	77
3.2.4 Stability of OFETs	80
3.3 Fabrication of SCO-based OFETs.....	83
3.3.1 Device designs	83
3.3.2 Experimental protocols	85
3.4 Characterization of Devices A and B	87
3.5 Analysis of the thermal stability of ‘standard’ bottom gate/top contact devices.....	90
3.6 Characterization of Device C	92
3.7 Conclusions and perspectives	97
Chapter 4 Integration of the spin crossover complex [Fe(HB(tz) ₃) ₂] into optical cavities ...	99

4.1 Motivation and state of the art for using SCO materials in photonic devices	99
4.2 Introduction to Fabry-Perot cavities	102
4.2.1 Principle of a Fabry-Perot interferometer	102
4.2.2 Tunable Fabry-Perot cavities	104
4.3 Optical properties of $[\text{Fe}(\text{HB}(\text{tz})_3)_2]$ thin films.....	104
4.4 SCO based Fabry-Perot cavities	108
4.4.1 Structure and design of SCO based Fabry-Perot cavities	108
4.4.2 Effect of SCO on the cavity resonance: simulation results.....	111
4.4.3 Effect of SCO on the cavity resonance: experimental results.....	113
4.5 Conclusions and perspectives	119
General conclusions and perspectives	121
References	125
Annexes	137

List of abbreviation

AFM = Atomic force microscopy

bapbpy = N,N'-di(pyrid-2-yl)-2,2'-bipyridine-6,6'-diamine

bipy = 2,2'-bipyridine

dpepd = 1-{6-[1,1-di(pyridin-2-yl)ethyl]-pyridin-2-yl}-N,N-dimethylmethanamine

FTIR = Fourier-transform infrared

HS = High spin

IR = Infrared

LD-LISC = Ligand-Driven Light Induced Spin Crossover

LIESST = Light Induced Excited Spin State Trapping

Liq = 8-hydroxyquinolinato lithium

LS = Low spin

NCS = N-Chlorosuccinimide

pap = N-2-pyridylmethylidene-2-hydroxyphenylaminato

Phen = 1, 10-phenanthroline

pypyr = 2-(2'-pyridyl)pyrrolide

pz = pyrazol-1-yl

qnal = quinoline-naphthaldehyde

qsal-I = 4-iodo-2-[(8-quinolylimino)methyl]phenolate

RRAM = resistance switching random access memory

SCO = Spin crossover

SQUID = Superconducting quantum interference device

SVA = Solvent vapor annealing

tz = 1,2,4-triazol-1-yl

UV = Ultraviolet

VIS = Visible

XRD = X-ray diffraction

General introduction

In the past decades, molecular materials have been increasingly considered for technological applications because the miniaturization of conventional silicon based devices is approaching various technological and physical limits. In this context, molecular science can bring novel solutions with the synthesis and integration of functional molecules into devices. Among these functional molecules, spin crossover (SCO) complexes of certain third-row transition metal ions exhibit reversible switching between their low spin (LS) and high spin (HS) electronic configurations. The switching between these two states can be triggered by various external stimuli such as temperature, pressure, light, intense magnetic fields, or the inclusion of solvent/guest molecules. SCO compounds in the two spin states display different physical properties, including magnetic, dielectric, optical, mechanical, thermal properties. Some of the SCO materials even present room temperature (above room temperature) switching, which is obviously a key asset for any application. Another important characteristic of SCO complexes is that the molecular spin state can be switched by light irradiation on a sub-ps time scale, which denotes possible fast operation. These attractive properties of SCO compounds generated interest to study their electrical properties in the context of electronic and spintronic devices. Indeed, the molecular nature of these materials offers unprecedented functions, which remain to be explored. The general idea is to investigate the various possibilities offered by SCO molecules in modulating the properties of electronic devices. Notably, the SCO leads to a considerable variation of the HOMO-LUMO gap, the magnetic moment, the mass density, complex dielectric permittivity (in a broad frequency range, from quasi-static to optical frequencies), and so forth. Hence, one can expect a substantial effect of the SCO on various device properties (resistance, magnetoresistance, capacitance and optical characteristics). The challenge is, however, to find a way to get use of these remarkable assets in a technologically relevant electronic device.

In this context, this thesis work takes benefit from the recent development in our team of high quality, crystalline thin films of the SCO complex $[\text{Fe}(\text{HB}(\text{tz})_3)_2]$ ($\text{tz} = 1,2,4\text{-triazol-1-yl}$), displaying robust, above room temperature SCO 0. This molecular complex can be deposited by vacuum thermal evaporation, which allowed us to integrate it into different fundamental device configurations, including two-terminal, multilayer resistance switching junctions and three-terminal field-effect transistors. In the course of this work, we fabricated various multilayer metal/SCO/metal structures and we recognized that these structures exhibit also

remarkable photonic functionalities, besides their electrical properties. This has led to an unforeseen outcome, which consists in the development of tunable optical resonators, based on the SCO phenomenon. The thesis is organized in four chapters:

Chapter 1 begins with a brief, general introduction to the SCO phenomenon, including ligand-field considerations and the description of different stimuli to trigger the SCO as well as techniques to characterize it. Then, we review the state-of-the-art of evaporable SCO thin films as well as SCO thin film based electronic devices, classified as two- or three-terminal devices.

Chapter 2 focuses on the integration of $[\text{Fe}(\text{HB}(\text{tz})_3)_2]$ thin films in two-terminal, large-area, multilayer electronic devices, aimed for resistance switching functionality. Purity of the starting bulk, thin film qualities, fabrication and device operation conditions were taken into account to explore and optimize the device performance (ON/OFF switching ratios, cycling endurance, ...). The charge transport mechanism associated with the resistance switching is also discussed. Finally, we present the fabrication and characterization of the first multilayer SCO junctions with magnetic electrodes.

Chapter 3 is devoted to the integration of $[\text{Fe}(\text{HB}(\text{tz})_3)_2]$ thin films into three-terminal, organic field-effect transistors (OFETs). Different device configurations are compared (bottom gate – bottom contact, bottom gate – top contact, ...), aiming for the use of the SCO phenomenon to modulate the transfer/output characteristics of the transistors.

Chapter 4 is built on the expertise gained during the development of multilayer metal/ $[\text{Fe}(\text{HB}(\text{tz})_3)_2]$ /metal stacks. Contrary to the previous chapters, here the focus is on the optical properties of these multilayer structures. In particular, the design and properties of Fabry Perot cavities are presented and the modulation of the cavity resonance due to the SCO phenomenon is demonstrated.

The thesis end with some general conclusions and perspectives.

Chapter 1 Introduction

In this chapter, we will first briefly discuss the basic aspects of molecular spin crossover (SCO) phenomenon, including the electronic and thermodynamical aspects as well as the different stimuli, which can induce the SCO. The second part of the chapter summarizes the state of the art of the fabrication and characterization of SCO films made by vacuum thermal evaporation, which will be the privileged fabrication technique we use all along this thesis. The chapter ends by a review about the state of the art of SCO-based electronic devices, including both 2- and 3-terminal devices. This review serves as the starting point for our work on SCO-based electronic junctions and SCO-based transistors, which will be discussed in Chapters 2 and 3, respectively.

1.1 Introduction to the spin crossover phenomenon

1.1.1 Molecular aspects of the spin crossover phenomenon

According to the crystal field theory, in an octahedral ligand field, the five degenerate d orbitals (in the case of the free metal ion) undergo energy splitting into two energy levels: a low energy level t_{2g} and a higher energy level e_g . For an octahedral complex with a $3d^4$ — $3d^7$ transition metal ion, according to the strength of the ligand field around the metal ion, its spin state can either be high spin (HS) or low spin (LS). In a weak ligand field, the crystal field splitting energy $10Dq$ is less than the electron pairing energy P , which is beneficial to the d electrons to occupy both the t_{2g} and e_g energy levels, *i.e.* a high-spin state with maximum spin multiplicity. Conversely, in a strong ligand field, the crystal field splitting energy $10Dq$ is greater than the electron pairing energy P , and the d electrons occupy fully the t_{2g} energy level before occupying the high energy e_g orbitals, *i.e.* a low-spin state with minimum spin multiplicity [2].

Among transition metal complexes with $3d^4$ — $3d^7$ electronic configurations, Fe(II) has been mostly investigated, although the SCO phenomenon has been also reported for Fe(III), Co(II), Co(III), Cr(II), Mn(II) and Mn(III) complexes [3-6]. In this thesis, we have worked exclusively with spin crossover complexes, which have an Fe(II) central ion ($3d^6$). Figure 1.1 shows the HS and LS electronic configurations of an octahedral ferrous complex. In the low spin state the complex is diamagnetic ($S=0$), whereas in the high spin state it is paramagnetic ($S=2$).

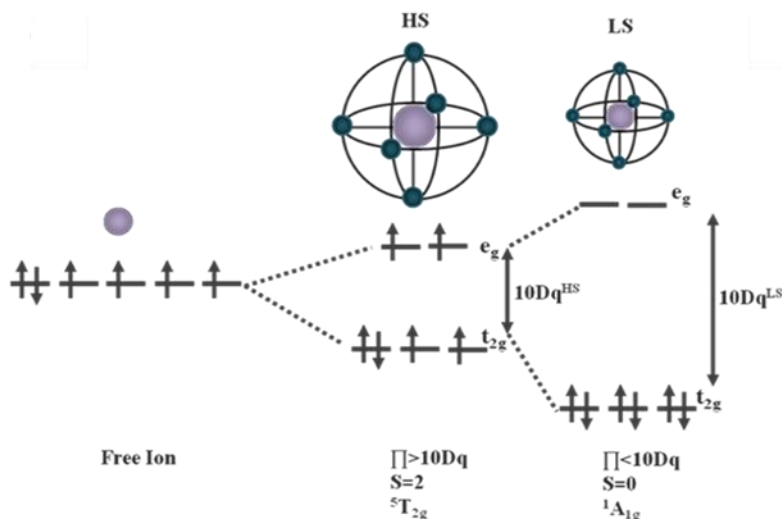


Figure 1.1: Energy splitting of the 3d orbitals of an Fe(II) ion in an octahedral environment induced by the ligand field ($10Dq$) – showing both the weak and strong field cases.

When the energy gap (ΔE_{HL}^0) between the high-spin and low-spin potential wells is small enough (comparable to the thermal energy), different external stimuli (temperature, light, pressure, *etc.*) could induce a change of spin state (Fig. 1.2).

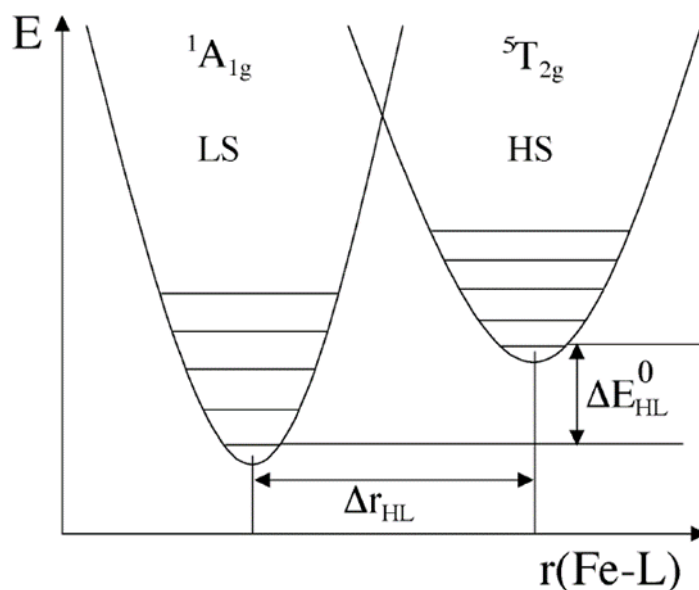


Figure 1.2. Simplified configurational diagram of the two molecular spin states (HS and LS) for an octahedral Fe(II) complex [2].

We call this phenomenon as spin transition or spin crossover. As a consequence of spin crossover, physical properties (magnetic, optical, electric, mechanical, *etc.*) of the complex thus change. It is important to notice that the SCO phenomenon is associated with a significant

change of the molecular structure. In particular, the metal-ligand distance increases substantially when going from the LS to the HS state. For example, in the case of Fe(II) complexes with 6 nitrogen donor atoms the mean Fe-N distance typically increases by 10% from *ca.* 2 to 2.2 Å [2].

1.1.2 Spin crossover induced by different stimuli

The spin crossover between the two spin states can be triggered by various external stimuli, such as temperature, light irradiation, pressure, an intense magnetic field, etc. Among these factors, the most usual way to change the spin state is to change the temperature, which is also the method applied in this thesis to detect the spin transition. From a thermodynamic point of view, the SCO originates from a competition between enthalpy, which tends to favor the lower energy fundamental state (LS) at low temperatures, and the entropy, which favors the most disordered thermodynamic phase (HS) at high temperatures [3, 7].

A spin transition curve, drawn as the high spin (HS) fraction versus temperature, can provide a lot of information based on its shape. The typically observed behaviors are shown in Figure 1.3 [7]. The gradual spin crossover (Fig. 1.3a), which spans over several tens or hundreds degrees range is typically observed in diluted systems (*e.g.* in a solution), although we can also observe sometimes this behavior in certain bulk solids, in which the SCO molecules do not (or weakly) interact with each other. The main reason that causes different spin crossover behavior is the degree of interactions (cooperativity) between molecules, which is determined by the characteristics of the crystal lattice. As such, the behaviors shown in Figures 1.3b-1.3e are encountered mostly in bulk crystalline SCO materials. The cooperativity of the SCO arises primarily from elastic interactions between the molecules and, in a first approximation, it can be traced back to the volume change associated with the spin transition (typically 1-10%). If the degree of coordination in the system increases, the spin transition curve becomes more and more abrupt (Figure 1.3b). When there is a high degree of cooperativity in the system, the spin transition may be associated with a hysteresis, as shown in Figure 1.3c. In such a system, the hysteresis may have two origins: either the interactions between the SCO molecules are very strong or it may be also related to a coupled structural phase change in the crystal lattice. (N.B. In the latter case, the HS and LS phases are not isostructural and the origin of the cooperativity becomes less clear.) In any case, the hysteresis loop confers a memory effect to the system, which can be used in different applications such as information storage devices, molecular switches, sensors or displays. This is the reason why SCO systems with hysteresis (especially around room temperature) are sought for by synthetic chemists [8].

For a small class of materials, the spin crossover that occurs in two or even more steps can be detected (Figure 1.3d). This behavior may occur for several reasons: either simply because the metal ions occupy two (or more) different lattice sites in the material, or a preferential formation of LS-HS pairs happens due to a competition between different interactions [11].

Finally, the incomplete spin transition, shown in Figure 1.3e, can be explained by the presence of some heterogeneities (defects, surfaces/interfaces, *etc.*) in the lattice sites capable of preventing the formation of LS and/or HS species. Another cause may be due to some kinetic effect found at low temperatures, when the conversion rate from one state to another is extremely low [7].

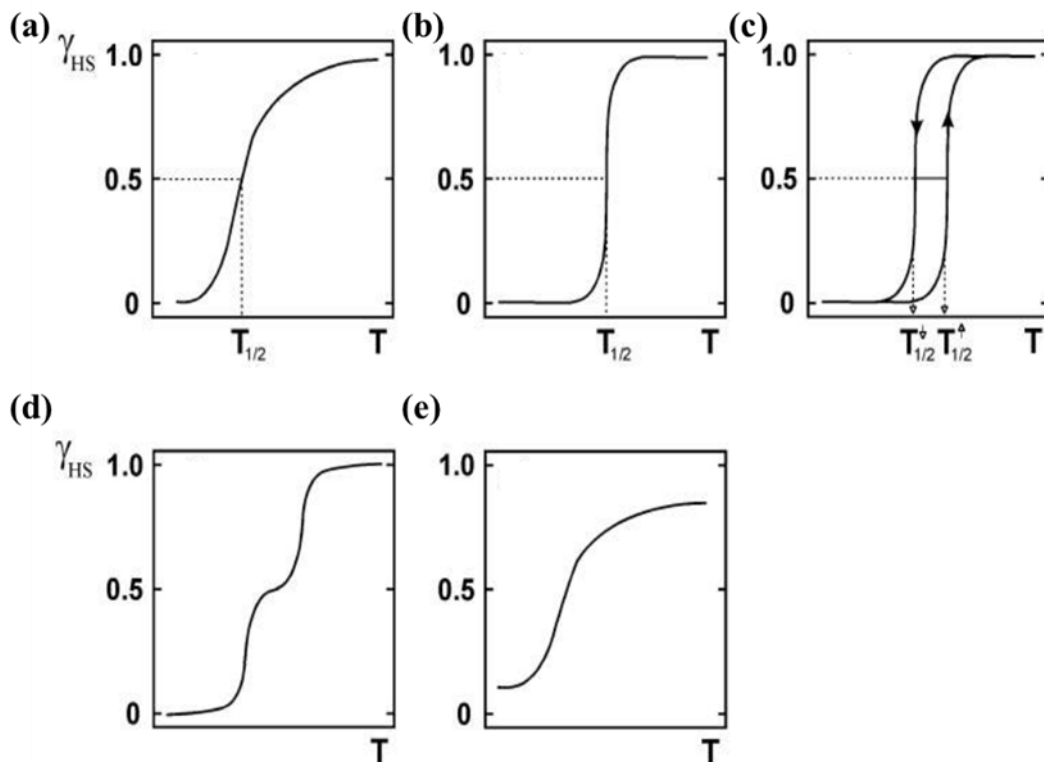


Figure 1.3: Representation of (a) gradual, (b) abrupt, (c) hysteresis, (d) two-step and (e) incomplete thermal spin transition curves [9].

Another stimulus that can trigger spin transition is pressure [12, 13]. From a thermodynamical point of view, higher pressure is favorable for the LS state, which has smaller volume. As a result, increasing pressure leads to a higher spin transition temperature, as shown in Figure 1.4. In addition, pressure could also modify the width of hysteresis. Whereas the width of hysteresis usually decreases when applying higher pressure on a SCO system, there are also

exceptions to this rule, indicating that the effect of pressure is more complex. (For example, it can induce also additional structural changes, *etc.*)

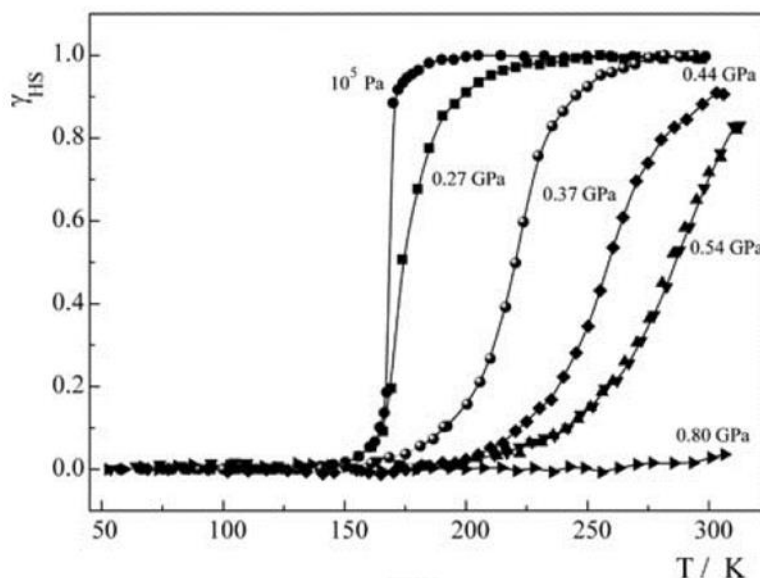


Figure 1.4: Pressure effect on spin transition behavior of the SCO complex $[\text{CrI}_2(\text{depe})_2]$ [17].

Light (x-ray, UV, visible or near IR) is also an important tool to induce the spin transition. The two most famous light-induced phenomena are the LIESST (Light Induced Excited Spin State Trapping) and the LD-LISC (Ligand-Driven Light Induced Spin Crossover) effects. The former is a direct effect on the metal ion and it occurs at low temperatures [14, 15]. The latter is an indirect effect through a photo-isomertizable coordinated ligand [16].

Besides the most common stimuli we mentioned above, it is worth to mention that many other physico-chemical stimuli/parameters, such as intense magnetic fields, electrons, guest molecules, pH, *etc.* could also influence the spin crossover process [18].

1.1.3 Experimental techniques to characterize the SCO phenomenon

The SCO is accompanied by a spectacular change of both the molecular structure and electronic properties. As a result, nearly all material properties (magnetic, optical, mechanical, electrical, *etc.*) are altered, which creates opportunities for using a broad variety of experimental techniques for the detection and investigation of the SCO phenomenon. The most common techniques to characterize spin crossover are magnetic susceptibility measurements, X-ray diffraction, electronic spectroscopy (UV-VIS), vibrational spectroscopy (Raman, FTIR), Mössbauer spectroscopy and calorimetry. With the development of technology, these

measurements can be conducted under different external stimuli, allowing for the study of temperature, pressure or light induced spin-crossover behavior. In our work, we used mostly variable temperature UV-VIS detection, combined in certain cases with magnetometry, Raman spectroscopy and grazing incidence x-ray diffraction.

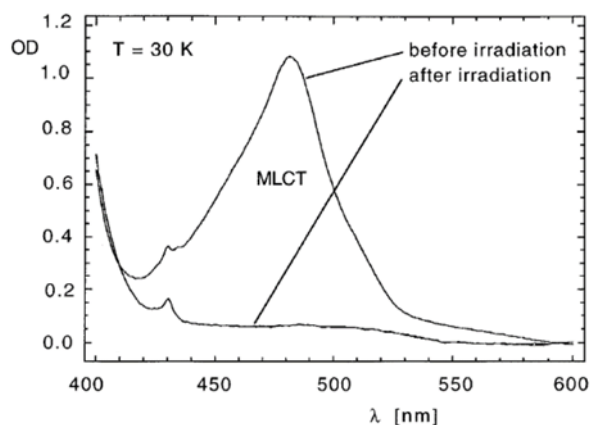


Figure 1.5: Optical absorption spectra of $[\text{Zn}_{1-x}\text{Fe}_x(\text{pic})_3]\text{Cl}_2 \cdot \text{EtOH}$ at 30 K in the LS (before irradiation) and HS (after irradiation) states [19].

The change of electronic configuration can be directly probed by variable temperature magnetic susceptibility measurements, which is the most common and direct means of characterization, as well as by optical absorption measurements in the UV-VIS spectral range. Nevertheless, it is worth to note that magnetic susceptibility can only provide the average value of the magnetic moment, whereas UV-VIS spectroscopy can clearly witness changes of spectral features associated with the two spin states (see for example Fig. 1.5). (N.B. The relevant spectral features can be either metal-centered ligand-field transitions or metal – ligand charge transfer transitions [2].) Since the thermally induced spin crossover usually leads to an obvious color change, variable temperature optical reflectivity provides also a simple, cheap and fast method for the detection of SCO. However, it is important to notice that contrary to the optical absorption, the quantitative analysis of reflectivity data is significantly more difficult.

Because the d electrons in the HS and LS states are distributed in different ways between the non-bonding t_{2g} and anti-bonding e_g orbitals (Fig. 1.1), an important change of metal-ligand bond lengths occurs at the SCO. These (and other) changes of the molecular (and crystal) structure can be conveniently investigated by x-ray diffraction methods on single crystals, microcrystalline powders and thin films as well [20]. Obviously, these structural changes also

affect the vibrational spectra (Raman scattering and IR absorption), which are often used as “fingerprints” to follow the spin state changes [21].

1.2. From bulk to thin film applications: vacuum thermal evaporation

The recent progress in developing SCO materials inspired several teams around the world to exploit the impressive physical/chemical property changes associated with SCO in functional devices, such as switches, memories, sensors, displays and more recently in mechanical actuators [22, 23]. To apply SCO materials in a ‘real-world’ applications, it is necessary to process them in thin-film form. However, the fragility of the SCO phenomenon and the relatively poor processability of SCO materials have limited their development for technological applications. The fragility of the SCO phenomenon depends on the fact that SCO properties critically depend on the molecular environment (*e.g.* packing, crystallinity, solvent molecules, anions, *etc.*), which, in order to preserve the SCO phenomenon, must be carefully controlled during the processing. In addition, it is important to underline that the SCO behavior usually varies from the bulk powder to thin film state, due to different factors. First of all, the mere fact that the film is obtained in different conditions than the bulk can lead to different SCO properties. In particular, when using vacuum thermal evaporation the as-deposited SCO films are often amorphous (*vide infra*). Furthermore, when reducing the film thickness, the impact of the surfaces/interfaces on the film properties will be more and more important [23]. For very thin films (*e.g.* a few monolayers) one may wonder if a comparison with the bulk makes sense. On the other hand, in this regime, the interactions with the substrate become predominant [24].

Recently a great progress has been made towards the growth of SCO thin films and the fabrication of SCO nanostructures [25]. The synthesis of new more stable and processable compounds and the development of new specifically dedicated procedures for processing have permitted this important progress, opening new technological perspectives for SCO compounds, and renewing the interest in the field. Among the most popular techniques, we can mention the Langmuir–Blodgett (LB) deposition [26], layer-by-layer assembly [27], drop casting [28], spin-coating [29], spray-coating [30], electrochemical deposition [31], blade casting [32] and vacuum thermal evaporation [49] techniques for the fabrication of SCO thin films [24, 33]. Among these techniques, vacuum thermal evaporation turns out to be a preferred method to deposit large-area, high quality, continuous and smooth SCO thin films with sub-micrometer thickness. The schematic diagram for a vacuum thermal evaporator is shown in Figure 1.6. The

technique of thermal evaporation involves heating evaporable materials (either by Joule effect, either by an electron gun) under high vacuum (typically ranging from 10^{-5} to 10^{-9} mbar). A homogeneous thickness can be achieved on relatively large areas (*e.g.* 4 inches) by rotating the substrate. In some instruments, it is also possible to heat or cool the substrate, which can be used to adjust the properties of the deposited films in-situ (*e.g.* crystallinity, morphology, *etc.*). The evaporation rate and film thickness are monitored in-situ by a quartz crystal microbalance.

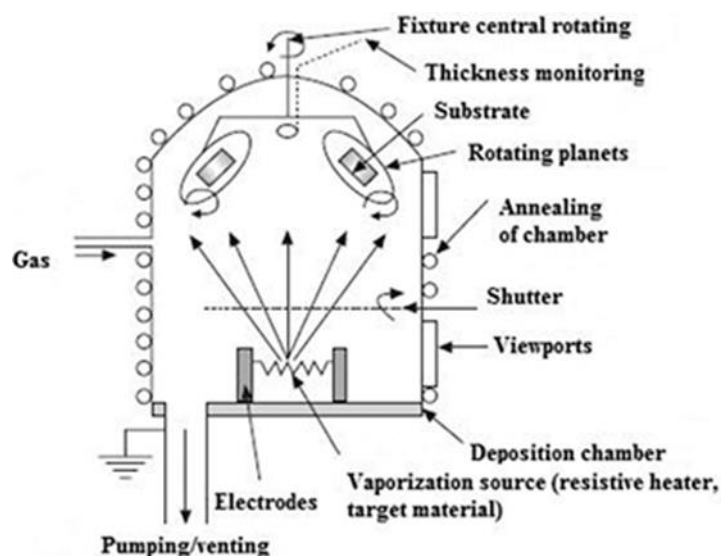


Figure 1.6: Schematic diagram of a vacuum thermal evaporation system [45].

A list (aimed to be exhaustive) and some basic characteristics of the reported thermally evaporable SCO molecules is provided in Table 1.1. Despite many efforts from different research teams, the list is rather short, because of the general requirements on the complexes to be evaporated (charge-neutral, small molecular weight, thermally stable, solvent free, *etc.*). In most cases, the thermally evaporable SCO complexes are Fe(II) complexes from the family of scorpionate complexes, *i.e.* pyrazolyl and triazolyl-borate derivatives [46]. In the following sections, we will provide some more details only on those evaporable SCO complexes, which have been integrated into an electronic device (*cf.* Section 1.3). Further information on the other sublimable SCO complexes can be found in recent reviews [24, 46].

Table 1.1: List of the sublimable SCO complexes reported in the literature. The SCO temperatures ($T_{1/2}$) and hysteresis widths (ΔT) in the bulk and thin film forms as well as the sublimation temperature (T_{sub}), and sublimation pressure (P_{sub}) are also shown.

Molecule	$T_{1/2}/\Delta T$ (K, bulk)	Thickness of thin film (nm)	$T_{1/2}/\Delta T$ (K, thin film)	T_{sub} (K) / P_{sub} (mbar)	Ref
[Fe(phen) ₂ (NCS) ₂]	176/ \approx 1	280	175	453/ 10^{-8}	[47]

[Fe(H ₂ B(pz) ₂) ₂ (phen)]	163.7/ ≈ 4	355	151/6	435/10 ⁻²	[48]
[Fe(H ₂ B(pz) ₂) ₂ (bipy)]	160	564	153/4	433/10 ⁻²	[48]
[Fe(H ₂ B(pz) ₂) ₂ L ¹]	141	>100	148	448/3×10 ⁻⁸	[50]
[Fe(H ₂ B(pz) ₂) ₂ L ²]	140	5		425/1×10 ⁻¹⁰	[51]
[Fe(H ₂ B(pz) ₂) ₂ L ³]	154	230	≈ 150	/4.3 × 10 ⁻⁸	[52]
[Fe(H ₂ B(pz) ₂) ₂ L ⁴]	197	10	176.5	423/	[53]
[Fe(dpepd)(NCS) ₂]	≈ 251	0.8 monolayer	235(6)	510/5×10 ⁻⁹	[54]
[Fe(HB(pz) ₃) ₂]	393			463/ ≈ 10 ⁻⁵	[56]
[Fe(HB(tz) ₃) ₂]	333/ ≈ 1	100	336	523/ ≈ 2×10 ⁻⁷	[58]
[Fe(HB(3,5-(CH ₃) ₂ (pz) ₃) ₂)]	190/31	130	152/17	393-413/10 ⁻⁸	[59]
[Fe(qnal) ₂]·xCH ₂ Cl ₂	220 (x=1) and 260 (x=0)	50	210	490/10 ⁻⁷	[60]
[Fe(pypyr(CF ₃) ₂) ₂ (phen)]	390	40 monolayer	330	433/5×10 ⁻⁹	[61]
[Fe(pap) ₂]ClO ₄ ·H ₂ O	172.5/15			~363/ 1×10 ⁻⁹	[62]

(phen = 1, 10-phenanthroline, NCS = N-Chlorosuccinimide, pz = pyrazol-1-yl, tz = 1,2,4-triazol-1-yl, bipy = 2,2'-bipyridine, dpepd = 1-{6-[1,1-di(pyridin-2-yl)ethyl]-pyridin-2-yl}-N,N-dimethylmethanamine, qnal = quinoline-naphthaldehyde, pypyr = 2-(2'-pyridyl)pyrrolide, pap = N-2-pyridylmethylidene-2-hydroxyphenylamino, qsal-I = 4-iodo-2-[(8-quinolylimino) methyl]phenolate, bapbpy = N,N'-di(pyrid-2-yl)-2,2'-bipyridine-6,6'-diamine, L¹ = 3,4,7,8-tetramethyl-1,10-phenanthroline, L² = 5,6-bis(2,5-dimethyl-3-thienyl)-1,10-phenanthroline, L³ = 5-amino-1,10-phenanthroline, L⁴ = dodecyl[2,2'-bipyridine]-5-carboxylate)

1.2.1 [Fe(phen)₂(NCS)₂] thin films

The first studied example of a thermal evaporable SCO complex in a thin film form is the compound [Fe(phen)₂(NCS)₂]. Figure 1.7a depicts the molecular structure. As described by Shi *et al.* [47], [Fe(phen)₂(NCS)₂] thin films with different thickness (from a few nanometers to hundreds of nanometers) were deposited on silicon or glass substrates by thermal evaporation at 180 °C from a molybdenum boat in a chamber with a base pressure of 10⁻⁸ mbar. The deposition rate was 0.1 nm/s. SQUID measurements were carried out to compare the spin transition of the bulk and thin film forms. As shown in Figure 1.7b, the [Fe(phen)₂(NCS)₂] complex in its bulk form exhibits an abrupt SCO with T_{1/2} ≈ 176 K. On the other hand, a 280 nm thick [Fe(phen)₂(NCS)₂] film exhibits gradual SCO with T_{1/2} ≈ 175 K [47]. It is worth to note that a LIESST effect was observed in the bulk material at low temperatures, but to our best knowledge, no light-induced switching was reported for thin films. The reported RMS roughness is 0.33 nm for the 280-nm-thick film on silicon and 0.29 nm for the 240-nm-thick film on glass. For both silicon and glass substrates, the films are smooth with no visible grains. However, the film morphology is sensitive to the environment and becomes coarse when exposed to air. Unfortunately, there were no reports on the structure/crystallinity of the films. It may be worth to note that by playing with the ligand, a similar complex, [Fe(dpepd)(NCS)₂] was obtained, which showed a gradual SCO with T_{1/2} ≈ 251 K in a *ca.* one monolayer thick film [54].

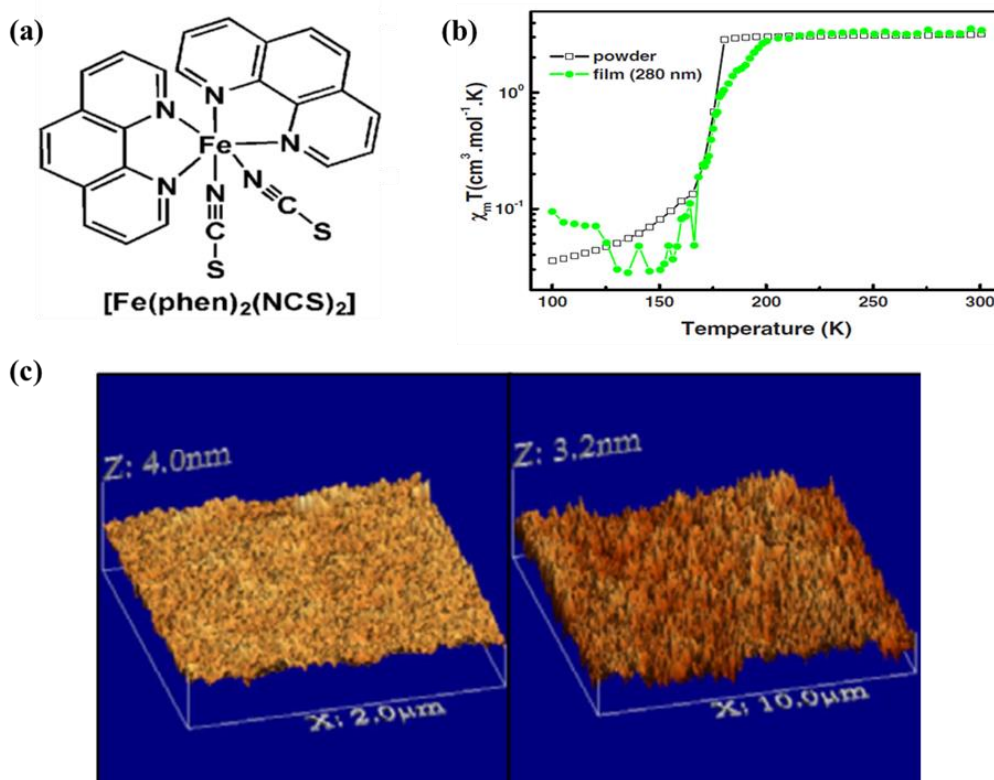


Figure 1.7: (a) Molecular structure of $[\text{Fe}(\text{phen})_2(\text{NCS})_2]$. (b) Temperature dependence of $\chi_m T$ for the powder and the 280-nm-thick film on silicon substrate. (c) AFM images of thin films deposited by high vacuum evaporation: Left: 280 nm on silicon substrate and right: 240 nm on glass substrate [47].

1.2.2 $[\text{Fe}(\text{H}_2\text{B}(\text{pz})_2)_2(\text{phen})]$ thin films

Figure 1.8a depicts the molecular structure of the complex $[\text{Fe}(\text{H}_2\text{B}(\text{pz})_2)_2(\text{phen})]$. The evaporation was carried out under a vacuum of 5×10^{-7} mbar with a nominal rate of 0.07 nm/s at 160 °C on glass, quartz, copper and Kapton substrates. AFM images show the thin film on Au substrate is homogeneous, smooth and pinhole free (Fig. 1.8) [48, 49]. Alternatively the spin transition behavior in thick films (several hundreds of nanometers on a Kapton tape) was investigated by magnetic susceptibility measurements. UV-VIS measurements were also conducted on films deposited on glass substrates [49]. Compared to its bulk counterpart, which exhibits an abrupt SCO with $T_{1/2} \approx 160$ K as well as a hysteresis of 4 K, $[\text{Fe}(\text{H}_2\text{B}(\text{pz})_2)_2(\text{phen})]$ films exhibit a rather gradual SCO with $T_{1/2} \approx 155$ K (Fig. 1.8b). This difference is most probably related to the fact that the evaporated films of $[\text{Fe}(\text{H}_2\text{B}(\text{pz})_2)_2(\text{phen})]$ are amorphous [48]. This can also explain the observation that the SCO curves in these films appears very similar both in thick and thin films [48]. It is important to note that the LIESST effect was observed both in the bulk and thin film forms of this complex.

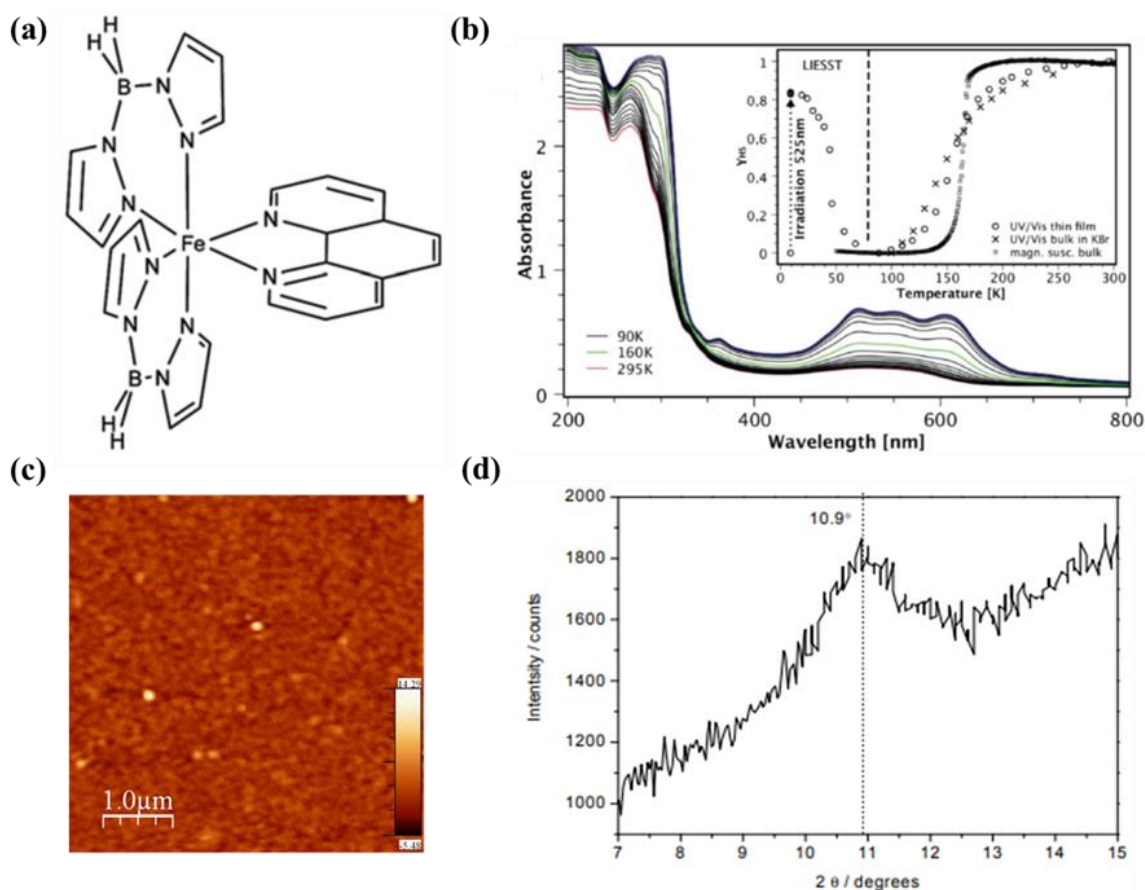


Figure 1.8: (a) Molecular structure of $[\text{Fe}(\text{H}_2\text{B}(\text{pz})_2)_2(\text{phen})]$. (b) UV/Vis spectra of thin films between 300 and 90 K. Inset: High-spin fraction γ_{HS} determined by UV/Vis spectroscopy and magnetic susceptibility. (c) AFM image of a thin film on gold substrate. (d) X-ray diffraction of a thin film on Cu substrate [48, 49].

1.2.3 $[\text{Fe}(\text{H}_2\text{B}(\text{pz})_2)_2(\text{bipy})]$ thin films

In parallel to $[\text{Fe}(\text{H}_2\text{B}(\text{pz})_2)_2(\text{phen})]$, the related complex $[\text{Fe}(\text{H}_2\text{B}(\text{pz})_2)_2(\text{bipy})]$ was also investigated in its thin film form, in the same publications [48, 49]. The vacuum thermal evaporation was carried out using similar equipment, but the deposition temperature for the bipy derivative was significantly lower (130 $^\circ\text{C}$). Figure 1.9a depicts the molecular structure of $[\text{Fe}(\text{H}_2\text{B}(\text{pz})_2)_2(\text{bipy})]$. The thermally-induced SCO in the films of $[\text{Fe}(\text{H}_2\text{B}(\text{pz})_2)_2(\text{bipy})]$ is centered around 165 K and it becomes more gradual with respect to the bulk material (Fig. 1.9b). Surface topography investigation with AFM shows clearly the formation of microcrystallites with micrometer lateral sizes and heights up to *ca.* 160 nm, as shown in Figure 1.9c. The X-ray diffractogram of the thin film on glass substrate indicates a high crystallinity, which was also observed for the thin film on Cu substrate [48].

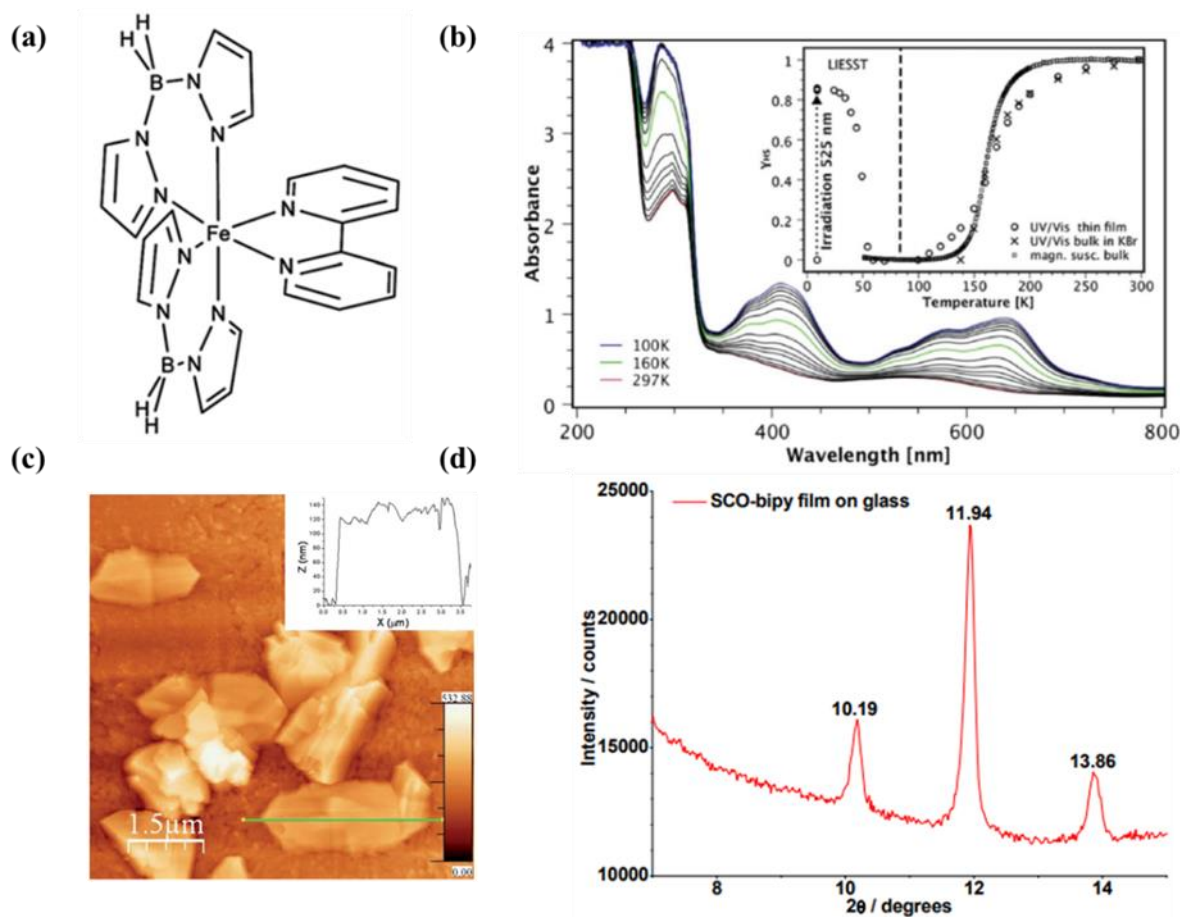


Figure 1.9: (a) Molecular structure of $[\text{Fe}(\text{H}_2\text{B}(\text{pz})_2)_2(\text{bipy})]$. (b) UV/Vis spectra of thin films between 300 and 90 K. Inset: High-spin fraction γ_{HS} determined by UV/Vis spectroscopy and magnetic susceptibility. (c) AFM image of a thin film on quartz substrate. (d) X-ray diffraction of a thin film on glass substrate [48, 49].

1.2.4 $[\text{Fe}(\text{HB}(\text{pz})_3)_2]$ thin films

Figure 1.10a depicts the molecular structure of the $[\text{Fe}(\text{HB}(\text{pz})_3)_2]$ complex. The SCO properties of this compound are rather peculiar. Indeed, when the bulk solid is thermally cycled for the first time an apparent hysteresis is observed (Figure 1.10b). However, for all subsequent cooling and heating treatments, the magnetic properties retrace the initial cooling curve and not the initial heating curve. One can thus conclude that the as-synthesized sample is thermodynamically metastable (due to structural reasons [55]). This irreversible behavior upon the first cycle is also seen in the temperature dependence of the conductivity of this complex (Figure 1.10c) [55]. This property was then exploited with thin films deposited by vacuum thermal evaporation on gold interdigitated microelectrodes, which afforded for a read-only

memory (ROM) device [56]. Unfortunately, no detailed study on the SCO properties and crystal structure were reported.

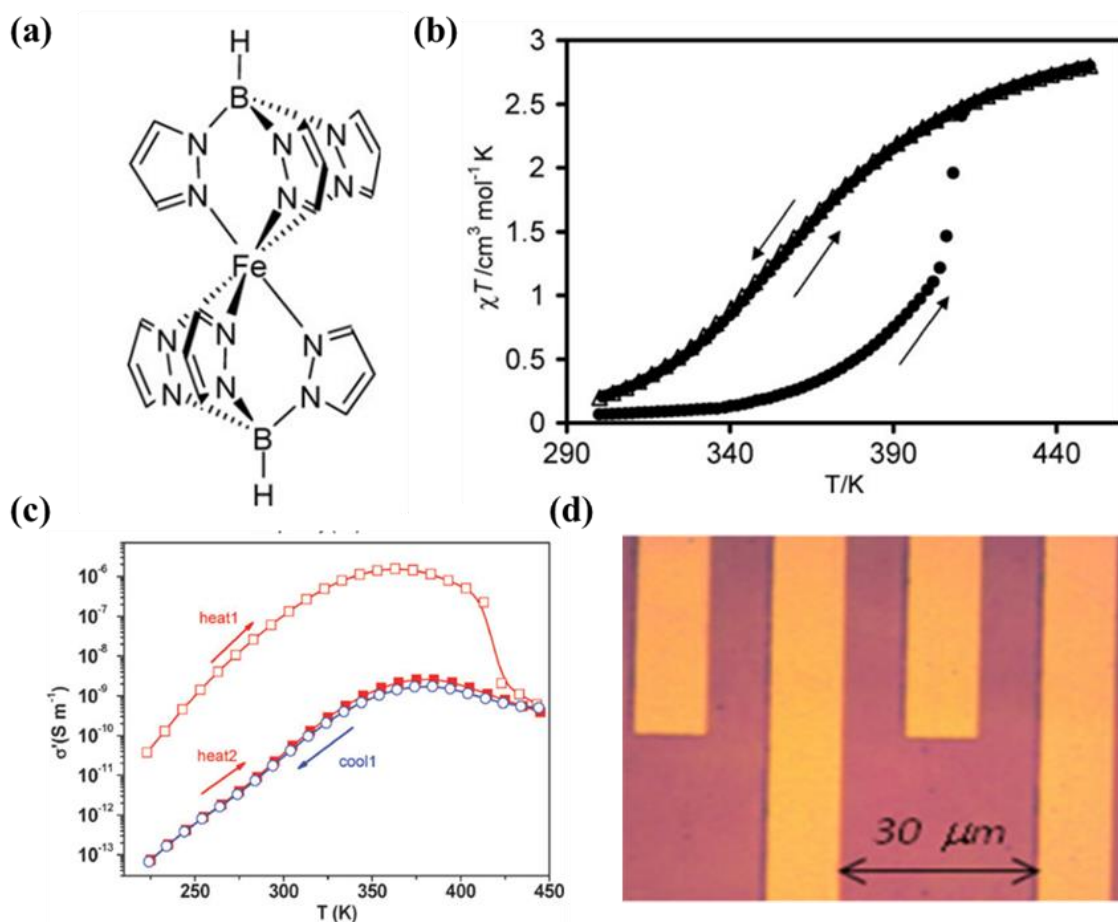


Figure 1.10: (a) Molecular structure of $[\text{Fe}(\text{HB}(\text{pz})_3)_2]$. Temperature dependence of the magnetic susceptibility (b) and ac conductivity (c) of the bulk. (d) Optical image of the thin film on interdigitated electrodes [55, 56].

1.2.5 $[\text{Fe}(\text{H}_2\text{B}(\text{pz})_2)_2\text{L}^3]$ thin films

The molecular structure of $[\text{Fe}(\text{H}_2\text{B}(\text{pz})_2)_2\text{L}^3]$ ($\text{L}^3 = 5\text{-amino}1,10\text{-phenanthroline}$) is shown in the insert of Figure 1.11a). The complex was deposited on patterned Au electrodes under a high vacuum of 4.3×10^{-8} mbar. The temperature dependence of the magnetic susceptibility of the bulk indicates that the transition temperature is *ca.* 154 K. X-ray absorption spectroscopy (XAS) confirmed the spin state change in the film samples (Fig. 1.11b), but the SCO in the films appeared rather incomplete (see also Section 1.3.1.2). Unfortunately, no information on the morphology and crystallinity of the films was provided [52].

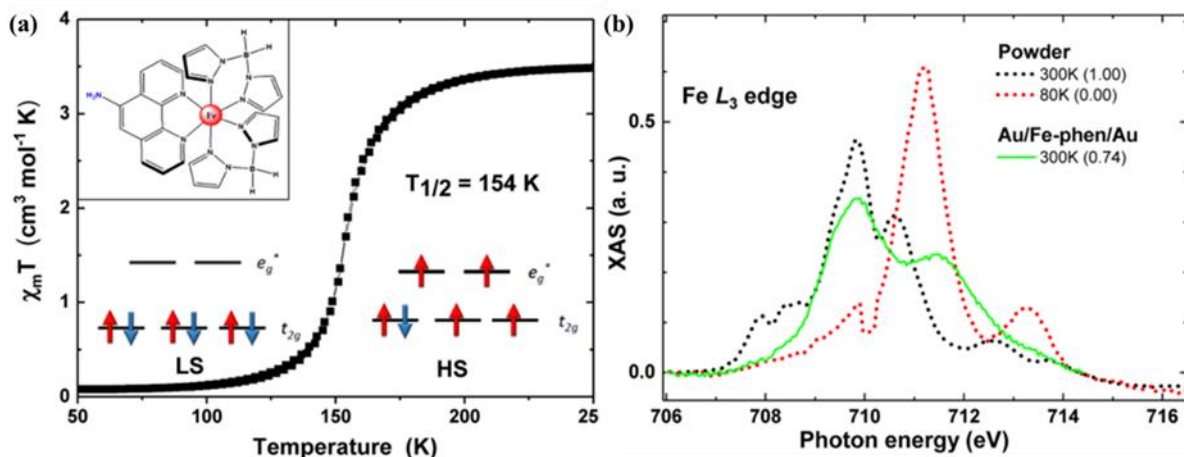


Figure 1.11: (a) $\chi_m T$ vs T plot of the $[\text{Fe}(\text{H}_2\text{B}(\text{pz})_2)_2\text{L}^3]$ bulk powder, insert : molecular structure. (b) X-ray absorption spectra at the Fe L_3 edge of the powder reference in the HS state (at 300 K, black) and LS state (at 70 K, red) and of the Au/ $[\text{Fe}(\text{H}_2\text{B}(\text{pz})_2)_2\text{L}^3]$ /Au trilayer at 300 K (green line) [52].

1.2.6 $[\text{Fe}(\text{HB}(3,5\text{-(CH}_3)_2(\text{pz})_3)_2]$ thin films

Figure 1.12(a) depicts the molecular structure of the $[\text{Fe}(\text{HB}(3,5\text{-(CH}_3)_2(\text{pz})_3)_2]$ complex. Films with various thicknesses from 130 to 8500 nm were thermally evaporated at 125 °C under an ultra-high vacuum [61]. The AFM topographic images show extended, dense coverages of the substrates formed by grains of matter. For example, the 130 nm thick films consist of two populations of nanograins whose sizes average around 110(30) and 230(60) nm. Temperature dependent of UV-vis absorption of a 130 nm thick film clearly reveals the spin transition of the thin film, as depicted in Figure 1.12b. However, the SCO in the films becomes complete only after thermal annealing. Indeed, the films show clear crystallinity and preferential orientation, as it can be deduced from the x-ray diffraction patterns (Figure 1.12d). However, the diffraction pattern changes upon annealing and the complicated polymorphism in the sample gives rise to unusual features, such as incomplete and strongly asymmetric hysteresis loops – both in the bulk and thin films samples.

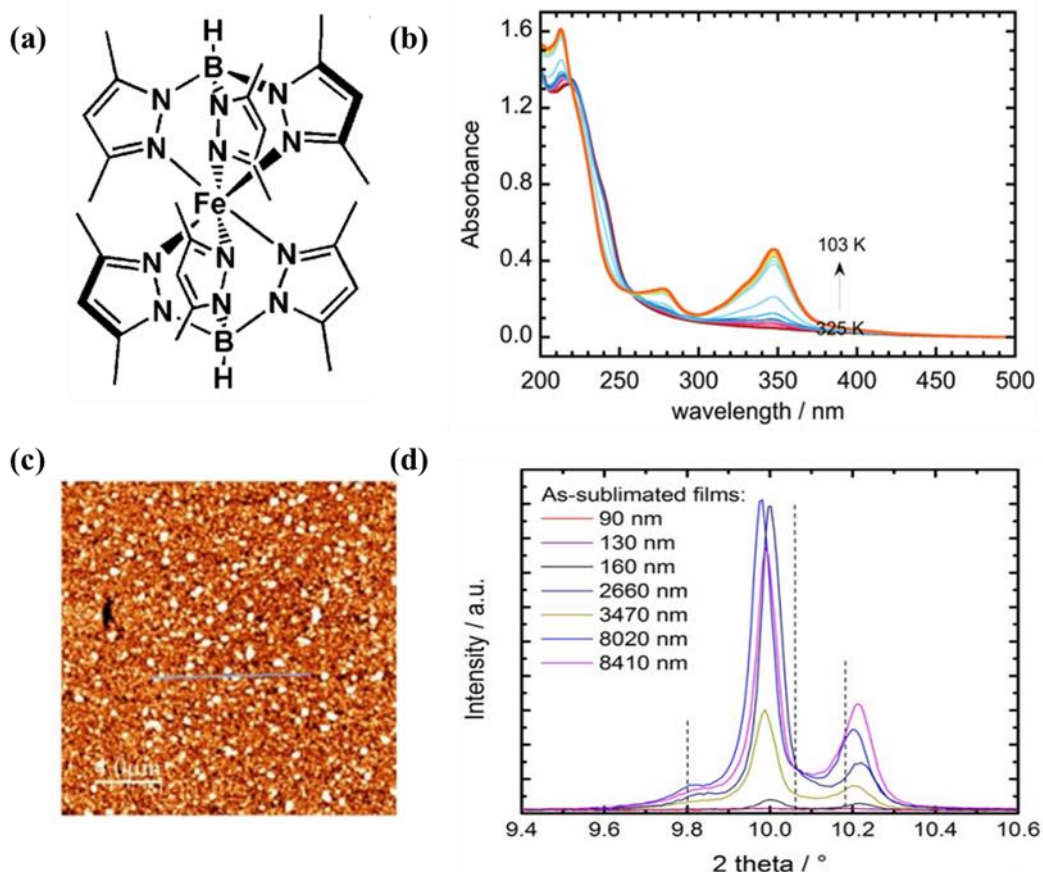


Figure 1.12: (a) Molecular structure of [Fe(HB(3,5-(CH₃)₂(pz)₃)₂]. (b) UV absorption spectra recorded upon cooling the as-sublimed 130 nm-thick film. (c) AFM topography image of the as-sublimed 130 nm-thick film. (d) X-ray diffraction patterns of as-sublimed films between 90 and 8500 nm thickness [59].

1.2.7 [Fe(qnal)₂] thin films

Figure 1.13 depicts the molecular structure of the [Fe(qnal)₂] complex. The thin film was obtained by thermal sublimation in a high vacuum chamber (10⁻⁷ mbar) at a temperature of *ca.* 590 K on a muscovite surface coated with 200 nm Au(111). Actually, the as synthesized bulk complex exists as a solvated crystalline form [Fe(qnal)₂]·CH₂Cl₂, but it can be turned into the unsolvated [Fe(qnal)₂] form, through a thermal treatment at 460 K under ambient pressure. The thin films showed thermally-induced SCO ($T_{1/2} = 210$ K) as well as light and X-ray induced spin state switching phenomena. As shown in Figure 1.13b, the SCO in the [Fe(qnal)₂] thin-film is very gradual and it is shifted to lower temperature in comparison to its solvated bulk counterpart. Using grazing-incidence XRD, the as-deposited films were shown to be crystalline with preferential orientation [60].

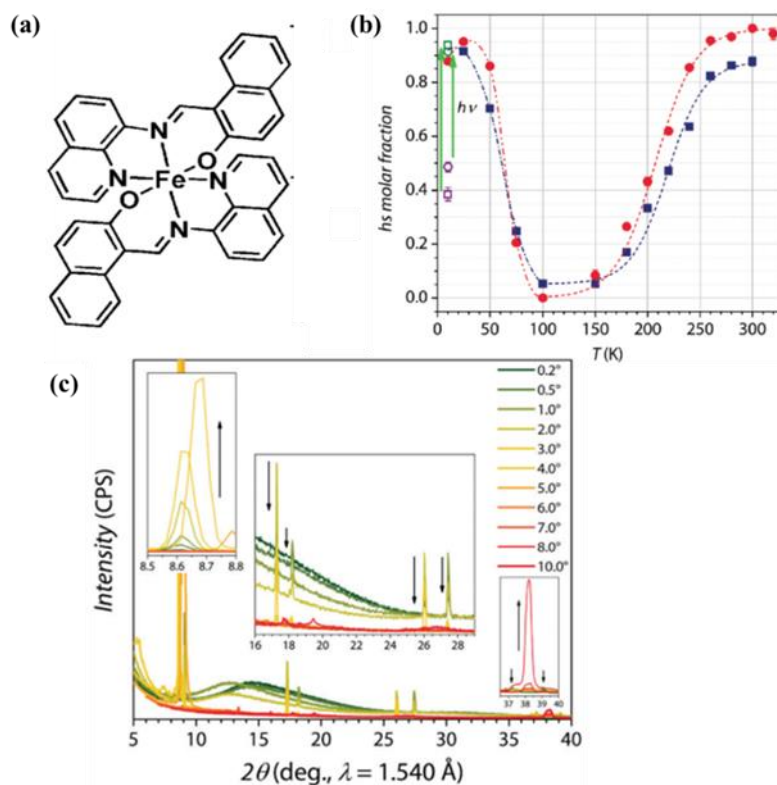


Figure 1.13: (a) Molecular structure of [Fe(qnal)₂]. (b) Temperature dependence of the HS fraction obtained from X-ray absorption spectra for a [Fe(qnal)₂] thin film (red circles) and the bulk [Fe(qnal)₂] \cdot CH₂Cl₂ sample (blue squares). The light-induced SCO is shown by green arrows. (c) GIXRD pattern at different incident angles. The insets show the principal diffraction peak (left), the higher-order peaks (middle), and the peak of the gold surface (right) in detail. Arrows indicate the intensity change upon incident angle increase [60].

1.2.8 [Fe(HB(tz)₃)₂] thin films

Finally, we discuss our ‘benchmark’ evaporable SCO complex, [Fe(HB(tz)₃)₂]. The molecular structure of [Fe(HB(tz)₃)₂] is shown in Figure 1.14a. According to the SQUID data, the microcrystalline bulk powder shows an abrupt SCO above room temperature ($T_{1/2} \approx 333$ K) with a small hysteresis loop ($\Delta T \approx 1$ K) [57]. Films of [Fe(HB(tz)₃)₂] with various thicknesses (20-200 nm) were deposited on different substrates (fused silica, Si(100) and polycrystalline Au). Thin films were grown by thermal evaporation at a base pressure of *ca.* 2×10^{-7} mbar. The bulk powder was heated until 250 °C in a quartz crucible and evaporated at a rate of 0.03 \AA s^{-1} . The as-deposited thin film is amorphous and exhibits unstable and ill-reproducible SCO behavior. However, it was discovered that a simple solvent vapor annealing (in water, diethyl-ether, acetone or ethanol) could allow for the recrystallization of the films [63]. AFM analysis

showed that the films are dense, continuous and smooth. GIXRD measurements on the solvent-annealed films revealed not only good crystallinity, but also a preferential orientation of the films along the c-axis of the orthorhombic unit cell. A detailed investigation of the solvent-annealed films with thicknesses in the range between 45 and 200 nm showed that all films exhibit a complete and fairly abrupt SCO ($T_{1/2} = 335\text{--}338\text{ K}$) with a tiny hysteresis loop ($< 1\text{ K}$). Figure 1.14b shows an example for the temperature dependence of the UV absorbance of a 90 nm thick film [58]. Taking into account the very robust and well reproducible SCO properties of these films as well as the fact that the SCO occurs above room temperature, we selected this compound to explore its SCO properties in functional devices in the frame of the present thesis work (*vide infra*).

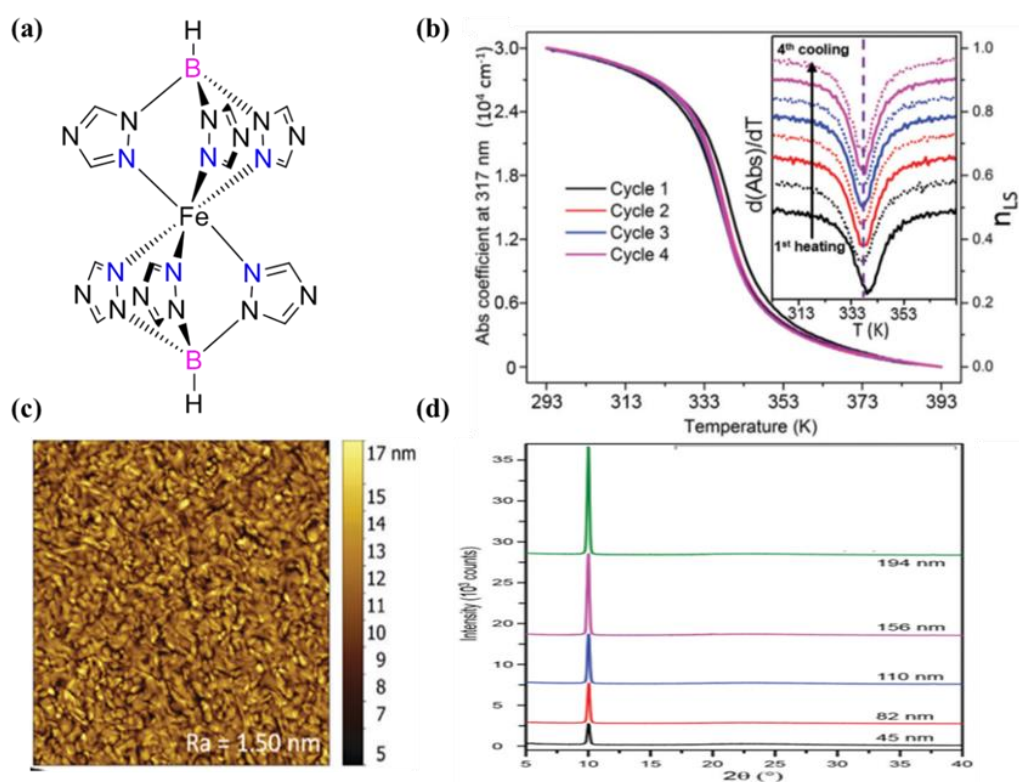


Figure 1.14: (a) Molecular structure of $[\text{Fe}(\text{HB}(\text{tz})_3)_2]$. (b) Temperature dependence of the absorbance at 317 nm in a 90 nm thin film along four heating–cooling cycles recorded at 1 K min^{-1} scan rate. The inset shows the derivatives of the transition curves. (c) AFM image ($10 \times 10\ \mu\text{m}^2$) of the solvent vapor annealed film. (d) XRD patterns of crystalline thin films for various thicknesses revealing preferential orientation 0.

1.3 State of art in SCO-based electronic devices

Thanks to spin state dependent physical properties (frontier molecular orbital energies, dielectric permittivity, *etc.*), SCO complexes (thin films, nanoparticles, nanorods, *etc.*) have been integrated into electronic devices aiming for the creation of new functional devices (switches, memories, *etc.*) [23, 73]. Both two-terminal devices, such as resistors, capacitors, generators, *etc.* and three-terminal devices, such as transistors, which act as fundamental, but significant elements in electronic circuits (Fig. 1.15) have been already considered in relation with SCO complexes. In this chapter, we will begin with a review of SCO-based electronic devices in two-terminal configuration, which will be further divided into horizontal (*i.e.* current in plane) and vertical (*i.e.* current out-of-plane) SCO devices for the discussion. More recently, SCO-based electronic devices with three-terminal configuration have been successfully fabricated and investigated, which we will introduce in the last section. (N.B. We must mention here that charge transport properties of SCO complexes have been also studied in 1D cavities of single-walled carbon nanotubes [34] and, using Scanning Tunneling Microscope, in 2D thin films - from sub-monolayer to bilayer coverage [35-43], but this exciting field is out of the scope of the present thesis.)

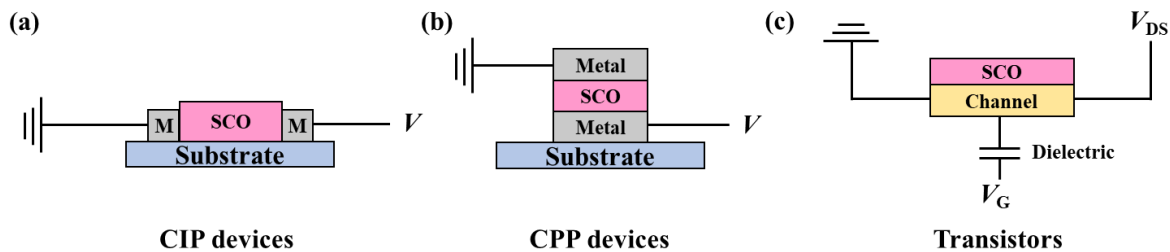


Figure 1.15: Representative schematic configurations of SCO-based (a) two-terminal CIP (current-in-plane) devices, (b) two-terminal CPP (current-perpendicular-to-plane) devices and (c) three-terminal transistors.

1.3.1 Two-terminal SCO-based electronic devices

1.3.1.1 Two-terminal SCO-based current-in-plane devices

The first two-terminal SCO-based horizontal electronic device was published in 2011 by Prins *et al.* [64]. Before the device fabrication, the gold electrodes were patterned with a nanogap (*i.e.* electrode distance) of 5 or 10 nm, and a width of 100 nm or 1 μm , as shown in Figure 1.16a. SCO nanoparticles with a $[\text{Fe}(\text{tz})_3](\text{BF}_4)_2$ core ($\text{tz} = 1,2,4\text{-triazol-1-yl}$) were synthesized with a surfactant shell and were then deposited in between the two Au electrodes,

as shown schematically in Figure 1.16b. Current-voltage characteristics were assessed before and after deposition to make sure the nanoparticles were successfully placed in between the electrodes. A temperature dependent conductance investigation on this kind of device was carried out for both types of devices (with 1- μm and 100-nm wide electrodes). As shown in Figure 1.16c, an electric conductance switching ratio of *ca.* 2 was observed in both devices, which has been assigned by the authors to switching between the LS and HS states, the latter being more conductive. The apparent hysteretic behavior of the temperature dependent conductance characteristics is indeed similar to the SCO curve of the particles.

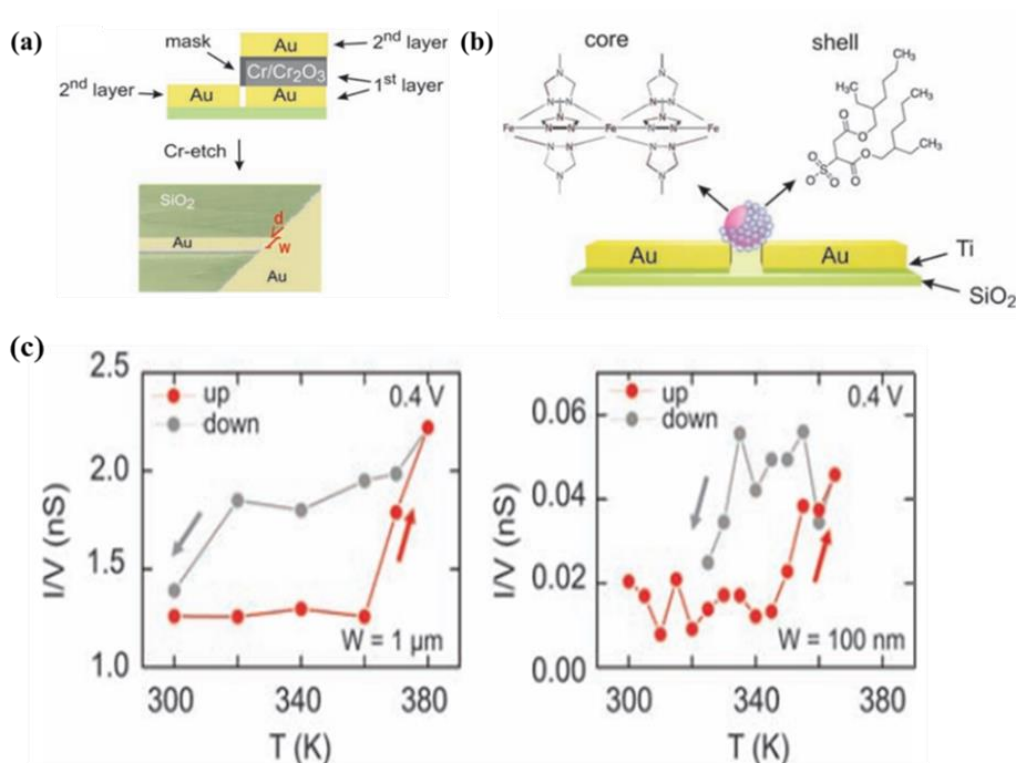


Figure 1.16: (a) Top: Schematic drawing of the device before Cr wet etching showing the different layers in the fabrication and the Cr₂O₃ shadow mask. Bottom: Scanning electron microscopy image of a device illustrating the different dimensions (electrode distance, *d* = 5–10 nm, width, *W* = 100 nm or 1 μm). (b) Schematic side view of the device geometry with the nanoparticle placed on top of the electrodes. The spin-crossover core is represented in purple, the surfactant shell in blue. (c) Conductance (*I/V*) as a function of temperature. Each point represents the average of the conductance at 0.4 V of 30 individual current–voltage characteristics. Left and Right: Device with 1- μm and 100-nm-wide electrodes, respectively [64].

In order to increase the current intensity, Rotaru *et al.* [65] successfully deposited $[\text{Fe}(\text{Htz})_2(\text{tz})](\text{BF}_4)$ nanorods from ethanol solution in between interdigitated gold electrodes with a gap of 4 μm . By applying an ac voltage, the electric field gradient allowed to preferentially align the SCO nanorods in the gaps between electrodes (Figures 1.13a-b). As shown in Figure 1.17c, temperature dependent current (I - T) measurements were carried out on this device and an unambiguous signature of the spin transition could be observed. When going from the LS to the HS (resp. HS to LS) states a decrease (resp. increase) of the current intensity can be depicted. As shown in the insert of Fig. 1.17c, this difference of device resistance between the two spin states was also evidenced by I - V measurements conducted at the same temperature (373 K) in the middle of the I - T hysteresis loop on heating (LS state) and cooling (HS state).

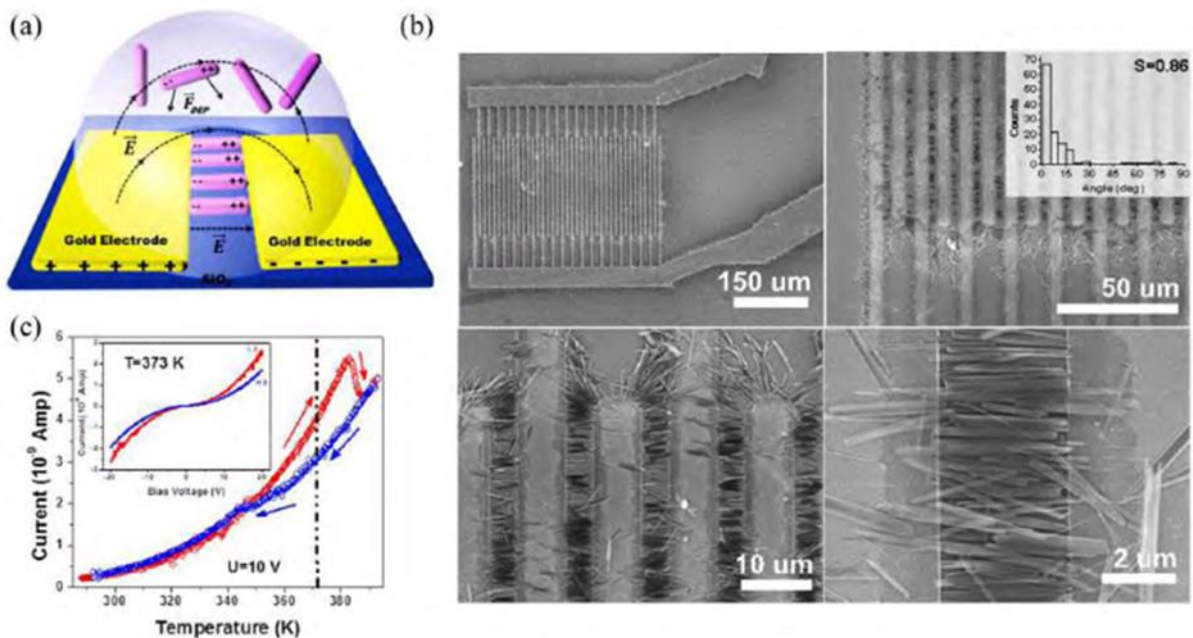


Figure 1.17: (a) Schematic representation of the dielectrophoresis process used to align $[\text{Fe}(\text{Htz})_2(\text{tz})](\text{BF}_4)$ particles between electrodes. (b) SEM images of a device showing the particle alignment. (c) Temperature dependence of the measured current in the device over a heating-cooling cycle under 10 V bias. Inset: I - V characteristic recorded at 373 K in the LS and HS states [65].

Following this first observation, several follow up papers have been published by different groups on different aspects of the charge transport in the same type of $[\text{Fe}(\text{Htz})_2(\text{tz})](\text{BF}_4)$ nanoparticles in a similar interdigitated device configuration, revealing

notably higher switching ratios, light irradiation effects, device reproducibility and so forth [66, 73].

Another interesting effect has been observed by Etrillard *et al.* [67] on the photoconduction in $[\text{Fe}(\text{Htz})_2(\text{tz})](\text{BF}_4) \cdot \text{H}_2\text{O}$ nanocrystals, which have been positioned in sub-100 nm gaps between gold electrodes. The particles were randomly dispersed on the substrate from an ethanol solution and effectively bridged the gaps between electrodes. A first experiment has been performed on the as-prepared device and no photocurrent has been measured. Then the electrodes were subjected to voltage poling. The current of the poled device increased considerably upon light irradiation and dropped to the same level when the light excitation was removed (Figure 1.18). Even though the experimental results are intriguing, it is not clear if the effect is characteristic of the SCO material.

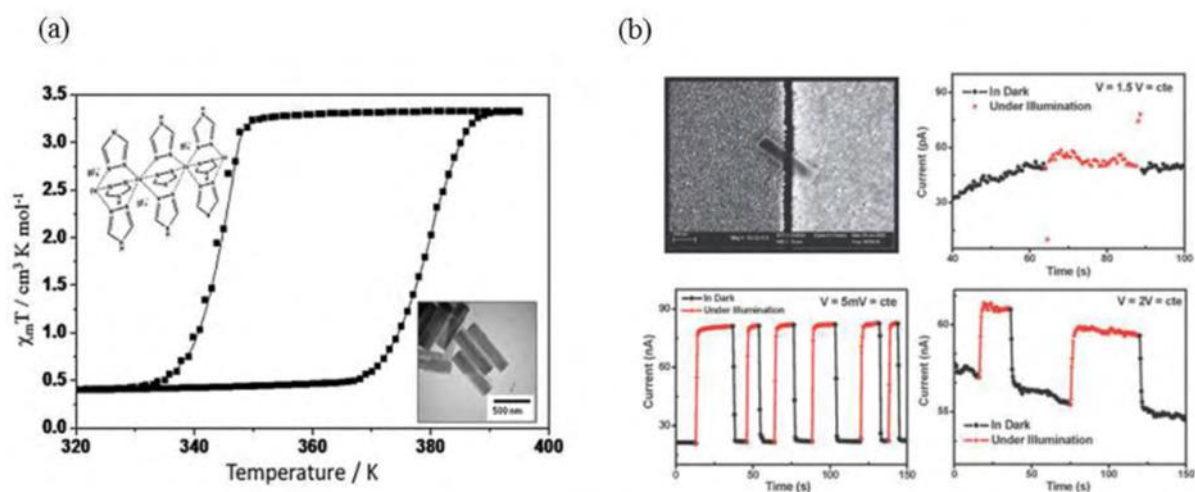


Figure 1.18: (a) Thermal hysteresis loop recorded using magnetic susceptibility measurements of the $[\text{Fe}(\text{Htz})_2(\text{tz})](\text{BF}_4) \cdot \text{H}_2\text{O}$ complex. The insets show the schematic representation of the molecular structure and the TEM micrograph of the obtained nanocrystals. (b) SEM picture of a SCO crystal bridging the electrode gap and the initial experiment showing the absence of photocurrent. In the bottom part of the panel, there are two examples of photoconductance after electrode poling [67].

More recently, Torres-Cavanillas *et al.* [68] reported an SCO-based horizontal electronic junction that exhibits a large current switching ratio due to the spin state switching. Since SCO materials are usually rather insulating, the authors synthesized a core-shell nanoparticle system with $[\text{Fe}(\text{Htz})_2(\text{tz})](\text{BF}_4)$ as core and gold as shell, to achieve high conductance. The nanoparticles were then deposited in between Au electrodes with a gap of 10 μm , as shown in Figure 1.19a-d. The temperature dependent current characteristic of this device showed that the

current switching ratio due to spin state switching reaches 4 orders of magnitude, the HS state being more insulating.

Besides nanoparticles, vacuum thermal evaporated SCO films have been also deposited on current-in-plane devices. The first device was reported by Mahfoud *et al.* [56] by using thermally evaporated $[\text{Fe}(\text{HB}(\text{pz})_3)_2]$ on interdigitated electrodes. SCO properties of the bulk material were preserved in the thin films. A *ca.* 1–2 orders of magnitude change of the conductivity of the thin films were observed under applied voltage bias. This property together with the fact that this compound is stable to exposure to light, electromagnetic fields, air, and water can be exploited in ROM type devices where the writing process can be performed by Joule-heating the cell and the read out can be achieved at room temperature by simply measuring the resistivity of the device [56].

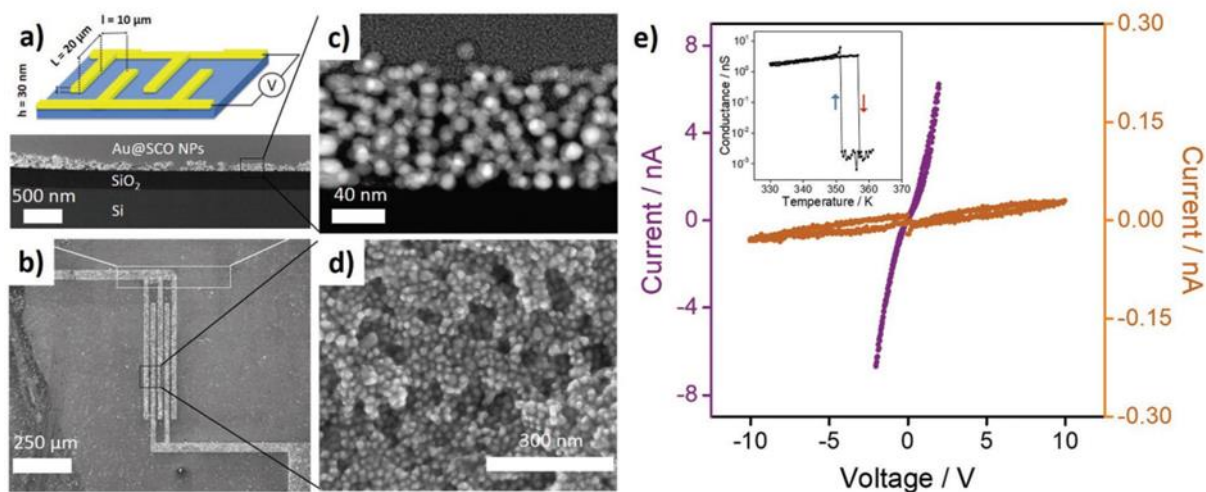


Figure 1.19: Left: Au finger-like electrode device used to measure the transport properties of an assembly of Au@SCO core-shell NPs. (a) Scheme and dimensions of the electrodes (top); STEM transversal cross-section of the device (bottom). A zoom of this image to show the packing of the NPs is displayed in (c). (b) SEM image of the device (top view). A zoom of this image is shown in (d). Right: (e) I – V curves of the high-conductive (purple) and low-conductive (orange) behaviours associated to the LS and HS states, respectively. Inset: Thermal variation of the electrical current for an applied voltage of 2 V in the heating and cooling modes at 1 K min^{-1} scan rate [68].

In addition to the above described thermal switching devices, recently, a nonvolatile voltage-switching SCO device aimed for memory application had been reported [69]. As shown in Figure 1.20a-b, a thermally evaporated thin film of the SCO complex $[\text{Fe}(\text{H}_2\text{B}(\text{pz})_2)_2(\text{bipy})]$ was deposited on top of a ferroelectric croconic acid ($\text{C}_5\text{O}_5\text{H}_2$) thin film to realize a two-terminal

Au/C₅O₅H₂/[Fe(H₂B(pz)₂)₂(bipy)]/Au electronic device. The nonvolatility comes from the adjacent ferroelectric layer and this property was observed as shown in Figure 1.19c. A similar idea was also achieved in a three-terminal device in the same article, which will be discussed in the Section 1.3.2.

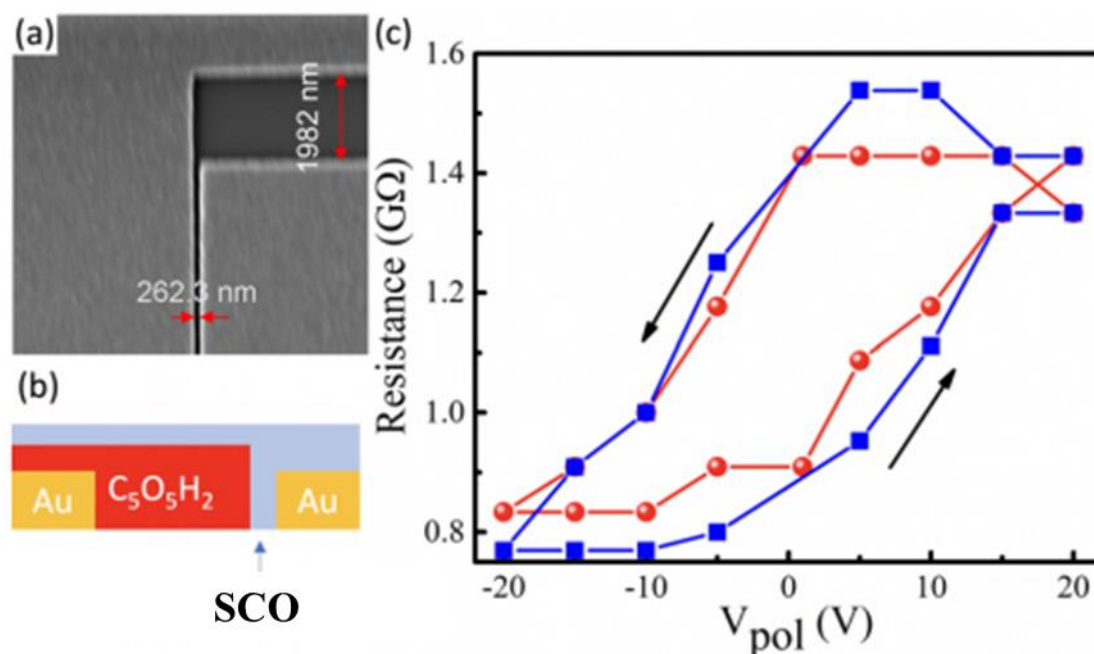


Figure 1.20: (a) Scanning electron microscopy image of the substrate, with Au electrodes. (b) Schematic structure of junctions in the device of 20 nm [Fe(H₂B(pz)₂)₂(bipy)] deposited on top of 200 nm thick croconic acid on the Au electrodes shown in (a). (c) Resistance of the device measured at 1 V (less than the coercive voltage for ferroelectric switching of this croconic acid film at room temperature), after applying a poling voltage (V_{pol}) displayed as the horizontal voltage at room temperature. Two successive loops are shown, first red and then blue, indicating reproducibility [69].

1.3.1.2 Two-terminal current out-of-plane SCO-based devices

The first two-terminal vertical (current out-of-plane) SCO-based electronic devices containing SCO molecules were reported by Matsuda and co-workers as early as in 2008 [70-72]. These devices consisted of the multilayer stack ITO/[Fe(dpp)₂](BF₄)₂:L/Al (ITO = indium tin oxide, dpp = 2,6-di(pyrazol-1-yl)pyridine, L = chlorophyll a or nile red) and alternatively a hole transport layer (poly(N-vinylcarbazole)) was also deposited between the ITO electrode and the active layer. These devices were investigated for the interplay between their SCO and electroluminescence properties, but to our best knowledge, the charge transport properties have not been reported. It is worth to note also that the SCO layer was made by spin coating.

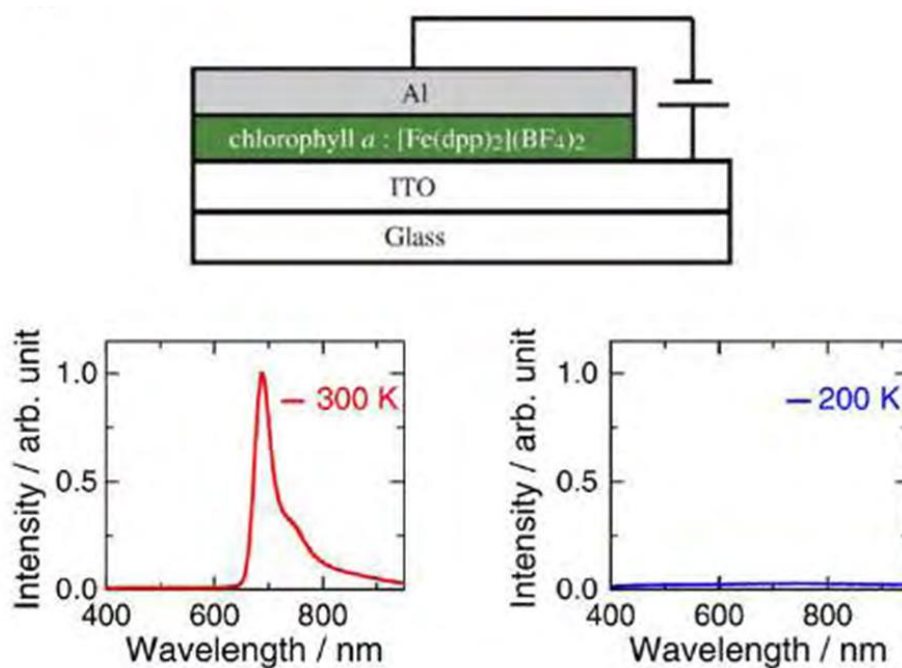


Figure 1.21: Scheme of the OLED device ITO/[Fe(dpp)₂](BF₄)₂:Chl-a/Al and its electroluminescence intensity in the HS (300 K) and LS (200 K) states [70-72].

In 2016, thin films of the SCO compound [Fe(H₂B(pz)₂)₂(phen)] (pz = pyrazol-1-yl and phen = 1,10-phenanthroline) were successfully embedded in large-area crossbar devices with the tri-layer structure of ITO/SCO/Al [73]. This work provided a well-reproducible protocol to investigate the switching property of SCO layers of various thickness. The thinnest junctions (*ca.* 10 nm) showed tunneling behavior between 5 – 300 K, while the thicker SCO layers (*ca.* 30 – 200 nm) gave rise to a diode-like rectifying behavior and thermal activation of the conductance. Whereas the thermal SCO could not be unambiguously distinguished from the thermal activation of the conductance, a clear evidence for the LIESST effect was observed in this type of devices. When shining visible light on the junction at cryogenic temperatures (5 K) the switching from the LS to the HS state led to a reversible drop of the resistance by *ca.* 10 - 50 % (*i.e.* ON/OFF ratio < 2). Mechanistic studies have revealed that in this type of devices the charge transport was limited by the ‘bulk conductance’ of the films, even for the thinnest junctions.

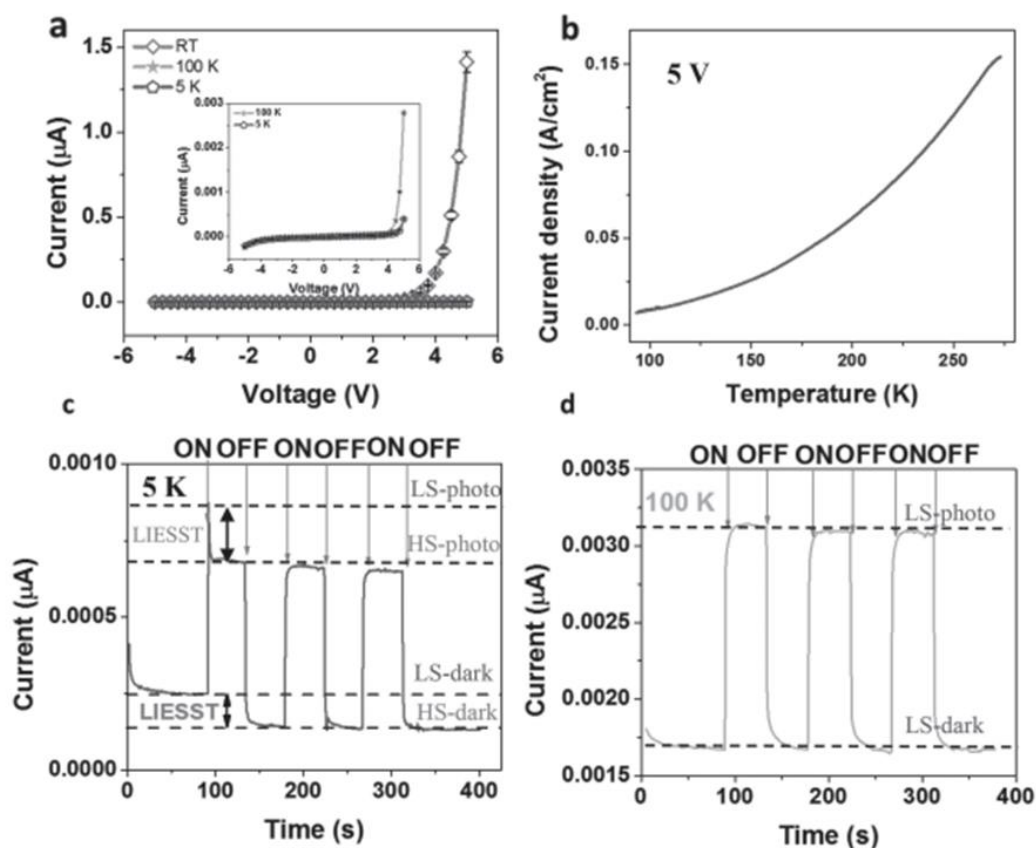


Figure 1.22: Electrical characteristics of a 30 nm ITO/[Fe(H₂B(pz)₂)₂(phen)]/Al junction. (a) I - V curves registered at room temperature, 100 and 5 K at a rate of 100 mV s⁻¹. The inset is a zoom on the 100 and 5 K data. (b) Temperature dependence of the conductivity of the junction registered at a rate of 5 K min⁻¹. (c,d) Visible light irradiation effect on the current flowing in the junction through three successive ON/OFF cycles at 5 K (c) and 100 K (d). Current intensities in the HS and LS states are indicated by dashed lines both in dark and in photostationary conditions. The applied bias in (b–d) was 5 V [73].

The same device structure was later also achieved with thin films of the SCO complex [Fe(HB(tz)₃)₂] (tz = 1,2,4-triazol-1-yl) [74]. The charge transport mechanism in junctions with different thicknesses (10 nm, 30 nm, 100 nm and 200 nm) was studied and an ON/OFF current ratio of *ca.* 8 was found when switching the molecules from the LS to the HS state near 330 K. The above-room-temperature switching behavior of these junctions provides scope for real-world applications. In Chapter 2 of the present thesis we will discuss further results we could obtain on this type of devices, including the study of ON-OFF ratios, the transport mechanism, device reproducibility and cycle life.

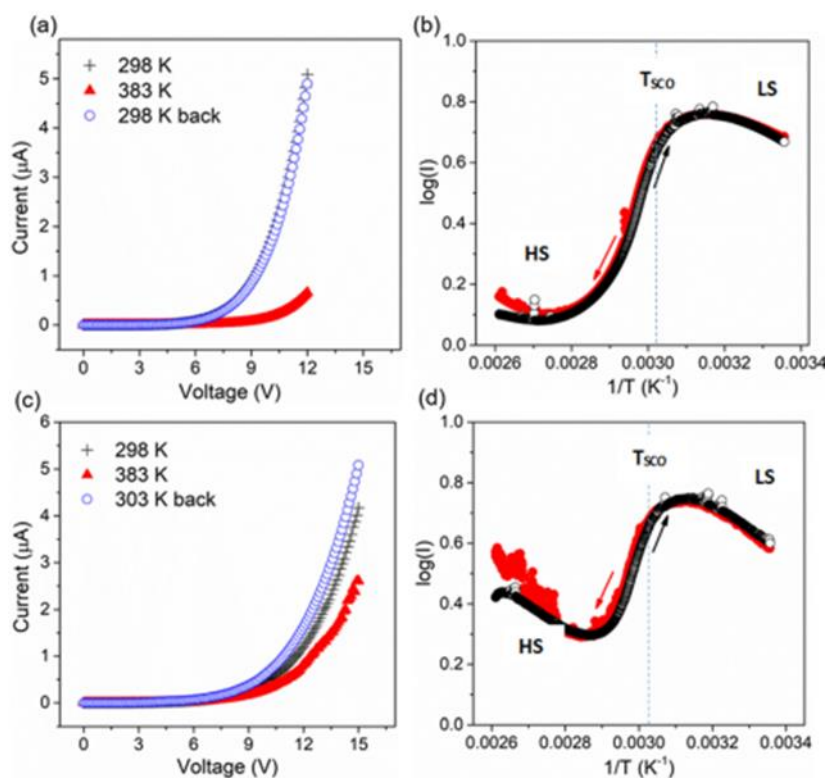


Figure 1.23: Typical electrical characteristics of 100 and 200 nm ITO/[Fe(HB(tz)₃)₂]/Al junctions [74]. *I*-*V* curves of 100 nm (a) and 200 nm (c) thick junctions recorded at 298 and 383 K and then back to 298/303 K at a scan rate of 100 mV s⁻¹. log*I* vs. 1/*T* curves of 100 nm (b) and 200 nm (d) thick junctions recorded with an applied bias of 12 V and 15 V, respectively, at a scan rate of 5 Kmin⁻¹. The dashed line shows the spin transition temperature.

The same compounds, [Fe(H₂B(pz)₂)₂(phen)] and [Fe(HB(tz)₃)₂], were also used to construct multilayer junctions with the structure of Au/SCO/Ga₂O₃/EGaIn (EGaIn = eutectic alloy of Ga and In) [75, 76]. The main advantage of using this type of liquid droplet electrodes (with respect to thermally evaporated or sputtered metallic electrodes) is that the electrode deposition is usually less invasive and allows to achieve junctions even for extremely thin SCO layers (6.7 nm in ref. [76]). Remarkably, the [Fe(HB(tz)₃)₂]-based junctions exhibited ON/OFF current ratios up to 100 upon the SCO, as shown in Figure 1.24b. Due to the very gradual SCO, in the [Fe(H₂B(pz)₂)₂(phen)]-based device it is less obvious to depict the effect of the SCO on the device resistance, which may be merged with the ordinary thermal activation of the current. Interestingly, the HS state appeared more conducting in these devices, which the authors rationalized in the frame of the Simmons' tunneling model by taking into account the variation of frontier molecular orbital energies upon the SCO. This finding indicates that the influence

of SCO on the device resistance can strongly differ depending on the charge transport mechanism.

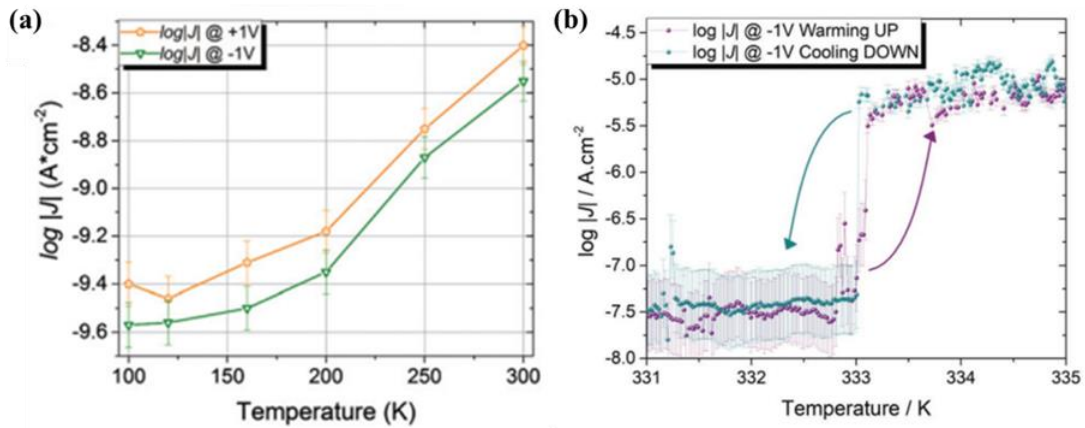


Figure 1.24: Current density as a function of temperature for the junctions (a) Au/[Fe(H₂B(pz)₂)₂(phen)]/Ga₂O₃/EGaIn [75] and (b) Au/[Fe(HB(tz)₃)₂]/Ga₂O₃/EGaIn [76].

The same group also succeeded in constructing crossbar devices using the evaporable SCO complex [Fe(qnal)₂] (qnal = quinoline-naphthaldehyde) in the Ag/SCO/LiF/Au multilayer device [77]. Variable temperature I - V characteristics were recorded, as shown in Figure 1.25. A correlation between the LS to HS spin conversion and the decrease of the device resistance was pointed out, although the gradual nature of the SCO makes an unambiguous assignment difficult.

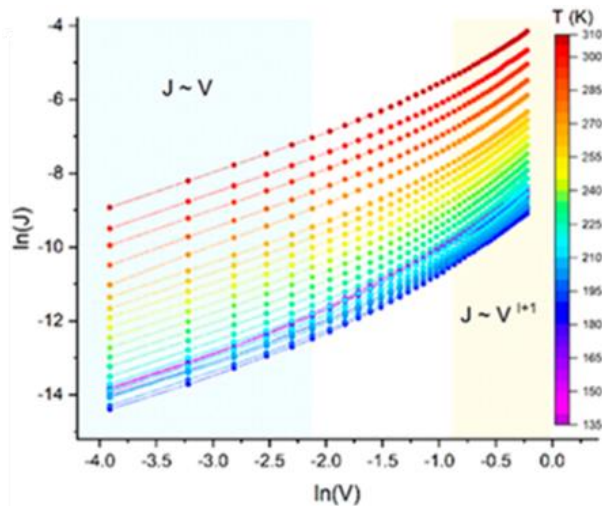


Figure 1.25: \log - \log plots of J - V characteristics at different temperatures (temperature color scaled as per the legend) for a Ag/[Fe(qnal)₂]/LiF/Au device. Low-voltage ohmic and high-voltage SCLC regimes voltage ranges are highlighted [77].

Thin films (*ca.* 40 nm) of the complex $[\text{Fe}(\text{H}_2\text{B}(\text{pz})_2)_2(\text{NH}_2\text{-phen})]$, were also investigated in a Au/SCO/Au crossbar configuration. Interestingly, a relatively small change of the HS/LS fractions could be correlated with a significant change of the device resistance - although the gradual nature of the SCO makes an unambiguous assignment difficult. In addition, the role of sample heterogeneity in the charge transport was highlighted using an operando x-ray absorption spectroscopy method.

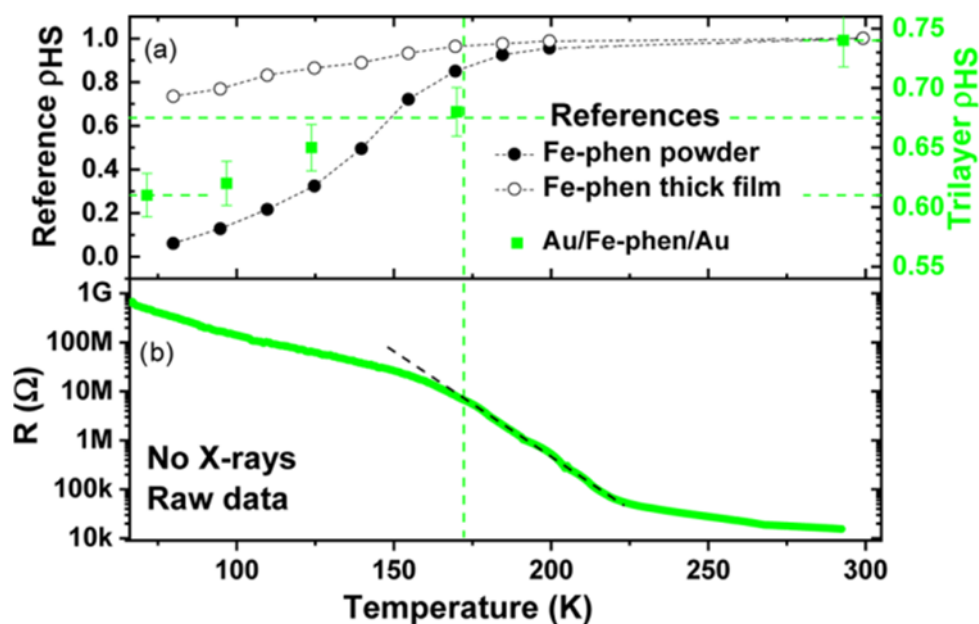


Figure 1.26: (a) Temperature dependence of the HS proportion ρ_{HS} in a Au/ $[\text{Fe}(\text{H}_2\text{B}(\text{pz})_2)_2(\text{NH}_2\text{-phen})]$ /Au stack (green), in the $[\text{Fe}(\text{H}_2\text{B}(\text{pz})_2)_2(\text{NH}_2\text{-phen})]$ reference powder (filled black), and in a 230 nm thick film deposited onto Au (open black). (b) Temperature dependence of the resistance of a Au/ $[\text{Fe}(\text{H}_2\text{B}(\text{pz})_2)_2(\text{NH}_2\text{-phen})]$ /Au device [52].

More recently, Karuppanan et al. [78] reported the first room temperature switchable Fe(III) molecular spin crossover (SCO) tunnel junction. They physisorbed $[\text{Fe}^{\text{III}}(\text{qsal-I})_2]\text{NTf}_2$ (qsal-I = 4-iodo-2-[(8-quinolylimino)methyl]phenolate) onto the SLG (single layer of graphene) by immersing the Cu/SLG substrate in a 1.0 mM solution of $[\text{Fe}^{\text{III}}(\text{qsal-I})_2]\text{NTf}_2$ in CH_2Cl_2 . Then, they fabricated the tunnel junction with the structure Cu//SLG// $[\text{Fe}^{\text{III}}(\text{qsal-I})_2]\text{NTf}_2$ (1.4 nm)//GaOx/EGaIn. SLG was inserted in between the Cu and SCO layers to decouple the SCO molecules from the Cu electrodes. A reversible SCO of the thin film was evidenced by temperature dependent XAS and XMCD studies. Temperature dependent current data revealed increasing conductance of the junction above 300 K, which could be associated with the SCO. This paper shows an example of the importance to decouple SCO molecules from the metallic substrates in order to preserve their SCO properties.

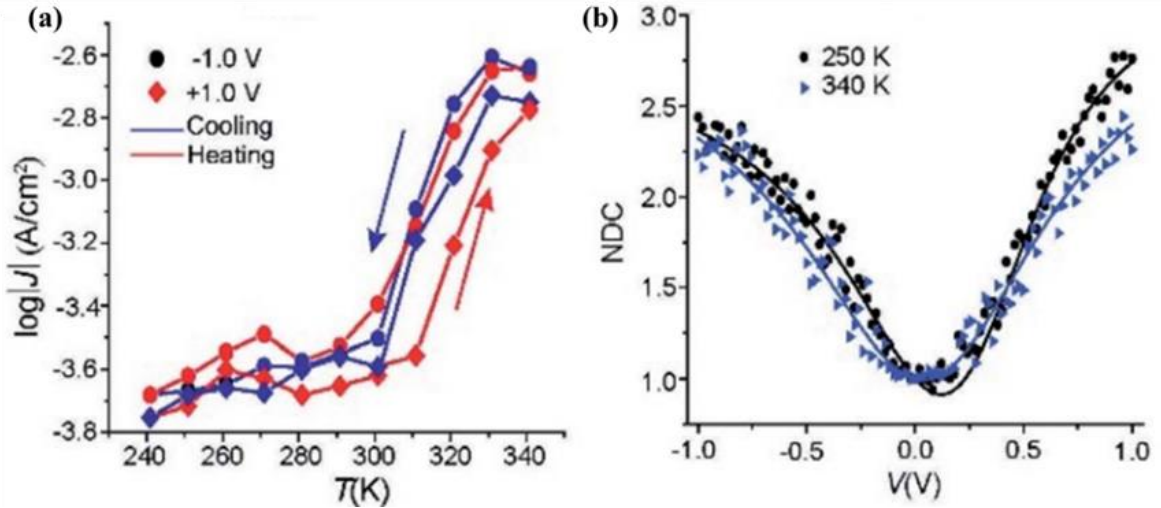


Figure 1.27: (a) Current density as a function of temperature at ± 1.0 V applied bias. (b) Normalized differential conductance for a Cu/SLG/[Fe^{III}(qsalI)₂]NTf₂ /GaOx/EGaIn junction at different temperatures [78].

1.3.2 Three-terminal SCO-based electronic devices

Recently, more and more research efforts have been focused on the fabrication of three-terminal SCO-based electronic devices, i.e. on the integration of SCO molecules into electronic devices with ‘transistor-like’ configuration.

Dugay et al. [79] reported in 2017 a graphene based device with a thin film of [Fe(Htz₂)(tz)](BF₄) spin-crossover nanoparticles deposited on the top of the graphene layer. The ambipolar field effect of graphene was confirmed by gate voltage dependence of the graphene resistance, before and after SCO deposition. Resistance at the Dirac point as a function of temperature for heating and cooling modes was recorded for both devices (before/after SCO deposition), as shown in Figure 1.28. It can be clearly witnessed that after SCO deposition, the graphene resistance shows jumps near the spin transition temperatures. This study showed for the first time that the transport properties (*e.g.* carrier mobility) of a thin film could be modulated by an SCO thin film, which is adjacent to it, via interface coupling. Using model calculations, the authors suggested that the coupling could be attributed to the spin-state dependence of the dielectric constant. Yet, other mechanisms (*e.g.* mechanical coupling to the SCO layer) might be (also) at work. We shall also note that the authors have operated the device solely in a two-terminal mode and have not mentioned about experiments in three terminal configuration using the SCO property.

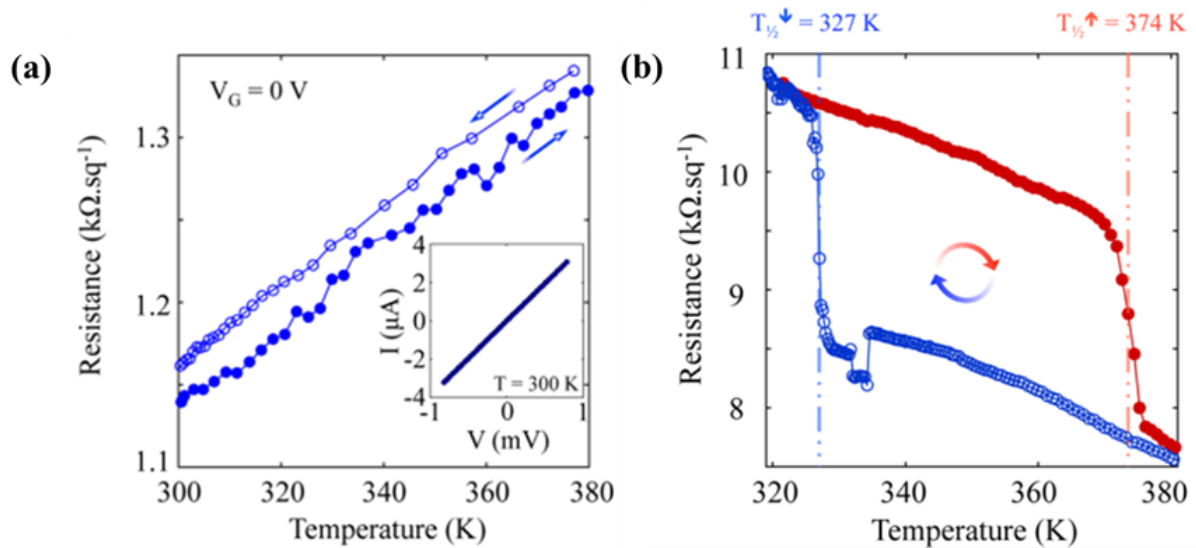


Figure 1.28: Modulation of graphene conductance by interface coupling to an SCO layer. (a) Temperature dependence of the resistance in heating and cooling modes (full and empty blue dots, respectively) at zero gate voltage recorded after the graphene was cleaned. The inset shows the representative behavior of the voltage (V) as a function of the injected current (I) indicating an ohmic contact for the electrodes on graphene. (b) Graphene resistance per square at the Dirac point as a function of temperature on heating and cooling after the deposition of SCO nanoparticles [79].

Van Geest et al. [80] have also used graphene to fabricate a three-terminal SCO device. A poly(methyl methacrylate) (PMMA) spacer (*e.g.* spacer thickness = 0.5 μm) was deposited on the top of graphene before SCO ([Fe(babpby)(NCS)₂] microcrystals) deposition. The thick spacer in between graphene and SCO was used to remove (or at least reduce) mechanical effects on graphene arising from spin state switching. When operated in a 2-terminal configuration their device displayed very clear resistance changes around the spin transition temperatures. Since the graphene layer was (*à priori*) mechanically decoupled from the SCO crystal, they suggested that the observed resistance change is a purely electrostatic effect due to the change of the electrostatic potential associated with the SCO. Then, they have carried out gating experiments using an ionic liquid (Fig. 1.28a) and demonstrated a shift of the Dirac point as a function of temperature, which they have correlated with the SCO phenomenon (Fig. 1.28b). Using computational modeling, the authors argued that the Dirac point shift observed in this device comes from electrostatic effect of the SCO layer. This effect is, however, less obvious in the reported data and further experimental work will be needed to confirm the cause of the Dirac point shift.

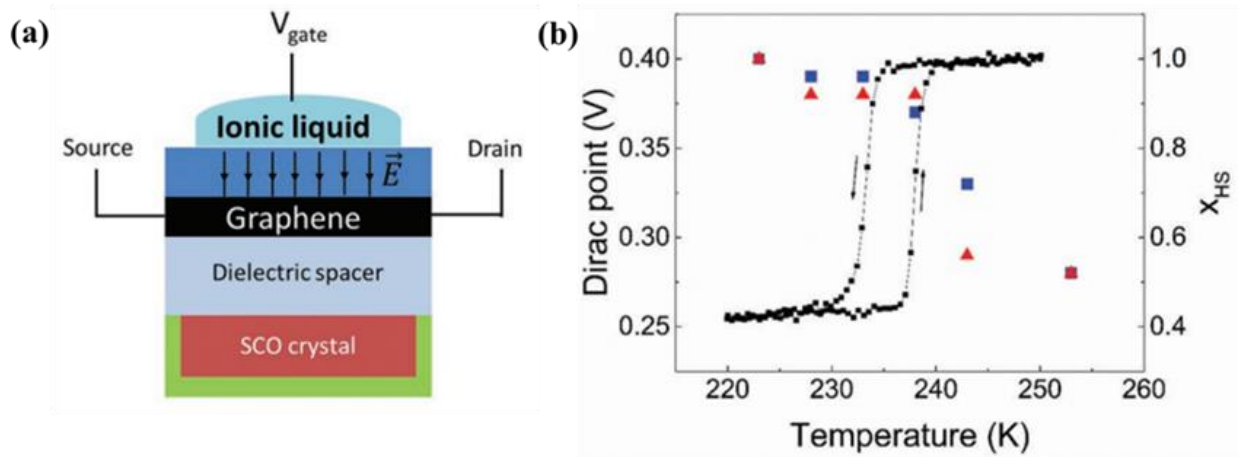


Figure 1.29: Dirac point shift induced by the spin transition in a top-gated GFET [ref]. (a) Side-view schematic illustration of a top-gated GFET. (b) Dirac point (left axis, blue squares and red triangles for the cooling and heating modes, respectively) and fraction x_{HS} of HS molecules in the SCO crystal (black squares, as determined by SQUID magnetic susceptibility measurements) versus temperature [80].

More recently, Konstantinov et al. [82] reported a graphene-based device wherein the $[\text{Fe}(\text{HB}(3,5\text{-}(\text{CH}_3)_2\text{Pz})_3)_2]$ complex was evaporated directly on the graphene layer. (The latter was lying on a Si/SiO₂ substrate.) As shown in Figure 1.30a, the thermally induced spin transition with hysteresis was clearly observed in the temperature dependent conductance characteristic of this device. In addition, the light induced spin crossover phenomenon was also investigated (Figure 1.30b) and both the LIESST and the reverse LIESST effects could be demonstrated using red and near-infrared light sources, respectively. Soon after this work, the same group reported a room temperature optoelectronic device with a similar device configuration, but using nanoparticles $[\text{Fe}(\text{Htz})_2(\text{tz})](\text{PF}_6)$ of the SCO complex, deposited on the graphene surface [83]. They observed a similar resistance switching upon the SCO, but in this case near room temperature. Gating experiments were also conducted by the authors, but the magnitude of the SCO-induced resistance switching appears to be independent of the gate voltage.

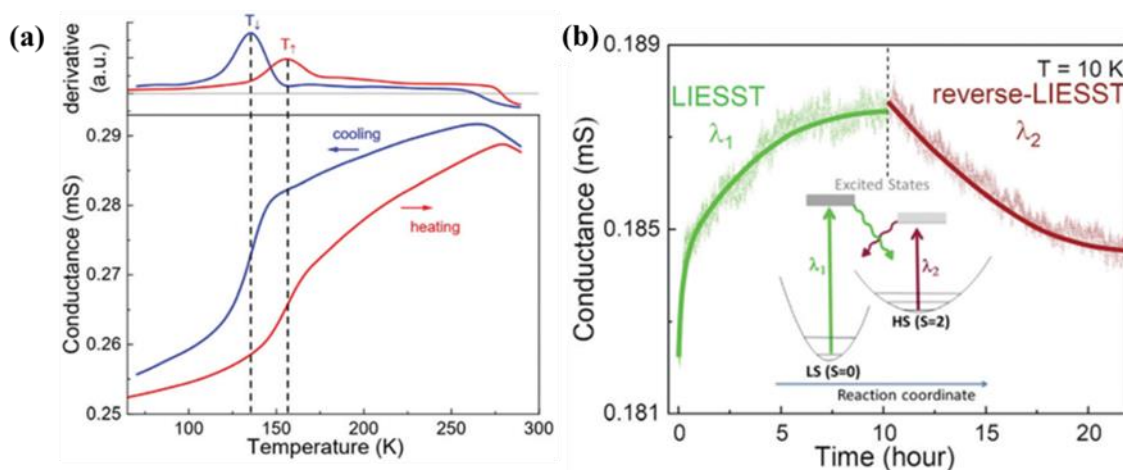


Figure 1.30: (a) Temperature dependence of the conductance of a $[\text{Fe}(\text{HB}(3,5\text{-(CH}_3)_2\text{Pz)}_3)_2]/\text{graphene}$ thin film heterostructure-based device. (b) Conductance vs. time plots of the SCO/graphene heterostructure device under continuous red light excitation ($\lambda_1 = 647 \text{ nm}$, $550 \mu\text{W mm}^{-2}$) during 10 hours demonstrating the LIESST effect, followed by excitation under near-IR light ($\lambda_2 = 820 \text{ nm}$, $100 \mu\text{W mm}^{-2}$) showing the reverse-LIESST effect. Inset: Energy band diagram describing the photoswitching mechanisms. In green (respectively, in brown), the LIESST effect (respectively, reverse-LIESST effect) results from photoexcitation of the SCO molecule from the diamagnetic LS state (respectively, paramagnetic HS state) to excited states under red light (respectively, Near-IR) excitation of wavelength λ_1 (respectively, λ_2), before relaxing towards the HS state (respectively, LS state) [82].

Hao *et al.* [69] reported a non-volatile three-terminal device, where a PVDF-HFP ferroelectric layer, adjacent to the SCO thin film ($[\text{Fe}(\text{H}_2\text{B}(\text{pz})_2)_2(\text{bipy})]$) appears to lock the spin state, depending on the ferroelectric polarization direction. The spin-state switching was inferred from X-ray absorption spectra (Fig. 1.31a). In this way, a voltage-triggered, isothermal SCO switching three-terminal device was successfully fabricated, as shown in Figure 1.31. In brief, the gate voltage controls the polarization of PVDF-HFP and thus the spin state of SCO. Since the measured drain-source current exhibits a difference between the two (locked) spin states, the device can be used as a nonvolatile resistance switch. Soon after this publication, a more detailed investigation of the same SCO complex with the same device configuration was carried out by Mosey *et al.* [84]. An ON/OFF current switching ratio of *ca.* 5 was observed in this device due to the spin state switching. Compared with the previous report, non-linear I - V characteristics with far better signal to noise ratio were presented [84].

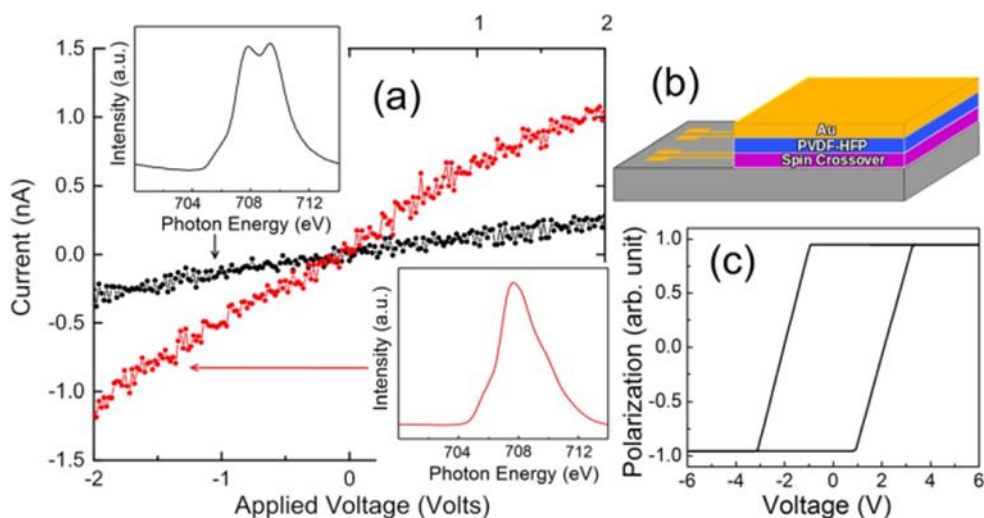


Figure 1.31: (a) Conductance switching of $[\text{Fe}(\text{H}_2\text{B}(\text{pz})_2)_2(\text{bipy})]$ on PVDF-HFP in a three-terminal device, whose structure is shown in (b). $[\text{Fe}(\text{H}_2\text{B}(\text{pz})_2)_2(\text{bipy})]$ is pinned mostly in the LS state when the ferroelectric polarization of PVDF-HFP is directed away from $[\text{Fe}(\text{H}_2\text{B}(\text{pz})_2)_2(\text{bipy})]$, as evident in the X-ray absorption (see insert), leading to low conductance (black curves). On the contrary, $[\text{Fe}(\text{H}_2\text{B}(\text{pz})_2)_2(\text{bipy})]$ is pinned in the HS state when the PVDF-HFP ferroelectric polarization is directed towards the SCO film, leading to higher conductance (red curves). (c) Hysteresis loop for the PVDF-HFP layer [69].

1.4 Conclusions and perspectives for further work

As a conclusion for this Chapter 1, we can note that since the first report in 2011 about charge transport in SCO-based electronic devices, the field has made a tremendous progress. Notably, besides SCO nanoparticles, high quality SCO thin films could be obtained by vacuum thermal evaporation. Of particular interest for us, thin films of the $[\text{Fe}(\text{HB}(\text{tz})_3)_2]$ complex revealed exceptional resilience of the SCO, tight reproducibility of the film deposition and above room temperature spin transition. These properties will be further explored and exploited used in this thesis. Nevertheless, it is important to stress that the number of evaporable SCO complexes remains low and it will be necessary to enlarge the portfolio of this type of compounds. Yet, some of the existing films could be successfully integrated into electronic devices with different configurations: either 2- or 3-terminal, planar or vertical.

An important breakthrough was the development of well-defined, large-area, multilayer junctions incorporating nanometric SCO films. Indeed, planar (current-in-plane) SCO devices with sub-micrometer electrode gaps are difficult to characterize due to the very insulating nature of SCO compounds. In contrast, multilayer (current out-of-plane) devices allow today for

systematic investigations of the charge transport mechanism with electrode separations from several hundreds of nm down to a few nm – while keeping current intensities reasonably high.

The most important results with SCO based two-terminal electronic junctions are summarized in Table 1.2. Basically, these junctions operate as ON-OFF resistance-switches, owing to the modification of the charge transport between the HS and LS states. One can remark, however, that the ON/OFF current ratios appear in general rather low, even if it is fair to say that the number of investigated SCO compounds and devices remains also rather restricted. In a few cases, more promising 2-3 orders of magnitude changes of the device resistance could be detected. A tangible correlation between the SCO and the current switching phenomena remains, however, problematic in several cases as it relies on the ex-situ evaluation of the spin-crossover properties. It is interesting to observe also that the same SCO compound may give rise to very different characteristics, depending on the device structure. This observation relates to the fact that the transport mechanism(s) may be different in different devices. However, very few mechanistic studies have been reported up to now. We shall note also that, in general, there is only few (or no) mention about ‘statistics’ in the publications, *i.e.* the reproducibility of the fabrication process, the reversibility of the current switching (cycle numbers) and the lifetime of the devices. This aspect certainly deserves to be considered more seriously in future reports.

Table 1.2: Current switching properties reported for various SCO junctions

SCO compound	Device structure	Current LS (A)	Current HS (A)	ON/OFF ratio	Ref.
[Fe(H ₂ B(pz) ₂) ₂ (phen)] film	ITO/SCO/Al	2.0×10 ⁻⁹	1.0×10 ⁻⁹	↓	2 [73]
[Fe(HB(tz) ₃) ₂] film	ITO/SCO/Al	5.0×10 ⁻⁶	5.0×10 ⁻⁷	↓	8 [74]
[Fe(H ₂ B(pz) ₂) ₂ (phen)] film	^{TS} Au/SCO/EGaIn	3×10 ⁻¹⁰	3×10 ⁻⁹	↑	10 [75]
[Fe(HB(tz) ₃) ₂] film	^{TS} Au/SCO/EGaIn	3×10 ⁻⁸	3×10 ⁻⁶	↑	100 [76]
[Fe(H ₂ B(pz) ₂) ₂ (NH ₂ -phen)] film	Au/SCO/Au	8×10 ⁻⁸	8×10 ⁻⁶	↑	100 [52]
[Fe(Htz) ₂ (tz)](BF ₄) nanorods	Au/SCO/Au	2.6×10 ⁻⁸	1.5×10 ⁻⁸	↓	1.7 [65]
[Fe(Htz) ₂ (tz)](BF ₄) nanoparticles	Au/SCO/Au	1×10 ⁻⁹	3×10 ⁻¹²	↓	300 [66]
Au@[Fe(Htz) ₂ (tz)](BF ₄) nanoparticles	Au/SCO/Au	6×10 ⁻⁹	4×10 ⁻¹²	↓	1500 [68]
[Fe(tz) ₃](BF ₄) ₂ NPs	Au/SCO/Au	0.26	0.88	↑	3 [64]
[Fe(tz) ₃](BF ₄) ₂ NPs	G/SCO/G				2 [79]
[Fe(tz) ₃](BF ₄) ₂ NPs	Au/G+SCO/Au	3×10 ⁻¹⁰	3×10 ⁻¹¹	↓	10 [81]
[FeIII(qsal-I) ₂]NTf ₂ thin film	Cu/SLG/SCO/Ga Ox/EGaIn	-3.6 (Log J)	-2.6 (Log J)	↑	10 [78]

* ↑ and ↓ refer to increasing or decreasing current in the HS state with respect to the LS state.

Another important development was the construction of graphene-based SCO devices. On one hand side, these devices allowed for a novel switching mechanism wherein the current is not flowing through the SCO layer. Instead, the latter is used to modulate the charge transport

in the graphene layer via some physical interaction(s) between the layers (electrostatic, mechanical, *etc.*). On the other hand, the SCO-graphene devices can be relatively easily fabricated in a 3-terminal configuration, providing a tangible opportunity for the development of SCO-based transistors. In this context, two- and three-terminal devices wherein the SCO molecules are coupled to a ferroelectric substrate represent also a very promising platform for future developments [85].

Based on these recent advances, this thesis work aimed for progress in two directions. First, we continued to work on multilayer SCO junctions in order to (i) achieve a high ON-OFF ratio, (ii) to analyze the charge transport mechanism and (iii) to explore and optimize the device stability and reproducibility (Chapter 2). Second, we initiated a new line of research wherein SCO layers are used as dielectric layers in OFET (organic field effect transistor) devices (Chapter 3). In these devices, the SCO layer may be used either to modulate the capacitance of the gate dielectrics and/or to alter the charge transport due to interfacial coupling between the organic semiconductor and SCO layers.

Chapter 2 Integration of the spin crossover complex [Fe(HB(tz)₃)₂] into two-terminal resistance switching devices

As discussed in Chapter 1, the [Fe(HB(tz)₃)₂] complex attracts our attention because of its well reproducible, abrupt and above room temperature SCO behavior. Importantly, previous investigations in our team revealed that this complex could be deposited by vacuum thermal evaporation to obtain thin films. A simple solvent vapor annealing technique allows turning the as-deposited films into high quality smooth, continuous, pinhole free crystalline films. In this chapter, we describe first the synthesis and characterization of the bulk powder and the thin films of this complex. Then, we discuss the fabrication and properties of large-area, multilayer junctions, based on these films. In particular, we have investigated the ‘benchmark’ ITO/[Fe(HB(tz)₃)₂]/Al junctions with the aim to explore the attainable ON-OFF switching ratios, device-to-device reproducibility and switching endurance. We have also investigated the mechanism of the resistance switching upon the SCO. Notably, ITO/[Fe(HB(tz)₃)₂]/Ca junctions provided interesting information in this context. Finally, we worked towards the fabrication of NiFe/[Fe(HB(tz)₃)₂]/Co junctions with magnetic electrodes, which open up new perspectives for SCO-based spintronic devices. The work described in this chapter was conducted jointly between the LCC-CNRS and the local micro/nanotechnology platform, LAAS-CNRS, in strong collaboration with Dr. Isabelle Séguy.

2.1 Resistance switching devices

Resistive switching phenomenon is a reproducible process, which differs from the dielectric breakdown phenomenon that induces an irreversible change in resistance. Crossbar architecture is universally used in resistance switching applications, in which each crossing point has a capacitor-like two-terminal configuration, as shown in Figure 2.1a. Basically, an active thin film is sandwiched between top and bottom electrodes. Resistive switching can be divided into two basic forms: volatile and non-volatile. In the former case, the sudden change of the resistance will spontaneously return to the initial state when the external stimuli disappear [87]. On the contrary, the non-volatile resistive switching phenomenon is semi-permanent: it does not return to the initial state immediately after the external stimuli disappear. These non-volatile resistive switching behaviors may be further classified in two sub-categories: unipolar (also called non-polar) and bi-polar [88]. The former refers to systems where the resistive change induced by a first pulse (SET) can be reversed by the application of a second electric

pulse (RESET) of either the same or opposite polarity. In contrast, the bi-polar systems require a second pulse with opposite polarity (*vs.* the first pulse). Figure 2.1b depicts some representative *I-V* characteristics of the different types of resistive switching phenomena [89].

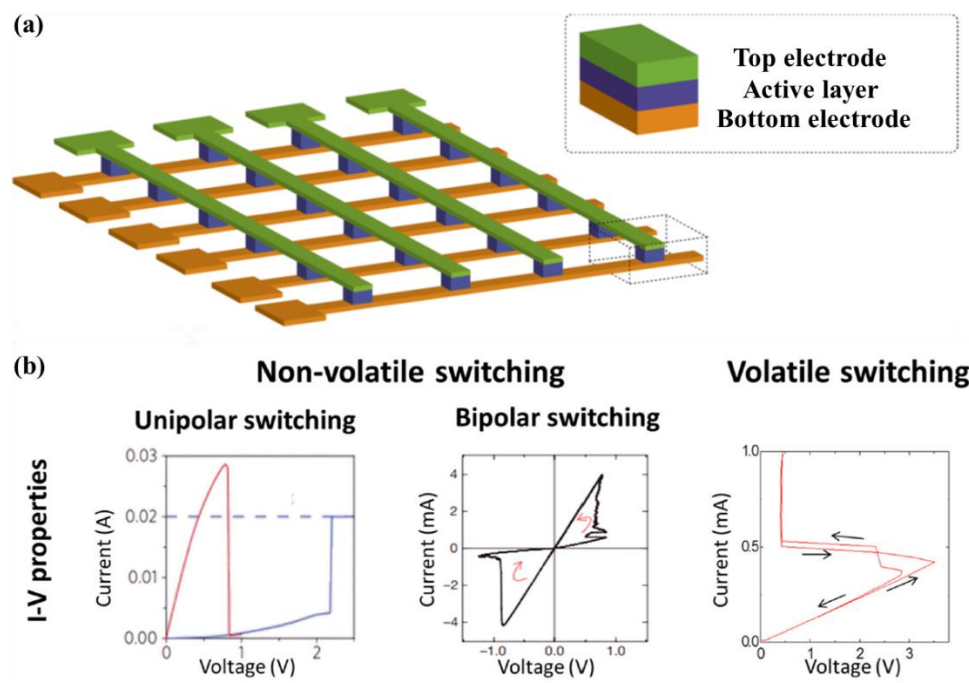


Figure 2.1: (a) Typical crossbar architecture used in resistive switching applications and (b) representative *I-V* characteristics of the different types of resistive switching phenomena. [89]

Until now, a large number of insulating materials (oxides, nitrides, chalcogenides, polymers, organic materials, *etc.*) have been reported in resistive switching applications [90]. Resistance switching random access memory (RRAM) is one of the most important systems, which is developed among these applications. Table 2.1 lists resistive switching performance reported on some well-studied RRAM devices [91]. Indeed, some of the RRAM devices exhibited very appealing properties with high ON/OFF resistive switching ratio (10^7) and high cycling endurance ($>10^{11}$).

As discussed in Chapter 1, recently, SCO materials have been integrated into similar crossbar-type devices. Due to the bistable physical properties of the SCO compounds, these devices can potentially afford for resistance switching behavior. Similar as RRAM systems, the key performance parameters of the SCO-based resistance switching devices will be resistive switching ratio, cycling endurance, switching time and retention time (if non-volatile).

Table 2.1: Resistive switching performance reported on selected RRAM devices [91].

System	Resistance ratio	Cycling endurance	Retention time	Programming time/ns
Ag/AgGeSe/Ni	$>10^3$	10^{11}	–	<100
Ag/GeSe/W	$>10^2$	10^6	$>10^4$ s	–
Ag/ α -Si/poly-Si	$>10^6$	10^8	$>10^4$ s	100
Pt/TaO _x /Pt	>5	10^9	>4 months	10
NiO	~ 10	10^6	8 months	10
Ag/ZnO:Mn/Pt	10^7	$>10^2$	4 months	5
Ti/HfO ₂ /TiN	>6	10^6	$>10^4$ s	10
ITO/(PEDOT:PSS)/Al	$>10^3$	10^4	16 h	<500

2.2 Synthesis and characterization of the bulk [Fe(HB(tz)₃)₂] complex

The synthesis of the microcrystalline powder of [Fe(HB(tz)₃)₂] followed previous work [86]. The scheme of the synthesis route is shown in Figure 2.2. All solvents and reagents were purchased from Sigma Aldrich and used without further purification. KHB(tz)₃ (0.372 g, 1.46 mmol) was mixed in a 2 : 1 ratio with Fe(SO₄)₂·7H₂O (0.201 g, 0.73 mmol) in water and kept under magnetic stirring for 30 minutes until the reaction is finished. The resulting suspension was purified by centrifugation (3 times with water, twice with ethanol and once with ethyl-ether) and left in a hood during 12 hours for drying in ambient conditions. This was followed by an annealing at 100 °C for 15 minutes to remove the residual solvents. The final microcrystalline powder [Fe(HB(tz)₃)₂] was obtained with 58% yield (0.206 g). Mass spectroscopy and IR spectroscopy were used to verify the structure of the complex (see Annex). This recipe affords for a good purity powder, which can be directly used for vacuum thermal evaporation. However, we must mention that for a better reproducibility the purity of the powder can be further improved. On one hand side, it can be purified by sublimation, but this requires an equipment, which can reach high temperatures (~ 250 °C) under secondary vacuum. On the other hand, some improvement was obtained also by conducting the synthesis in slightly non-stoichiometric conditions ($>2:1$). The likely reason here is that the as-received ligand salt contains some impurities.

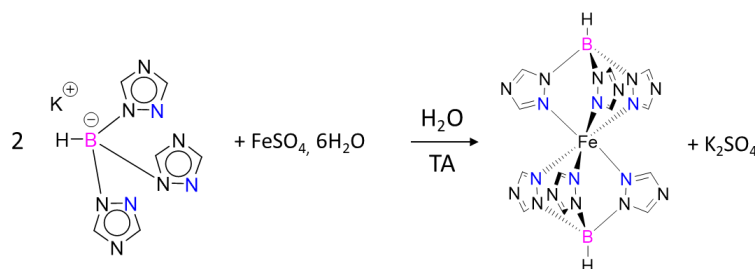


Figure 2.2: Scheme of the synthesis of [Fe(HB(tz)₃)₂].

As mentioned before, a color change due to the SCO is usually observed in the iron(II) complexes. In the case of Fe-triazole complexes, the HS state is usually white (colorless), whereas the LS state is purple due to a weak ligand-field absorption in the visible spectral range (centered near 540-550 nm). Therefore, we used optical reflectance measurement to characterize the SCO property of the $[\text{Fe}(\text{HB}(\text{tz})_3)_2]$ complex in the solid state. Variable-temperature optical reflectivity data were acquired with a MOTIC SMZ-168 stereomicroscope equipped with a MOTICAM 1000 color CMOS camera and with a THMS-600 heating-cooling stage (Linkam Scientific). A 2 K/min rate was used for both heating and cooling in the 20 - 100 °C range. As shown in Figure 2.3, the first and second thermal cycles recorded on the powder sample reveal an abrupt spin transition around 62 °C upon heating and cooling with a very small hysteresis loop. The SCO property of $[\text{Fe}(\text{HB}(\text{tz})_3)_2]$ inferred from our optical reflectance measurements shows good agreement with magnetic measurements previously reported for this compound [57]. One can remark that the hysteresis width slightly decreases between the first and second thermal cycles. This kind of ‘run-in’ phenomenon is typical for SCO complexes. Further variable-temperature optical reflectivity curves of the $[\text{Fe}(\text{HB}(\text{tz})_3)_2]$ complex from different synthesis batches can be found in [Annex 2.3](#). It shows that the spin transition behavior of the samples (*i.e.* the shape of the curve) is slightly different from batch to batch – this might be an indication of different purity. Nevertheless, the SCO phenomenon was clearly observed in each batch - all of them displaying an abrupt transition around 62 °C.

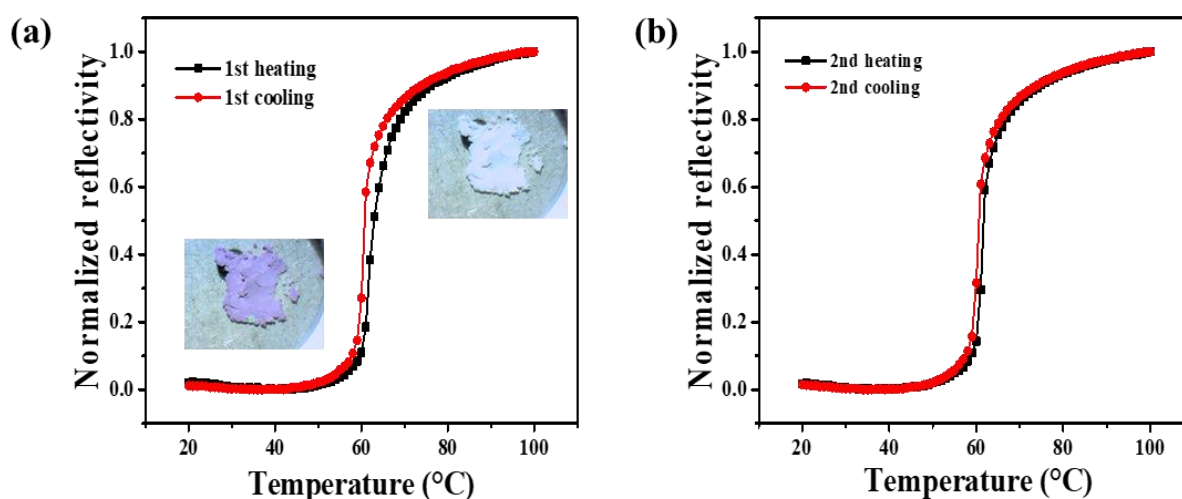


Figure 2.3: Variable-temperature optical reflectivity curves of the as-synthesized powder of $[\text{Fe}(\text{HB}(\text{tz})_3)_2]$ for (a) the first and (b) second thermal cycles. The insert shows photographs of the powder in the LS (purple) and HS (white) states.

Figure 2.4 shows the thermogravimetry analysis (TGA) of the powder of $[\text{Fe}(\text{HB}(\text{tz})_3)_2]$, which was performed with a PERKIN ELMER DIAMOND TG/TDA thermobalance, under a nitrogen atmosphere at a heating rate of $10\text{ }^\circ\text{C}/\text{min}$ under inert atmosphere. A high decomposition temperature (T_d) of *ca.* $330\text{ }^\circ\text{C}$ was observed, which indicates good thermal stability of this complex, *i.e.* the complex shows good endurance to high temperature, which guarantee the structural integrity of the molecules deposited on the substrates by vacuum thermal evaporation.

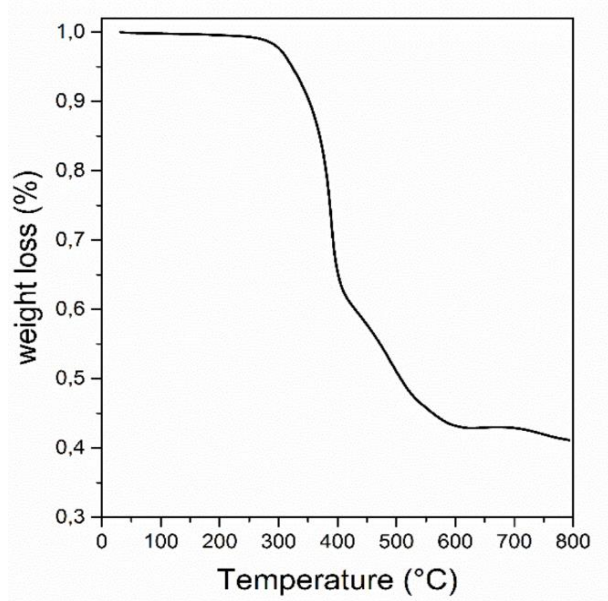


Figure 2.4: Thermogravimetry analysis of the bulk powder of $[\text{Fe}(\text{HB}(\text{tz})_3)_2]$.

2.3 Fabrication and characterization of $[\text{Fe}(\text{HB}(\text{tz})_3)_2]$ thin films

In this section, we describe the details of vacuum thermal evaporation and solvent vapor annealing of $[\text{Fe}(\text{HB}(\text{tz})_3)_2]$ thin films. The characterization of the films is based on X-ray diffraction, variable temperature UV-vis spectroscopy, AFM and optical microscopy.

2.3.1 Deposition of $[\text{Fe}(\text{HB}(\text{tz})_3)_2]$ thin films by vacuum thermal evaporation

Before the thin film deposition, the silicon and fused silica substrates were rinsed successively by acetone (VLSI, 99.5%) and ethanol (VLSI, 99.9%) for 5 min under sonication to remove the contaminants. The substrates were dried by an argon or nitrogen gas flow. Then, $[\text{Fe}(\text{HB}(\text{tz})_3)_2]$ thin films were deposited by thermal evaporation either in a PREVAC thermal deposition system at the LCC-CNRS or in a PLASSYS thermal evaporation system in the clean-room of LAAS-CNRS, both equipped with several organic material effusion cells (Figure 2.5). With the PLASSYS system, which was used for device fabrication, a rotating substrate holder

was used for both organic and metallic deposition to improve film thickness uniformity. In addition, to avoid any organic layer damage during the top electrode fabrication, the sample temperature was maintained below 30 °C by a water-cooled substrate holder. An evaporation rate of ca. 0.05 \AA s^{-1} is achieved at 250 °C in a vacuum of 2.7×10^{-7} mbar. The evaporation rate and film thickness were monitored *in situ* using a quartz crystal microbalance. The final control of the film thickness was carried out using a combination of stylus profilometry (Tencor P17), AFM (SmartSPM, Horiba) and optical reflectivity (Filmetrics model F-20). The Annex 2 gives selected examples for the thickness measurement protocol.

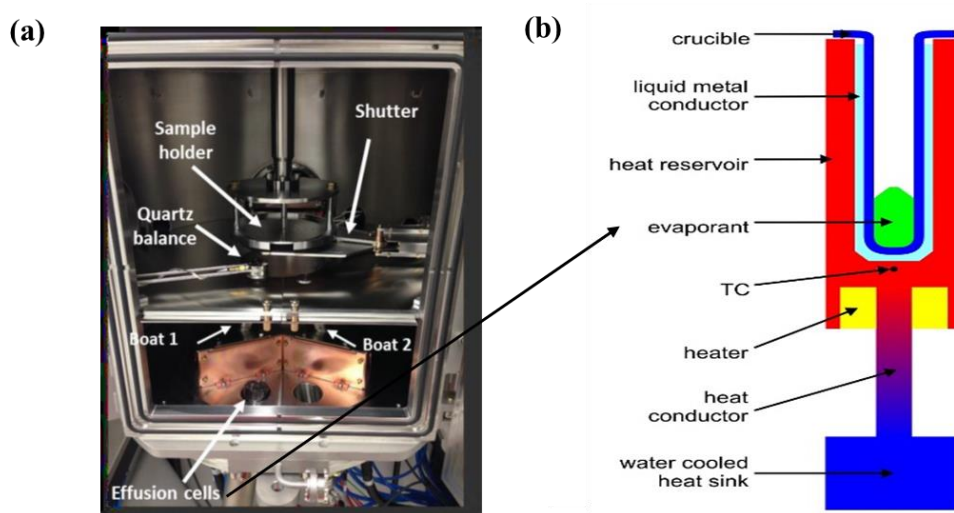


Figure 2.5: (a) Photo of the PREVAC thermal deposition system. (b) Scheme of the organic material effusion cell.

We have confirmed that the as-deposited thin films of $[\text{Fe}(\text{HB}(\text{tz})_3)_2]$ are amorphous and the SCO property in this kind of thin films is not stable and reproducible. To overcome these problems, water vapor annealing has been used to convert the amorphous as-deposited thin films to a preferentially-oriented crystalline form (see Section 1.2.8 for more details) 0. This treatment consists in simply placing the sample in a sealed box with ca. 75 % relative humidity at room temperature for 10 minutes.

Whereas preferential orientation of films can be an advantage for some applications, it can be also detrimental in others. For example, $[\text{Fe}(\text{HB}(\text{tz})_3)_2]$ thin films have been used to actuate MEMS cantilevers [92], but it turned out that most of the mechanical strain generated by the oriented SCO film is orthogonal to the cantilever axis and does not produce any useful mechanical work. On the other hand, a randomly oriented film of $[\text{Fe}(\text{HB}(\text{tz})_3)_2]$ (or a film with different orientation) would have produced a more substantial effect. This example highlights

the interest for growing films of $[\text{Fe}(\text{HB}(\text{tz})_3)_2]$ with different texture and even with no texture at all. As it was shown by Bas *et al.* [93], besides water, other polar solvents (diethyl ether, acetone, ethanol, ...) can be also used for solvent vapor annealing (SVA) of $[\text{Fe}(\text{HB}(\text{tz})_3)_2]$ films and they provide similar results. However, it was also observed that dichloromethane vapor treatment leads to less crystalline films with reduced preferential orientation. It was suggested that the reduced ability of CH_2Cl_2 to form hydrogen bonds (*vs.* the other solvents) led to a different crystallization mechanism. This result encouraged us to explore also the effect of non-polar solvents (octane, pentane, *etc.*) to treat the thin films. Interestingly, we have found that non-polar solvents allow us to obtain a metastable crystalline form of $[\text{Fe}(\text{HB}(\text{tz})_3)_2]$ thin films. In the following, we will compare in more detail water-vapor and octane-vapor treated films. For the octane vapor annealing, similar as the water treatment, we put the as-deposited sample in a sealed box at room temperature for half an hour under a saturated octane atmosphere. All thin films described in the following sections had a thickness of *ca.* 100 nm and they were thermally evaporated on both fused silica and Si substrates in the same conditions. The films were then characterized using (1) GI-XRD to determine their crystallographic structure, (2) variable-temperature UV-vis spectroscopy to assess their SCO properties and (3) optical microscopy (OM) and AFM to investigate their surface morphology. Finally, we have also deposited analogous $[\text{Zn}(\text{HB}(\text{tz})_3)_2]$ thin films. Obviously, these films do not display SCO and our objective with these films was to use them as reference, ‘SCO-inactive’ samples for device fabrication. Water vapor annealing was also applied on $[\text{Zn}(\text{HB}(\text{tz})_3)_2]$ thin films.

2.3.2 Crystallinity of the films

GIXRD experiments were carried out by means of a PANalytical X’Pert PRO MPD system using Cu-K α radiation (45 kV and 40 mA) with a parallel-beam configuration. The incident beam optics consisted of a mirror with a $1/32^\circ$ divergence slit. A parallel plate collimator (0.18°) and Soller slits (0.04°) were mounted on the path of the diffracted beam. An X’Celerator detector in receiving slit mode was used for X-ray collection.

As shown in Figure 2.6a, the diffraction pattern of the water vapor annealed $[\text{Fe}(\text{HB}(\text{tz})_3)_2]$ thin film shows an intense and single peak at $2\theta = 10.02^\circ$ indicating a highly preferential crystallographic orientation. In previous works, this peak has been clearly assigned to the 002 reflection, which means that the films are oriented with the *c*-axis of their orthorhombic unit cell normal to the substrate plane 0. (N.B. The as-deposited $[\text{Fe}(\text{HB}(\text{tz})_3)_2]$ thin film is amorphous and its GIXRD picture is shown in [Annex 2.x](#))

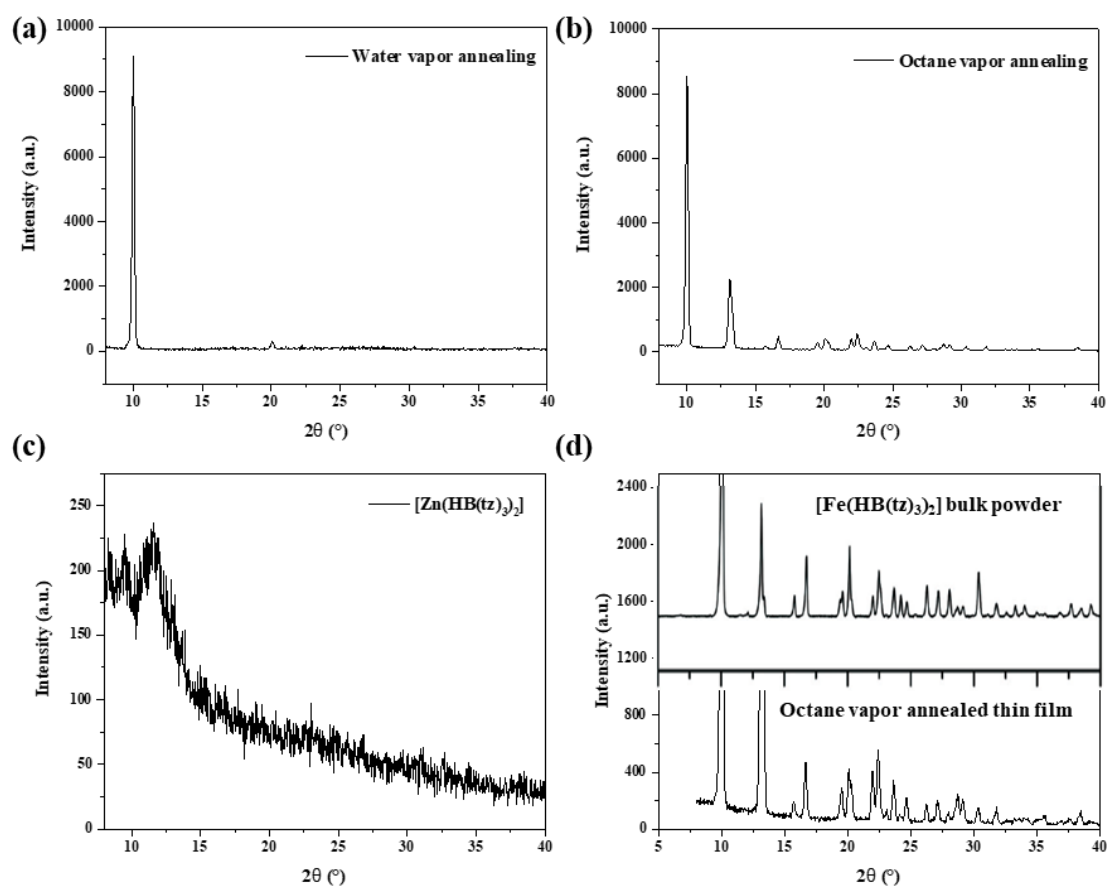


Figure 2.6: GIXRD spectrum of (a) $[\text{Fe}(\text{HB}(\text{tz})_3)_2]$ treated in water vapor, (b) $[\text{Fe}(\text{HB}(\text{tz})_3)_2]$ treated in octane vapor and (c) $[\text{Zn}(\text{HB}(\text{tz})_3)_2]$ treated in water vapor. (d) X-ray powder diffractogram of the microcrystalline bulk powder of $[\text{Fe}(\text{HB}(\text{tz})_3)_2]$ compared to the diffractogram of the octane-treated film shown in (b).

Remarkably, the diffraction pattern of the octane vapor annealed $[\text{Fe}(\text{HB}(\text{tz})_3)_2]$ thin film shows several smaller intensity diffraction peaks besides the 002 reflection (Fig. 2.6b). These peaks can be readily compared with the diffraction pattern of $[\text{Fe}(\text{HB}(\text{tz})_3)_2]$ in its bulk powder form in the LS state (Fig. 2.6d). We can thus conclude that octane (and non-polar solvents) lead also to a crystalline film, but with reduced preferential orientation.

Finally, we can observe that the $[\text{Zn}(\text{HB}(\text{tz})_3)_2]$ thin film is amorphous (Fig. 2.6c). We can infer from this result that the water vapor annealing does not allow the recrystallization of this type of films.

2.3.3 SCO properties of the $[\text{Fe}(\text{HB}(\text{tz})_3)_2]$ thin films

The temperature dependent absorbance spectra of the thin films were collected at wavelengths between 200 and 600 nm using a Cary 50 (Agilent Technologies)

spectrophotometer and a Linkam FTIR-600 liquid nitrogen cryostat (equipped with UV-transparent fused silica windows). The sample chamber was purged with dry nitrogen and spectra were acquired in the 30–100 °C range with 1 °C / min rate. The variable-temperature UV-vis absorbance spectra and temperature dependence of the absorbance at 317 nm along two heating–cooling cycles of water vapor annealed [Fe(HB(tz)₃)₂] thin film are shown in Figure 2.7a-2.7c. The sample is fully transparent in the visible-NIR spectral regions over the whole temperature range. On the other hand, three intense absorption bands can be seen at *ca.* 272, 305 and 318 nm at 30 °C (LS state), which vanish upon heating to 100 °C (HS state). When plotting the absorbance at 318 nm as a function of temperature (Figure 2.7c) one can depict an abrupt drop around 65 °C with nearly no hysteresis due to the SCO phenomenon. The shape of the SCO curves as well as the magnitude of absorbance changes are quantitatively comparable with previous results from the team⁰, confirming once more the robustness of this film fabrication process.

The variable temperature UV-vis absorbance spectra of an octane vapor annealed film are shown in Figure 2.7d-2.7f. The octane treated film shows a similar absorbance spectrum and a similar spin transition curve as the water vapor annealed [Fe(HB(tz)₃)₂] film. The absorbance change (at 318 nm) between the LS and HS states is comparable in the two samples (*ca.* 0.3 – 0.33). This means that the spin transition is closely complete in both samples. The spin transition temperatures are also similar (*ca.* 65 °C). Meanwhile, the SCO in the octane treated sample displays a small hysteresis of *ca.* 2 °C (with a $T_{1/2\uparrow} = 67$ °C and $T_{1/2\downarrow} = 65$ °C). Actually, we have found that the hysteresis width is systematically larger in octane treated samples. In addition, one can notice also that this hysteresis is not the “usual” hysteresis, associated with the SCO, because it occurs also far from the spin transition temperature (Figure 2.7f). We believe therefore that the origin of this hysteresis is not linked to the SCO, but rather to some other irreversible phenomena in the films.

Finally, let us note that the absorption spectrum of the [Zn(HB(tz)₃)₂] thin films (obviously) did not reveal any temperature dependence and showed no absorbance above *ca.* 270 nm (see Annex).

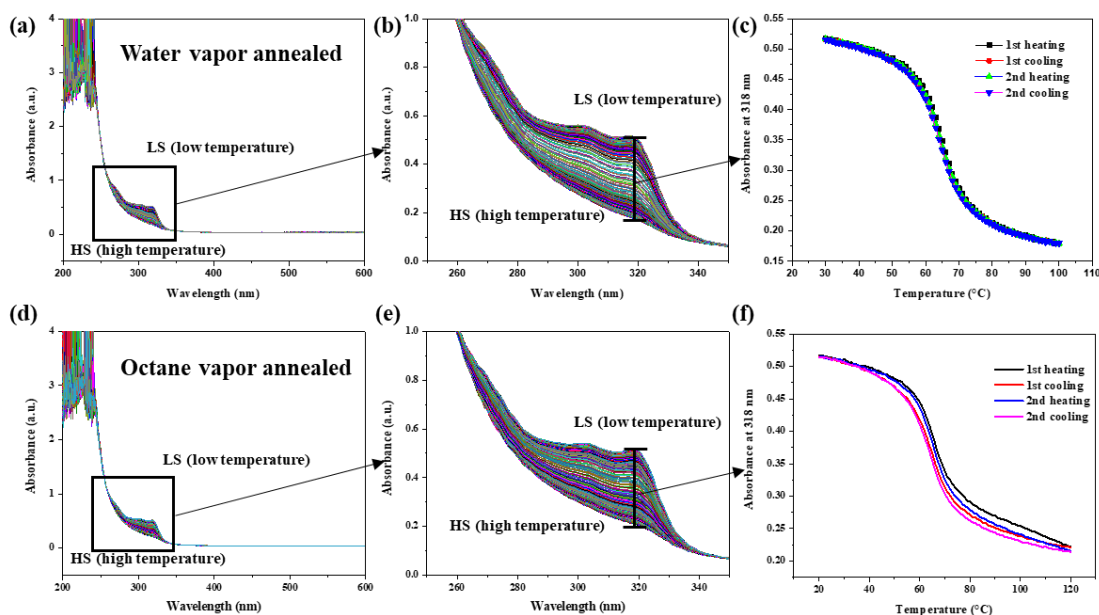


Figure 2.7: (a-b) Absorbance spectra of a 100 nm thick, water vapor annealed $[\text{Fe}(\text{HB}(\text{tz})_3)_2]$ film acquired between 30 and 100 °C in the heating mode. (c) Temperature dependence of the absorbance at 318 nm along two heating–cooling cycles recorded at 1 °C / min scan rate. (d-e) Absorbance spectra of a 100 nm thick, octane vapor annealed $[\text{Fe}(\text{HB}(\text{tz})_3)_2]$ film acquired between 30 and 100 °C in the heating mode. (f) Temperature dependence of the absorbance at 318 nm along two heating–cooling cycles recorded at 1 °C / min scan rate.

2.3.4 Surface morphology of $[\text{Fe}(\text{HB}(\text{tz})_3)_2]$ thin films

In many cases, film morphology plays an important role in the final electronic property of thin film based devices. For the analysis of the surface topography of our films, we used an atomic force microscope (SmartSPM, Horiba) in tapping mode in ambient conditions. Figure 2.8 shows typical AFM images for the different samples. Overall, we can say the films at the micrometric scale are continuous and smooth with an RMS roughness typically of a few nanometers. Whereas this level of roughness is certainly interesting for the construction of devices, we must be aware that in some cases (*e.g.* organic field effect transistors) the requirements for the film quality can be even more stringent.

Since we are interested in constructing large-area devices, it is important to have a larger scale view of the surface quality, which can be achieved by optical microscopy. As we can see from the OM images in Figure 2.9, compared with the smooth, continuous pristine thin film, water vapor annealing may induce a ‘branch-like’, dendritic structure in the thin film, which

can reach hundreds of μm in size. Note that except the area with ‘branch-like’ structures, the remaining surface area appears smooth and homogeneous, just as the pristine thin film. We believe that during the solvent-induced recrystallization of the film a large amount of nucleation events lead to a homogeneous film formation. However, due to various reasons (impurities, imperfection of the substrate, *etc.*) heterogeneous nucleation and growth inevitably occurs to some extent. This difference of roughness from area to area of the water vapor annealed $[\text{Fe}(\text{HB}(\text{tz})_3)_2]$ thin film suggests there might be a distribution of defect sites and domain boundaries (*i.e.* potential charge carrier traps) in the thin film, which can significantly influence the electronic behavior of the SCO-based electronic devices.

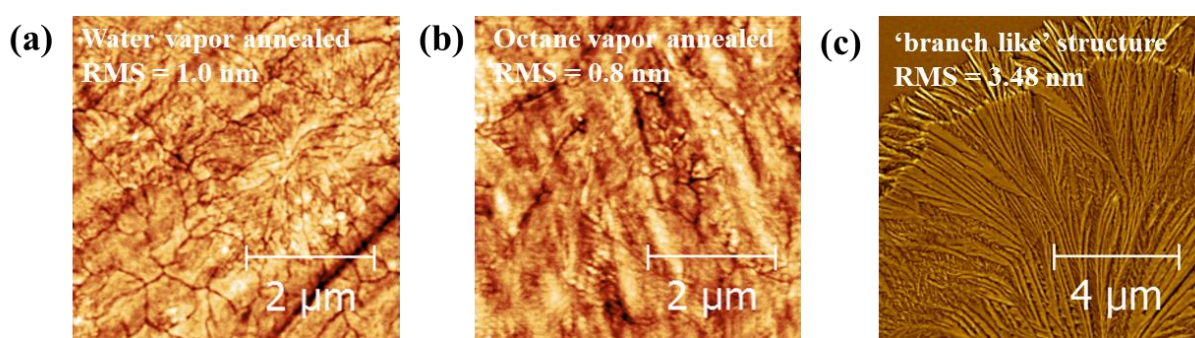


Figure 2.8: Representative AFM images ($5 \mu\text{m} \times 5 \mu\text{m}$) of water (a) and octane (b) vapor annealed $[\text{Fe}(\text{HB}(\text{tz})_3)_2]$ thin films and (c) typical ‘branch-like’ structures on both treated films.

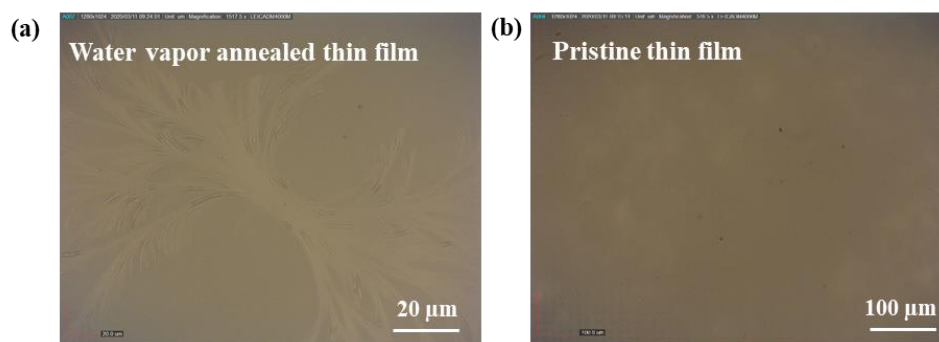


Figure 2.9: Optical microscopy (OM) images of (a) water vapor annealed and (b) pristine $[\text{Fe}(\text{HB}(\text{tz})_3)_2]$ thin films.

2.4 SCO-based resistance switching devices

As discussed in Section 1.2.8, the $[\text{Fe}(\text{HB}(\text{tz})_3)_2]$ complex exhibiting an abrupt and robust spin transition slightly above room temperature represents an attractive platform for device development. The first report on an electrical junction using $[\text{Fe}(\text{HB}(\text{tz})_3)_2]$ thin films as the

active layer was published in 2018 [74]. The resistance switching property in ITO/[Fe(HB(tz)₃)₂]/SCO junctions with different SCO layer thicknesses (10, 30, 100 and 200 nm) was studied and an ON/OFF current ratio of *ca.* 8 was found when switching the molecules from the LS to the HS state (see also Section 1.3.2 and Fig. 1.23). These first results provided the starting point for this thesis work, which aimed for a more comprehensive investigation of these junctions with the following objectives. (1) First, for any real-world application of a resistance switching device, it is necessary to reach a high resistance difference between the conducting and resistive states. We have therefore paid a particular attention on the ON/OFF switching ratio of the devices, which can be simply defined in our case as the ratio between the current intensities in the two spin states. (2) Device fabrication reproducibility and switching fatigue are also important considerations, which have not much been investigated before on SCO devices. (3) Last, but not least, it is crucial to analyze the mechanistic aspects of the resistance switching property in terms of modification of charge transport upon the SCO.

2.4.1 Fabrication and characterization of ITO/[Fe(HB(tz)₃)₂]/Al junctions

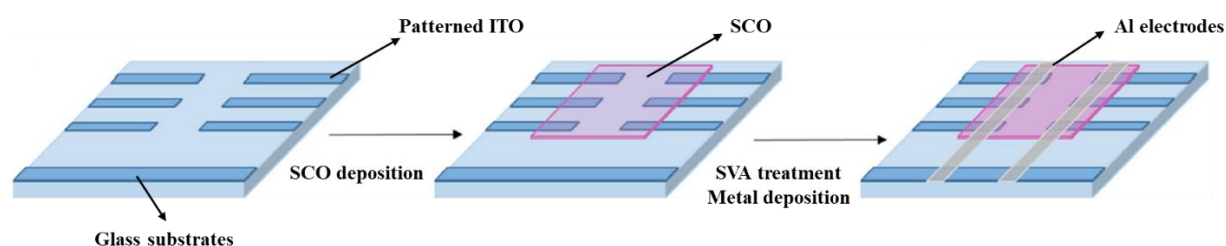


Figure 2.10: Fabrication procedure of ITO/[Fe(HB(tz)₃)₂]/Al junctions.

Figure 2.10 demonstrates the procedure to fabricate the ITO/SCO/Metal crossbar junctions, here specifically, SCO and Metal corresponding to [Fe(HB(tz)₃)₂] and Al, respectively. Before the fabrication, the ITO substrates (CEC010S from Praezisions Glas & Optic GmbH) were rinsed successively by acetone (VLSI, 99.5%) and ethanol (VLSI, 99.9%) for 5 min under sonication. The substrates were dried by a nitrogen gas flow. Then, a 100 nm thick film of [Fe(HB(tz)₃)₂] was deposited by thermal evaporation at 180 °C under high vacuum (2.7×10^{-7} mbar) at a rate of *ca.* 0.3 \AA s^{-1} , followed by water-vapor annealing in *ca.* 80% relative humidity air at room temperature for 10 min. Finally, a 100 nm thick Al film was deposited through an evaporation mask under a vacuum pressure of about 3.0×10^{-6} mbar at a rate of 10 \AA s^{-1} to form the upper electrodes of the ITO/[Fe(HB(tz)₃)₂]/Al junction. A rotating substrate holder was used for both SCO and metallic deposition to improve film thickness

uniformity. In addition, to avoid any SCO layer damage during the top electrode fabrication, the sample temperature was maintained below 50 °C by a water-cooled substrate holder. The obtained effective junction area is *ca.* 3 mm².

The ITO/[Fe(HB(tz)₃)₂]/Al junctions were first characterized for their room temperature resistance. Current–voltage and current–temperature characteristics of the junctions were investigated using a Keithley-6430 source-meter and a heating-cooling probe station (Linkam Scientific HFS350EV-PB4) equipped with gold-tipped tungsten probes (Figure 2.11).

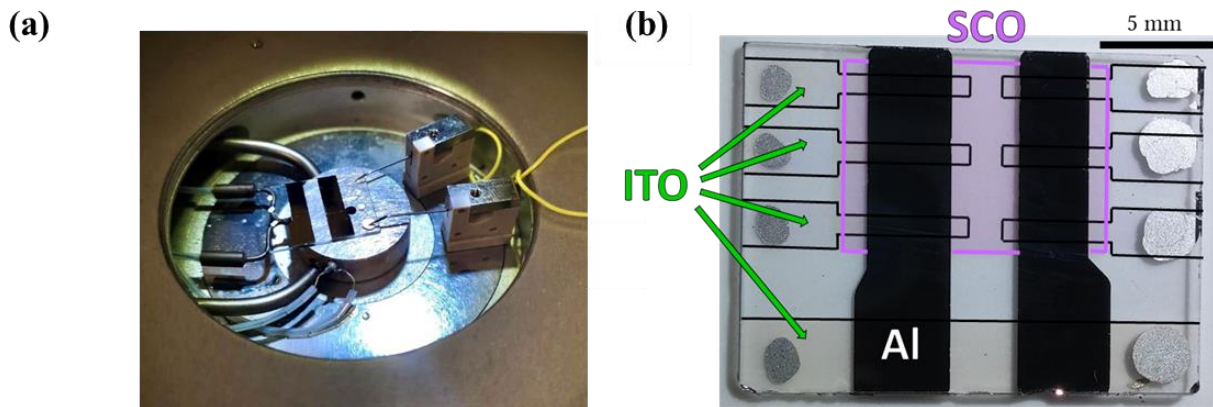


Figure 2.11: Photos of (a) a chip with six ITO/[Fe(HB(tz)₃)₂]/Al junctions placed on the variable-temperature probe station and (b) a zoom on the junctions.

Table 2.2 reports the resistance data obtained as the average of three measurements under 1 μA current bias for 24 junctions (on 4 chips). None of the junctions were short-circuited and the global mean resistance value of 3.0 ± 0.4 MΩ is well reproduced device-to-device. The room temperature *I–V* characteristics averaged for 12 as prepared devices are shown in figure 2.12. The device-to-device reproducibility of the current value for 5 V applied bias was found *ca.* 15%.

Table 2.2: Comparison of the room temperature electrical resistance of a batch of ITO/100 nm [Fe(HB(tz)₃)₂]/Al junctions

Device n°	1	2	3	4	5	6	7	8	9	10	11	12
Resistance (MΩ)	3.7	2.7	2.5	3.4	3	2.7	3.5	2.8	2.5	3	3.1	2.8
Device n°	13	14	15	16	17	18	19	20	21	22	23	24
Resistance (MΩ)	3.4	2.9	2.7	3.4	3.1	2.8	3.2	2.7	2.3	3.3	3	2.6

Similar to our previous report, we found that the *I–V* curves of the junctions are strongly nonlinear – as one can expect for a metal-insulator-metal junction. Importantly, the junctions

behave in a reproducible manner only under forward bias, i.e. when the Al electrode is the cathode. Under reverse bias, not only the measurements become less reversible, but also the devices were more promptly degraded. The origin of the instability of the junctions under reverse bias remains unclear.

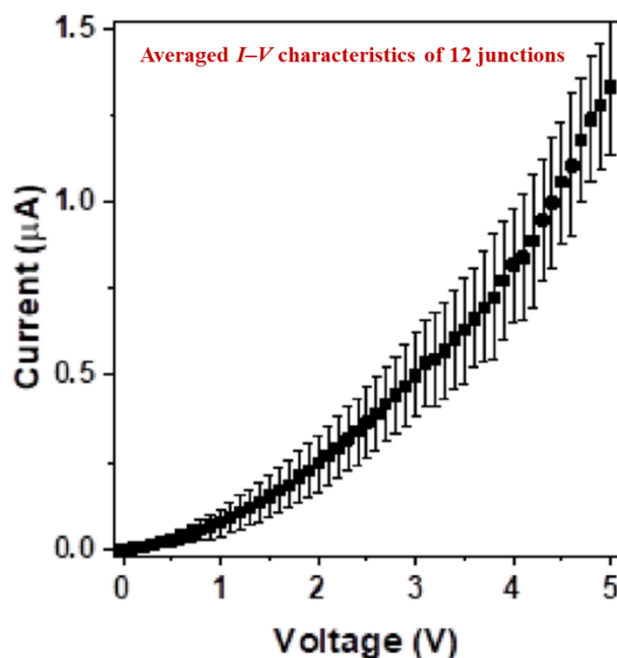


Figure 2.12: Averaged I - V characteristics of twelve as-prepared ITO/100 nm $[\text{Fe}(\text{HB}(\text{tz})_3)_2]/\text{Al}$ junctions recorded in ambient conditions at rates of $\pm 100 \text{ mV s}^{-1}$. The error bars show the standard deviation of the measured current intensity.

2.4.2 Resistance switching properties of ITO/ $[\text{Fe}(\text{HB}(\text{tz})_3)_2]/\text{Al}$ junctions

Figure 2.13 depicts the temperature dependent I - V and I - T characteristics of a ITO/ $[\text{Fe}(\text{HB}(\text{tz})_3)_2]/\text{Al}$ junction. Figures 2.12(a)–(d) refer to the first, second, third and fourth successive thermal cycle, respectively, acquired for the same junction. The I - T curves show a weak thermal activation and, in perfect agreement with our previous report [74], a substantial change from a high conductance state to a low conductance state occurs at around $65 \text{ }^\circ\text{C}$ while heating. Since this resistance-switching phenomenon is opposed to the thermal activation of the conductance, we can unambiguously distinguish the two processes and extract properly the ON/OFF switching ratio arising solely from the SCO.

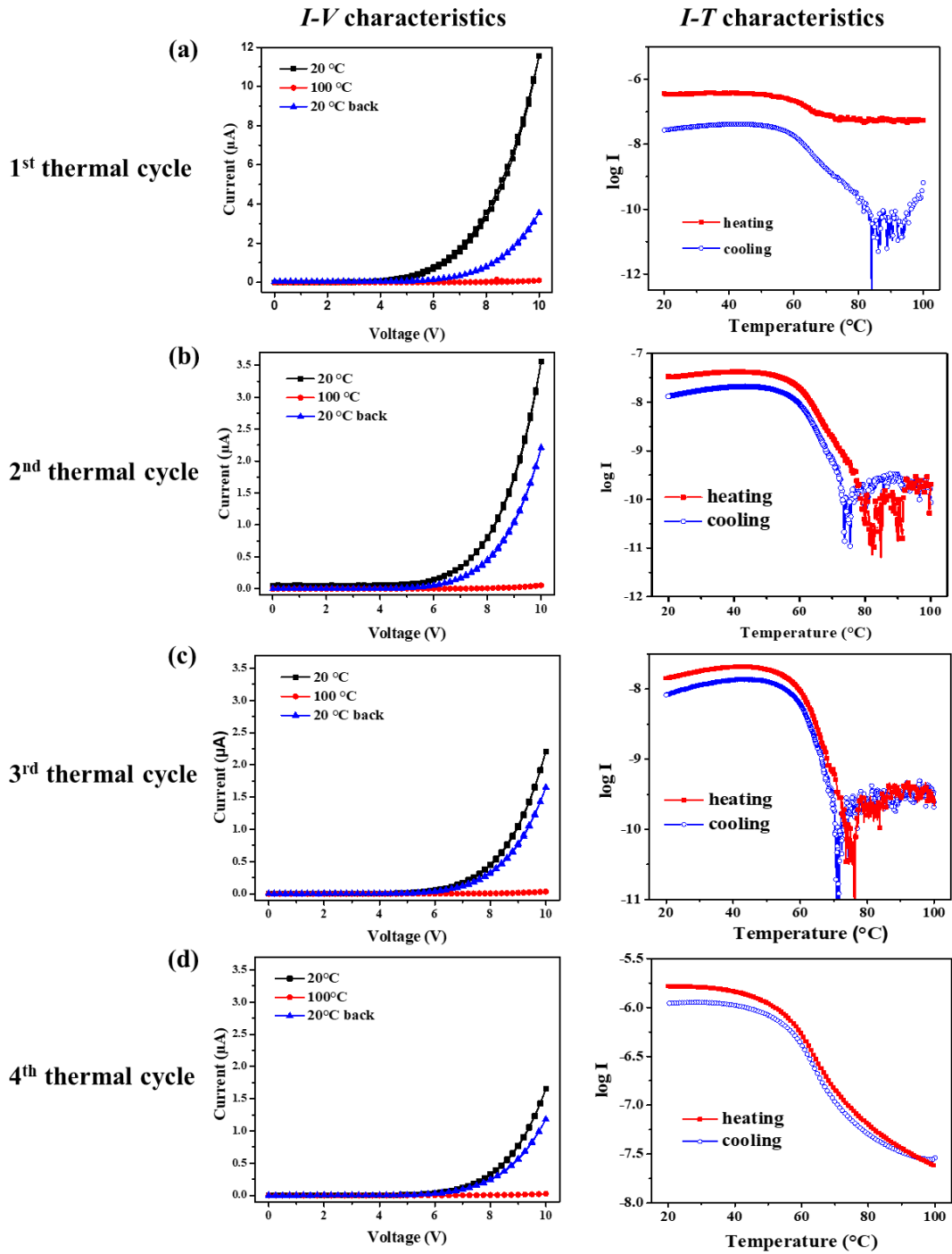


Figure 2.13: Electrical characteristics of an ITO/100 nm $[\text{Fe}(\text{HB}(\text{tz})_3)_2]/\text{Al}$ junction. The results of four successive thermal cycles are showed in (a), (b), (c) and (d). Left: I - V curves recorded at 20 °C and 100 °C and then again at 20 °C at rates of ± 100 mV/s. Right: $\log I$ - T curves recorded with an applied bias of 5 V for first three thermal cycles (a, b and c, respectively) and 10 V for the fourth thermal cycle (d), at scan rates of ± 10 °C/min.

In figures 2.13a–d, one can note that upon successive thermal cycles the junction properties are modified. In particular, the first heating leads always to an anomalous response,

but starting from the first cooling curve the device resistance becomes sensibly less affected by the heating-cooling cycle. (N.B. In order to reduce the noise at high temperatures, in the 4th thermal cycle we applied higher voltage, leading obviously to higher current intensities.) This ‘run-in’ effect may be linked to stress relaxation phenomena in the devices. It is important to note that reasonably reproducible device characteristics upon heating-cooling could be achieved by optimizing the experimental conditions. In particular, the measurement reproducibility is increased by applying only low bias (5 V) and by reducing the exposure of the junctions to high temperatures. This latter condition was achieved by limiting the temperature span to 100 °C and increasing the scan rate to 10 K min⁻¹. However, it is fair to say that despite all our efforts each investigated junction showed continuous ageing, which was accelerated by thermal/voltage cycling. (See further details on the question of cycling fatigue in Section 2.3.3.)

The data in figure 2.13 reveal another important finding. In contrast to the previously reported ON/OFF ratio of 8 (*i.e. ca.* one order of magnitude switching), in the present experiments the resistance changes reach 2–3 orders of magnitude in several devices, with ON/OFF ratios up to 400. We believe that this spectacular improvement of ON/OFF switching ratios, with respect to the devices reported in, is likely related to the more careful handling of the devices in terms of exposure to air, high voltages and high temperatures.

Another important issue here is the strong nonlinearity of the I - V curves. As shown in figure 2.14, when switching from the LS to the HS state, the current intensity drops by the same factor (ON/OFF \approx 100) in the high voltage regime ($>ca.$ 6.5 V), wherein both the HS and LS conductions are effectively voltage activated. On the other hand, at low bias ($<ca.$ 4 V) the conduction vanishes in both spin states. There exists however, an intermediate voltage range between *ca.* 4–6.5 V wherein the LS conduction is activated, whereas the HS state remains strongly resistive. In this voltage window, we observe a peak ON/OFF = 400 switching ratio, which arises clearly from the decrease of the turn-on voltage (V_{ON}) when going from the HS to the LS state. (N.B. The peak ON/OFF ratio we observe here is limited by the dark current as well as by the noise floor of our electrometer.)

In order to examine the possible role of the preferential orientation of the SCO film on the junction behavior, we also integrated octane vapor annealed [Fe(HB(tz)₃)₂] thin films (with reduced preferential orientation) in a few junctions. Non-linear I - V characteristic and SCO-induced resistance-switching with a ratio of *ca.* 2 can be depicted in Figure 2.6. Unfortunately, the low device-to-device reproducibility of the ON/OFF switching ratios make it difficult to

draw a clear conclusion, but this result indicates that the crystalline orientation is likely not a major factor in determining the device properties. At this point, it is worth to mention that devices were also fabricated using SCO inactive $[\text{Zn}(\text{HB}(\text{tz})_3)_2]$ films, which quite expectedly, did not show any switching property (Annex).

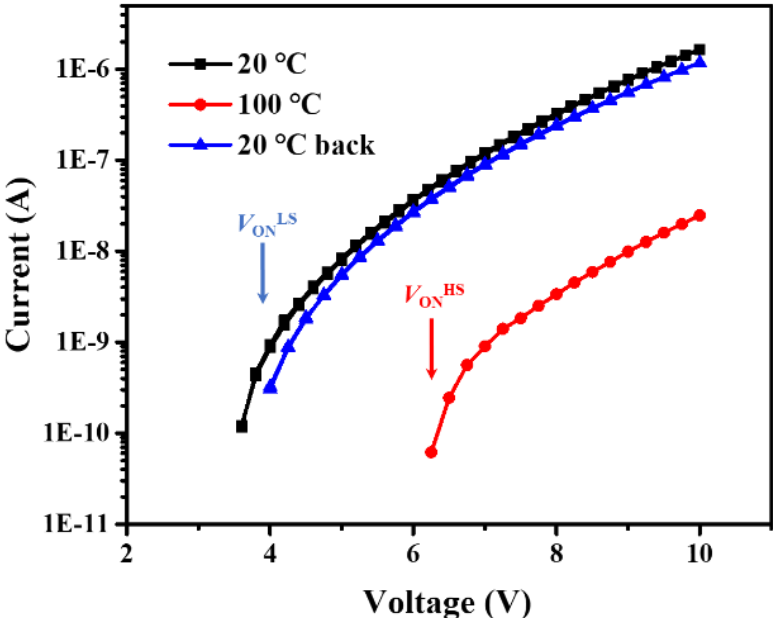


Fig 2.14: Log I - V representation of a ITO/100 nm $[\text{Fe}(\text{HB}(\text{tz})_3)_2]$ /Al device characteristics at different temperatures evidencing a shift of the turn-on voltage (V_{ON}) between the LS and HS states.

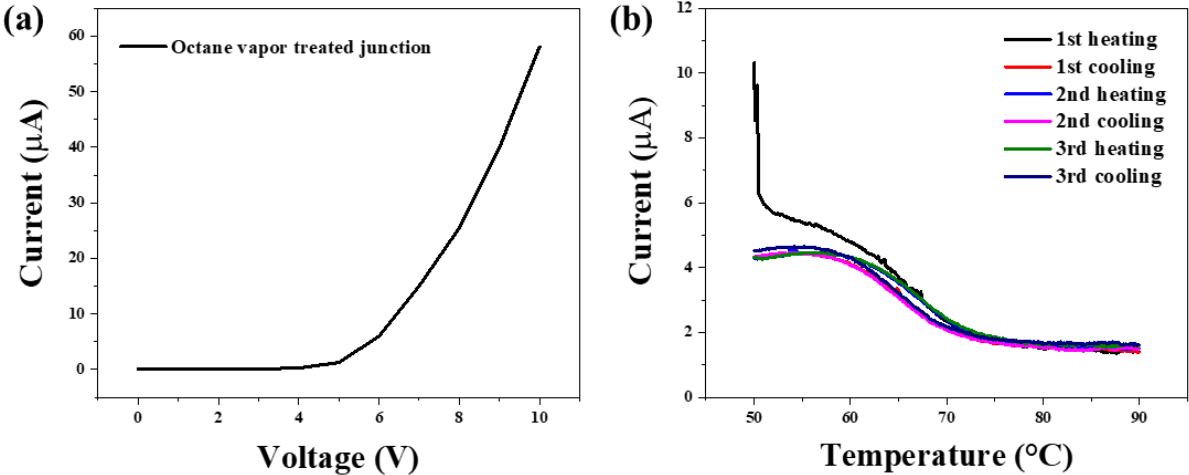


Figure 2.15: Electrical characteristics of an ITO/100 nm $[\text{Fe}(\text{HB}(\text{tz})_3)_2]$ (octane vapor annealed)/Al junction. Left: I - V curve recorded at 20 °C at a rate of 100 mV/s. Right: I - T curves recorded under 8 V applied bias for the first three thermal cycles at scan rates of ± 2 °C/min.

2.4.3 Stability of ITO/[Fe(HB(tz)₃)₂]/Al junctions

Improving both the long-term stability and switching endurance of SCO-based electronic devices is critical to the deployment of this technology. Despite many different SCO materials with different device configurations were investigated and reported, there are very few publications, which have addressed the stability issue of those SCO-based electronic devices.

The degradation of SCO-based electronic devices is affected by multiple parameters whose impact on device stability remains to be understood. With regard to experience with other types of molecule-based electronic devices, the main factors that influence the stability of the devices are oxygen, humidity, temperature, voltage/current bias and mechanical stress. For instance, oxygen is a well-acknowledged factor that reduce the stability of organic electronic devices. First, the metal electrodes (*e.g.* Al and Ca) can be oxidized due to oxygen permeation. The metal oxide layer, which exhibits an insulating property, will induce a barrier between the electrode and the active layer, thus influencing the electron injection and degrade the performance of the device [94]. Second, oxygen molecules may react with the molecules in the active layer and then the change of structure of the complex will result in the change of MO energy levels and charge carrier mobility of the active layer [95]. This concern is particularly important for Fe(II) SCO molecules, which can be oxidized to Fe(III). Last but not least, oxygen in the active layer will enhance hole concentration and thereby increase the density of deeper traps for electrons [96]. Besides, heating (working temperature, Joule effect) also plays a vital role in device degradation. Normally, the working temperature is still far below the decomposition temperature of active layer, but it can be a co-factor, which accelerates device degradation [97].

We conducted a series of experiments to investigate the stability of the benchmark ITO/[Fe(HB(tz)₃)₂]/Al junctions, which aimed to have an insight in how the factors above would influence the stability of these devices and potentially other SCO-based electronic devices. In order to check the long-term stability of two-terminal devices, we left a non-encapsulated ITO/SCO/Al junction in the ambient laboratory environment (*ca.* 20-25°C and 50-80 % relative humidity). Figure 2.16 displays the *I-V* characteristics of the fresh and “1 year aged” junctions. As we can see from this figure, the non-encapsulated ITO/100 nm [Fe(HB(tz)₃)₂]/Al preserves reasonably well the initial electrical characteristic of the device after 1 year.

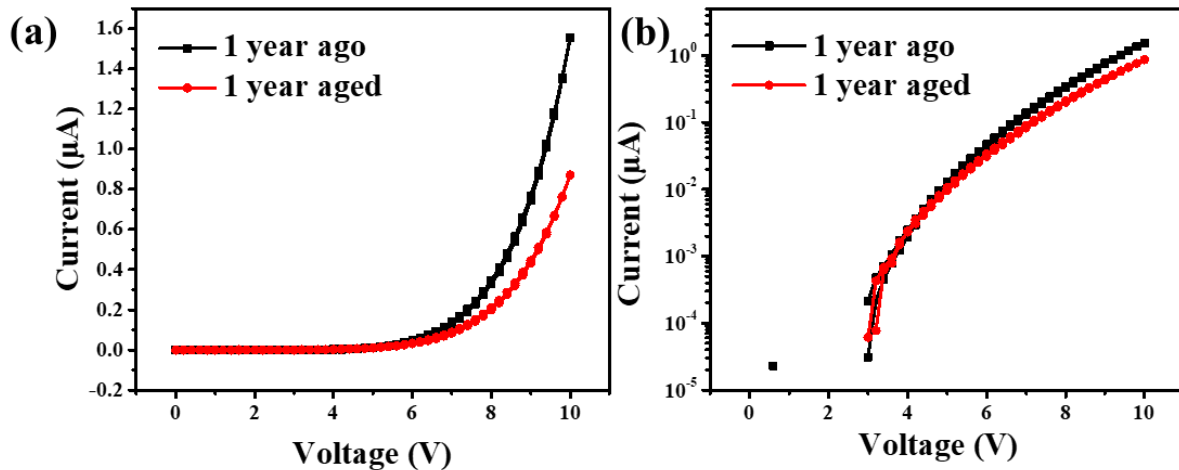


Figure 2.16: Room temperature *I-V* characteristics of a non-encapsulated ITO/100 nm [Fe(HB(tz)₃)₂]/Al junction just after fabrication and following 1 year storage in ambient conditions. Both linear (a) and logarithmic (b) representations are shown.

In a next step, we compared the *I-T* characteristics of the non-encapsulated ITO/100 nm [Fe(HB(tz)₃)₂]/Al junction, as shown in Figure 2.17. These measurements were conducted in ambient atmosphere without additional protection. Figure 2.17(a) and (b) refers to the *I-T* characteristics of the fresh and “1-year aged” aged junction, respectively. In agreement with the *I-V* characteristics, the *I-T* curves confirm the increased resistance of the junction after 1-year storage. More importantly, they reveal that the resistance switching property is maintained in the junction. The ON/OFF current ratio reaches a value around 3, both the fresh junction and the “1-year aged” junction. Note that we observed a ‘run-in’ phenomenon in this junction, which can be clearly seen from Figure 2.17b (black curve): the *I-T* characteristics of the first heating is different from all the successive thermal cycles. It is interesting to underline here that this sample was previously heated several times, but after one-year storage, we can see again the run-in phenomenon.

We further examined if such run-in phenomenon can be observed in other experimental situations. As shown in Figure 2.18, a series of bias voltage of 3, 4, 5, 6, 7 and 8 V was applied to the junction for *I-T* measurements, with the same temperature ramping rate of ± 1 °C/min. It can be clearly seen that a ‘run in’ phenomenon took place in all of the cases, the *I-T* characteristics of the first heating is always different – just after changing the bias voltage. For further thermal cycles, the *I-T* characteristics are well reproducible. One shall note that this good reproducibility is obtained by working in a reduced temperature range between 45-85 °C. It is interesting to remark also that in most cases the current through the junction at the

beginning of the measurement is always lower than the current after the first thermal cycle. We tentatively attribute this observation to a device relaxation phenomenon [98].

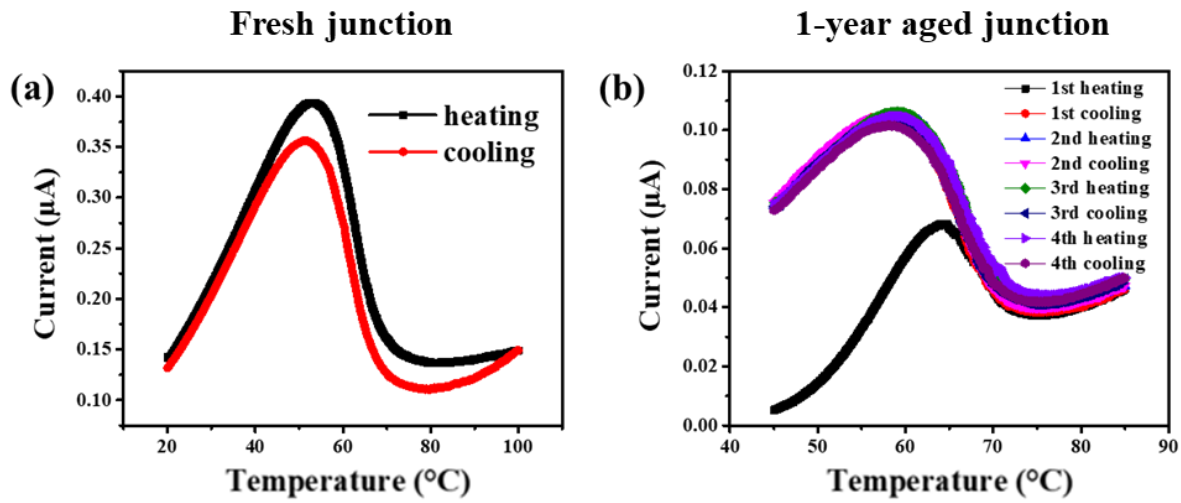


Figure 2.17: I - T characteristics of a non-encapsulated ITO/100 nm $[\text{Fe}(\text{HB}(\text{tz})_3)_2]/\text{Al}$ junction: (a) fresh (in the 2nd thermal cycle) and (b) 1-year aged. The I - T curves were recorded with an applied bias of 5 V at scan rates of ± 1 °C/min.

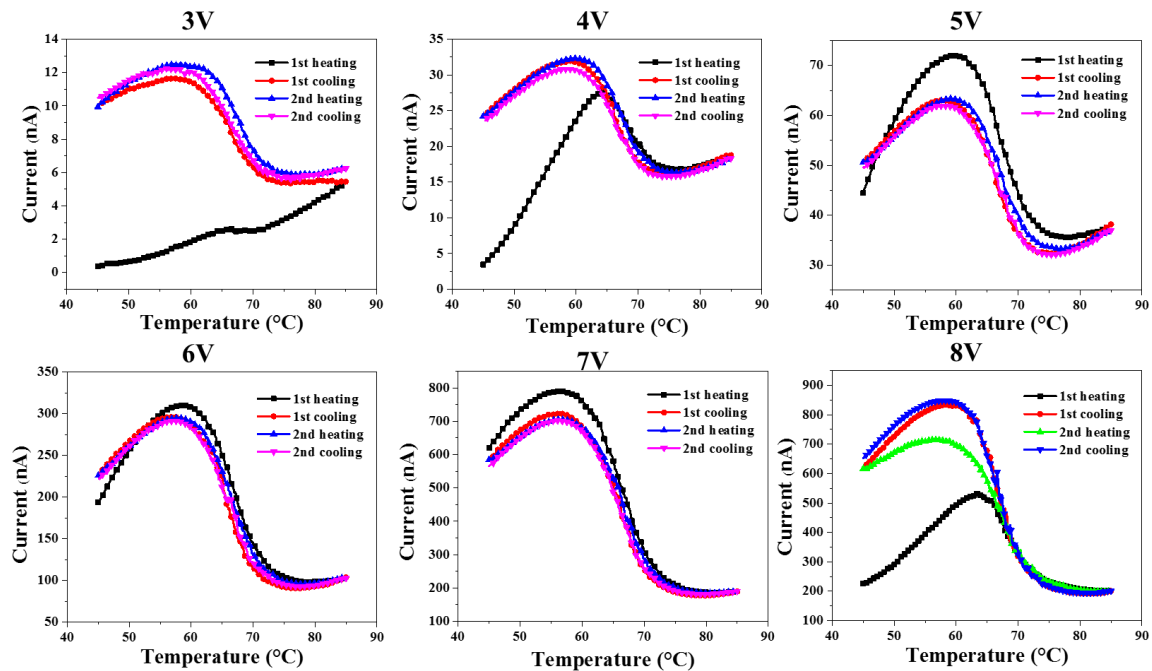


Figure 2.18: I - T characteristics of a “1-year aged” non-encapsulated ITO/100 nm $[\text{Fe}(\text{HB}(\text{tz})_3)_2]/\text{Al}$ junction. I - T curves were recorded with different applied bias between 3 and 8 V at scan rates of ± 1 °C/min. For each bias, two successive heating-cooling cycles were carried out.

Figure 2.19 shows the ON/OFF current switching ratio for different applied bias voltages. When the applied bias voltage is above 4 V, the ON/OFF current switching ratio keeps increasing with the voltage. However, when the applied bias voltage is under 4 V, the ON/OFF current switching ratio seems to change in an opposite direction. We tried to measure the I - T characteristics of the “1-year aged” non-encapsulated ITO/100 nm [Fe(HB(tz)₃)₂]/ Al junction in a lower applied bias than 3 V. However, due to the detection limit of our setup, we failed to obtain clear I - T curves (Annex).

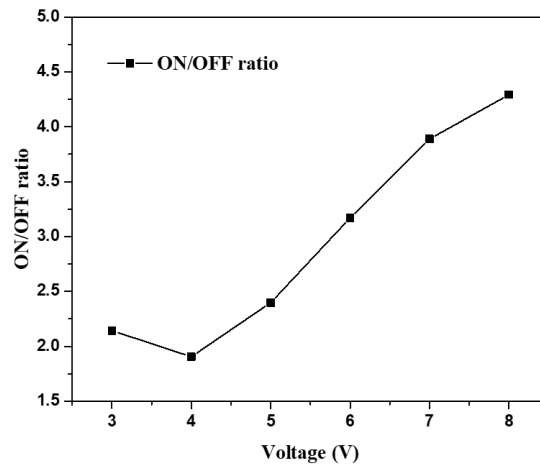


Figure 2.19: ON/OFF current switching ratio as a function of the applied bias voltage of a 1-year aged non-encapsulated ITO/100 nm [Fe(HB(tz)₃)₂]/Al junction.

We also investigated the cycling endurance of the 1-year aged non-encapsulated ITO/100 nm [Fe(HB(tz)₃)₂]/Al junction upon thermal cycles under a constant bias voltage of 3 V with a temperature ramping rate of ± 20 °C/min range between 50 and 80 °C. During a non-stop, 2-weeks long electrical measurement in ambient conditions (without any protection of the environment), we recorded >10.000 resistance switching cycles between the high spin (low current intensity) and low spin (high current intensity) molecular spin states in our ITO/[Fe(HB(tz)₃)₂]/Al junction (Fig. 2.20). Astonishingly, the junction retained the resistance switching property after such a large number of switches. These findings provide a direct proof that SCO-based electronic devices could have an unprecedented long-term stability, with careful device integration and measurement condition controls. Even if the ON/OFF ratio (ca. 3) is remarkably stable all along these switching cycles, it is fair to mention that at the beginning of the experiment, the current intensity was switched between *ca.* 12 and 4 nA, which has been reduced by a factor of two towards the end of the cycling (*i.e.* 6 and 2 nA).

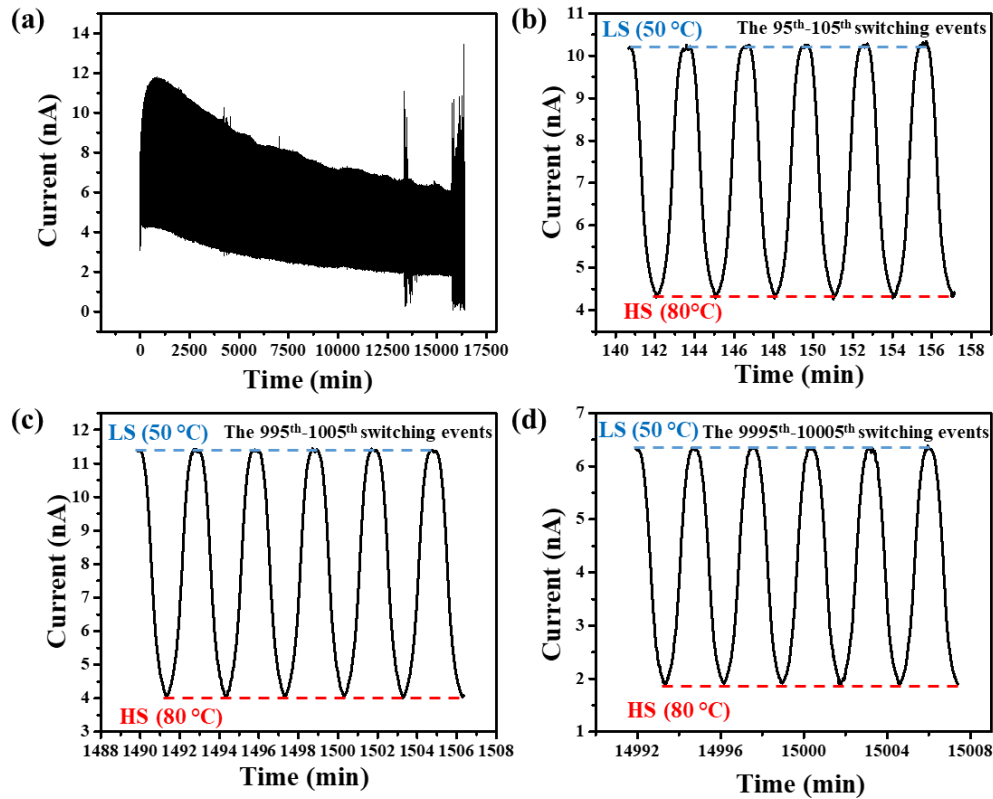


Figure 2.20: (a) Current switching cycles between the HS (low current intensity) and LS (high current intensity) states in a ITO/[Fe(HB(tz)₃)]/Al large-area vertical junction during >10.000 switches under a constant bias voltage of 3 V with a temperature ramping rate of ± 20 °C/min range between 50 and 80 °C. Zooms are also shown on the 95th – 105th (b), the 995th – 1005th (c) and the 9995th – 10005th (d) switching events.

In Figure 2.20, one can note some noise of the current intensity towards the end of the long-time measurement. This phenomenon is related most likely to a slight movement of the measurement tips during the experiment. To remove the doubt that this noise comes from the junction itself, we repositioned properly the probes and we carried out another successive *I-T* characterization. These resistance switching cycles are shown in Figure 2.21. As we can see, the junction retained the current switching property for more than 800 switches and there is no more spurious ‘noise’ during this measurement. Note that we observed that the degradation of the current seems to be irreversible during the long-time measurement, no ‘relaxation/recovery’ phenomenon happened in the junction during this kind of measurement. This indicates that heat together with electric stress (electric measurement) may induce a degradation to the electronic device. As we shall see later, this phenomenon is strongly dependent on the device architecture. Notably, we found similar, but much faster degradation in 3-terminal devices (SCO-OFET transistors), which we will discuss more in chapter 3.

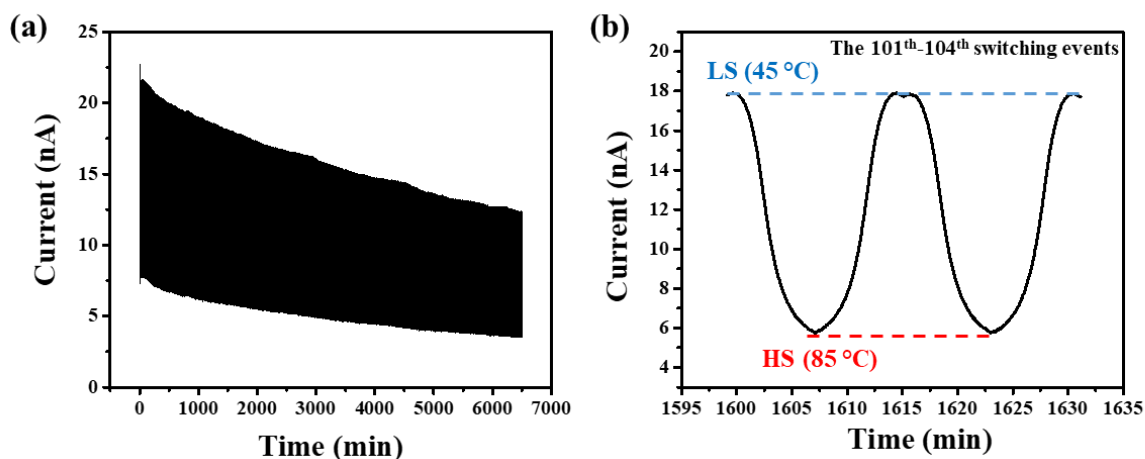


Figure 2.21: a) Current switching cycles between the HS and LS states in a ITO/[Fe(HB(tz)₃)₂]/Al large-area vertical junction during >800 switches under a constant bias voltage of 3 V with a temperature ramping rate of ± 5 °C/min range between 45 and 85 °C. (b) A zoom on the 101th – 104th switching events.

2.4.4 Charge transport mechanism underlying the resistance-switching phenomenon

2.4.4.1 General considerations

In bulk SCO materials, the dominant transport mechanism is charge carrier hopping via localized electronic states. This process is also termed polaron hopping and corresponds, in essence, to redox phenomena between neighboring molecules. Hopping through “thick” films (>*ca.* 50 nm) takes place thus in numerous steps and involves a substantial nuclear motion (relaxation) at each hopping event. This type of conduction is therefore generally associated with low mobility and pronounced voltage and thermal activation [99]. Such charge transport by polaron hopping is customary in organic electronics and has been investigated also for many SCO systems, including bulk materials, nanoparticles and films [100, 101, 56]. The general picture, which emerges from these experiments, is a moderate effect of the spin state of the molecule on the conductivity (less than 1-2 orders of magnitude change), due to the relatively small, and sometimes opposed, variation of hopping parameters upon the SCO (interatomic/intermolecular distances, vibrational frequencies and reorganization energies). In all reported cases, the LS state appears more conducting, which was ascribed to the higher phonon (*i.e.* hopping) frequencies of the LS molecules [102], but it was predicted that there might be exceptions to this general trend [101, 103].

In the opposite size limit, charge transport is governed by direct tunneling from one electrode to the other. This mechanism is limited by the localization of the electron wave function to junctions below approx. five nm thickness [99]. This type of charge transport concerns essentially single molecule SCO junctions, which have been extensively investigated by scanning tunneling microscopy (STM) and quantum chemical calculations in the past decade [104-112]. The general picture, which emerges from these studies, is a very significant spin-state dependence of the tunneling current, which arises from the concomitant changes of barrier height and barrier length upon the SCO event. In general, the HS state appears more conducting. This was attributed to the sizeable decrease of the HOMO-LUMO gap when the ligand field decreases [110]. We shall note, however, that SCO in molecular junctions was achieved in general when strong electronic interactions between the electrode(s) and the molecule(s) were prevented [107, 112]. In this weak coupling limit, a simple orbital-alignment scheme becomes questionable as the junction exhibits Coulomb blockade behavior (*i.e.* charging).

Besides these opposite (bulk and molecular) size limits, there have been also reports on SCO devices operating in the “intermediate” range of charge transport (between *ca.* 5 and 50 nm) [64, 73-[], 104]. The transport mechanism in these cases is usually unclear and may include resonant tunneling (via one or more localized sites), field emission, directed inelastic hopping, *etc.*

In the previous investigation of the charge transport in ITO/[Fe(HB(tz)₃)₂]/Al junctions (with *ca.* 100-200 nm thickness) two working hypothesis have been proposed [58], according to which the transport may be either injection-limited or bulk transport-limited. The transport mechanism in devices made of such low mobility materials is often discussed through the analysis of the thickness dependence of current density vs. electric field plots: the lack of thickness dependence indicates an injection-limited transport, whereas a pronounced thickness dependence hints for bulk-limited transport. Indeed, in the ITO/[Fe(HB(tz)₃)₂]/Al devices a thickness dependence can be readily observed (Fig. 2.22). Hence, one can infer a mostly bulk-limited mechanism. In support of this idea, the conductivity of the bulk powder was also measured (Fig. 2.23) and the material displayed extremely low conductivity in the low-frequency DC limit (*ca.* 10⁻¹⁴ S/cm at 313 K). In agreement with the observations made with the junctions, the conductivity of the powder is also higher in the LS state, although the ON/OFF ratio in the powder is extremely low (< 2).

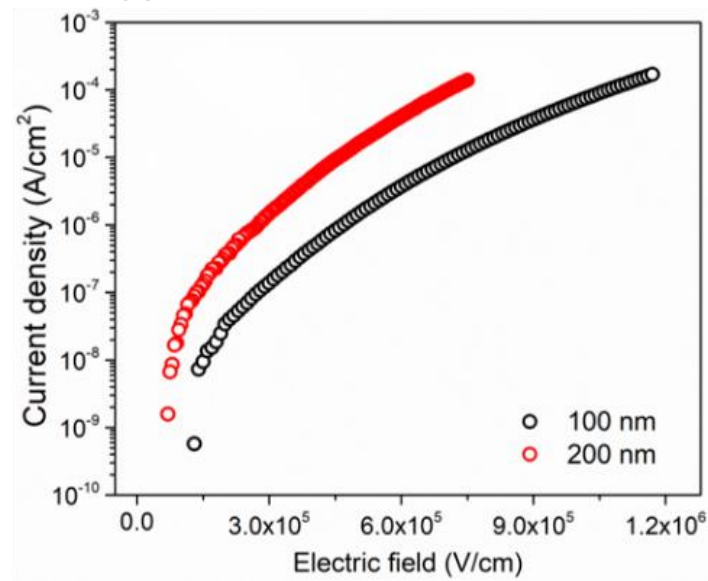


Figure 2.22: Current density vs. the average electric field ($E - E_{bi}$, where E_{bi} is the estimated built-in potential of ~ 0.3 V) for two ITO/[Fe(HB(tz)₃)₂]/Al junctions with 100 and 200 nm SCO thickness, respectively [58].

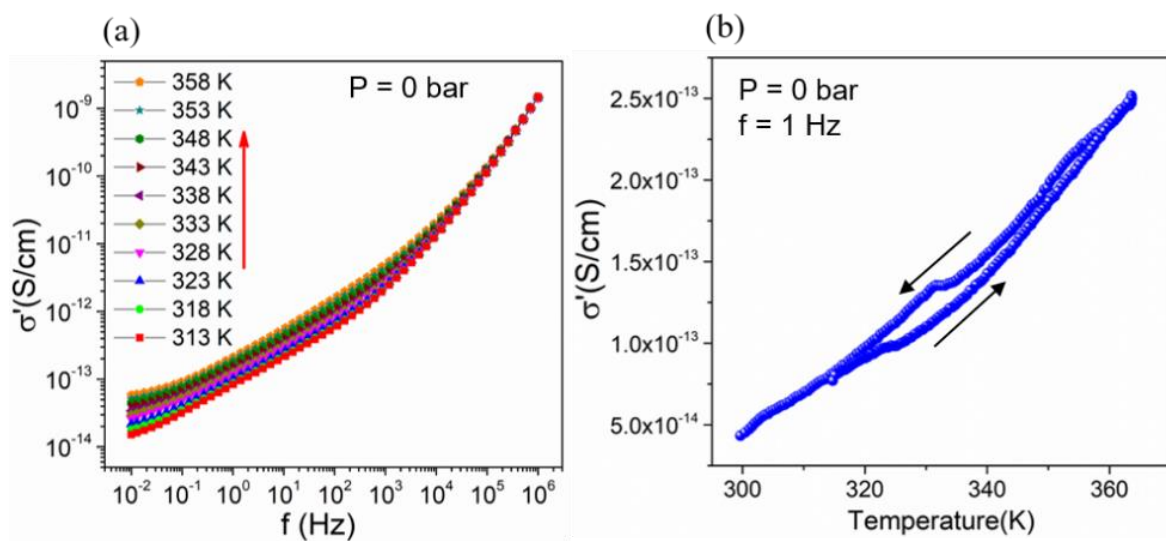


Figure 2.23: AC conductivity vs applied frequency for the bulk powder [Fe(HB(tz)₃)₂]. (a) Frequency dependence of the AC conductivity at various temperatures. (b) Temperature dependence of the AC complex conductivity at 1 Hz [58].

Despite these general considerations and experimental findings, which point toward a bulk-limited transport in our junctions, we cannot discard the role played by the electrode-molecule interfaces. Indeed, the key point here is that we seek for the dominant transport mechanism underpinning the resistance-switching behavior, which may not be the same as the transport mechanism, which governs the absolute value of the current intensity. In particular,

recent DFT calculations showed that the frontier molecular orbital energies change drastically upon the SCO in $[\text{Fe}(\text{HB}(\text{tz})_3)_2]$ [117]. As shown in Figure 2.24, the HOMO–LUMO gap significantly decreases when going from the LS (4.4 eV) to the HS (2.8 eV) state, which results obviously also in a change of the injection barriers. This result, which is basically a consequence of the drastically different ligand-field values in the LS and HS states, is in agreement with previous experimental and theoretical data on various SCO molecules. (N.B. As discussed in [117], strictly speaking, the key quantity here is not the MO energy of the neutral molecules, but the free energy change associated with their reduction/oxidation. Nevertheless, a simple reasoning in terms of frontier molecular orbital energies provides here a useful qualitative picture.)

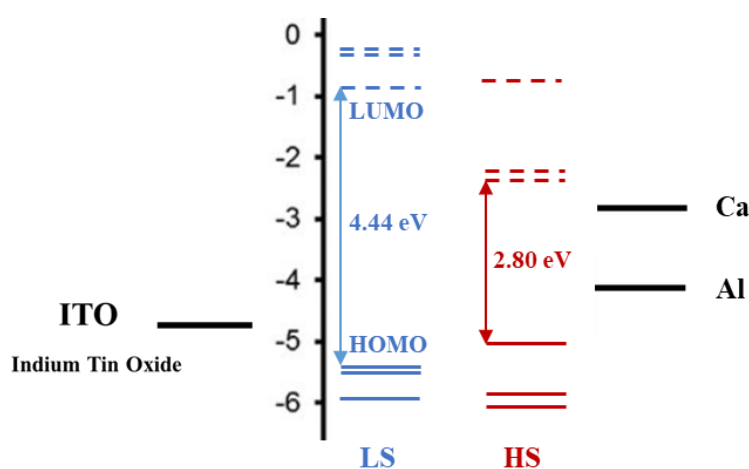


Figure 2.24: Simplified scheme showing the HOMO–LUMO gap for $[\text{Fe}(\text{HB}(\text{tz})_3)_2]$ in the HS and LS states vs. the electrode work functions (adapted from [117]).

In order to get deeper insight into the role of molecule-electrode interfaces in the resistance switching property of the junctions, we designed different devices aiming for the modulation of the injection barrier(s) between the SCO layer and the electrode(s). There are several experimental possibilities to modulate electron/hole injection properties of our devices. In a first attempt, we tried to introduce interlayers between the electrodes and the SCO layer – both for the ITO/SCO and SCO/Al interfaces. To achieve this goal, different hole-injection materials (PEDOT:PSS, poly(3,4-ethylenedioxythiophene) polystyrene sulfonate and HAT-CN, hexaazatriphenylenehexacarbonitrile) had been inserted in the ITO/SCO interface. On the other hand, we also tried to insert a Liq (8-hydroxyquinolino lithium) interlayer at the SCO/Al interface. Besides, systematically the ‘standard device’ (ITO/SCO/Al) was also fabricated in the same batch for comparison. However, these multilayer junctions, including even the

‘standard device’ did not show the expected characteristics in terms of the I - V and I - T characteristics and, unfortunately, we could not make a clear conclusion on these series of devices. (The results are shown in the [Annex2.X](#).) The reasons for this failure are still not clear, but we believe that it can be linked to the fact that a different batch of SCO powder was used in this series of experiments, which apparently contained an unexpectedly high amount of impurities. On the other hand, we have also tried to play with the nature of the metal electrode (and therefore its work function), which will be described in the next section.

2.4.4.2 Fabrication and characterization of ITO/SCO/Ca junctions

Aluminum and calcium are frequently used as electrodes in organic electronics. These two metals are characterized by very different work functions ($WF_{Al} = 4.3$ eV, $WF_{Ca} = 2.9$ eV) and allow thus for largely different device characteristics in terms of electron injection properties. Al is reasonably stable in air, but Ca would be quickly oxidized in ambient environment and encapsulation, isolating the device completely from the external environment, becomes mandatory. Based on the established junction structure, we have put in place a simple encapsulation protocol (Figure 2.25).

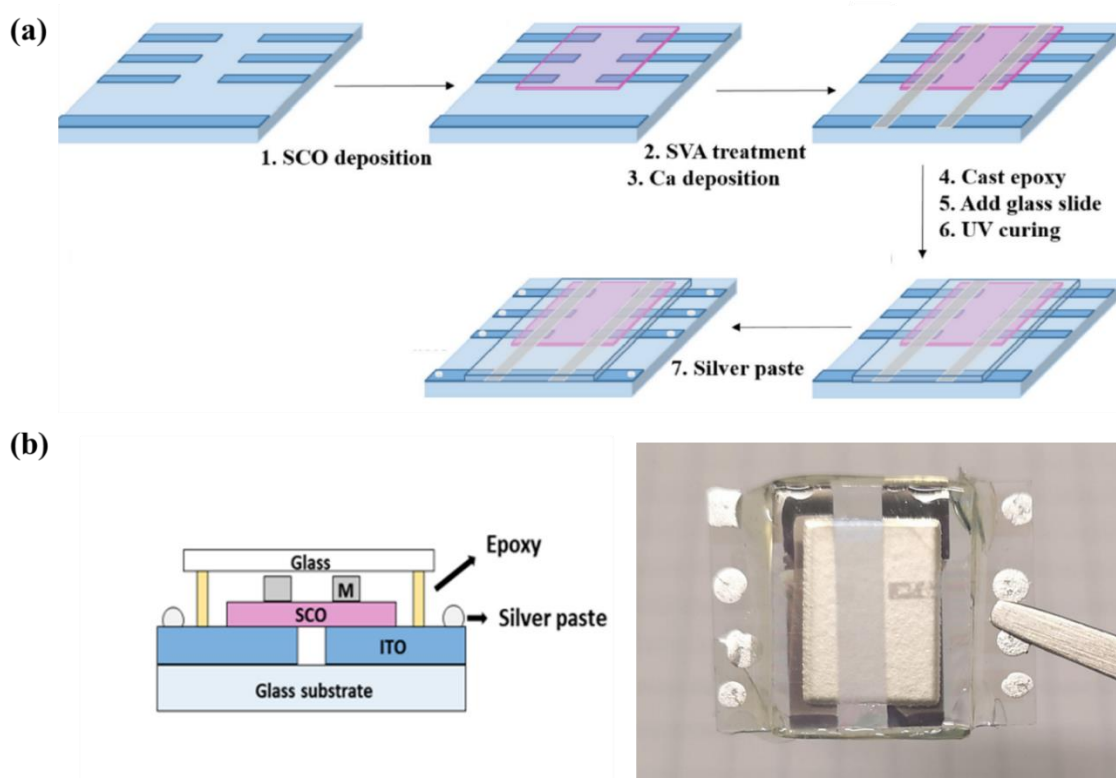


Figure 2.25: (a) Fabrication procedure of ITO/[Fe(HB(tz)₃)₂]/Ca junctions. (b) Schematic drawing of the junction side section (left) and photograph of the encapsulated device (right).

Substrate cleaning, SCO deposition and SVA treatment are the same as we introduced before in section 2.3.1. For the top electrode, Ca was evaporated at a vacuum pressure of 2.6×10^{-7} mbar at a rate of 2.7 \AA s^{-1} . Contrary to the Al devices, the Ca devices were encapsulated by an epoxy resist to protect them from oxidation. After the Ca electrodes were deposited, the junctions were transferred from the evaporator to a glove box ($\text{O}_2/\text{H}_2\text{O} < 5$ ppm) and a thin layer of epoxy resist was coated carefully around the junctions, taking care to not contaminate the SCO layer. A clean glass slide was placed on top of the epoxy layer, which was then cured under UV irradiation for 20 min. Finally, silver paste was attached to the ITO electrodes to establish good electrical connection.

The ITO/[Fe(HB(tz)₃)₂]/Ca junctions were first characterized for their room temperature resistance. Table 2.3 reports the resistance data obtained as the average of three measurements under 1 μA current bias for 6 junctions (on 1 chip). None of the junctions were short-circuited and the mean resistance value was 5.8 ± 4.6 k Ω for these 6 devices. The resistance data shows a much higher standard deviation than Al-electrode junctions, perhaps due to high penetration of active metal Ca and/or a certain degree of oxidation of the electrode (despite the protection).

Table 2.3: Comparison of the room temperature electrical resistance of a batch of ITO/100 nm [Fe(HB(tz)₃)₂]/Ca junctions

Device n°	1	2	3	4	5	6
Resistance (k Ω)	2.3	3.8	12.5	1.9	3.5	10.6

Figure 2.26 depicts representative *I-V* and *I-T* characteristics of an encapsulated ITO/100 nm [Fe(HB(tz)₃)₂]/Ca junction. These measurements were conducted in ambient atmosphere without additional protection. Figures 2.26a and b refer to the first and second successive thermal cycles, respectively. The ON/OFF current ratio reaches a value of 50, which is comparable in magnitude with the devices made with Al cathode. The *I-V* curves are also similar for the two types of devices, but the current intensity is higher in the Ca-based devices. We can thus conclude that decreasing the electron injection energy barrier between the cathode (from Al to Ca) and the SCO material, as expected, electron injection is facilitated. However, this does not affect considerably the resistance switching properties. This finding seems to corroborate our hypothesis that the resistance switching phenomenon is related to the hopping-type charge transport in the SCO film. Different explanations, such as Fermi-level pinning at the molecule–electrode interface [118] and/or the pinning of the spin states of molecules adsorbed on the electrodes [23] may account for the lack of influence of the electrode–molecule

interface on the resistance switching properties. In addition, one cannot exclude that the conduction of the junction might be dominated by hole transport.

Quite predictably, the device stability was significantly improved (Figure 2.26) when compared to the non-encapsulated devices (Figure 2.13), even though Ca is much more reactive than Al. This indicates that reaction with the atmosphere, presumably from exposure to oxygen and water, is a non-negligible co-factor leading to device degradation and failure. More surprisingly, the spin transition in the Ca-based devices is associated with a much wider hysteresis loop than for the Al-based devices or for the neat SCO films of $[\text{Fe}(\text{HB}(\text{tz})_3)_2]$. We speculate that this phenomenon may be linked to the less effective dehydration of the SCO film in the encapsulated device following the water vapor annealing step.

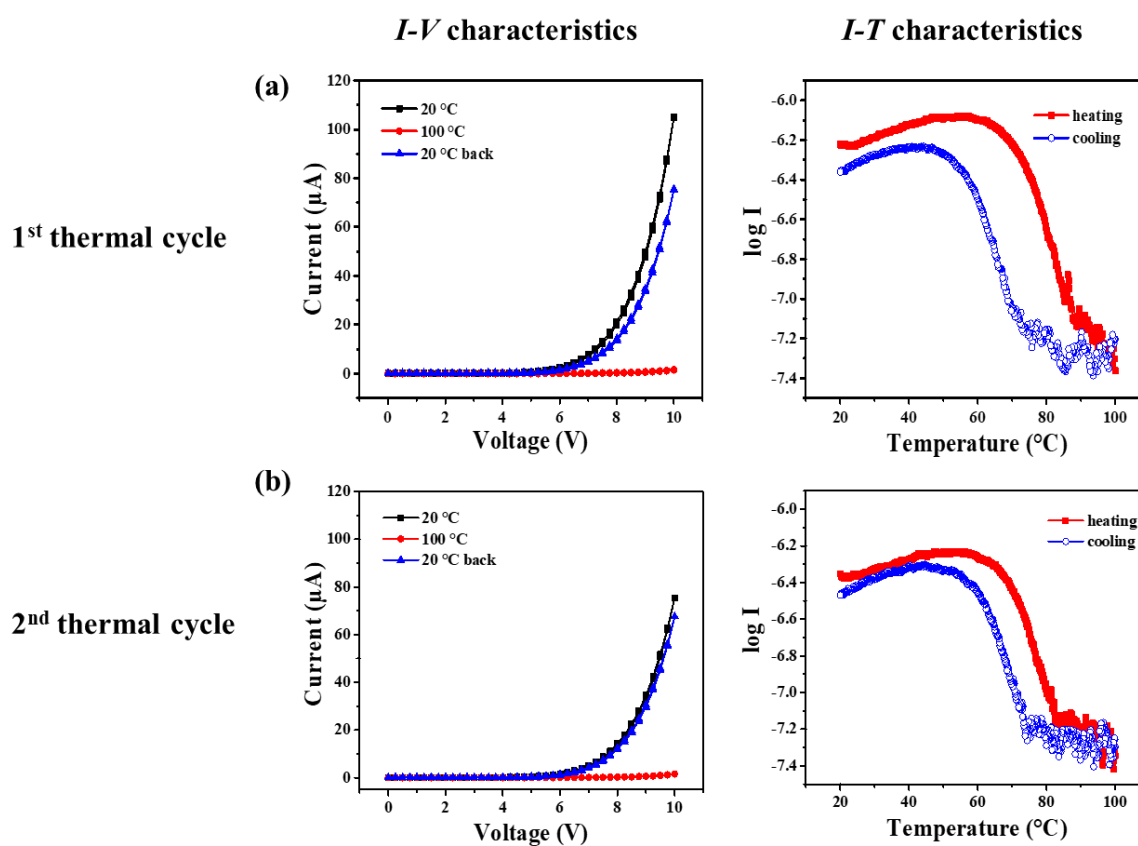


Figure 2.26: Electrical characteristics of an ITO/100 nm $[\text{Fe}(\text{HB}(\text{tz})_3)_2]$ /Ca junction. The results of two successive thermal cycles are showed in (a) and (b). Left: *I-V* curves recorded at 20 °C and 100 °C and then again at 20 °C at rates of ± 100 mV/s. Right: the log *I-T* curves recorded with an applied bias of 5 V at scan rates of ± 10 °C/min (a) and ± 5 °C/min (b).

2.5 Fabrication and characterization of NiFe/SCO/Co junctions

The interest in the use of the spin degree of freedom of electrons in electronic devices (spintronics) has continuously increased since the discovery of the tunneling magnetoresistance and giant magnetoresistance phenomena. These (and related) effects have been explored in various material combinations and led to a revolution in the information storage technologies (*e.g.* MRAM) and hold promises for further revolutions in logic devices [120]. The interest in organic materials (organic spintronics) was mainly initiated by the expected longer spin lifetime of spin polarized carriers and higher working temperatures [121, 122]. On the other hand, it has been recently unveiled that new spintronics tailoring opportunities, unachievable with inorganic materials, could arise from the chemical versatility brought by molecular engineering [123, 124]. In particular, it was shown that the molecular structure, the local geometry at the molecule-electrode interface and more importantly the magnetic metal/molecule hybridization could strongly influence the interfacial spin properties [125].

In this context, the multifunctionality of SCO materials represent a particular interest as the spin-state switching is associated with the change of the HOMO-LUMO gap, the local magnetic moment, the dielectric permittivity as well as the molecular volume, which can all provide powerful means to tune the spin polarization at the metal-insulator interface and thus to tune the overall device properties. This kind of use of SCO molecules remains up to now completely unexplored in macroscopic devices – albeit many efforts from different teams working in the SCO field. To our best knowledge the only report on spin-dependent transport in a molecular-scale SCO junction was published by Aragonés *et al.* [108, 109]. The authors have demonstrated this phenomenon both experimentally and computationally for molecular wires made of SCO Fe(II) complexes bridging an Au electrode and a ferromagnetic Ni electrode.

In order to explore possible magnetoresistance phenomena and to work towards SCO junctions displaying spin polarized currents, we decided to transform the ITO/[Fe(HB(tz)₃)₂]/Al structure into a NiFe/[Fe(HB(tz)₃)₂]/Co junction with magnetic electrodes (Figure 2.27a) and characterize its (magneto)transport properties. This work was carried out in a collaboration with Aurelian Rotaru (University Stefan cel Mare of Suceava, Romania).

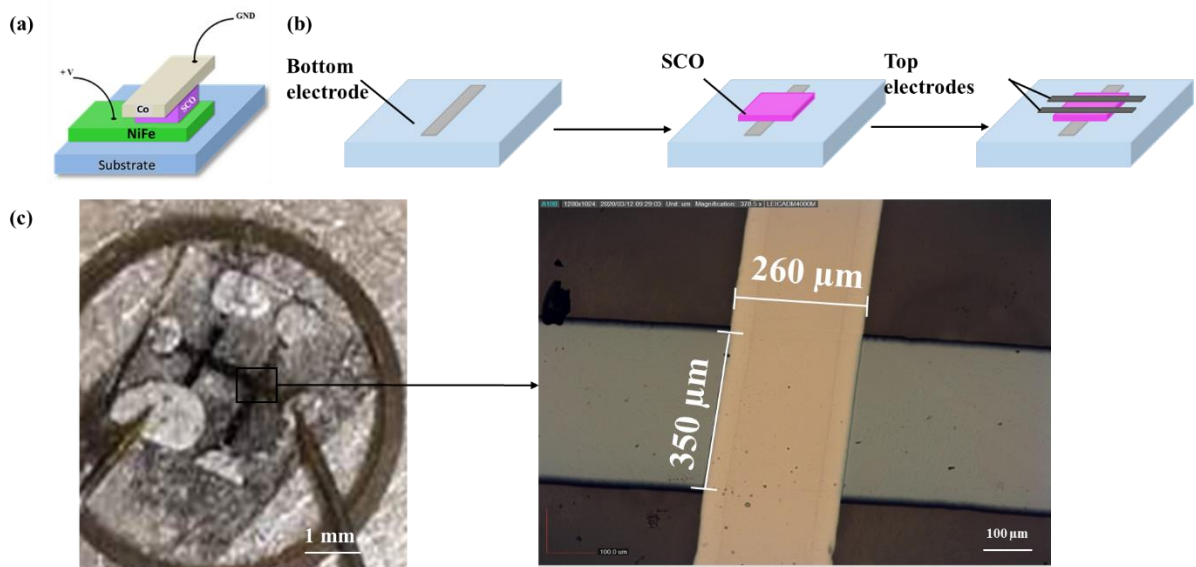


Figure 2.27: (a) Schematic structure, (b) fabrication procedure and (c) photo and optical microscopy image of a NiFe/[Fe(HB(tz)₃)₂]/Co junction.

Figure 2.27b depicts the fabrication procedure of the large-area multilayer device NiFe/[Fe(HB(tz)₃)₂]/Co. Substrate cleaning, SCO deposition and SVA treatment is the same as we introduced before in chapter 2.3.1. [Fe(HB(tz)₃)₂] films with various thickness (30, 50, 75 and 100 nm) had been used. NiFe was deposited by electron-beam evaporation technique whereas Co was deposited by thermal evaporation. We used an evaporation mask to form a patterned crossbar junction with side length of ca. 260 μm and 350 μm (see Fig. 2.27c). A first series of devices fabricated either with NiFe and Co top electrodes were systematically short-circuited, even for the thickest SCO layers. Nevertheless, after careful optimization of the deposition conditions, we were finally able to fabricate junctions without short-circuits using Co top electrodes.

The magnetic properties of the junctions were investigated at 10 K and 300 K (Figure 2.28). The magnetic hysteresis of DC magnetization vs. applied magnetic field curves reveal the expected magnetic behavior of a spin valve comprising a non-magnetic layer between two ferromagnetic layers. For the positive field values, the two magnetizations are parallel (the saturation region). When the field is reversed, due to the different coercive behavior of the two electrodes, one will switch first and as the field increased further, the magnetization of the other electrode will follow to align along the magnetic field. As it can be expected, the coercive field of the multilayer at 300 K is less than that at 10 K.

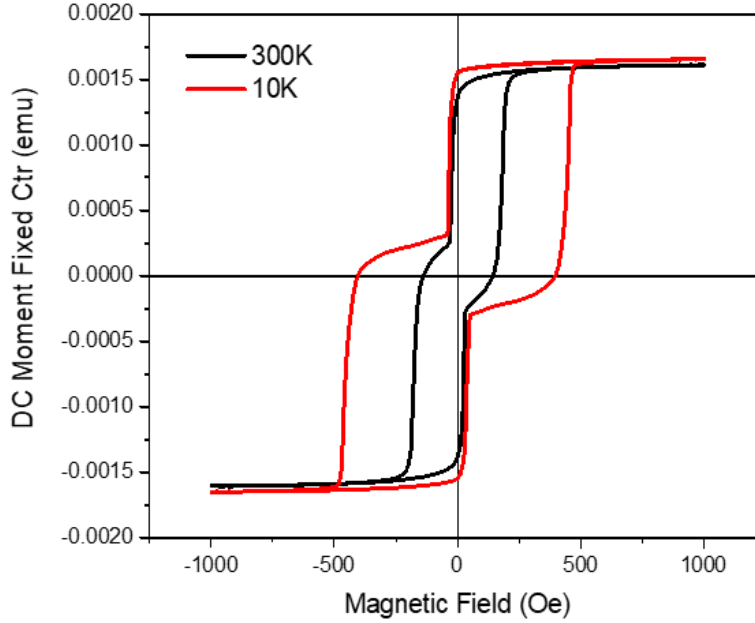


Figure 2.28: Magnetization curves (major hysteresis loops) recorded on plain layer (NiFe/10 nm SCO/Co) at various temperatures at 300K and 10K.

After confirmation of their magnetic properties, the NiFe/[Fe(HB(tz)₃)₂]/Co junctions were characterized for their room temperature electrical resistance. The properties of a representative batch of spintronic junctions are summarized in Table 2.4. The resistance data were obtained as the average of three measurements under 1 μ A current bias for 8 junctions (2 junctions in each thickness). As we can see from the table, unlike the ITO/SCO/Al junctions, when the thickness of SCO layer in this type of junctions is relatively low (30-75 nm), the electrical resistance equals the electrical resistance of the electrodes (\sim 0.2 k Ω), *i.e.* they are short-circuited due to the high penetration of Co in the SCO thin film. On the other hand, junctions with 100 nm [Fe(HB(tz)₃)₂] as the active layer, afforded for higher electrical resistance, but the resistance was rather different from device-to-device. It is important to underline that these measurements were carried out in the absence of an applied magnetic field. We have also tried to establish the magnetoresistive properties of these junctions, but we could not observe any magnetic field effect on the device resistance (for the 100 nm thick junctions).

Table 2.4: Comparison of the room temperature electrical resistance of a batch of NiFe/[Fe(HB(tz)₃)₂]/Co junctions with different thickness of SCO layer.

Thickness of SCO (nm)	30	30	50	50	75	75	100	100
Junction N ^o	1	2	3	4	5	6	7	8
Resistance (k Ω)	0.2	0.2	0.2	0.2	0.2	1.2	900	100

The I - V characteristics of the two working junctions (N°7 and N°8) with 100 nm $[\text{Fe}(\text{HB}(\text{tz})_3)_2]$ layer are shown in Figure 2.29. Junction N°7 exhibits a hysteresis of current between voltage sweeps up and down. An interesting finding is that for sweep rates below *ca.* 20 mV/s, the I - V characteristic becomes reproducible and rate-independent. The large hysteresis of current vs. voltage indicates likely the existence a large amount of charge carrier traps in this junction. Compared to junction N°7, junction N°8 exhibits a reduced hysteresis and more reproducible I - V characteristics, no matter what the voltage sweep rate is. Since the junctions N°7 and N°8 belong to the same chip, the very different I - V characteristic indicate heterogeneities in the deposits (*e.g.* SCO film morphology, Co penetration, *etc.*). Here it is worth to notice that the crossbar area of these junctions is considerably smaller than that of the ITO/SCO/Al junctions (0.09 mm^2 vs. 3 mm^2), which may become an important factor for the device-to-device reproducibility.

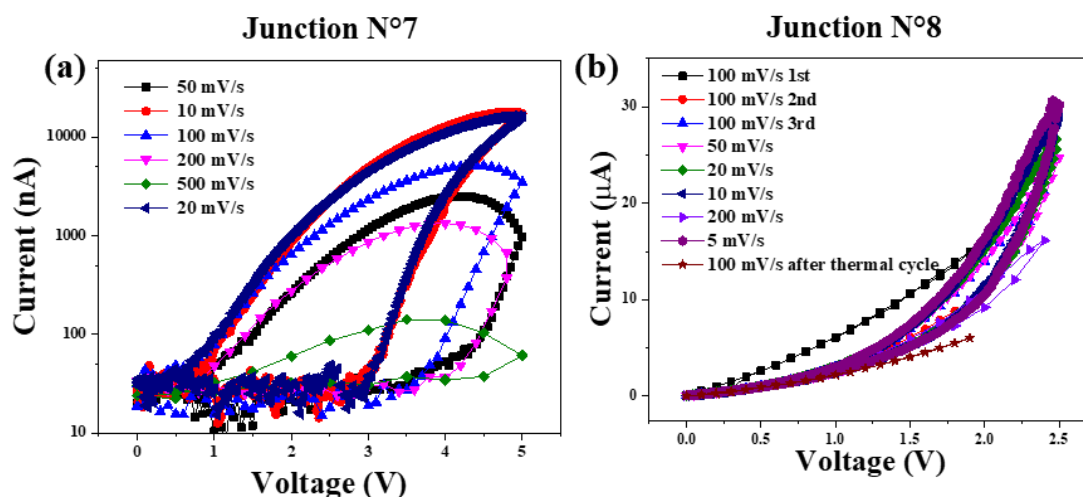


Figure 2.29: Room temperature I - V characteristics of NiFe/100 nm $[\text{Fe}(\text{HB}(\text{tz})_3)_2]$ /Co junctions for different voltage sweep rates: (a) junction N°7 and (b) junction N°8.

We finally tried to clarify the interplay between the SCO phenomenon and the electrical properties of the junctions via their I - T characteristics. Figure 2.30 depicts some representative results. In most cases, the current keeps increasing during the whole temperature range of the thermal cycles, which can be mostly attributed to ordinary thermal activation of the conductance. Despite many efforts, we could unfortunately not see any I - T characteristics, which could be clearly assigned to the SCO. This behavior of the NiFe/SCO/Co junctions in comparison with the ITO/SCO/Al and ITO/SCO/Ca devices is not yet understood. We believe it may be linked to the higher work function of the magnetic electrodes (*ca.* 5 eV), but this issue will require further investigations.

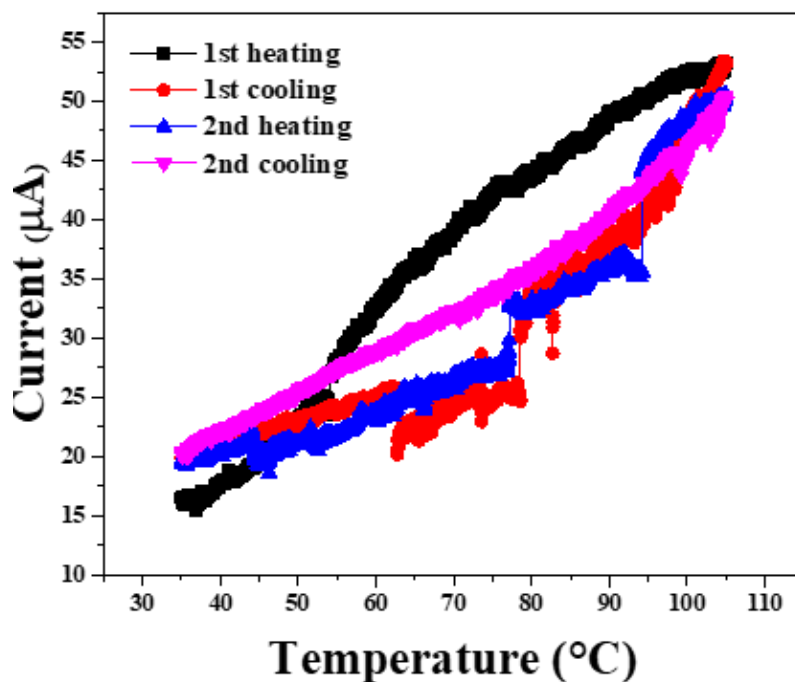


Figure 2.30: Representative I - T characteristics of NiFe/100 nm $[\text{Fe}(\text{HB}(\text{tz})_3)_2]/\text{Co}$ junctions (measured at 2 V applied bias with temperature scan rates of $\pm 2^\circ\text{C}/\text{min}$).

2.6 Conclusions and perspectives

High quality thin films of the spin crossover complex $[\text{Fe}(\text{HB}(\text{tz})_3)_2]$ have been successfully deposited by high-vacuum thermal evaporation with an accurate control of the film thickness. The as-deposited amorphous films could be crystallized using solvent-vapor annealing. From a combination of GI-XRD, variable-temperature UV-vis spectroscopy, optical microscopy and AFM measurements we concluded that water vapor allows for a highly oriented crystalline structure, whereas octane vapor annealed thin films showed texture that is more random and SCO that is less reproducible, when compared to water vapor treated films. Few hundreds micrometers size, two-dimensional ‘branch-like’ structures were observed regularly in both water/octane vapor annealed thin films. Despite this, the thin films still exhibit high quality with relatively low roughness (RMS 1-2 nm), they are pinhole free and continuous.

The $[\text{Fe}(\text{HB}(\text{tz})_3)_2]$ thin films had been integrated in two-terminal, large-area, multilayer electronic devices, aimed for resistance switching functionality. Robust, high resistance switching ON/OFF ratios, up to three orders of magnitude, had been observed in ITO/ $[\text{Fe}(\text{HB}(\text{tz})_3)_2]/\text{Al}$ structures. Because of the non-linearity of the I - V curves, the switching ratios depend, however, on the applied voltage bias. A detailed stability investigation of the devices upon temperature cycling as well as electric stress (voltage bias) had been carried out.

First, we found a good device-to-device reproducibility of the junction resistances (and I - V curves). On the other hand, the resistance switching amplitude (*i.e.* the I - T curves) are less reproducible from junction to junction, with ON/OFF ratios spanning from (less than) 1 to (at most) 3 orders of magnitude. In this context, we must note that some uncertainty persists as for the quality of the starting SCO powder and other possible sources of impurities, which may arise from the device fabrication. It would be important to establish a robust protocol in this regard as well. Second, it turned out that the devices preserve their electrical properties in ambient storage conditions over extended periods (1 year). Third, we demonstrated a remarkable endurance to a large number of resistance switching events ($> 10,000$) in ambient conditions, which is a crucial milestone, towards the ‘real-world’ applications. Key to this switching stability is a reduced working temperature range ($< \sim 80^\circ\text{C}$) and constant voltage bias. As for the origin of the resistance switching in these junctions, we have investigated more in detail the possible role played by the electrode injection barriers. In particular, we could compare devices with Al and Ca cathodes. Despite the very different work function of these two metals, we found comparable device characteristics. This indicates that the resistance switching in these devices is most likely governed by the intrinsic switching of bulk conductivity of the SCO material. One interesting perspective of this work would be to correlate the charge transport properties with crystalline orientation of the films. One possibility here would be to use current-in-plane junctions where the film of $[\text{Fe}(\text{HB}(\text{tz})_3)_2]$ is evaporated on planar “nanogaps”. Opposite to the multilayer junctions, the current would flow in this case perpendicular to the main crystallographic axis of the SCO compound. Another important perspective would be the investigation of multilayer junctions with different film thicknesses, down to a few nanometers in order to reach a charge transport regime, which is not dominated by the bulk transport properties of the SCO film.

Finally, we have made the first steps towards the fabrication of a spin valve device wherein the SCO layer is sandwiched between two magnetic electrodes. We were able to fabricate $\text{NiFe}/[\text{Fe}(\text{HB}(\text{tz})_3)_2]/\text{Co}$ junctions with *ca.* 100 nm SCO layer thickness, which displayed the expected I - V and magnetic characteristics. At this stage, however, we could not yet evidence any magnetoresistance property neither a clear effect of the SCO on the device electrical properties. Nevertheless, we believe these devices represent a promising platform for further work enabling us to come up with new spintronic material combinations and functionalities.

Chapter 3 Integration of the spin crossover complex [Fe(HB(tz)₃)₂] into three-terminal electronic devices

This chapter is devoted to the investigation of the possibility to integrate the SCO molecules into organic field-effect transistor (OFET) devices in order to modulate the device characteristics via the SCO phenomenon. To this aim we used the benchmark SCO film [Fe(HB(tz)₃)₂] already introduced in Chapter 2 in the context of resistance switching devices. It is important, however, to remark the fundamental conceptual difference of these SCO-OFET devices in comparison with the resistance-switching junctions. Indeed, whereas the SCO compound was the active layer in the junctions, here we designed different three-terminal geometries wherein the SCO layer is a complementary element aimed to interact with the active organic semiconductor layer. The work described below was conducted in close collaboration with Dr. Isabelle Séguy in LAAS-CNRS.

3.1 General considerations

In such an era that information technologies develops rapidly, microelectronics have provided great convenience to human's daily life. Field-effect transistors (FETs) are one of the basic, but important components of various electronic products, such as computers, mobile phones, televisions and cameras. Traditional FETs are built on the basis of inorganic semiconductors, in most cases using silicon. However, several other material platforms have been also developed. In particular, the fast development of novel organic semiconductors opened the era of organic electronics, including organic light emitting diodes (OLEDs), organic photovoltaics (OPV) and organic field-effect transistors (OFETs) among others. The main advantages of OFETs are as follows [126]: (1) A wide range of materials is available through synthetic chemistry. Various types of compounds can be synthesized according to the end-user requirements to achieve different performance. (2) Various thin film deposition technologies can be used including both conventional (*e.g.* vacuum evaporation) and non-conventional (*e.g.* printing, spraying) methods. (3) The materials are lightweight and can be used in flexible devices. (4) The size of the device can be adjusted from large area to the nanoscale - potentially reaching the single molecule level [127]. (5) Perhaps most importantly, OFETs exhibit more versatile application possibilities than the traditional FETs. For example, they have been used in solar cells, biochemical sensors, electronic paper and flexible flat panel displays, *etc* [128].

As such, developing new functions and using various functional materials in OFETs is an increasingly important research line [129].

Among these materials, the integration of photochromic molecular switches (*e.g.* azobenzene, spiropyran) is already in an advanced stage and provides therefore strong inspiration for our work with SCO compounds. As shown in Table 3.1 (adapted from [130]), various photochromic molecules had been integrated in different location in organic transistors with the aim to use light irradiation either to modulate/tune the transistor properties, or to achieve novel functionalities (*e.g.* non-volatile memory). The two isomers of such photochromic molecules differ in various physical properties including their steric conformation, dipole moment and HOMO-LUMO energy levels. These different properties have been then considered to modulate the injection, transport, trapping, scattering of charge carriers in the conducting channel as well as to switch the capacitance of the dielectric layer in the OFET.

Table 3.1: Selected examples of photochromic molecules used in OFETs [130].

Photochromic molecule	Locations in transistors	Physical properties in photochromism	Modulated transistor properties	Photoswitching performance & remarks
Azobenzene	At electrode/channel interface	Steric conformation	Carrier injection	On/off ratio of I_D : 1.2
Azobenzene	At gate dielectric/channel interface	Steric conformation	Capacitance	On/off ratio of I_D : 3 photoresponsivity: 2 A W^{-1}
Azobenzene	In gate dielectric layer	Dipole moment	Capacitance	On/off ratio of I_D : 2
Stilbene	Direct-use as transistor channel	Steric conformation	Carrier transport	On/off ratio of I_D : 20
DAE	At gate dielectric/channel interface	HOMO-LUMO	Carrier trapping	ΔV_{th} : 35 V
DAE	In transistor channel	HOMO-LUMO	Carrier trapping	On/off ratio of I_D : 2
DAE	At electrode/channel interface	HOMO-LUMO	Carrier injection	On/off ratio of I_D : 3
DAE	Direct-use as transistor channel	π -Conjugation	Carrier transport	On/off ratio of I_D : 10^3
DAE	At gate dielectric/channel interface	HOMO-LUMO	Carrier trapping	On/off ratio of I_D : 10^3 – 10^4 , ΔV_{th} : 10 V
Spiropyran	In transistor channel	Dipole moment	Carrier transport	On/off ratio of I_D : ~ 1.01
Spiropyran	At electrode/channel interface	Dipole moment	Carrier injection	On/off ratio of I_D : 1.1–1.2
Spiropyran	In transistor channel	Ionic/non-ionic states	Carrier scattering	On/off ratio of I_D : 1.5
Spirooxazine	At gate dielectric/channel interface	HOMO-LUMO	Carrier trapping	On/off ratio of I_D : 10^4 , ΔV_{th} : 5 V
Spiropyran	At gate dielectric/channel interface	HOMO-LUMO	Carrier trapping	On/off ratio of I_D : 10^6 , ΔV_{th} : 20 V
Spiropyran	In gate dielectric layer	Dipole moment	Capacitance	On/off ratio of I_D : 2.5
Spiropyran	At gate dielectric/channel interface	Dipole moment ionic/ non-ionic states	Carrier doping	Light-induced superconductivity in Mott insulator

This research about functional OFETs with photochromism can be extended to other functional molecules, such as SCO molecules, which are known to exhibit bistable physical properties, including huge variations of frontier orbital energies, dielectric permittivity, mechanical properties, dipole moment, and so forth. It is important to note that, at present, due to the low conductivity of SCO compounds [131, 132], they cannot be directly used as conducting channel in transistors. However, as we shall see later, the performance of OFETs is strongly related to various physical phenomena taking place at interfaces (metal/semiconductor, dielectric/semiconductor), which provide numerous possibilities for the effective integration of

SCO molecules. Indeed, as already discussed in Chapter 1, the dielectric and mechanical properties as well as dipole moment changes due to the SCO have already been considered in the context of three-terminal devices based on either graphene [133-136] or ferroelectric materials [137, 138], but not in OFETs yet. In this Chapter, following a brief general introduction on OFETs, we devise different fabrication strategies to introduce our SCO film [Fe(HB(tz)₃)₂] in between the oxide dielectric and the organic semiconductor layer aiming to act both on the capacitance of the dielectric layer and the transport of charge carriers in the channel. We shall remark that the first effect is quite predictable on the basis of the dielectric properties of the SCO material. On the other hand, the interfacial properties modulating the charge transport are much less obvious to foresee as they can affect the carrier mobility via numerous mechanisms (trapping, scattering, *etc.*), whose disentanglement is not straightforward.

3.2 Introduction to OFETs

3.2.1 Basic structure of OFETs

An organic field-effect transistor (OFET) or organic thin-film transistor (OTFT), is made of a source electrode (S), a drain electrode (D), an organic semiconductor (OSC), a dielectric and a gate electrode (G). The source and drain electrodes allow the injection of charge carriers into or from the semiconductor. The potential difference between source and drain will allow a current to flow in the semiconductor at the OSC/dielectric interface, which is called the conduction channel. The gate electrode makes it possible to modulate the quantity of charge carriers injected into the OSC and therefore the current between source and drain. The dielectric acts as an insulator by preventing charges in the conduction channel at the OSC/dielectric interface from migrating to the gate electrode.

The different layers of the organic thin film transistors can be arranged in four basic configurations as shown in Figure 3.1. The position of the source and drain electrodes with respect to the semiconductor makes it possible to distinguish whether it is a top contact (TC) (Figures 3.1a and c), or, vice versa, bottom contact (BC) (Figures 3.1b and d) configuration. Likewise, the relative positions of the gate electrode and the dielectric with respect to the semiconductor make it possible to differentiate the bottom gate (BG) configurations (Figures 3.1a and b) from the top gate (TG) configurations (Figures 3.1c and d).

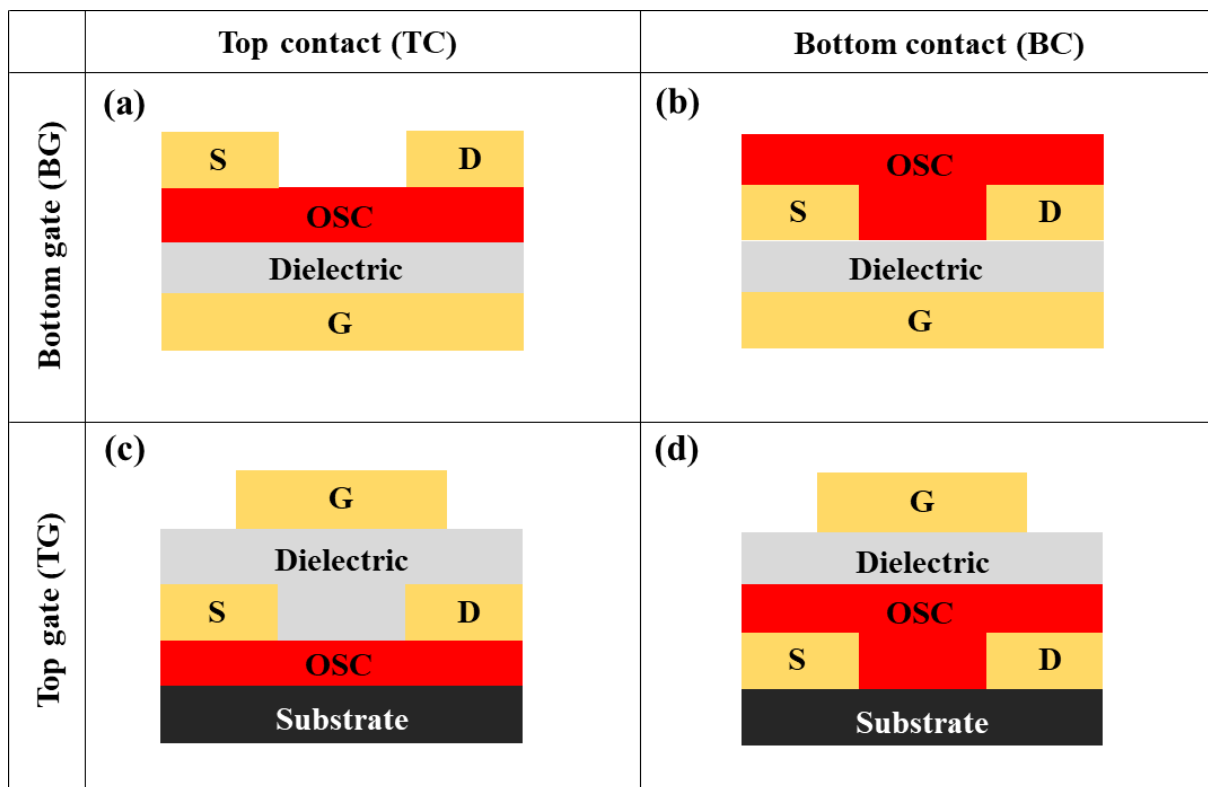


Figure 3.1: The different configurations of organic transistors (a) bottom gate/top contacts (BG/TC); (b) bottom gate/bottom contacts (BG/BC); (c) top gate/top contacts (TG/TC); (d) top gate/bottom contacts (TG/BC).

Depending on the application, the materials and manufacturing processes, one or the other of the geometries will be preferred. Notably, the deposition of a dielectric on a semiconductor can be complicated since the solvent and the annealing process used must not damage the active layer below. Hence, the BG configuration is generally preferred from a manufacturing point of view because the OSC is deposited in the last step(s). The position of the source/drain contacts with respect to the semiconductor can also play a role in the performance of the transistors. The BC configuration generally allows better channel resolution compared to a top contact geometry. In fact, because of the high sensitivity of the active semiconductor layer, it is complicated to use high-resolution photolithography to deposit the contacts after deposition of OSC, due to the compatibility of solvents. Hence, printing or evaporation techniques must be used, which do not usually allow a resolution of less than 1 μm [139].

The transistors studied during this thesis have a bottom gate (BG) configuration with either bottom contact (BC) or top contact (TC). The OSC in this geometry is in the top layer thus an encapsulation will be needed to avoid the degradation of the semiconductor, which is very sensitive to the environment.

3.2.2 Operation mechanism of OFETs

The OFET is a device that can achieve controllable off/on states. The gate electrode/dielectric/OSC part of the device is considered as a capacitor. The operation of OFETs involves two voltages: one between the gate and the source V_G and another between the drain and the source V_{DS} . When the gate voltage (noted as V_G or V_{GS} in the literature) is zero, no charge is induced in the active layer and the device is off. The corresponding source-drain current (I_{DS}) is the OFF state current. Then, by applying a voltage V_G , a charge builds up in the electrode/dielectric and dielectric/OSC interfaces (see Fig. 3.2 for the charge accumulation scheme in a p-type OFET). The additional positive charges accumulated at the dielectric/OSC interface are supplied by the source and drain electrodes. A conducting channel forms at the dielectric/OSC interface and charges can move from source to drain by applying a second voltage V_{DS} (the transistor is in its ON state). This channel is defined by two quantities, the length L between the source and the drain as well as its width W . The source-drain voltage (V_{DS}) controls the value of the source-drain current (I_{DS}). The control of the charge carrier density of the conductive channel is achieved by applying an appropriate gate voltage (Figure 3.2). One can see it as a “valve” of the conductive channel. Hence, if a certain voltage (V_G) is applied to the gate, the induced electric charges can participate to the conduction under the appropriate V_{DS} . Therefore, I_{DS} can be modified by adjusting V_G .

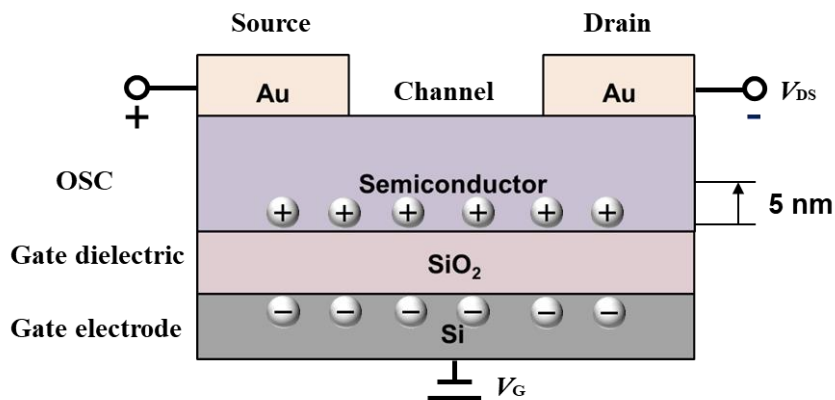


Figure 3.2: Scheme of a typical bottom-gate top-contact p-type OFET.

3.2.3 Basic parameters of OFETs

The performance of OFETs is evaluated through several parameters, including threshold voltage, current switching ratio, subthreshold slope and so forth. These parameters can be calculated from the so-called “transfer curve” (I_{DS} - V_G) and “output curve” (I_{DS} - V_{DS}). In this

section, we will first introduce the definition of these two characteristic curves of OFETs, followed by basic performance parameters.

The electrical characteristics of the transistor refer to the measurement of the drain current as a function of the gate or drain-source voltage for a fixed drain-source or gate voltage, respectively. These two types of curves are shown in Figure 3.3. Generally, the transfer characteristics (Figure 3.3a) are measured at low and high V_{DS} corresponding, respectively, to the linear and saturated regime of the transistor. These curves allow the extraction of important parameters of the transistor such as the threshold voltage V_T , subthreshold slope SS , the ratio I_{ON}/I_{OFF} and so forth. The output characteristics (Figure 3.3b) are used to determine the contact resistances between the source/drain electrodes and the semiconductor and therefore to quantify the charge injection problems that may result.

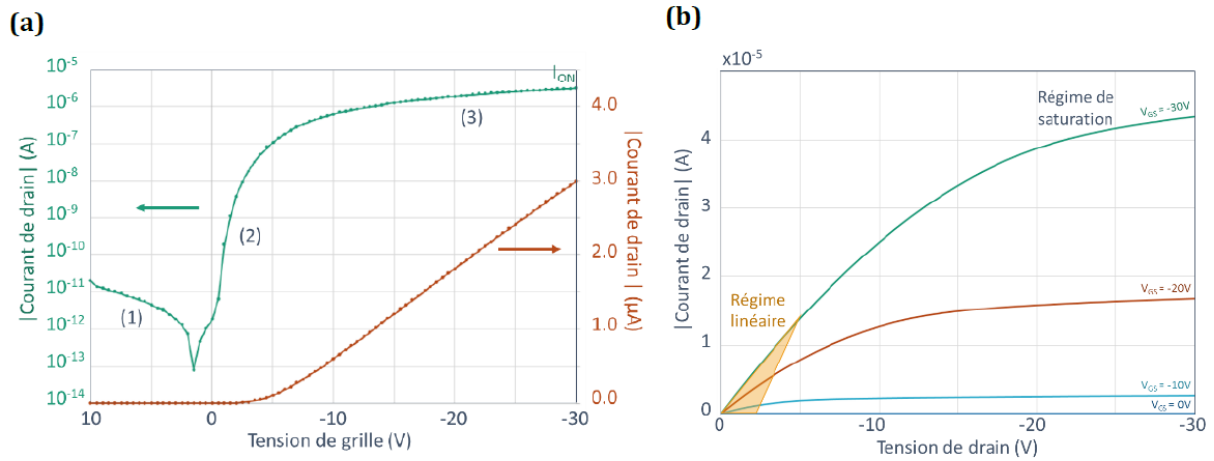


Figure 3.3: Electrical characteristics of an OFET: (a) Transfer curves $I_{DS} = f(V_G)$ for a constant V_{DS} value. (b) Output curves $I_{DS} = f(V_{DS})$ for four different constant V_G values [142].

The general equation of organic transistors has been adapted from the classical MOSFET theory and will notably allow the extraction of several parameters of the transistor in strong accumulation regime (*i.e.* when $V_G > V_T$) [140]:

$$I_{DS} = W/L \cdot \mu_{eff} \cdot C [(V_G - V_T) V_{DS} - 1/2 \cdot V_{DS}^2] \quad \text{Eq.3.1}$$

where L and W are the length and width of the conductive channel, μ_{eff} the effective mobility, C is the capacitance of the dielectric layer and V_T is the threshold voltage.

The effective mobility (μ_{eff}) is one of the most important parameters to measure the performance of organic semiconductors in field effect transistors. It is defined as the drift rate of charge carriers (holes and electrons) under a certain electric field, which determines the

switching speed of the device. The mobility is affected by many factors, such as the type, crystallinity and purity of organic semiconductor materials, grain size, conductive channel L/W ratio, contact between semiconductor layer and source/drain electrodes, the interface between the dielectric layer and the active layer, the nature of the dielectric layer and the device configuration. Normally, if the intrinsic mobility of the semiconductor material is greater, the effective mobility of the corresponding device will also be greater. The value of mobility can be calculated for the linear and the saturated regimes as:

$$\mu_{lin} = \frac{L}{WCV_{DS}} \cdot \left(\frac{\partial I_{DS}}{\partial V_G} \right), \text{ applicable at } (V_{DS} < V_G - V_T) \quad \text{Eq. 3.2}$$

$$\mu_{sat} = \frac{2L}{W} \frac{1}{C} \left(\frac{\partial \sqrt{|I_{SD}|}}{\partial V_{GS}} \right)^2, \text{ applicable at } (V_{DS} > V_G - V_T) \quad \text{Eq. 3.3}$$

if the following assumptions are verified: (1) the transverse gate electric field is much greater than the source-drain electrical field and (2) the field mobility is carrier density independent.

The threshold voltage V_T is generally defined by the minimum gate voltage to be applied to observe a “significant” source-drain current. In reality, the notion of V_T has been introduced by analogy with MOSFET transistors where it corresponds to the voltage V_G necessary to go from the low inversion regime to the strong inversion regime. However, OFETs only work in accumulation and not in inversion [141]. Actually, the notion of V_T for organic transistors being questionable, some people prefer to use the term “starting voltage” V_{ON} . This voltage is defined as the value of V_G from which the drain current I_{DS} begins to increase when observing a logarithmic scale transfer curve (Figure 3.4). Ideally, $V_{ON} = 0$ V, corresponding to an accumulation of charges as soon as the gate bias changes sign and becomes, for example, negative for a p-type OTFT. However, in reality, the presence of impurities in the OSC or at the OSC/dielectric interface can induce a shift in the starting voltage [142].

The current switching ratio, I_{ON}/I_{OFF} is defined by the ratio of the drain-source current I_{DS} in the “on state” vs. the “off state” for selected values of V_G and V_{DS} . Devices with higher switching current ratios have better stability and anti-interference ability. The off state current is essentially a leakage current. If its value is large, it will make the device difficult to turn off, and at the same time, I_{ON}/I_{OFF} will decrease. The level of the off state current is primarily related to the nature of the active layer.

The subthreshold slope (SS) refers to how fast the current changes when the device switches from the off state to the on state. It is defined as:

$$SS = dV_G/d(\log(I_{Ds})) \quad \text{Eq. 3.4}$$

The unit is mV/decades. The subthreshold slope (SS) can reflect the quality of the interface between the insulating layer and the active layer in the device. The smaller the SS value, the faster the device switching speed and the smaller the gate voltage change required.

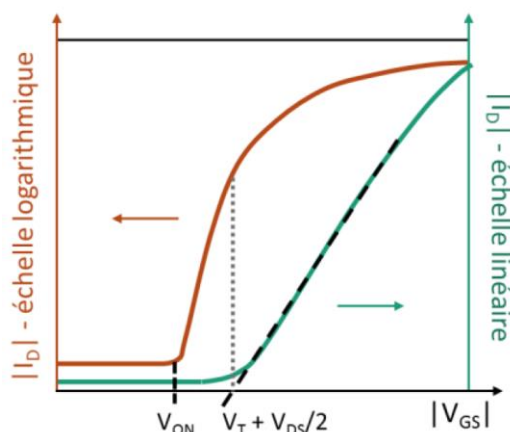


Figure 3.4: Extraction of V_T and V_{ON} from transfer curves in linear and semi-logarithmic scales [142].

3.2.4 Stability of OFETs

In general, organic materials can be rather sensitive to various environmental (light, temperature, humidity, oxygen, *etc.*) and operational (voltage stress, *etc.*) parameters. This sensitivity can cause a change, sometimes premature, in the characteristics of the transistor. Obviously, it is important to have robust and reliable OFETs for the various possible applications such as active matrices and addressing circuits of sensors. A study of the stability of OFETs is therefore necessary for the future development of these technologies. As we shall see later, actually, this issue appears as the main bottleneck in our work as well.

The stability under voltage stress (or "bias stress") is an important aspect in accounting for the reliability of the transistor in the electronic circuit, which will be subjected to repeated and/or prolonged applied voltages. In order to observe the evolution of the characteristics of the transistor over time, an electrical stress consists of the application of a gate and / or drain voltage in a continuous or pulsed manner. Aging of OFETs is a ubiquitous problem, especially during prolonged operation of gate bias. It can result in a variation of the threshold voltage, a decrease in mobility, a degradation of the subthreshold slope and/or a decrease in the drain current in the on state (I_{ON}). Figure 3.5 shows an illustration of this point from the literature [143]. Note that temperature may also play a vital role for accelerating device degradation in this case.

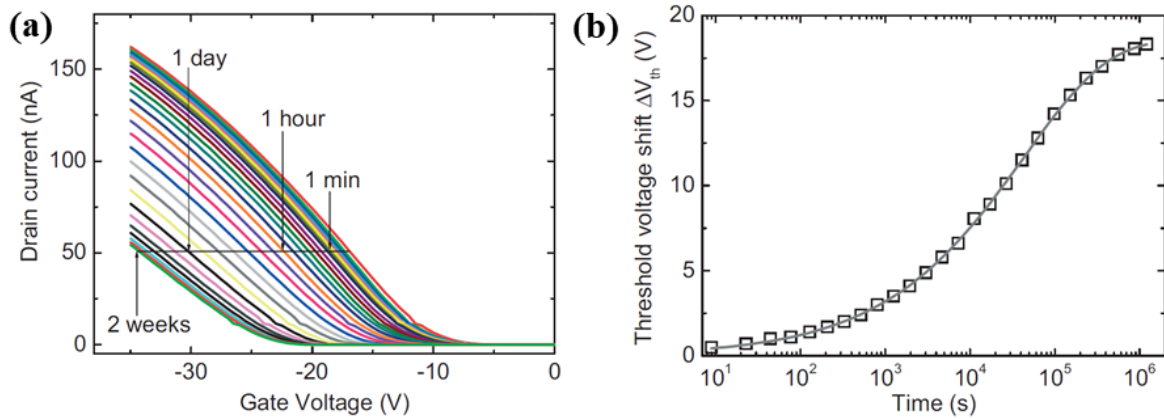


Figure 3.5: (a) Transfer curves of PTAA transistors studied under repeated bias stress over a two weeks period. The gate bias during stress was -20 V and the temperature 140 °C. (b) The threshold voltages obtained from (a) presented as a function of time on a logarithmic scale. The fully drawn curve is a fit with a stretched-exponential time dependence [143].

In the following, we will briefly introduce several factors that may induce degradation in OFETs. For most transistors, the most noticeable degradation observed following the prolonged operation of a voltage stress is a shift in the transfer curves, which comes from the shift of the threshold voltage. This degradation is generally attributed to trapping of charge carriers (*i.e.* holes for p-type OSCs) [145]. Indeed, the trapped charges, by electrostatic effect, will compensate the gate electric field. It is then necessary to use a higher gate voltage to obtain a similar current, which implies an increase in the threshold voltage and therefore a shift of the curves. Charge carriers can be trapped in the semiconductor, in the gate dielectric or at the OSC/dielectric interface. The origin of these traps is usually not well established, whether they are intrinsic structural defects or extrinsic impurities, or even a combination of the two. A decrease in mobility under voltage stress may also occur. This is usually attributed to the presence of polar dielectrics [146]. This is because when an electric field is applied, the dipoles present in the dielectric will align with this external field. The charge carriers in the channel will be attracted by these oriented dipoles. This results in an accentuated self-trapping of the channel charges. The situation becomes worse when the dielectric layer has a large dielectric constant.

In addition to electrical stress, the environment can also have an effect on change of the characteristics of OFETs. For example, several studies have shown that visible light can accelerate transistor relaxation after electrical stress [147]. Indeed, if a previously stressed transistor is illuminated at a wavelength corresponding to an energy greater than the exciton

energy of the OSC, then the electron-hole pairs generated will be able to recombine with the trapped charges and help the relaxation. Likewise, the energy generated by an increase in temperature can help the trapped charges relax [148]. On the other hand, temperature can also accelerate the degradation of transistors under voltage stress. This is illustrated in Figure 3.6, which shows the results of Pannemann *et al.*, who exposed OFETs for up to 200 min at a constant temperature of 65 °C. They used a BG/BC structure with pentacene as a semiconductor, which is therefore directly in contact with the environment. Already after 20 min of exposure, they observed a degradation of both mobility and the I_{ON}/I_{OFF} ratio by an order of magnitude. Besides temperature, humidity also plays an important role, in particular under electrical stress. It had been reported that the presence of humidity can lead to reduced mobility, but hydrophobic treatments can reduce its impact [149]. This degradation can be explained by the effect of the polar water molecules on charge carriers. As for exposure to air (and therefore oxygen), according to Häusermann and Batlogg [150], it may initially boost OSC performance, leading to increased mobility. However, trap states are then created in the semiconductor upon exposure to oxygen. This results in a degradation of the OSC, which can be further accelerated by exposure to UV light (*e.g.* sunlight), which can generate radicals and ozone. In general, the top gate configurations are preferred to protect the OSC from moisture and/or oxygen. For transistors in bottom gate configuration, another solution is to encapsulate the device.

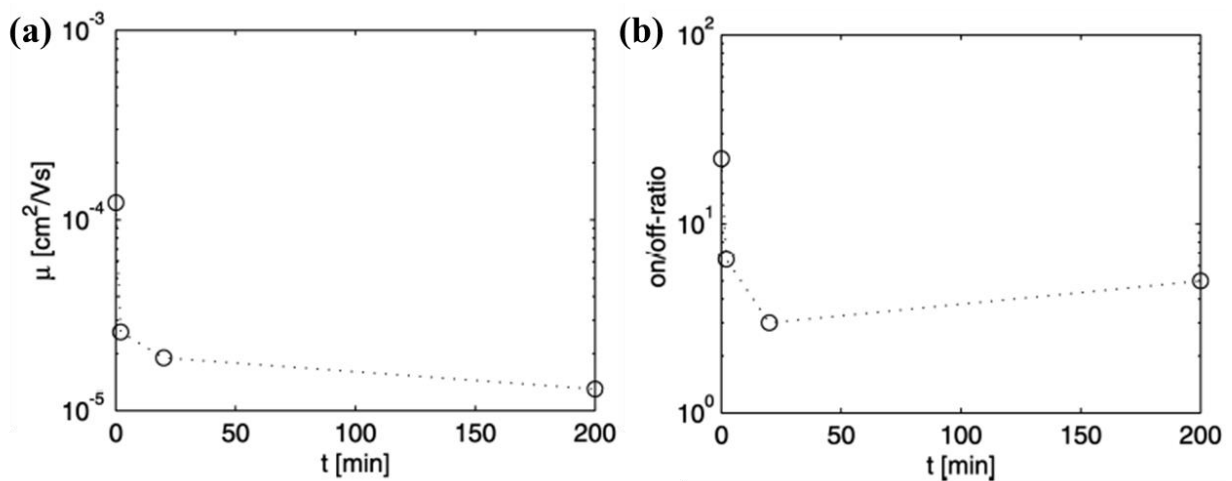


Figure 3.6: Diagrams of (a) μ - t and (b) on/off-ratio- t for an OTFT of $W = 1000 \mu\text{m}$ and $L = 1.5 \mu\text{m}$, exposed to a thermal treatment at 65 °C for 0, 2, 20, and 200 min. The BG/BC device comprised a 60-nm-thick pentacene layer and Ni-contacts. $V_{DS} = -20 \text{ V}$ and $V_G = -10 \text{ V}$ for all diagrams [149].

3.3 Fabrication of SCO-based OFETs

3.3.1 Device designs

In this section, we describe the fabrication of SCO-based transistor devices. For device fabrication, we used $[\text{Fe}(\text{HB}(\text{tz})_3)_2]$ thin films, which were introduced in Chapter 2. Three different OFET devices were designed and fabricated in either bottom gate – bottom contact or bottom gate – top contact configurations. The fabrication process is slightly different from one configuration to another.

Device A is a BG/BC OFET, whose fabrication is shown in Figure 3.7a. It is made on a highly n-doped Si substrate ($\rho \sim 10^{-3} \Omega.m$), which was then insulated by a thermally grown dielectric SiO_2 layer (225 nm), on top of which the drain and source electrodes (10 nm Cr and 50 nm Au) were patterned by lift-off using a 5 μm negative resist. In the next step a $[\text{Fe}(\text{HB}(\text{tz})_3)_2]$ film was deposited (with variable thicknesses between 5 and 30 nm), followed by the deposition of the OSC layer (with variable thicknesses between 20 and 100 nm). The OSC material was tetracene, synthesized and graciously provided for our experiments by Dr. André Gourdon and Dr. Andrej Jankaric in CEMES-CNRS. Finally, the device was encapsulated by an epoxy glue. In this Device A, the SCO layer acts as a dielectric together with the SiO_2 layer. In order to verify its insulating nature as well as the capacitance switching at the SCO phenomenon, impedance spectroscopy measurements were conducted on a ITO/ $[\text{Fe}(\text{HB}(\text{tz})_3)_2]$ /Al junction as a function of temperature. As shown by Figure 3.8a, the conductivity of the SCO film appears indeed extremely low, in good agreement with our previous observations on the powder sample (see Fig. 2.23 in Chapter 2). Equally important for our work, is the fact that the capacitance of the junction shows a drop at the spin transition temperature (Fig. 3.8b). The change is relatively small in contrast to some other SCO compounds [Lefter 2014, Bousseksou 2003], but very clear and reversible. As discussed above, this capacitance change provides scope for the modulation of the transistor characteristics via the SCO phenomenon. Nevertheless, in this configuration, one might also expect the SCO phenomenon alter the semiconductor – dielectric interfacial properties as well (*e.g.* charge trapping).

Device B is also a BG/BC device, which was fabricated in a similar manner, but in this case, the SCO layer was deposited on top of the OSC layer (Fig. 3.7b). This configuration was inspired by the report of van Geest *et al.* [134] on SCO-graphene three terminal devices. According to these authors, the electrostatic effect of the SCO layer may have a substantial

impact on the active layer of the transistor even through a relatively thick spacer layer, which we tried therefore to explore through this device configuration.

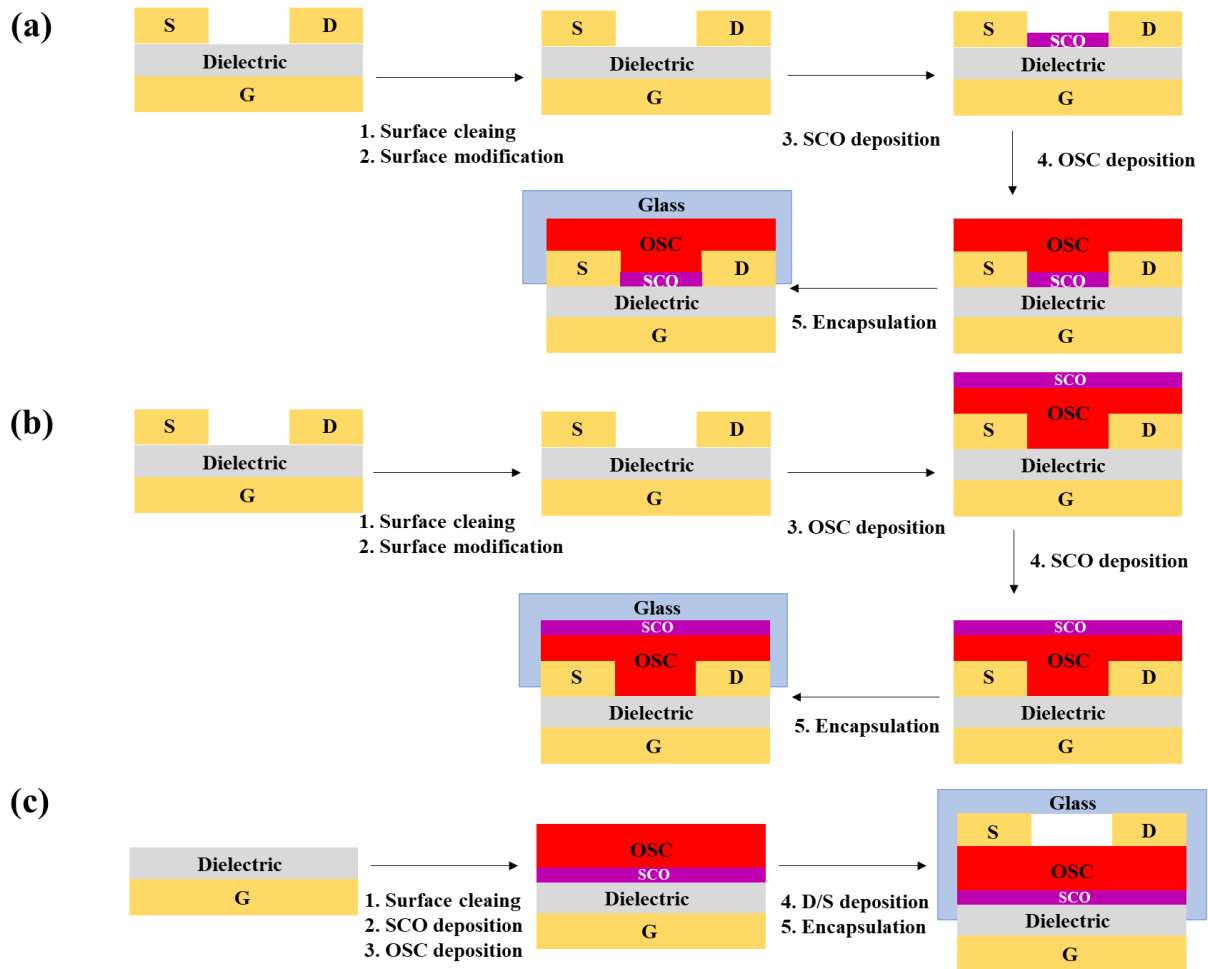


Figure 3.7: (a) The process scheme of bottom gate (BG) bottom contact (BC) OFETs with SCO as a dielectric (Device A). (b) The process scheme of bottom gate (BG)/bottom contact (BC) OFETs with SCO to investigate its electrostatic effect (Device B). (c) The process scheme of bottom gate (BG)/top contact (TC) OFETs with SCO as a dielectric (Device C).

Finally, we designed also a BG/TC configuration (Device C), which is shown in Figure 3.7c. In this case, the SCO film takes part of the gate dielectrics (similar to Device A), but the source and drain electrodes are deposited on top of the OSC layer in the last step of fabrication. It is important to note that for this Device C we used benzo-hexacene as OSC, instead of tetracene. The reason for this change is that we did not succeed in depositing top contact electrodes on tetracene. (This issue is still under investigation, but we believe at this stage that it is most likely linked to the different surface roughness of the OSCs.)

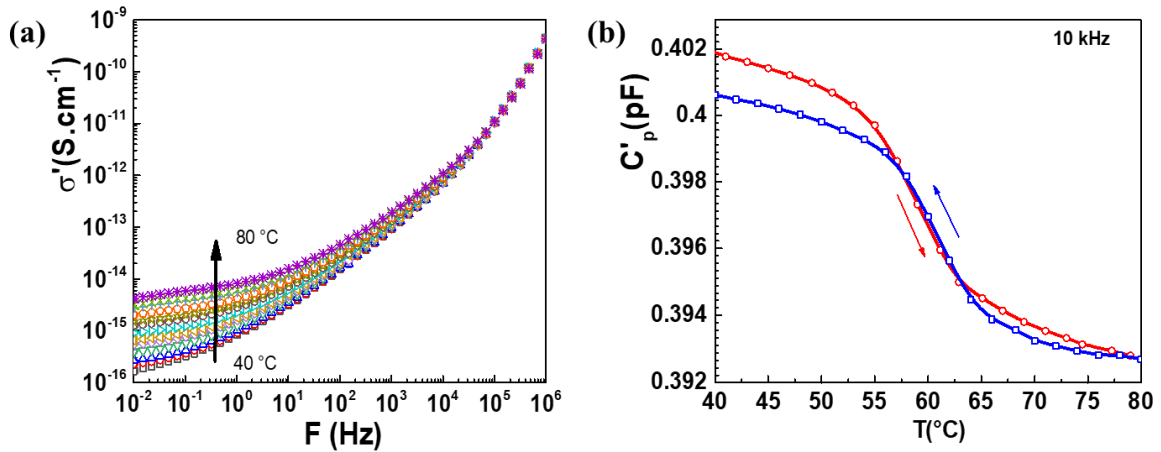


Figure 3.8: (a) Variable temperature conductivity spectra and (b) capacitance (10 kHz) of a ITO/[Fe(HB(tz)₃)₂]/Al junction extracted from impedance measurements.

3.3.2 Experimental protocols

Oxidized silicon wafers need to be cleaned before use. The main purpose is to remove organic contaminants (such as photoresist, organic solvents, grease, *etc.*), inorganic contaminants and particulate contaminants adsorbed on the substrate surface (Fig. 3.9). These contaminants will induce defects and roughness on the surface of the dielectric layer, which will affect not only the interface contact between the dielectric layer and the OSC layer, but also the surface conductivity, resulting in large leakage current, which will weaken the performance of the device. The main steps of cleaning are as follows: first, we place the Si/SiO₂ substrates (with source and drain already patterned for Device A and B) in a Teflon rack and sonicate it with acetone (VLSI, 99.5%) and ethanol (VLSI, 99.9%) for 10 min, respectively. After the sonication, the substrates were dried by a nitrogen gas flow, followed by a 10 min UV-ozone treatment to remove the residual solution.

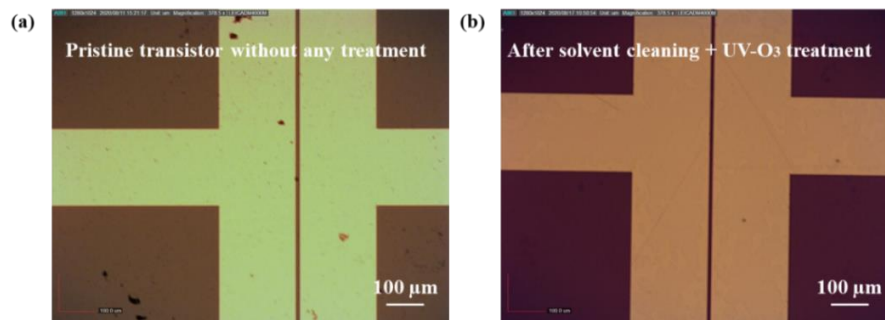


Figure 3.9: Optical microscope image of the surface of drain-source electrodes in a transistor: (a) pristine surface and (b) surface after cleaning.

The first dielectric layer used in our devices is silicon dioxide (SiO_2), which is an inorganic insulating material with appropriate dielectric properties. However, it is characterized by strong surface hydrophilicity and high surface free energy, which are not favorable to the adsorption of the organic layer on the substrate. In addition, the surface roughness of the dielectric layer has also a very important influence on the growth of the organic layer of the OFETs and its carrier transport performance. Modification of the dielectric layer can effectively reduce the free energy of the surface, improve the hydrophobicity of the surface, reduce the interface roughness and surface defects, etc., which are all beneficial to the transport of carriers in the conductive channel. Self-assembled monolayers (SAMs) can be formed on (semi-)conductor and dielectric surfaces using silanes. In our case, a SAM, consisting of octadecyltrichlorosilane (OTS), was systematically deposited (from solution) on the SiO_2 surface in Device A and Device B to improve their performance. (N.B. It may be worth to mention that the energy barrier between the metal and the semiconductor can sometimes turn out to be too large for the injection of charge carriers. In this case, self-assembly can be also an effective strategy to lower the injection barrier by creating a dipole at the electrode/semiconductor interface.)

The preparation of source and drain electrodes include either conventional photolithography (for Devices A and B), or the evaporation mask method (for Device C). In the former case, we used a 5 μm negative NLOF 2035 resist purchased from MicroChemicals, whereas in the latter case a high-resolution nickel mask was prepared by the TEAM service (David Bourrier) in LAAS-CNRS. In both cases, gold was deposited through the mask openings by thermal evaporation. In order to ensure the good adhesion of gold, a thin layer of Cr was intercalated between the SiO_2 substrate and the electrodes. Both approaches allowed us to obtain devices with channel lengths (L) of 10, 30, 50, 70 and 110 μm and channel widths (W) of 0.5, 1 and 1.5 mm.

Organic semiconductors and the SCO layer were deposited by vacuum thermal evaporation. After depositing the SCO film, a water vapor annealing treatment was carried out (see Chapter 2). Finally, the device was encapsulated.

A representative photo of Device C is shown in Fig. 3.10. Each chip contains five transistors. For electrical measurements, three gold-coated tungsten tips were placed in contact with the extension of drain/source/gate electrodes with the chip placed on a heating-cooling stage (Linkam Scientific, HFS600EV-PB4). The measurements were conducted either in an

ambient environment or under primary vacuum (10^{-2} mbar). We used two measurement setups: either an Agilent 4142B source-meter unit (SMU) associated with a probe station (Karl Suss PA200 or Cascade Summit 12000) or a combination of two Keithley SMUs (6430 and 2420). The data acquisition consisted in acquiring output and transfer curves at fixed temperatures.

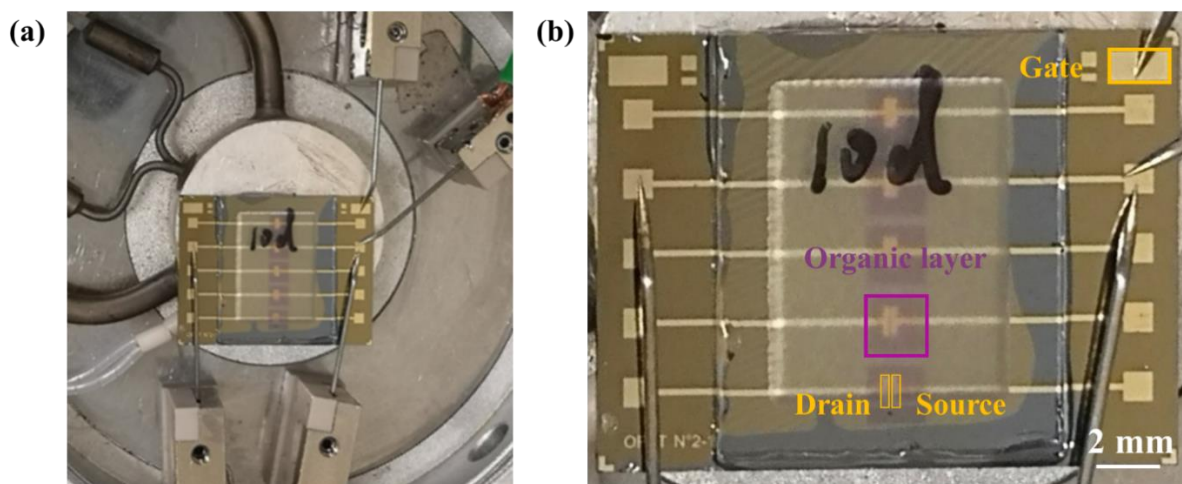


Figure 3.10: Photos of (a) a chip with five transistors on the heating-cooling stage and (b) a zoom on the chip. One can depict also the probes used for the measurements.

3.4 Characterization of Devices A and B

Different thicknesses (2, 10 and 30 nm) of $[\text{Fe}(\text{HB}(\text{tz})_3)_2]$ were integrated in Device A. Figure 3.11 depicts a representative output characteristic (a) and transfer characteristic (b) of a Device A with SCO thickness of 30 nm. From the output curve we can see that the source-drain current is very low ($< 10^{-10}$ A) indicating that the channel is not conducting. In addition, when increasing the gate voltage from -10 V to -50 V, no significant increase of I_{DS} occurs. Overall, this device does not show any expected characteristics of a working transistor.

We believe the failure of Device A is linked to the presence of an SCO ‘interlayer’ between the source/drain electrodes and the organic semiconductor. Indeed, as shown in Figure 3.7a, in this fabrication protocol, when the SCO layer is deposited on the substrates, it covers inevitably the ‘wall’ of the source/drain electrodes due to an angle between the effusion cell (used for the evaporation of the SCO material) and the substrate. Hence, during the thermal evaporation, SCO molecules will be deposited in every corner on the ‘wall’ of the gold electrodes due to the rotation substrate when operating (Fig. 3.12). Unfortunately, this SCO layer appears to be an efficient injection barrier to impede current flowing in the OSC channel.

(N.B. We have fabricated the same device without SCO layer, which showed appropriate transistor characteristics – see Annex 3.X.)

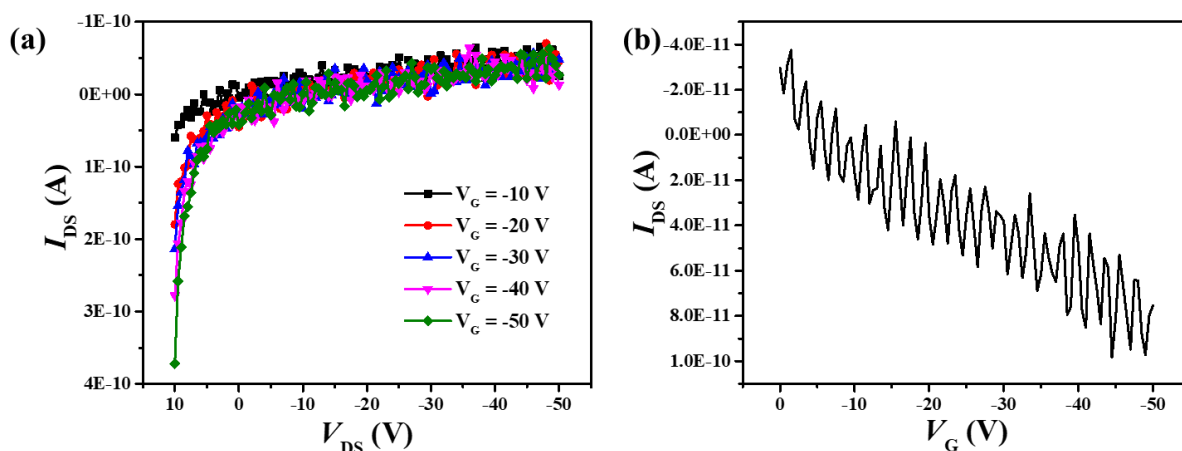


Figure 3.11: Representative (a) output characteristic ($V_G = -10, -20, -30, -40$ and -50 V) and (b) transfer characteristic ($V_{DS} = -30$ V) of Device A. $W = 50 \mu\text{m}$, $L = 1500 \mu\text{m}$.

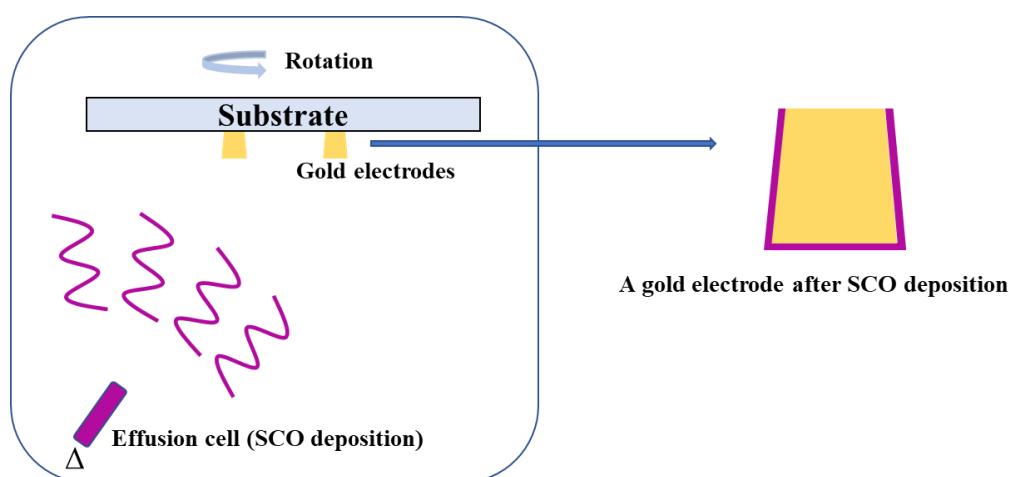


Figure 3.12: A scheme of SCO deposition on the ‘wall’ of Au electrodes.

We also examined the electrical characteristics of Device B. In this configuration, a 75 nm thick tetracene film was first deposited on the clean, SAM-functionalized substrate, which was followed by the deposition of a 150 nm thick $[\text{Fe}(\text{HB}(\text{tz})_3)_2]$ film in the last step of the device fabrication. Figure 3.13 depicts a representative output characteristic (a) and transfer characteristic (b) of a Device B. It can be seen from the output characteristic curve that the drain-source current (I_{DS}) is in the order of 10^{-6} A with a significant field effect, indicating that the transistor is working. In other words, the drain-source current (I_{DS}) can be tuned by changing the gate voltage. As shown in Figure 3.13a, the drain-source current (I_{DS}) keeps increasing when changing the gate voltage from 0 to -50 V, in line with the p-type characteristics. Both the linear

and saturated zones can be clearly depicted in this figure. From Figure 3.13b, we can infer a threshold voltage of *ca.* -12 V and an ON/OFF ratio of 2-3 orders of magnitude for this transistor. We also notice that there is some noise in these two characteristics, which we attribute to traps in between the dielectric and OSC layers.

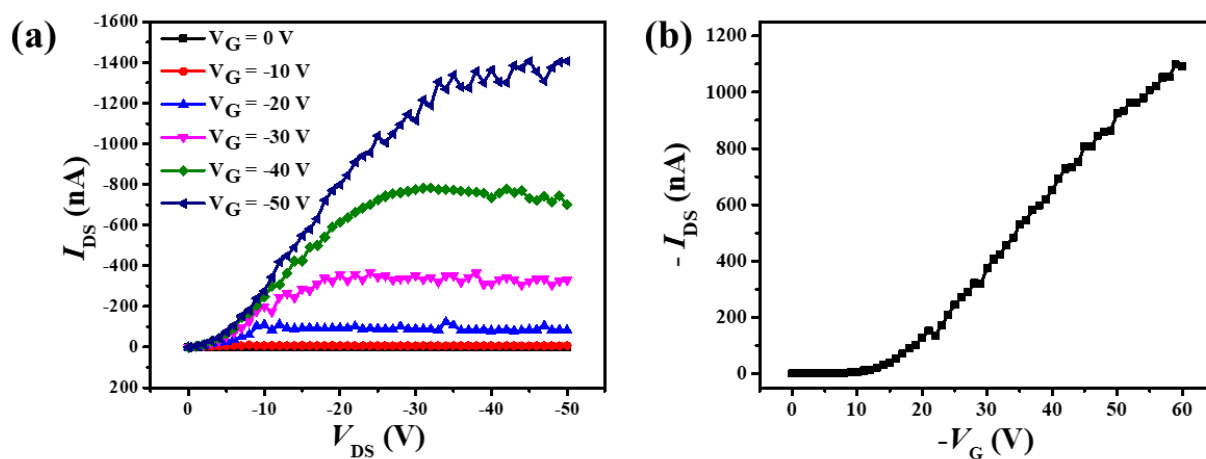


Figure 3.13: Representative (a) output characteristic ($V_G = 0, -10, -20, -30, -40$ and -50 V) and (b) transfer characteristic ($V_{DS} = -30$ V) of Device B. $W = 50 \mu\text{m}$, $L = 1000 \mu\text{m}$.

In the next step, we have examined the temperature dependent behavior of Device B in order to assess the effect of the SCO on the device properties. As discussed by van Geest et al. [134], we shall consider here the electrostatic effects occurring when the top layer of the transistor undergoes spin crossover. DFT calculations showed [144] that due to the swelling of the coordination sphere, the SCO is always associated with a change of the molecular dipole moment, which can change by a factor of two or three upon the SCO. Since the molecules are preferentially oriented in the films of $[\text{Fe}(\text{HB}(\text{tz})_3)_2]$, the dipole moments of individual molecules sum up, creating an electrostatic potential that interacts with the OSC layer to a different extent in the LS and HS states. To explore this effect a constant gate voltage of -10 V and drain-source voltage of -30 V was applied on this transistor, and the drain-source current was recorded during successive thermal cycles between 45-85 °C (ramping rate of 5 °C/min). A representative result (from several thermal cycles) is shown in Figure 3.14. The variation of the current intensity was often noisy and ill reproducible. More importantly, no clear sign for changes related to the SCO phenomenon could be inferred. For this reason, our attention has turned to the optimization of Device C both in terms of fabrication process and characterization protocols, enabling better device stability.

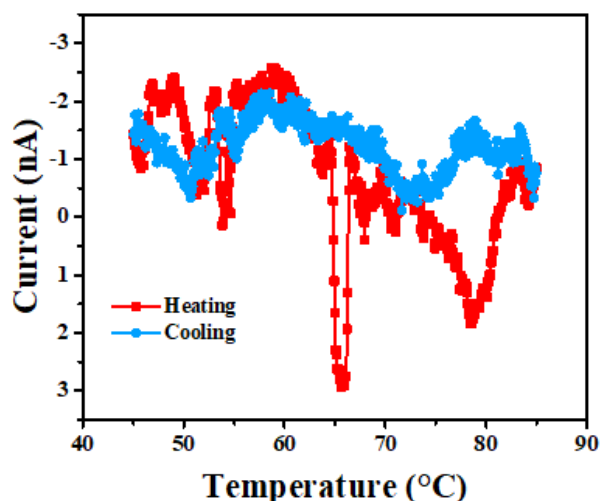


Figure 3.14: Representative temperature dependent current measurement for Device B. Measurement condition: $V_G = -10$ V, $V_{DS} = -30$ V, $dT/dt = 5$ °C/min. $W = 50$ μm , $L = 1000$ μm .

3.5 Analysis of the thermal stability of ‘standard’ bottom gate/top contact devices

As we discussed in Section 3.2.4, several factors may influence the stability of the OFETs, among which one has to consider in particular temperature, voltage stress and environmental effects. The transistor we investigate here has a bottom gate/top contact configuration (without SCO layer), with 50 nm thickness of benzo-hexacene as OSC layer. For convenience, we will cite this transistor as the ‘standard device’. Because our key interest is the temperature-dependent characteristics of the transistor, experiments were carried out through several in many thermal cycles with different conditions. Table 3.2 shows the main parameters for six successive thermal cycles on a standard device characterized in ambient air. The temperature range is the same in the first five thermal cycles, which aim to compare the influence of different electric measurement conditions (electric stress). Compared with the second and the third thermal cycles, the first thermal cycle represents more measurements, including not only transfer, but also rather time-consuming output characteristics in every measurement point. The 4th-6th thermal cycles were conducted using the same gate voltage and drain-source voltage, but with different temperature intervals or different temperature ranges. The I - T curves extracted from these experiments are shown in Figure 3.15. Nearly all the curves show a positive slope during the thermal cycles, which is consistent with an ordinary thermal activation process of the conduction. However, we can observe a systematic decrease of the current intensity during the first five heating ramps above *ca.* 70-75 °C, which indicates that the device underwent

degradation in these conditions. Most importantly, it turns out that the degradation occurs as a combined effect of high temperature and applied voltage and by decreasing the effective measurement time (Cycles 2 & 3) it is possible to reach a reasonably good reversibility with a current drop $(I_{\text{final}} - I_{\text{initial}})/I_{\text{initial}}$ of ca. -10-20 %. What is more, cycles 2 and 3 were obtained from transfer characteristics, which contain potentially more information as simple I - T curves measured at fixed gate and drain-source voltages. To better understand the stability of our OFET devices, we carried out further temperature dependent current characterizations on a standard device, investigated under a vacuum of 10^{-3} mbar to remove doubts of potential effects of water and oxygen of the ambient environment, even though the devices were all encapsulated. The details of these and some other tests are given in [Annex 3.X](#). Most importantly, the device degradation does not seem to be affected by the environmental effects to any significant extent, hence, all further measurements were conducted in ambient air. Overall, these tests confirmed that, unfortunately, the devices are rather sensitive to combined voltage/temperature stress, but with some care, temperature-dependent transfer characteristics can be acquired with an acceptable reproducibility.

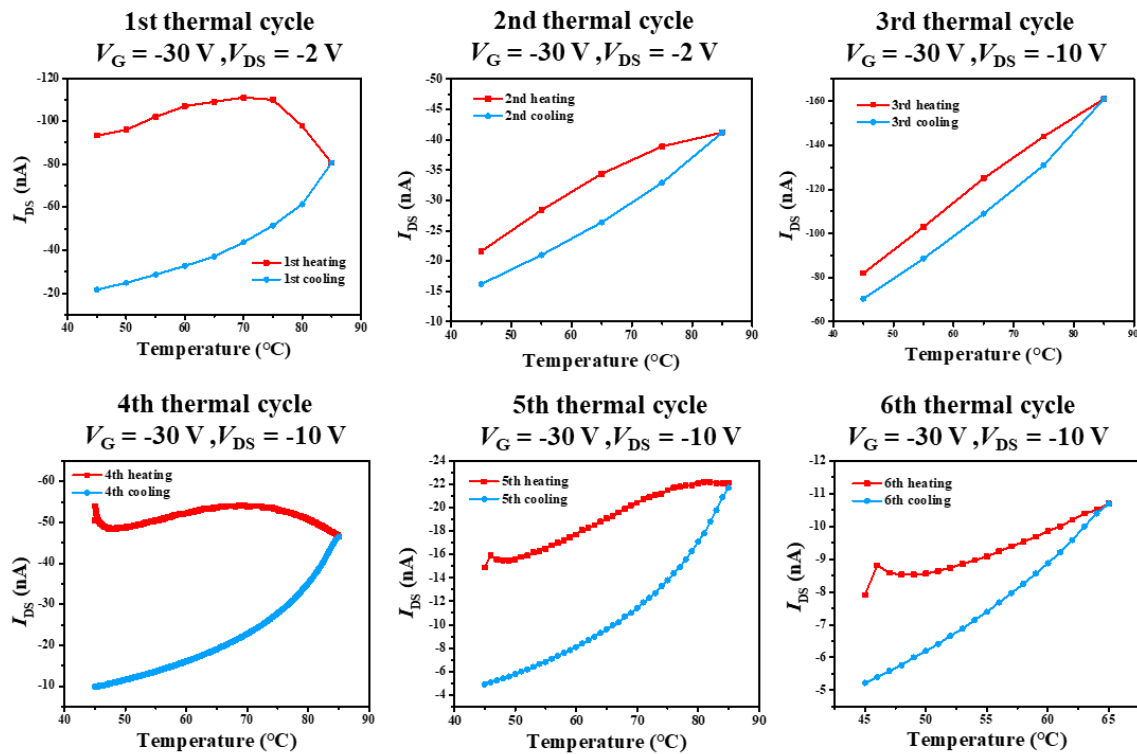


Figure 3.15: Current-temperature (I - T) characteristics of a standard device for six successive thermal cycles under different measurement conditions – shown in Table 3.2. (The data for the first three cycles were extracted from the transfer characteristics.) $W = 70 \mu\text{m}$, $L = 1000 \mu\text{m}$.

Table 3.2: Parameters of the temperature cycles shown in Fig. 3.15.

Thermal cycles	Measurements
1 st (45-85-45 °C)	Output and Transfer ($V_{DS} = -2, -5, -10$ & -50 V) characteristics, temperature interval = 5 °C
2 nd (45-85-45 °C)	Transfer ($V_{DS} = -2$ & -5 V) characteristics, temperature interval = 10 °C
3 rd (45-85-45 °C)	Transfer ($V_{DS} = -10$ & -50 V) characteristics, temperature interval = 10 °C
4 th (45-85-45 °C)	I-T characteristic ($V_G = -30$ V, $V_{DS} = -10$ V), temperature interval = 0.083 °C, 5 °C/min
5 th (45-85-45 °C)	I-T characteristic ($V_G = -30$ V, $V_{DS} = -10$ V), temperature interval = 1 °C, 5 °C/min
6 th (45-65-45 °C)	I-T characteristic ($V_G = -30$ V, $V_{DS} = -10$ V), temperature interval = 1 °C, 5 °C/min

3.6 Characterization of Device C

As mentioned before, Device C is a bottom gate/top contact device, wherein a 50 nm thick layer of $[\text{Fe}(\text{HB}(\text{tz})_3)_2]$ is deposited between the SiO_2 and OSC layers. Similar to Device A, the SCO layer may act here by modulating the effective capacitance of the dielectric and/or by altering the charge transport in the conducting channel. The obvious advantage with respect to Device A, however, is that the SCO layer is not in contact with the drain/source electrodes, avoiding thus potential pitfalls in charge injection. For comparison, device characterization was done simultaneously on Device C as well as on the ‘standard device’, the only difference between the two devices being the presence or absence of the SCO layer, respectively.

Figure 3.16 depicts the output and transfer characteristics of a ‘standard device’ acquired at 45 °C. (More data of the electric characteristics at different temperatures are shown in the [Annex 3.X](#).) The output curves in Figure 3.16a are smooth indicating good quality interfaces and materials. The field effect is clear as the drain-source current can be tuned in a broad range by changing the gate voltage. When the applied drain-source voltage (V_{DS}) is small, the source-drain current (I_{DS}) changes linearly with increasing V_{DS} and gradually tends to be saturated when V_{DS} is high enough. From the transfer characteristics in Figure 3.16b, we can infer a threshold voltage of *ca.* -9 V and an ON/OFF ratio of 10^3 for this transistor at $V_{DS} = -10$ V. One can notice the small hysteresis of the transfer curves between increasing and decreasing values of V_G indicating presumably the presence of charge traps at the OSC/dielectric interface.

Output and transfer characteristics of Device C at 45 °C are shown in Figure 3.17. As we can see from Figure 3.17a, the current intensity in Device C with respect to the ‘standard device’ is reduced by *ca.* 3 orders of magnitude – most likely due to the reduced quality of the SCO/OSC interface in comparison with the SiO_2 /OSC interface. This reduced quality may come from the relatively rough surface of the $[\text{Fe}(\text{HB}(\text{tz})_3)_2]$ thin film (see Chapter 2) or the SCO thin film

may unfavorably influence the growth of the OSC film in terms of crystallinity and morphology. Still, the output characteristic curve of Device C shows a clear field effect: the drain-source current can be tuned by the gate voltage and the linear/saturation regions can be clearly distinguished. To our best knowledge, this is the first working OFET incorporating a spin crossover material in the dielectric layer. The leakage current (*i.e.* OFF state current) is several tens of pA, whereas the ON-state current can reach several nA. One can also note a hysteresis in the transfer characteristics denoting the presence of charge traps.

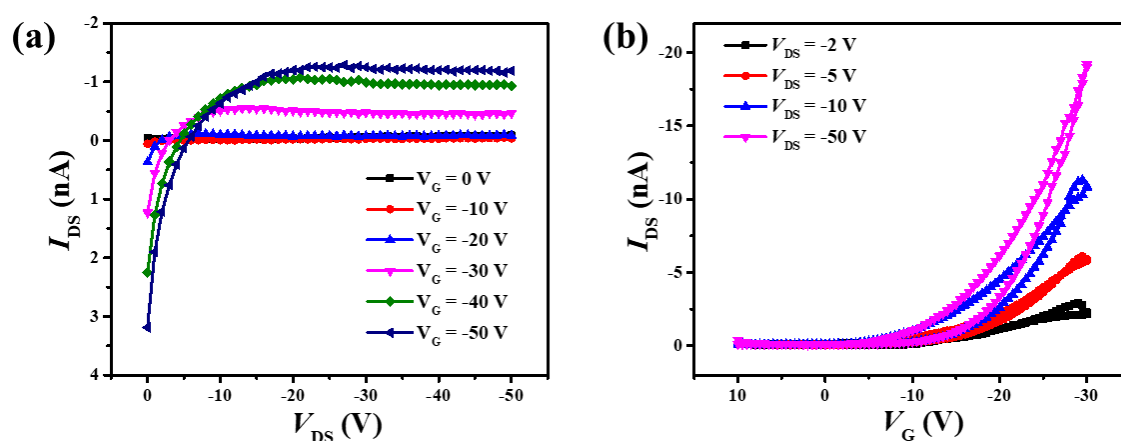


Figure 3.16: (a) Output characteristic ($V_G = 0, -10, -20, -30, -40$ and -50 V) and (b) transfer characteristic ($V_{DS} = -2, -5, -10$ and -50 V) of a ‘standard device’ measured at 45 °C. $W = 70$ μm , $L = 1000$ μm .

Figure 3.17: (a) Output characteristic ($V_G = 0, -10, -20, -30, -40$ and -50 V) and (b) transfer characteristic ($V_{DS} = -2, -5, -10$ and -50 V) of a Device C measured at 45 °C. $W = 110$ μm , $L = 1000$ μm .

Using UV-vis spectrophotometry we have also assessed the SCO properties of the $[\text{Fe}(\text{HB}(\text{tz})_3)_2]$ films integrated into Device C (Figure 3.18). The spin transition in these films occurs, as usual, near $60\text{-}65$ °C, but it is somewhat less abrupt and accompanied by a broad hysteresis. We remark that such unusual hysteresis was observed in a few other cases as well (see Figure 2.7f and 2.26) and we can attribute this phenomenon most likely to an incomplete crystallization of the film. Nevertheless, we note that the magnitude of the absorbance change (*ca.* 0.15) corresponds to the value expected for a 50 nm thick film.

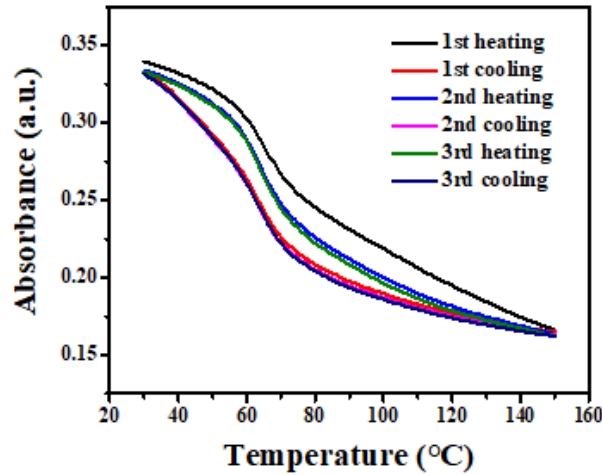


Figure 3.18. Temperature dependence of the UV absorbance (318 nm) during three successive heating-cooling cycles for the $[\text{Fe}(\text{HB}(\text{tz})_3)_2]$ film integrated into Device C.

In the next step, temperature dependent measurements were carried out both on the ‘standard device’ and Device C. As discussed above, in order to minimize device degradation, we recorded only the transfer characteristics at a few temperatures (see Figure 3.19 and Annex 3.X) from which we extracted then the temperature dependence of the drain-source current and that of the threshold voltage. As shown in Figure 3.19, increasing temperature leads to significant changes in the transfer characteristics, which are reversible to a reasonable extent upon cooling, confirming thus the pertinence of our measurement protocol. These temperature-induced changes arise obviously from a combination of different phenomena, including ordinary thermal activation of the conduction, charge trapping, thermally induced spin crossover and so forth. In order to try to disentangle the effect of the SCO on the behavior of the transistor we have extracted from the transfer curves of both Device C and a ‘standard device’ the temperature dependence of the drain-source current at fixed values of V_{DS} and V_{G} as well as that of the threshold voltage for a fixed V_{DS} value. These results are summarized in Figures 3.20 and 3.21, respectively. (See also Annexes 3.x for further data.)

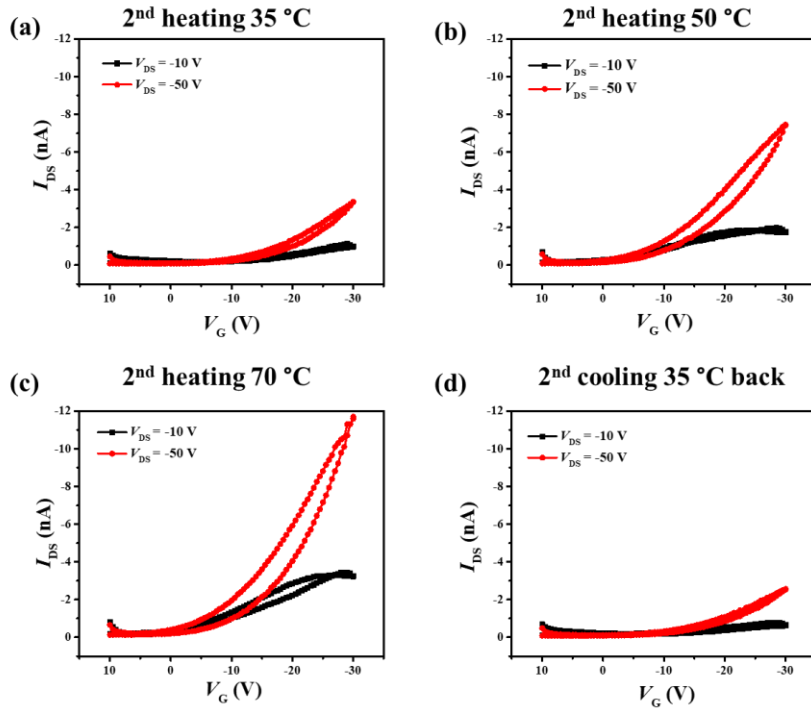


Figure 3.19: Transfer characteristics of a Device C recorded at selected temperatures. $W = 50 \mu\text{m}$, $L = 1000 \mu\text{m}$.

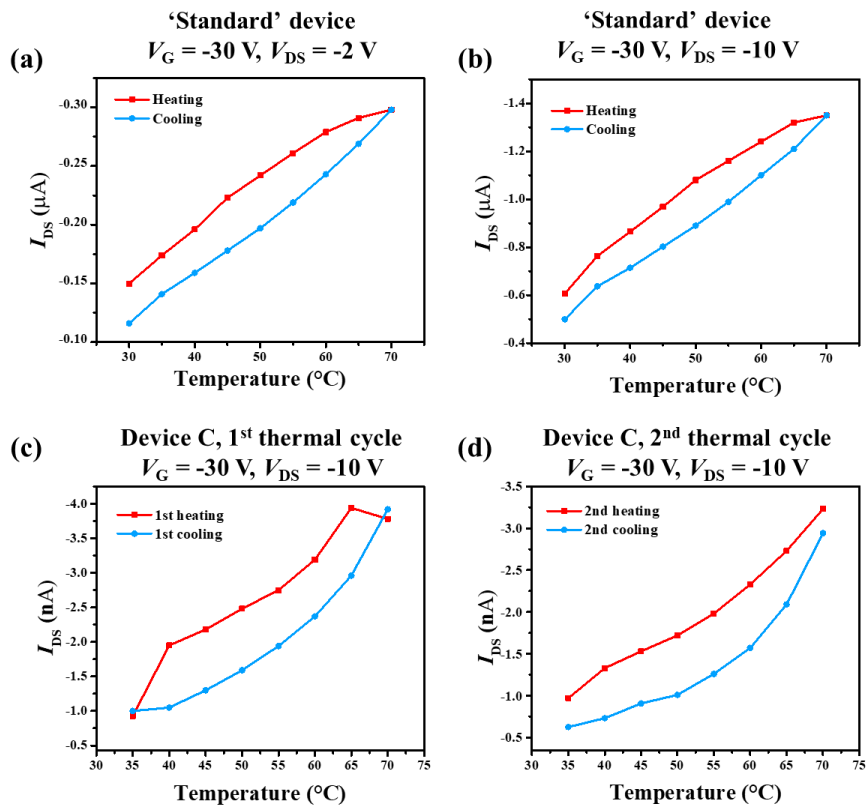


Figure 3.20: Representative temperature dependent drain-source current characteristics of a 'standard device' (top panel) and Device C (bottom panel). $W = 50 \mu\text{m}$, $L = 1000 \mu\text{m}$.

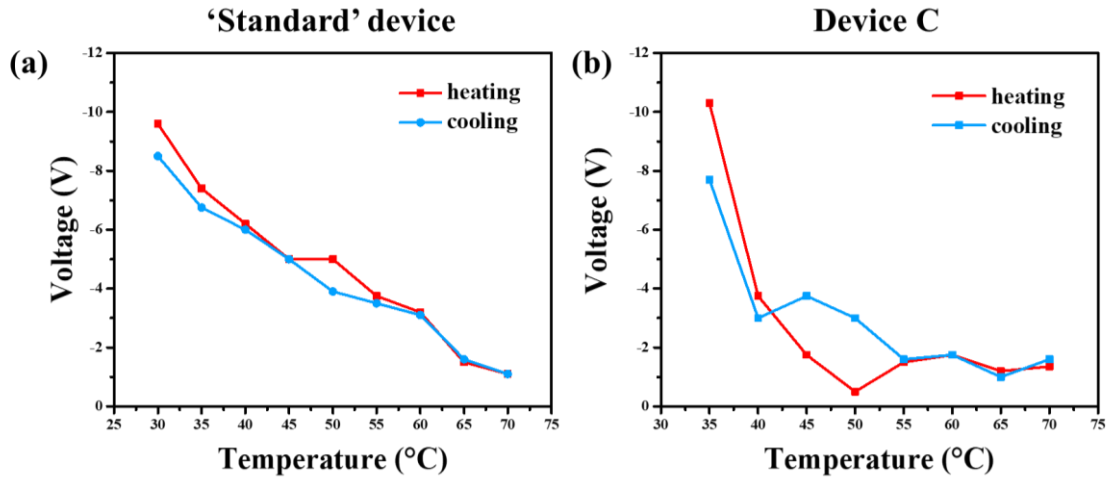


Figure 3.21: Temperature dependence of the threshold voltage for a ‘standard device’ (a) and for a Device C (b) extracted from transfer curves at $V_{DS} = -10$ V. $W = 50$ μm , $L = 1000$ μm .

The temperature dependence of the drain-source current extracted from the transfer characteristics are shown in Figure 3.20 both for a ‘standard device’ and for Device C. All temperature dependent data exhibit thermal activation. For the ‘standard device’ this dependence is nearly linear in the investigated temperature range (30-70 °C) and for all combinations of V_{DS} - V_G , although some deviation is observed near 70 °C on heating. On the other hand, the I_{DS} vs. T curves for Device C deviate from a linear behavior and the slope in the low- and high-temperature ranges are systematically different. In a similar manner, we can compare the temperature dependence of the threshold voltage for the two devices in Figure 3.21. The ‘standard device’ exhibits again a quasi-linear behavior, whereas the Device C incorporating the SCO layer shows again a different tendency with a marked difference at high and low temperatures. It would be tempting to correlate these curves with the SCO behavior of the $[\text{Fe}(\text{HB}(\text{tz})_3)_2]$ film shown in Figure 3.18. However, we must stress that we have no direct proof for such correlation and more experiments should be done to confirm the spin crossover effect on the OFETs.

Even if the physical origin of the different behaviors of these transistors with and without SCO layer remains to be explored, it is important to underline that these differences are real and not related to device degradation. This robustness of the devices (and of the measurement protocol) is clearly illustrated in Figure 3.22, which shows the output characteristics of a Device C recorded near ambient temperature (35°C) before the thermal cycles and after the first and second heating-cooling cycles (involving the acquisition of the transfer characteristics shown in Figures 3.20 and 3.21). One can observe that the first cycle leads to a small increase of the

output current, which might be related to thermally activated charge detrapping. However, the output characteristics recorded after the first and second cycles are closely comparable.

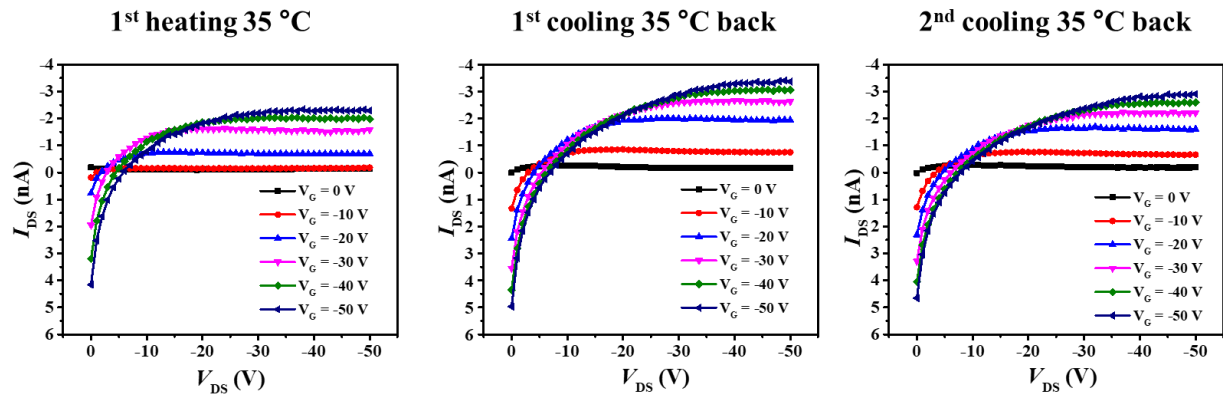


Figure 3.22: Output characteristics of the Device C before/after thermal cycles. $W = 50 \mu\text{m}$, $L = 1000 \mu\text{m}$.

3.7 Conclusions and perspectives

In summary, we successfully integrated $[\text{Fe}(\text{HB}(\text{tz})_3)_2]$ thin films into two different configurations of three-terminal OFET devices.

The first device is a bottom gate/bottom contact type. When the SCO layer was inserted between the OSC and dielectric layer in this device, it failed to form a proper conductive channel. We suggested this failure may come from the insulating SCO layer deposited on the drain and source electrodes obstructing charge injection. Nevertheless, when the SCO layer was deposited on the top of OSC layer these devices showed proper transistor output and transfer characteristics. Unfortunately, the temperature dependence of the transistor characteristics did not show any remarkable feature – most probably due to the inappropriate experimental protocol. Further work on this type of device could involve the use of a mask before the deposition of the SCO layer to avoid any interlayer between the electrodes and the OSC film. Alternatively, we can also deposit the electrodes after the SCO deposition. Independently from the fact if the SCO deposited before or after the OSC, a more careful characterization should be conducted avoiding long exposures to high temperatures under voltage stress.

The second device is bottom gate/top contact type. Having learnt from the first experiences on the BG/BC type devices, in this case, we conducted a more in depth investigation and we were able to establish measurement protocols, which minimize the device degradation. The SCO film was then successfully inserted in between the SiO_2 and OSC layers

and the devices exhibited clear field-effect characteristics. From the variable temperature transfer characteristics, we could extract the temperature dependence of the drain-source current and of the threshold voltage. The comparison of these data obtained either in the presence or in the absence of the SCO film revealed small, but significant differences. Further work should confirm to what extent these differences could be linked to the SCO phenomenon. To do this, we can envision three main axes for future work: (i) One of the priorities would be to use a more robust organic semiconductor, which can sustain reasonably high temperature. (ii) We should also find a solution to preserve the OSC/dielectric interface quality, for example by embedding the SCO compound within a dielectric polymer matrix. (iii) It would be also preferable to use another SCO material, which displays a spin transition with hysteresis close to room temperature as well as an important change of the dielectric permittivity. These properties could give rise not only to better device stability, but also to a very useful applicative possibility, which is a non-volatile memory effect.

Chapter 4 Integration of the spin crossover complex [Fe(HB(tz)₃)₂] into optical cavities

In this chapter, we describe the design, fabrication and optical properties of multilayer Ag/[Fe(HB(tz)₃)₂]/Ag Fabry-Perot cavities. These devices use the remarkable refractive index switching ($\Delta n = 0.04 - 0.2$) between the low-spin and high-spin states in the [Fe(HB(tz)₃)₂] film to achieve modulation of the cavity resonance. We show that this wavelength tuneability is coupled with low absorption losses in the visible and near infrared spectral ranges, providing scope for reconfigurable and self-adaptive photonic applications. This work was conducted in a strong collaboration with Dr. Stéphane Calvez and Dr. Isabelle Séguy from LAAS-CNRS.

4.1 Motivation and state of the art for using SCO materials in photonic devices

Materials that undergo electronic and/or structural phase change associated with a reversible switching of their optical properties have recently received increased attention for the development of active photonic devices [151, 152]. These phase-change materials (PCMs) exhibit changes of their refractive index in response to external stimuli (*e.g.* heat, voltage bias or light irradiation), and have been exploited for a variety of applications, such as smart windows, optical memories, spatial light modulators and photonic integrated circuits. The most widely studied PCMs are chalcogenide alloys (*e.g.* Ge₂Sb₂Te₅) showing amorphous-crystalline phase change [153-155], transition metal oxides (*e.g.* VO₂) exhibiting metal-insulator transitions [156, 157], and liquid crystals (*e.g.* 5CB) displaying order-disorder type transitions [158](Fig. 4.1). Among these materials, however, mostly liquid crystals have been employed in practical applications requiring transparency in the visible spectral range. Yet, the intrinsic limitations of liquid crystals (slow speed, high scattering losses, intricate processing and need for encapsulation) call for new material developments. In this context, emerging nanomaterials of molecular spincrossover (SCO) compounds represent a promising novel class of PCMs with high potential for active photonics applications.

The first switch-type optical device using SCO compounds was developed by Kahn et al. [159, 160] for data storage and display applications. These pioneering devices were based on absorbance readout and thermal addressing, which are conceptually contradictory principles in terms of device size. Indeed, slow heat dissipation becomes a limiting factor at macroscopic

scales, while the low optical density becomes quickly a shortcoming at reduced sizes. Indeed, in the VIS-NIR spectral range mostly weak ligand-field absorption bands appear, with extinction coefficients between 1 - 100 cm^{-1} , while substantially more intense charge transfer bands ($\alpha = 10^4 - 10^5 \text{ cm}^{-1}$) arise usually in the ultraviolet range [161]. On the other hand, the real part of the complex refractive index ($n^* = n + ik$) of SCO compounds exhibits remarkable changes in different spectral regions. This refractive index modulation finds its origin in combined electronic (polarizability change) and structural (density change) effects [162]. Nevertheless, the available experimental data suggests that the key parameter is the substantial mass density change (*ca.* 1 - 15 %). Density can be linked to the refractive index through the empirical Gladstone-Dale relationship, which predicts an increase of the refractive index of *ca.* 0.01 – 0.1 for each SCO compound in the whole VIS-NIR range when going from the HS to the LS state [163]. This was indeed observed by a variety of photonic methods for different compounds and in different spectral ranges [23]. The possibility to modulate the refractive index via the SCO opens up interesting prospects for manipulating light propagation in photonic devices. On the other hand, the small value of the absorption coefficient is actually a desirable property in this context. To integrate photonic devices, however, it is necessary to work with very high quality, low absorption loss SCO films, which should be also patterned in order to enlarge the scope of their integration into different types of devices (waveguides, resonators, gratings, *etc.*).

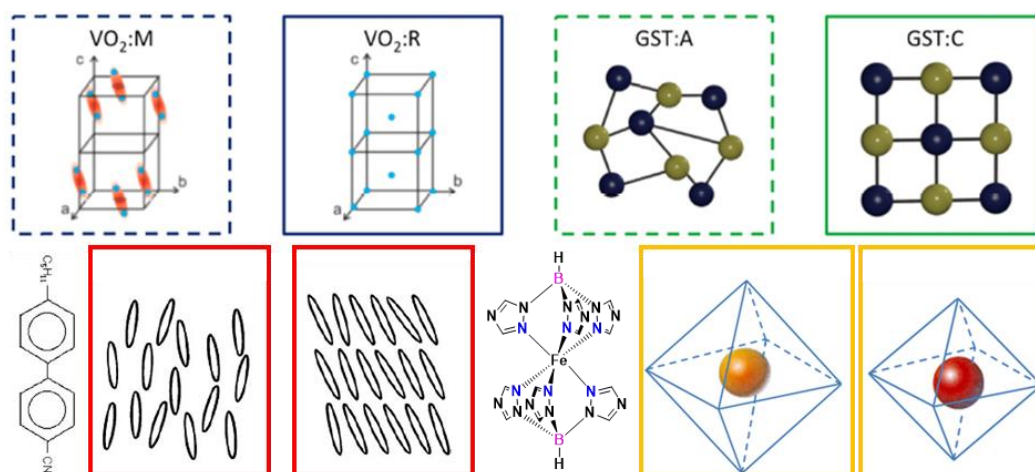


Figure 4.1: PCM materials (clockwise): VO_2 in the metallic (M) and insulator (R) phases with only V atoms shown in blue. $\text{Ge}_2\text{Sb}_2\text{Te}_5$ (GST) in the amorphous (A) and crystalline (C) phases with Te and Sb/Ge atoms shown in blue and gold, respectively. 4-pentyl-4'-cyanobiphenyl (5CB) molecules in the nematic (N) and smectic (S) phases. $[\text{Fe}(\text{HB}(\text{tz})_3)_2]$ molecule in the LS and HS states. Only the FeN_6 coordination octahedron is shown.

Overall, SCO complexes appear as a very promising novel class of PCMs for applications as active materials in photonic devices (see Fig. 4.2) for the following:

- (1) Most SCO films exhibit a substantial change of their refractive index ($\Delta n = 10^{-2} - 10^{-1}$) in the visible-near infrared spectral ranges, while absorption losses remain small. [163]
- (2) The SCO can occur in ambient conditions and can be triggered by a variety of stimuli, such as temperature, mechanical strain and light irradiation. [164]
- (3) In case of pulsed optical excitation, the SCO has been shown to occur on 100s fs time scales [165], while relaxation can occur on 100 ps scale [166].
- (4) SCO complexes have been successfully processed recently as thin films and nanopatterns [23].
- (5) The all-solid nature of SCO materials should afford for an easier processing, a better reliability and a simpler integration into systems than LC based PCMs.

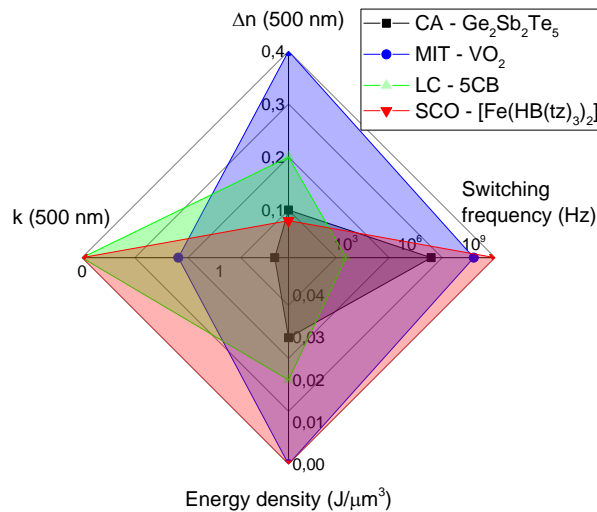


Figure 4.2: Comparison of key material characteristics of different classes of phase change materials (chalcogenide alloys, metal-insulator transition materials, liquid crystals) with those of spin crossover materials for photonic applications in the visible spectral range (500 nm). The lower modulation depth in SCO materials is balanced by several key advantages, such as low insertion losses, low switching power and high modulation frequency (adapted from [167]).

In the past, the refractive index change in SCO materials has been investigated from the UV to the THz spectral ranges either as a means for detecting the spin transition in nanoscale objects [168-172] or with the aim to develop switchable optical materials/devices. The latter comprise transient phase gratings [166], tunable Bragg filters for the sub-millimeter wavelength range [168], diffractive gas sensors [169] and active plasmonic switches based on lithographically patterned [171] or on chemically synthesized [172] gold nano-rods. However, the SCO materials used in these studies suffered from certain limitations, such as poor

processability (*e.g.* powders), low environmental stability, weak cycling endurance and SCO far from room temperature [23]. In the present work, we make use of the refractive index change associated with the SCO to render wavelength-tunable a Fabry–Perot resonator, using our high-quality $[\text{Fe}(\text{HB}(\text{tz})_3)_2]$ films, which effectively overcome all these pitfalls, marking an important leap towards SCO-based photonics.

4.2 Introduction to Fabry-Perot cavities

4.2.1 Principle of a Fabry-Perot interferometer

Fabry–Perot interferometers are widely used in optical instruments, such as spectrometers, lasers, filters and so forth. They are constituted of a material (of arbitrary thickness) sandwiched in between two semi-transparent mirrors. Impinging light is bounced back and forth between the two mirrors and, at the resonance wavelength(s), effectively passes multiple times through the central material. As a result, the wavelength-selective constructive interaction with this layer occurs over an artificially increased length, which equivalently means that energy is stored in the device, which behaves as a resonator. As the simplest case, we can consider a Fabry-Perot interferometer with flat, parallel mirrors as an example (Figure 4.3), whose properties can be adjusted by changing the distance L between the mirrors or the refractive index n of the cavity medium.

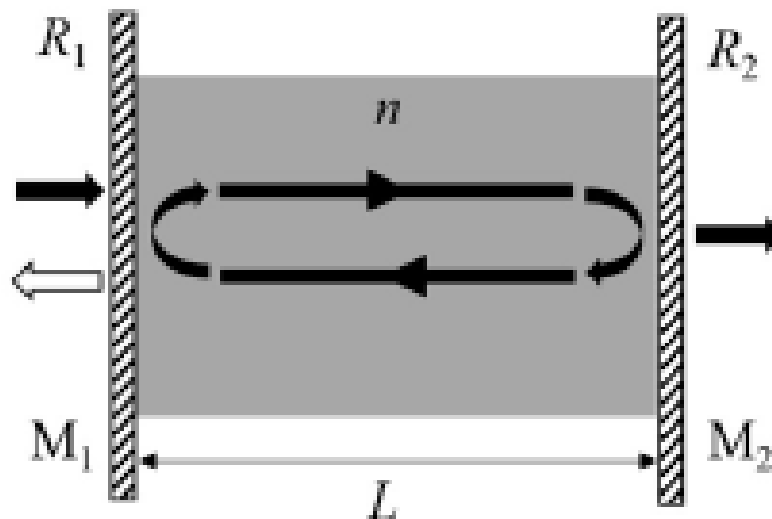


Figure 4.3: Scheme of a parallel mirror (M) Fabry-Perot resonator with a cavity medium characterized by a refractive index n and a thickness L . Light entering one mirror undergoes multiple reflections, leading to partial transmission from the other mirror.

Free spectral range (FSR) and finesse (F) are the most important factors to determine the property of a Fabry-Perot interferometer. The free spectral range (FSR) is a measure of the frequency separation ($\Delta\nu$) between two adjacent resonance peaks in the transmission (or reflection) spectrum of a Fabry-Perot interferometer (see Fig. 4.4), which can be calculated by [173]:

$$FSR = \frac{c}{2nL\cos\theta} \quad \text{Eq.4.1}$$

where c is the speed of light in vacuum, n is the index of refraction of the cavity medium, θ is the angle of incidence and L is the thickness of the cavity.

Dividing the free spectral range by the full-width half-maximum (ν_m) of a resonance peak, the value obtained is called the finesse (see Fig. 4.4) [174]:

$$F = \frac{FSR}{\nu_m} \quad \text{Eq.4.2}$$

The finesse represents the average number of round-trips made by a resonant photon before it leaves the cavity. Cavities with high finesse show sharper transmission peaks and lower transmission. Alternatively, the quality factor Q is also used to quantify the frequency selectivity of a Fabry-Perot cavity. Q is defined as the energy stored in the cavity divided by the energy lost during an oscillation cycle and multiplied by 2π . In most cases, Q is calculated (to a good approximation) as the ratio of the resonance frequency and the full width at half maximum ($Q = \nu_r / \nu_m$). We can see thus that the finesse is proportional to the quality factor Q , which means that the finesse represents also the dissipation of the resonant cavity: the higher the finesse, the lower the dissipation.

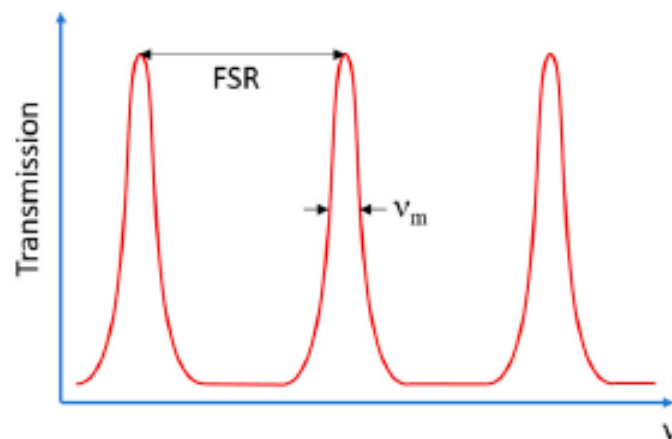


Figure 4.4: Schematic diagram illustrating the free spectral range (FSR) and full width at half maximum of a resonance peak (ν_m) of a Fabry-Perot interferometer.

4.2.2 Tunable Fabry-Perot cavities

Tunable Fabry-Perot filters are amongst the key components in fiber grating sensing and fiber communication systems [175]. In fiber grating sensing, the tunable Fabry-Perot filter is used as the demodulator, and its performance directly determines the performance of the entire measurement system. In optical communication systems, tunable Fabry-Perot filters are used for wavelength division multiplexing (WDM), demultiplexing, signal demodulation, etc., playing an extremely important role. In addition, it can also be used as a signal filter in fiber amplifiers, and has important applications in fiber lasers and spectrum analysis.

In a Fabry-Perot cavity, each transmitted wavefront undergoes obviously an even number of reflections (0, 2, 4, . . .). Whenever there is no phase difference between emerging wavefronts, interference between these wavefronts produces a transmission maximum. This occurs when the optical path difference is an integral number of whole wavelengths, *i.e.*, when [176]:

$$m\lambda = 2nL\cos\theta \quad \text{Eq.4.3}$$

where n is the refractive index of the cavity, L is the thickness of the cavity, θ is the angle of incidence, λ is the center wavelength of the transmitted light and $m = 1, 2, 3, \dots$ is an integer representing the mode order. We can thus deduce that the peak wavelength transmitted by the filter can be tuned in three ways: (1) one is to tune by changing the thickness L of the cavity, (2) the other is to tune by changing the refractive index n of the resonant cavity material and (3) finally one can also change the angle of incidence of the impinging light beam.

In this thesis, we used thin films of the SCO material $[\text{Fe}(\text{HB}(\text{tz})_3)_2]$ as the cavity material in order to take advantage of the refractive index and thickness changes associated with the SCO and thus to tune the resonance wavelength of the Fabry-Perot cavity. In a first step, we have thus characterized in detail the temperature-dependent changes of the thickness and refractive index in these SCO films.

4.3 Optical properties of $[\text{Fe}(\text{HB}(\text{tz})_3)_2]$ thin films

Nano-crystalline thin films of $[\text{Fe}(\text{HB}(\text{tz})_3)_2]$ were obtained by thermal evaporation and treated by water vapor annealing after deposition, as discussed in Chapter 2. Films of $[\text{Fe}(\text{HB}(\text{tz})_3)_2]$ with different thicknesses between 100 – 1000 nm were prepared on silicon substrates for the optical properties investigation. The optical constants (refractive index n and extinction coefficient k) of these films were determined by using a Filmetrics F20 film analyzer and a Horiba UVISEL ellipsometer. The former is based on the measurement of spectrum

intensity changes of normal incidence light reflected back from the surface, whereas the latter measures the change of polarization of the reflected light at various angles of incidence. In both cases, we used a Peltier stage (Linkam Scientific) to vary the sample temperature step-by-step in the range between 25 and 95 °C.

It is important to mention that neither spectral reflectance, nor spectroscopic ellipsometry are direct techniques. A dispersion model must be used to obtain thickness/optical properties of the thin films. The F20 instrument uses the Cauchy dispersion formula, which is a simple empirical dispersion law. When the material has no light absorption in the visible spectrum, it usually has “normal dispersion”, which means that the refractive index decreases monotonously with the increase of wavelength. The following equation relates the refractive index to the wavelength (in units of nm):

$$\begin{cases} n(\lambda) = A + \frac{10^4 B}{\lambda^2} + \frac{10^9 C}{\lambda^4} \\ k(\lambda) = 0 \end{cases} \quad \text{Eq.4.4}$$

where A is a dimensionless parameter: when $\lambda \rightarrow \infty$ then $n(\lambda) \rightarrow A$. B (in units of nm²) affects the curvature and the amplitude of the refractive index for medium wavelengths in the visible. C (in units of nm⁴) affects the curvature and amplitude for smaller wavelengths in the UV. Since nanometric films of [Fe(HB(tz)₃)₂] exhibit very low absorption in visible light range, we used the Cauchy dispersion model to fit the visible-NIR spectral range in the reflectance spectra.

The software of the UVISEL instrument implements various dispersion models. After a few trials, we decided to use the so-called “new amorphous dispersion” formula, which takes into account also the extinction and therefore the data analysis was extended to the UV spectral range. In this model, the refractive index and the extinction coefficient are given by:

$$n(\omega) = n_\infty + \frac{B(\omega - \omega_j) + C}{(\omega - \omega_j)^2 + \Gamma_j^2} \quad \text{Eq.4.5}$$

$$k(\omega) = \begin{cases} \frac{f_j(\omega - \omega_g)^2}{(\omega - \omega_j)^2 + \Gamma_j^2}; & \text{for } \omega > \omega_g \\ 0 & ; \text{for } \omega \leq \omega_g \end{cases} \quad \text{Eq.4.6}$$

where $B_j = \frac{f_j}{\Gamma_j}(\Gamma_j^2 - (\omega_j - \omega_g)^2)$ and $C_j = 2f_j\Gamma_j(\omega_j - \omega_g)$. n_∞ is an additional parameter, equal to the value of the refractive index when $\omega \rightarrow \infty$. f_j ($j = 1, 2, 3$) (in eV) is related to the strength (amplitude) of the extinction peak. Γ_j ($j = 1, 2, 3$) (in eV) is the broadening

term of the absorption peak. ω_j (in eV) is approximately the energy at which the extinction coefficient is maximum (peak of absorption). ω_g (in eV) is the energy band gap.

Figure 4.5a shows a typical spectral reflectance curve of a thick film of $[\text{Fe}(\text{HB}(\text{tz})_3)_2]$ displaying the undulating interference pattern. The film thickness and refractive index as a function of the temperature for a nominally 800 nm film is shown in Figures 4.5b and 4.5c, respectively. One can see an impressive change of the film thickness from *ca.* 765 nm in the LS state to *ca.* 825 nm in the HS state, denoting a *ca.* 7.8 % increase, which is fully reversible on cooling. In the same time, the refractive index drops from *ca.* 1.60 (LS) to 1.51 (HS) in an abrupt fashion around the spin transition temperature ($\sim 65^\circ\text{C}$).

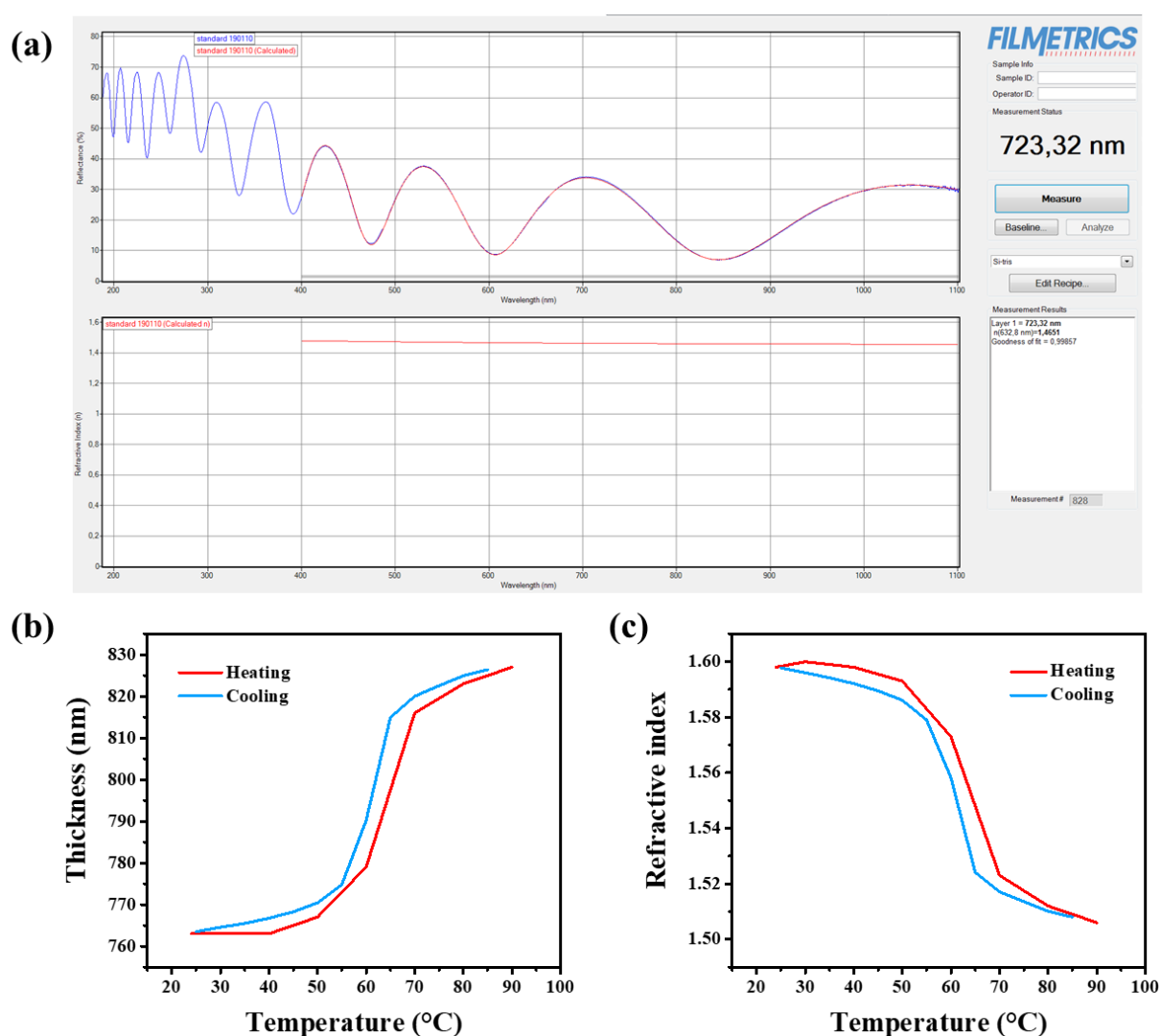


Figure 4.5: (a) Typical spectral reflectance of a nominally 720 nm film of $[\text{Fe}(\text{HB}(\text{tz})_3)_2]$. Variation of the thickness (b) and refractive index at $\lambda = 500$ nm (c) of a nominally 800 nm thick film of $[\text{Fe}(\text{HB}(\text{tz})_3)_2]$ upon heating and cooling.

Whereas the spectral reflectance method worked well for thick films, it failed to provide reliable data for thin films, which are more relevant in the context of the Fabry-Perot devices we fabricated. Ellipsometric data were therefore acquired on a 100 nm thick film of $[\text{Fe}(\text{HB}(\text{tz})_3)_2]$ for wavelengths between 250 and 1000 nm at various angles of incidence (AOI = 56–60°) and selected temperatures (25–95 °C).

Figure 4.6 a and b depict the obtained refractive index n and the extinction coefficient k , respectively, as a function of the wavelength. In the visible and near-infrared spectral regions, the extinction coefficient k remains negligibly low (below *ca.* 10^{-4}) through the whole temperature range. On the other hand, n exhibits ‘classical’ dispersion behavior – decreasing monotonously with increasing wavelength. Indeed, in the Vis-NIR region, only a few very weak ligand-field transitions occur in $[\text{Fe}(\text{HB}(\text{tz})_3)_2]$ with absorption coefficients in the order of 100 and 10 cm^{-1} in the LS and HS states, respectively. These weak absorption bands are hardly detectable even in micrometer thick films [177]. Below 350 nm, the extinction coefficient steeply increases and peaks at a value of 0.23 around 315 nm. Since k and n are interlinked, n exhibits ‘anomalous dispersion’. As we have already seen in Chapter 2, the associated strong UV absorption is assigned to charge-transfer transitions in the LS state and it can be conveniently used to probe the SCO phenomenon in the thin films.

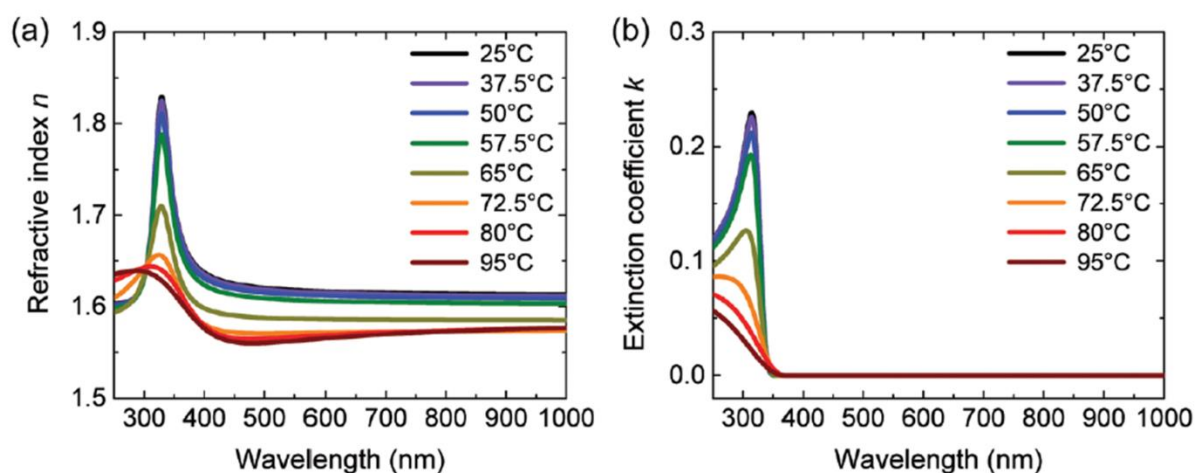


Figure 4.6: Ellipsometric characterization of a nominally 100 nm-thick film of $[\text{Fe}(\text{HB}(\text{tz})_3)_2]$: Refractive index (a) and extinction coefficient (b) acquired between 250–1000 nm at selected temperatures between 25 and 95 °C.

The temperature dependences of the refractive index n and film thickness L are depicted in Fig. 4.7a and b, respectively. These curves show a compelling correlation. Far from the spin transition, both n and t are weakly temperature dependent, in agreement with the nearly zero

thermal expansion coefficient of $[\text{Fe}(\text{HB}(\text{tz})_3)_2]$ [28]. Around the spin-transition temperature (65°C), the film thickness abruptly increases by $4.6(4)\%$, from $91.2(3)$ in the LS state to $95.4(2)$ nm in the HS state. This variation is in reasonable agreement with the $5.4(8)\%$ expansion of the orthorhombic c -axis of the unit cell upon the SCO revealed by single crystal X-ray diffraction [Rat2017]. (N.B. Remind that the film is oriented with the c -axis normal to the substrate.) On the other hand, the value of n concomitantly drops by *ca.* $0.2\text{--}0.04$ (depending on the wavelength) at the LS-to-HS transition. In particular, at 500 nm we extracted a change from $n=1.62$ to 1.56 when going from the LS to the HS state.

We notice that the two approaches (spectral reflectance and ellipsometry) has revealed similar trends, but there are also some notable differences. In particular, the film thickness change is estimated more accurately from ellipsometry and in the further work, we used these data with preference. Nevertheless, it is fair to say that further comparative measurements would be necessary to better understand the observed differences: whether they are linked to measurement/analysis uncertainties and/or to differences in sample properties.

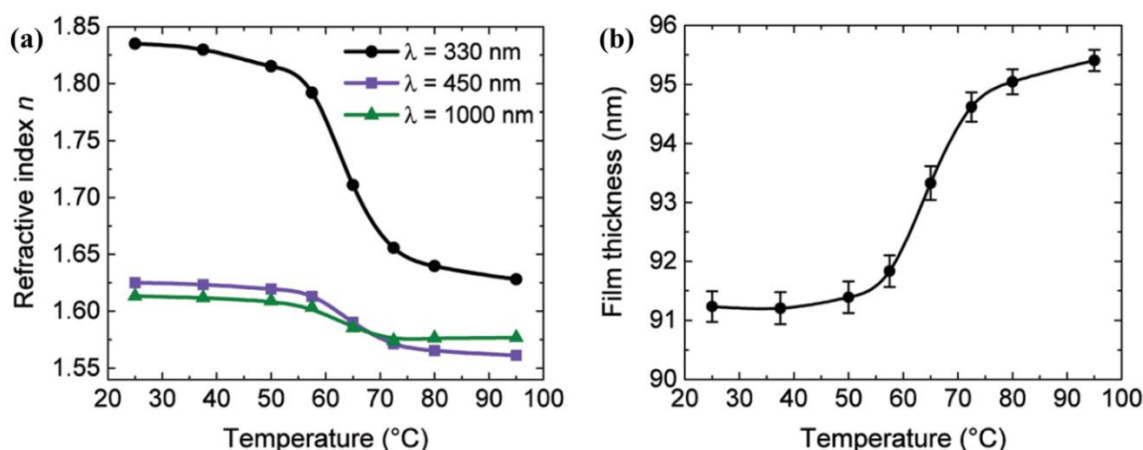


Figure 4.7: Ellipsometric characterization of a nominally 100 nm-thick film of $[\text{Fe}(\text{HB}(\text{tz})_3)_2]$. (a) Temperature dependence of the refractive index n at selected wavelengths (heating mode). (b) Variation of the film thickness L as a function of the temperature (heating mode).

4.4 SCO based Fabry–Perot cavities

4.4.1 Structure and design of SCO based Fabry–Perot cavities

To translate the impressive change of refractive index of $[\text{Fe}(\text{HB}(\text{tz})_3)_2]$ into a functional property, we fabricated metal-based, multilayer Fabry–Perot structures on glass substrates (Fig. 4.8).

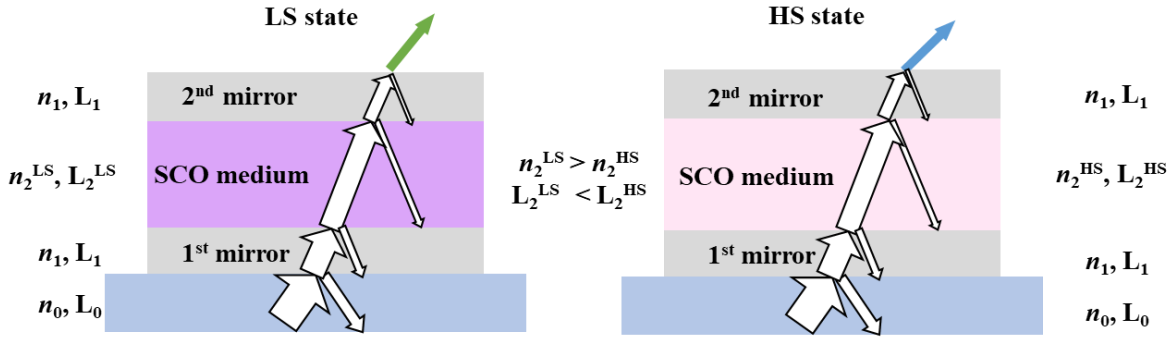


Figure 4.8: Schematic diagram of the SCO based Fabry–Perot cavity in the LS and HS states showing the change of optical thickness of the cavity due to the SCO phenomenon.

This thin-film Fabry-Perot filter is actually a multilayer structure, so the theory of optical properties of multilayer stacks is the basis for the design of this filter. As long as the thickness and refractive index of each layer of the system are known, assuming that the layers are smooth, planar and uniform, the transmittance and reflection at each specific incident angle and wavelength can be calculated by the repeated use of the Fresnel equations [178]. This so-called transfer matrix method is the most popular approach for investigating the optical properties of multilayer structures. A numerical algorithm of this method is implemented in the software of the Filmetrics F20 instrument, allowing us the simulation of the expected optical characteristics of the multilayer stacks. The design of the Fabry-Perot filter is the inverse problem, wherein we seek to find the optimal thickness of each film in the stack to achieve the highest possible change of the filter transmittance (or reflectance) due to the spin crossover phenomenon – taking into account also the polarization and angle of incidence (AOI) of the incoming light beam.

The design of the Fabry–Perot cavity was carried out by Stephane Calvez (LAAS-CNRS). The simulations took into account the optical properties of SCO thin film determined by ellipsometry. However, to simplify the calculations the refractive index of the SCO film was set to be 1.62 and 1.57 in the LS and HS states, respectively, for the whole wavelength range (*i.e.* neglecting the dispersion, which has only marginal effect). Due to our experimental constraints, we considered only the visible wavelength range between 400 and 700 nm as the operational range of the Fabry-Perot filter. Since we had extensive experience with the deposition of aluminum on our SCO film (see Chapter 2) we started the simulations using this metal, but we quickly turned to silver for its superior optical properties in the visible spectrum.

Figure 4.9 depicts the calculated reflection/transmission intensities, resonance wavelength and Q-factor of the Fabry-Perot device as a function of the thickness of the metal mirrors for both silver and aluminum. The thickness of the SCO layer was fixed to 115 nm. From these calculations it can be clearly seen that within the selected metal thickness range (10-100 nm), the transmission of the Ag-based cavity is always higher than that of the Al-based cavity. In particular, the transmission intensity of Al-cavity does not exceed 0.2 even for very low thicknesses (which become difficult to fabricate by conventional techniques) and it decreases to nearly zero above *ca.* 20 nm. Of course, the superior optical properties of silver are well known, but these simulations highlight that the operational window for Al mirror based resonators is extremely small. On the other hand, the Ag mirrors exhibit a significant transmittance: at a metal thickness of 50 nm, the transmission still has a value of *ca.* 0.2. However, it is important to notice that the Q-factor displays an opposite behavior: when the metal thickness increases, the Q-factor of the device increases. This means that one has to find a compromise between the transmission and the Q-factor of the cavity. From the data in Fig. 4.9, we can see that the optimal Ag thickness is approximately in the 40-60 nm range.

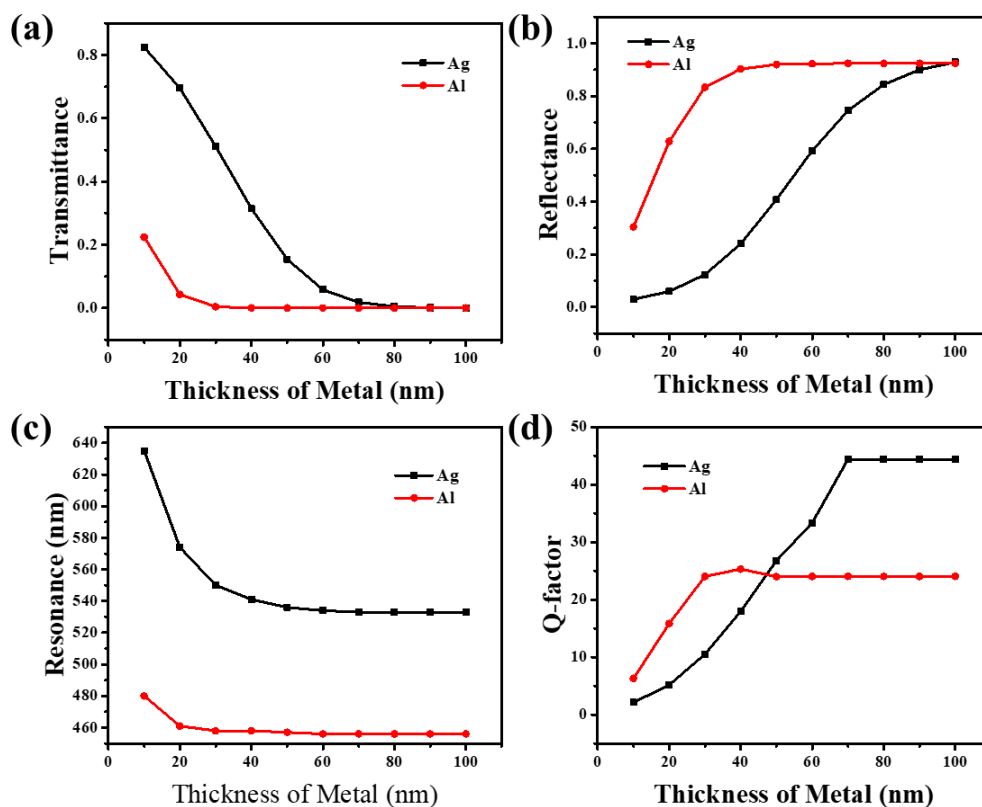


Figure 4.9: Calculated optical properties of M/SCO/M multilayer stacks (M = Al or Ag) for an SCO thickness of 115 nm: (a) transmittance, (b) reflectance (c) resonance wavelength and (d) Q-factor as a function of the metal mirror thickness.

Figure 4.10 depicts the reflection/transmission intensities and the Q-factor of a Ag/SCO/Ag cavity as a function of the thickness of the SCO layer. The thickness of the metal mirrors was fixed to 50 nm. In these figures, we select systematically the resonance peak, which falls in the 350-700 nm wavelength range, which is compatible with our experimental setup. These calculations reveal that we can adjust the SCO film thickness in a fairly broad range without much deteriorating the performance. This is an important property because the cavity resonance is adjusted primarily by changing the cavity thickness (see Eq. 4.3). One can also note in Figure 4.10 that the cavity transmittance shows an opposite trend to the Q-factor as a function of the thickness of the SCO film. Again, we can identify an optimal range between *ca.* 100-130 nm allowing for a compromise between these two parameters.

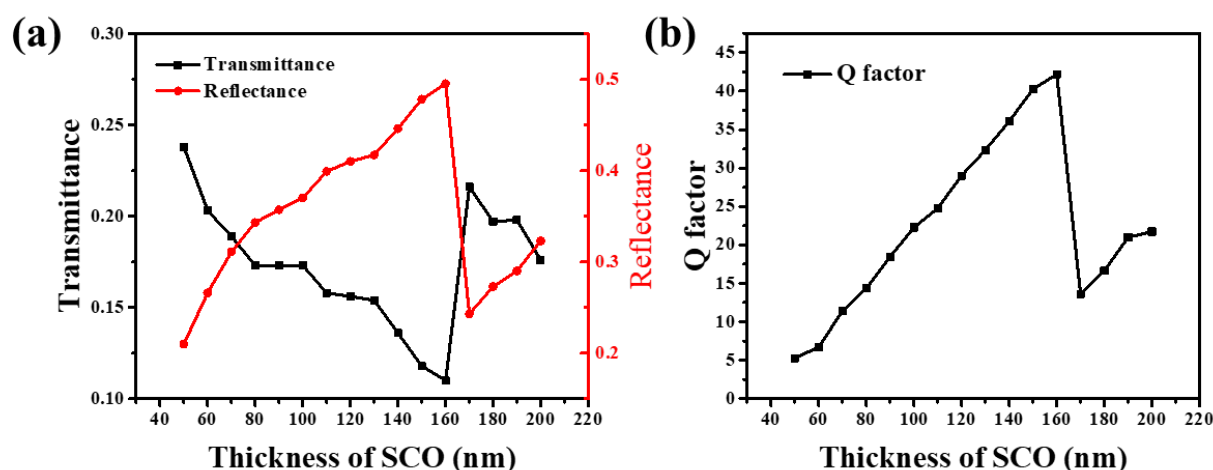


Figure 4.10: Theoretical calculations of a SCO based Fabry–Perot cavity with 50 nm thick silver layers. (a) transmittance/reflectance and (b) Q-factor as a function of SCO thickness.

Overall, since SCO based Fabry–Perot cavity with Ag reflectors seems to have a better performance in the selected wavelength range (reflection, transmission, Q-factor, etc.) and taking all numerical results into consideration, we chose for the experimental work a configuration of 50 nm Ag/115 nm SCO/50 nm Ag on a glass (AF32) substrate.

4.4.2 Effect of SCO on the cavity resonance: simulation results

Figure 4.11 shows the modulation depth induced by the switching between LS and HS states (defined in reflection as $|R_{HS}-R_{LS}|$) for an Ag/115 nm SCO/Ag stack at normal incidence. These types of plots can be used to search for the optimum conditions where the SCO allows for the highest possible change of reflectance (or transmittance) of the cavity. For example, in

the particular case shown in this figure, one can expect the highest modulation depth around 530 nm achieved with a mirror thickness between 50-60 nm.

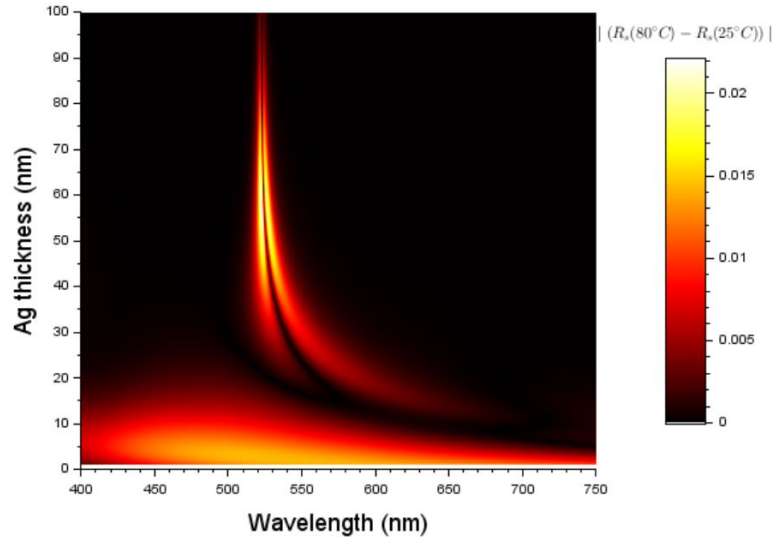


Figure 4.11: Modulation depth $|R_{HS}-R_{LS}|$ for an Ag/115 nm SCO/Ag stack at AOI=0°.

The simulated reflectance and transmittance spectra of the 50nm Ag/115 nm SCO/50 nm Ag Fabry–Perot cavity is shown in Figure 4.12 for two ‘extreme’ angles of incidence (0° and 85°). In the simulations, we considered unpolarized light impinging on the device. The refractive index of the SCO film was set to 1.62 and 1.57 in the LS and HS states, respectively, and we considered an expansion of the cavity thickness by 4.6% in the HS state. Due to the variation of the optical thickness of the SCO material between the HS and LS states, the reflection and transmission properties of the cavity change. However, these changes strongly depend on the experimental conditions.

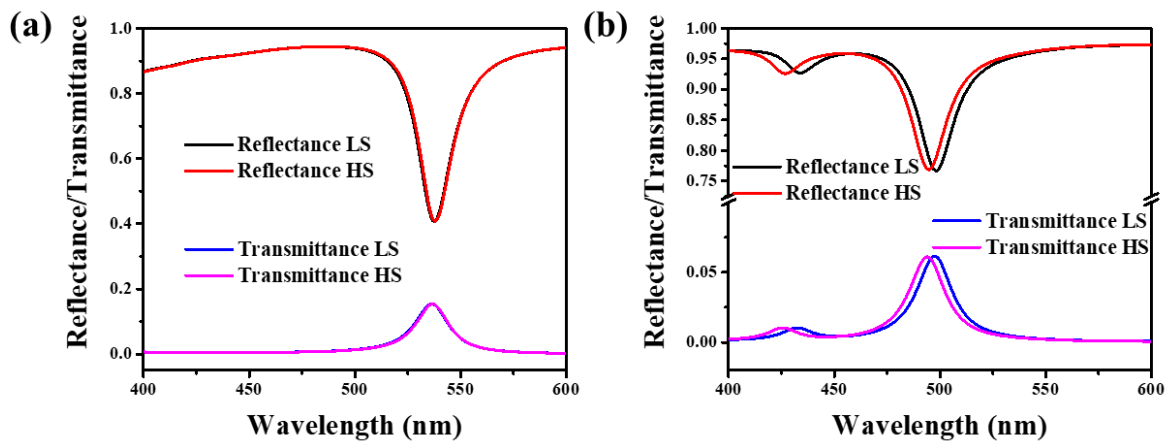


Figure 4.12: Simulated reflectance and transmittance spectra (unpolarized light) of a 50 nm Ag/115 nm SCO/50 nm Ag stack in the LS and HS states for (a) AOI=0° and (b) AOI = 85°.

At normal incidence ($\text{AOI} = 0^\circ$), a single resonant peak is observed around *ca.* 537 nm. Neither the spin state of the cavity nor the polarization of the light beam appear to have any considerable effect. However, for higher angles of incidence ($\text{AOI} = 85^\circ$) one can observe two resonance peaks, which can be attributed to the two different light polarizations: transverse electric (TE) and transverse magnetic (TM). For TM polarization, the resonance appears respectively around 498 and 494 nm in the LS and HS states, denoting an SCO-induced wavelength modulation of *ca.* 4 nm. For TE polarization, the effects are even more spectacular, the resonance wavelength downshifts by 8 nm from 433 to 425 nm when going from the LS to the HS state.

4.4.3 Effect of SCO on the cavity resonance: experimental results

We used vacuum thermal evaporation to deposit successively Ag, $[\text{Fe}(\text{HB}(\text{tz})_3)_2]$ and Ag layers under a base pressure of *ca.* 5×10^{-7} Torr. Before the deposition of the second silver layer, the SCO film was water vapor annealed to render it more crystalline (see Chapter 2 for details). The target configuration of the device was 50 nm Ag/115 nm SCO/50 nm Ag on a glass substrate. A photo of a device is shown in Figure 4.13.

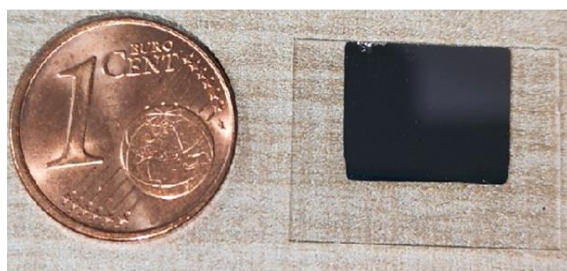


Figure 4.13: Photo of an Ag/SCO/Ag stack.

The normal incidence (angle of incidence, $\text{AOI} = 0^\circ$) transmittance of the cavities was first assessed as a function of the temperature using a Cary50 UV-VIS spectrophotometer and a Linkam THM600 variable temperature stage. Then, the variable-incidence ($\text{AOI} = 8-60^\circ$) reflectance spectrum of the cavity was subsequently qualified, for both transverse electric (TE) and transverse magnetic (TM) polarizations, using a PerkinElmer Lambda 950 spectrophotometer equipped with an universal reflectance accessory (URA). This accessory has its own kinematic detector module and path length compensator, maintaining identical path lengths and angles of incidence between the background and the sample measurement. URA-based measurements include a sample measurement, which involves another reflection at the sample, and a baseline measurement. This is illustrated in the case of measurement at 70°

incidence, as shown in Figure 4.14. Even if the URA can provide absolute reflectance values, we have systematically recorded also a reference reflectance spectrum of a broadband dielectric mirror (Thorlabs BB2-E02) displaying *ca.* 99% reflectance between 400-800 nm with minor dependence on wavelength, polarization and AOI of the incident light (Fig. 4.15a).

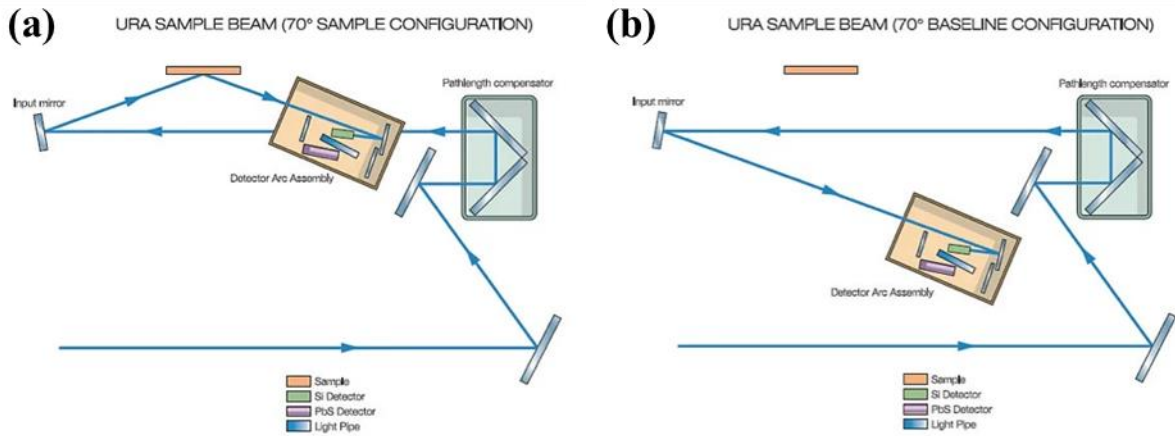


Figure 4.14: URA sample (a) and baseline (b) measurement configurations at AOI = 70°.

The sample compartment region of the Lambda 950 is also equipped with a polarization drive accessory, fitted with a film polarizer (Perkin Elmer B2205022), allowing for automated switching between 0° and 90° polarization angles. This polarizer displays reasonably flat transmission between *ca.* 420 - 700 nm with a polarization efficiency superior to 99%. Due to the particular geometry of the sample holder of the URA, we could not use the usual Linkam heating-cooling stage for these experiments. Instead, we have mounted the samples ‘upside down’ using a thermally-conductive double-sided adhesive tape (Thorlabs, TCDT-1) on a Peltier module (Radiospares) powered by a stabilized current source. The temperature of the sample was measured by a K-type thermocouple.

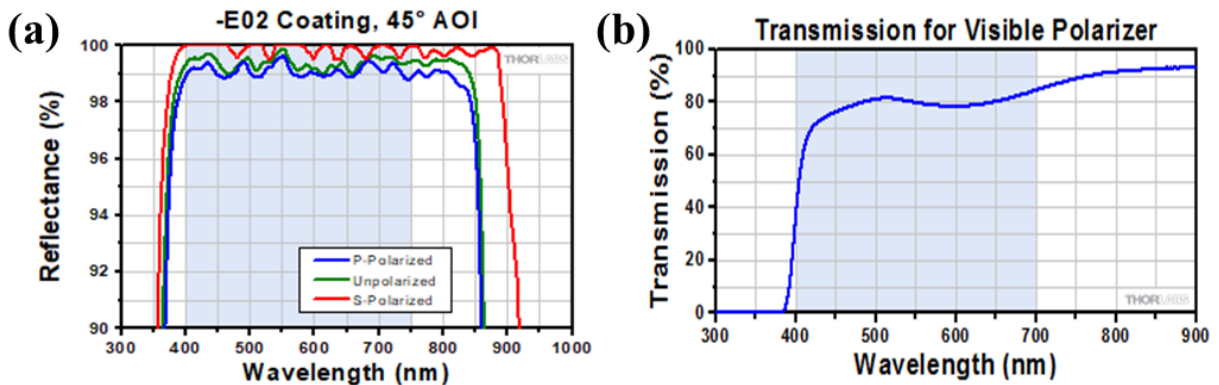


Figure 4.15. Spectral characteristics of (a) the reference mirror and (b) the polarizer used in the reflectance measurements.

Figure 4.16a shows the normal incidence transmittance spectra of an Ag/SCO/Ag stack recorded at various temperatures between 30-100 °C. One can clearly depict two transmittance peaks, one near 529 nm, which can be unambiguously associated with the cavity resonance and another peak near 329 nm, which is associated with the silver plasma frequency [179]. Fortuitously, this second, intrinsic transmittance window of the Ag films closely coincides with the LS absorption peak of $[\text{Fe}(\text{HB}(\text{tz})_3)_2]$ centered at 318 nm. This allowed us to observe the optical absorbance change in the Fabry-Perot cavity upon the spin transition (see Fig. 4.16b) – similar as we have seen for the neat films in Chapter 2.

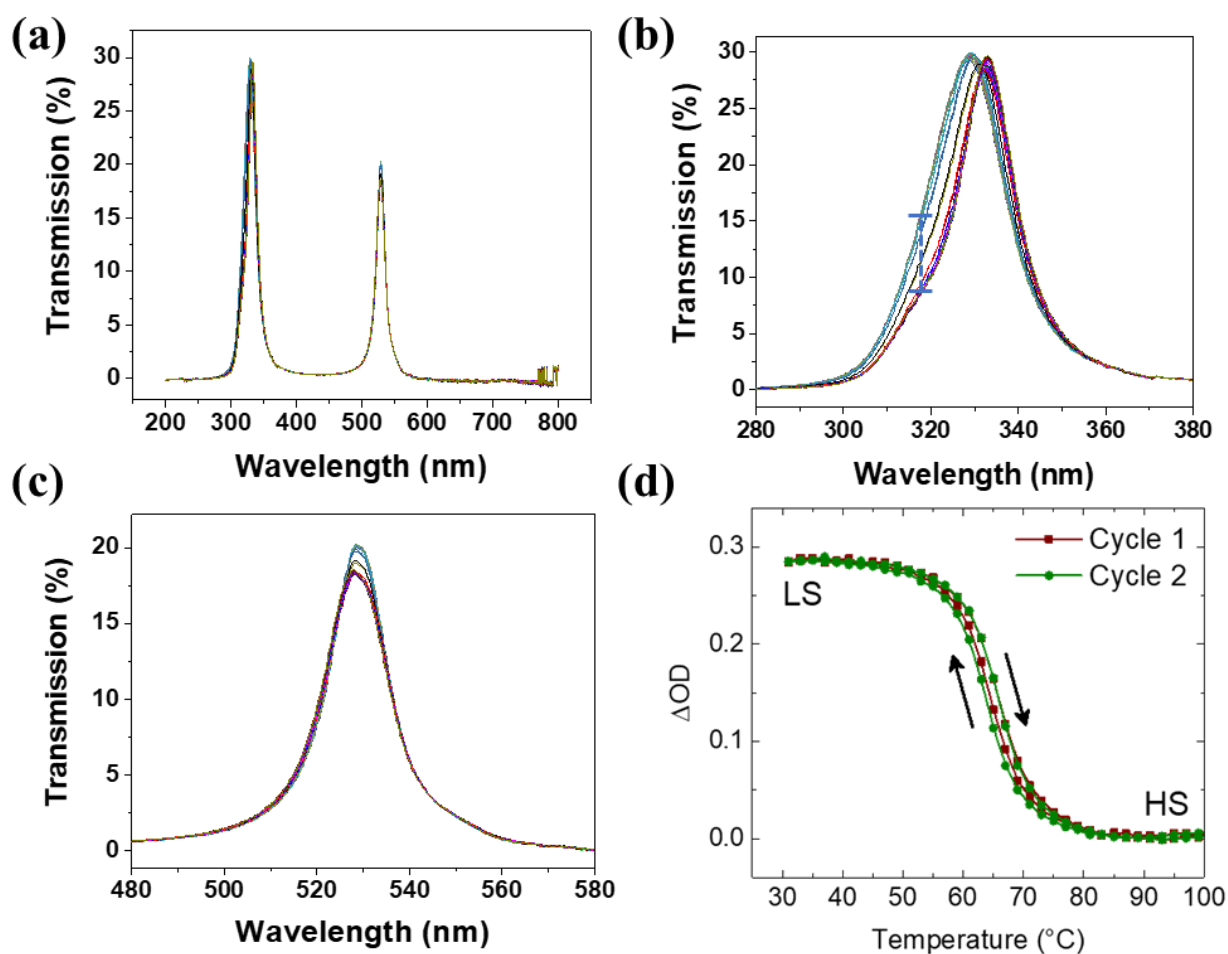


Figure 4.16: Normal incidence transmittance spectra of Ag (50 nm)/SCO (115 nm)/Ag (50 nm) stacks acquired between 30 and 100 °C. (a) Full spectrum and zoom on the peaks near (b) 329 nm and (c) 529 nm. (d) Temperature dependence of the optical density change of the cavity ($\lambda = 318$ nm, normal incidence, non-polarized light) along two heating-cooling cycles at 2 °C min^{-1} scan rate. (The dashed line in 4.16b shows the corresponding transmittance data.)

As shown in Figure 4.16d, the spin transition in the cavity occurs in a reproducible and abrupt fashion near 65 °C. The total absorbance change ($\Delta\text{OD} = 0.29$ at 318 nm) indicates that

the spin transition is nearly complete in the 115 nm-thick film. These results unambiguously confirm that the presence of the Ag films – below and on top of the SCO layer – does not substantially affect the spin-transition properties. (N.B. This observation was confirmed for four Fabry–Perot devices.) Intriguingly, a zoom on the visible resonance peak (Fig. 4.16c) reveals that the peak transmittance varies also with the temperature (*i.e.* with the spin state). This phenomenon has not been predicted in the design simulations, as they did not include the thermo-optic dependence apart from the index switching. Furthermore, the weak ligand-field absorption of $[\text{Fe}(\text{HB}(\text{tz})_3)_2]$ near 540 nm, characteristic of the LS state, had not been considered in the simulations either. Indeed, taking into account the thickness of the SCO film (115 nm) and the coefficient of absorption associated with this band (*ca.* 100 cm^{-1}) no detectable absorbance change is expected at this wavelength ($\Delta A = 0.0011$). Yet, one should take into account the quality factor of the cavity ($Q = 36$), which shows that the resonant photon is reflected forth and back many times within the SCO layer, increasing thus the ‘effective thickness’ of the SCO film. We therefore suggest that the detected absorbance change at 529 nm ($\Delta A = 0.045$) corresponds to a cavity-induced enhancement of the absorber thickness. This observation provides thus an interesting scope for probing the SCO in ultrathin films, which is a current challenge in this research field.

In the next step, we examined the variable angle reflectance spectra of the Ag/SCO/Ag stacks. Figure 4.17a shows representative reflectance spectra of the cavities recorded in the LS (25 °C) and HS (80 °C) states at selected angles of incidence under TE polarized illumination. On the other hand, Figure 4.17b compares the cavity reflectance for TE and TM polarizations at a fixed AOI (60°). As predicted in the simulations (Fig. 4.12), the Ag/SCO/Ag multilayer structure exhibits pronounced resonances with a significant dependence on both the AOI and the polarization state of the impinging light wave. This combined effect of AOI and polarization is more clearly depicted in the dispersion curve of the cavity shown in Figure 4.17c. Again, we note the good correspondence with the simulation results. Importantly, the resonance peaks display a blue shift when going from the LS to the HS state. This shift can be better appreciated in Figure 4.17d, which shows a detailed temperature scan (for AOI=45° and TE polarization). The largest shift we could observe at the SCO was *ca.* 8 nm for AOI 60° at TE polarization. As shown by Fig. 4.17b, this wavelength shift translates into a cavity reflectance modulation by *ca.* 30 %.

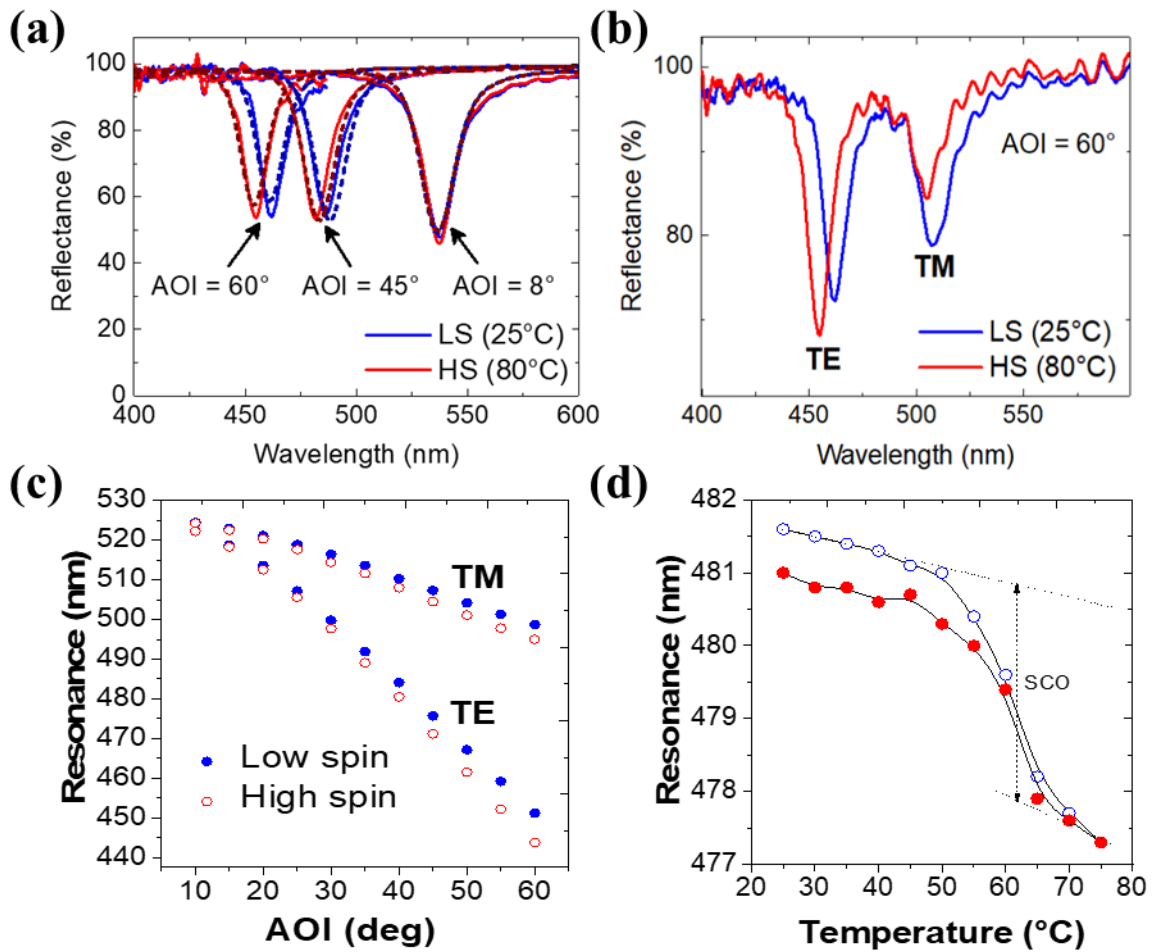


Figure 4.17: Optical properties of Ag (50 nm)/SCO (115 nm)/Ag (50 nm) multilayer Fabry–Perot cavities. (a) Reflectance spectra at selected AOI values in the two spin states for TE polarization. (b) Reflectance spectra at a fixed AOI of 60° in the two spin states for TE and TM polarizations. (c) Dispersion curves in the two spin states for TE and TM polarizations. (d) Cavity resonance (TE polarization, AOI = 45°) as a function of temperature for a complete heating – cooling cycle.

We shall note that in the first experiments the temperature dependence of the resonance was not fully reversible along a complete heating-cooling cycle (Fig. 4.17d). This observation is not related to the SCO itself, which is fully reproducible (see Fig. 4.16d). Instead, we believe it is an experimental artifact linked to the rather rudimentary heating-cooling setup – involving an adhesive tape in between the sample and the heater. For this reason, and also with the aim to extend our experimental capabilities, we have constructed a new optical setup (Figure 4.18a), comprising a fibered halogen lamp (400-1000 nm), a collimator, a film polarizer, a heating-cooling stage (Linkam Scientific PE120) mounted on a rotating stage, a collector lens and a fiber coupled spectrograph (BW Tek BTC112E). The latter has a detection wavelength range

between 400 - 750 nm. The first advantage of this setup (vs. the previous experimental bench) is that it allows us to collect not only reflectance, but also transmittance data as a function of the angle and polarization state of the incident light beam. Furthermore, it allows running automated and detailed temperature scans between 20 and 120 °C. In order to assess the reproducibility of the fabrication process we have prepared a new batch of Ag/SCO/Ag cavities, aimed to display the same characteristics as the first batch. Figure 4.18b show the room temperature dispersion curve of a new cavity acquired in reflection mode. The comparison with the data shown in Figure 4.17c is compelling: the dispersion curves are closely matching each other (with 3-4 nm deviation). With the new setup, the dispersion was also recorded in transmission mode as shown by Figure 4.18c. Last but not least, Figure 4.18d depicts two successive heating – cooling cycles recorded at temperature scan rates of ± 2 °C/min at a high sampling rate (1 spectrum/°C) for AOI=55° and TM polarization. One can observe a sharp drop of the resonance wavelength at the spin transition (by *ca.* 3 nm), which is perfectly reproducible between the two thermal cycles.

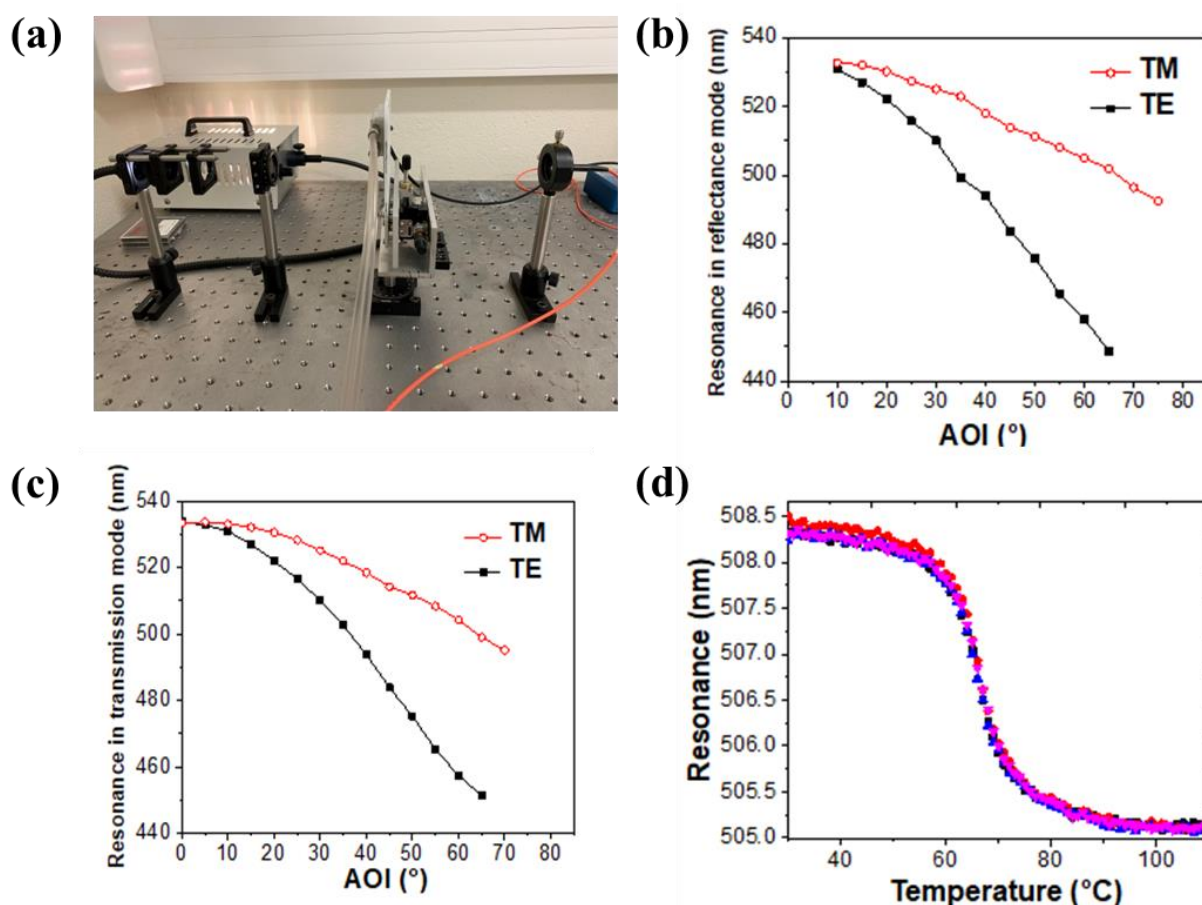


Figure 4.18: (a) Photo of the custom-built optical characterization bench. (b-c) Room temperature dispersion curves of the cavity (2nd fabrication batch) for TE and TM polarizations

recorded in reflectance (b) and transmittance (c) modes. (d) Cavity resonance (TM polarization, AOI = 55°) as a function of temperature for two successive heating – cooling cycles.

4.5 Conclusions and perspectives

In summary, we have shown that thin films of the molecular SCO complex [Fe(HB(tz)₃)₂] exhibit a substantial change of their refractive index ($\Delta n = 0.04 - 0.2$) in the UV-Vis-NIR spectral ranges upon the spin transition, whereas absorption losses remain negligible ($k \leq 10^{-4}$) for wavelengths above *ca.* 350 nm. Using transfer matrix calculations, we simulated the expected optical characteristics of metal/SCO/metal multilayer stacks with different layer thicknesses, which has led us to suggesting an optimal device configuration consisting of 50 nm thick silver mirrors in between a 115 nm SCO layer is embedded. The overall aim was to achieve a Fabry-Perot cavity with a resonance located in visible light range associated with reasonably high transmittance and Q-factor. High-quality films of [Fe(HB(tz)₃)₂] were then incorporated in between silver layers by vacuum thermal evaporation. The resulting Fabry-Perot cavities were characterized for their reflectance and transmittance properties through the visible spectral range at variable temperatures and for different polarizations and angles of incidence. Most importantly, the cavities displayed spectrally tunable resonances (up to 8 nm shift) allowing for *ca.* 30% transmittance modulation (at a fixed wavelength). These changes were traced back – using simulations – to the refractive index and film thickness changes upon the spin transition. The present results, together with the previously demonstrated fast switching speed [177] and high cycling endurance [180] of the films (under ambient conditions), demonstrate that the quality of spin crossover nanomaterials has reached today performance thresholds, which qualify them as viable technological solutions for demanding photonic applications. As such, this work opens up prospects for a wealth of reconfigurable and self-adaptive applications, including spatial light modulators, photonic integrated circuits and tunable optical components – with particular relevance for the visible wavelength range wherein other families of phase change materials fall short.

An immediate perspective of this work would be to design and fabricate resonators with higher Q factors allowing for large transmittance/reflectance modulation amplitudes at the SCO. Of particular interest would be for us the fabrication of gratings and other micro/nano-patterned structures incorporating the SCO complex [Fe(HB(tz)₃)₂]. To this aim, we have already launched a collaboration with the service TEAM of LAAS-CNRS (David Bourrier) with whom we designed, fabricated and tested Ni-based shadow masks. As shown in [Annex 4...](#), we

successfully deposited patterned Al and SCO films by vacuum thermal evaporation through the openings of the masks with a spatial resolution as high as 1 μm . These preliminary results open notably the way to construct optical waveguides, guided-mode resonance gratings and other devices incorporating a thin layer of evaporable SCO compounds. This work is ongoing in collaboration between the LCC and LAAS CNRS.

General conclusions and perspectives

There have been several decades, since Olivier Kahn proposed and foreseen the potential integration of spin crossover molecules into electronic devices. Indeed, spin crossover materials exhibit interesting assets for technological applications due to their bistable physical properties (optical, magnetic, electric, ...) and because of the fact that the spin state switching can be triggered by various external stimuli, such as temperature, pressure, light and X-ray irradiation, intense magnetic fields, or the inclusion of solvent/guest molecules (*i.e.* chemical stimuli). These properties along with fast switching speed and the versatility of these materials (several hundreds SCO compounds known), make them appealing for different applications, including switches, memories, displays, sensors, actuators and so forth. Notably, several research teams have been working in the past decades to incorporate SCO materials in electronic devices and there are several remarkable outcomes. However, it is fair to admit that, we are still at an initial stage in transferring the SCO properties into different device forms as well as in understanding the relevant physical mechanisms. In addition, device lifetime/fatigability is increasingly considered as an important issue from the point of view of 'real-world' applications. Starting from these motivations, the thesis was constructed aiming for integrating SCO materials as thin films into different devices (configurations), building the connection between the SCO phenomenon and device characteristics, investigating the factors that influence SCO-based electronic device lifetime and digging out the protocols with a comprehensive understanding of above points to improve the general performance.

Thanks to the recent progress in our team with high quality, crystalline thin films of the SCO complex $[\text{Fe}(\text{HB}(\text{tz})_3)_2]$, displaying robust, above room temperature SCO, we have successfully integrated these thin films via vacuum thermal evaporation into different fundamental device configurations, which were implemented in collaboration with the microtechnology platform of the LAAS-CNRS.

For the first experimental step, we built two-terminal, large-area, multilayer ITO/SCO/Al electronic junctions to investigate their resistance switching functionality. We examined various details, including the synthesis route, purification methods, preparation of substrates, thin film deposition, post-deposition treatments, device encapsulation, characterization protocols, *etc.*, in order to obtain the best device performance. As a result, we could observe a resistance switching due to the SCO phenomenon, up to three orders of magnitude, in devices with a 100 nm thick SCO layer. Remarkably, the junctions are rather robust and we have shown

that the resistance switching property can be preserved even after storage in the ambient environment for one year without encapsulation. These junctions exhibited a high resistance to fatigability (high endurance towards temperature cycling), with a considerable and stable ON/OFF resistance switching ratio during more than 10,000 switching events. We found that the key parameters to attain this switching stability are the reduced working temperature range ($< \sim 80^{\circ}\text{C}$) and constant voltage bias. We also gave an insight into the transport mechanism of the devices by replacing the cathode material. Despite the fact that the work functions of Al and Ca are very different (providing thus very different electron injection barriers), the junction performance appears quite similar with comparable ON/OFF resistance switching ratios, which indicates that bulk limited transport is the dominating mechanism in our devices. One interesting perspective of this work would be to correlate the charge transport properties with crystalline orientation of the films. Another important perspective would be the investigation of multilayer junctions with different film thicknesses, down to a few nanometers in order to reach a charge transport regime, which is not dominated by the bulk transport properties of the SCO film.

We also integrated $[\text{Fe}(\text{HB}(\text{tz})_3)_2]$ thin films into a spin valve device configuration with two magnetic electrodes. At the present stage of our work, we could not yet evidence any magnetoresistance property, neither a clear effect of the SCO on the device electrical properties. Nevertheless, we believe these devices represent a promising platform for further work towards new spintronic material combinations and functionalities.

In the next step of our experiments, SCO materials have been integrated into functional OFETs. This type of the three-terminal devices represent an inspiring topic with an increase of design freedom in comparison with simple two-terminal diode configurations. Indeed, in our experiments, we could investigated different OFET configurations. For the bottom-gate bottom-contact OFETs, we came across a technical problem to insert the SCO film in between the OSC and the dielectric layers without depositing the SCO molecules on the drain/source electrodes, leaving the resulting device rather insulating. Nevertheless, we devised that this issue could be solved later by depositing the drain/source electrodes after SCO deposition or by using a shadow mask. In our work, to avoid this problem, we have chosen to work with bottom-gate top-contact OFETs. We performed an in depth investigation of device stability and we were able to establish measurement protocols, which allowed us to minimize the device degradation to an acceptable level. The comparison of the temperature dependence of the drain-source current and of the threshold voltage either in the presence or in the absence of the SCO

film revealed small, but significant differences. Further work should confirm to what extent these differences could be linked to the SCO phenomenon. Future prospects include the use of more robust organic semiconductors in conjunction with the use of SCO materials, which display a room temperature spin transition with hysteresis as well as an important change of its dielectric permittivity. These properties could give rise not only to better device stability, but also to a very useful applicative possibility, which is a non-volatile memory effect.

Capitalizing on the expertise gained during the development of multilayer metal/[Fe(HB(tz)₃)₂]/metal stacks, we have also developed SCO-based optical cavities that exhibit switchable optical properties. First, we have shown that the [Fe(HB(tz)₃)₂] films exhibit a substantial change of their refractive index upon the spin transition, whereas they preserve their good transparency for VIS-NIR wavelengths. Using the measured optical constants, we performed calculations to simulate and predict the characteristics of metal/[Fe(HB(tz)₃)₂]/metal Fabry-Perot cavities. Based on these calculations, the device configuration was set to 50 nm Ag/115 nm SCO/50 nm Ag with a resonance located in the visible spectral range and associated with reasonably high transmittance and Q-factor. The fabricated cavities displayed spectrally tunable resonances (up to 8 nm shift) upon the spin transition, which could be traced back to the refractive index and film thickness changes associated with the SCO. This work opens up prospects for a wealth of reconfigurable and self-adaptive applications, including spatial light modulators, photonic integrated circuits and tunable optical components – with particular relevance for the visible wavelength range wherein other families of active optical materials are less performant. In future work, we seek to construct optical waveguides, guided-mode resonance gratings and other photonic devices incorporating a thin layer of evaporable SCO compounds.

To conclude, we have successfully incorporated SCO materials into two-/three-terminal electronic devices and photonic devices. As such, this work provides a small brick to the different efforts towards the transformation of SCO compounds from a scientific curiosity to engineering materials. Although there remains myriad of unknowns worth to explore in these topics, we can prophesy a broad window for SCO-based technologies. In particular, our results revealed that some of the SCO-based devices exhibit fully predictable device performance (e.g. Fabry Perot cavities) as well as quite considerable cycling endurance in operational mode (e.g. resistance switching junctions), which are undoubtedly quite significant issues for any ‘real-world’ application. We believe in a not far future, with the continuous efforts and deep

investigations from physicists, chemists and engineers, SCO molecules will make their way out of academia.

References

- [1] Shalabaeva, V., Rat, S., Manrique-Juarez, M. D., Bas, A. C., Vendier, L., Salmon, L., ... & Bousseksou, A. (2017). Vacuum deposition of high-quality thin films displaying spin transition near room temperature. *Journal of Materials Chemistry C*, 5(18), 4419-4425.
- [2] Hauser, A. (2004). Ligand field theoretical considerations. *Spin Crossover in Transition Metal Compounds I*, 49-58.
- [3] Gütlich, Philipp, Andreas Hauser, and Hartmut Spiering. "Thermal and optical switching of iron (II) complexes." *Angewandte Chemie International Edition in English* 33.20 (1994): 2024-2054.
- [4] Gütlich, P., & Goodwin, H. A. (Eds.). (2004). *Spin crossover in transition metal compounds I* (Vol. 233, pp. 1-47). Berlin: Springer.
- [5] Gütlich, P., & Goodwin, H. A. (Eds.). (2004). *Spin Crossover in Transition Metal Compounds II* (Vol. 234). Berlin: Springer.
- [6] Gütlich, P., & Goodwin, H. A. (Eds.). (2004). *Spin Crossover in Transition Metal Compounds III* (Vol. 235). Berlin: Springer.
- [7] Nicolazzi, William, and Azzedine Bousseksou. "Thermodynamical aspects of the spin crossover phenomenon." *Comptes Rendus Chimie* 21.12 (2018): 1060-1074.
- [8] Kahn, Olivier, and C. Jay Martinez. "Spin-transition polymers: from molecular materials toward memory devices." *Science* 279.5347 (1998): 44-48.
- [9] Gütlich, Philipp, Ana B. Gaspar, and Yann Garcia. "Spin state switching in iron coordination compounds." *Beilstein journal of organic chemistry* 9.1 (2013): 342-391.
- [10] Gütlich, P., Hauser, A., & Spiering, H. (1994). Thermal and optical switching of iron (II) complexes. *Angewandte Chemie International Edition in English*, 33(20), 2024-2054.
- [11] Halcrow, M. A. (2011). Structure: function relationships in molecular spin-crossover complexes. *Chemical Society Reviews*, 40(7), 4119-4142.
- [12] Gaspar, A. B., Molnár, G., Rotaru, A., & Shepherd, H. J. (2018). Pressure effect investigations on spin-crossover coordination compounds. *Comptes Rendus Chimie*, 21(12), 1095-1120.
- [13] Varret, F., Bleuzen, A., Boukheddaden, K., Bousseksou, A., Codjovi, E., Enachescu, C., ... & Verdaguer, M. (2002). Examples of molecular switching in inorganic solids, due to temperature, light, pressure, and magnetic field. *Pure and applied chemistry*, 74(11), 2159-2168.
- [14] Hauser, A. (1995). Intersystem crossing in iron (II) coordination compounds: a model process between classical and quantum mechanical behaviour. *Comments on Inorganic Chemistry*, 17(1), 17-40.
- [15] Hayami, S., Gu, Z. Z., Shiro, M., Einaga, Y., Fujishima, A., & Sato, O. (2000). First observation of light-induced excited spin state trapping for an iron (III) complex. *Journal of the American Chemical Society*, 122(29), 7126-7127.
- [16] Roux, C., Zarembowitch, J., Gallois, B., Granier, T., & Claude, R. (1994). Toward ligand-driven light-induced spin changing. Influence of the configuration of 4 styrylpyridine (stpy) on the magnetic properties of FeII (stpy) 4 (NCS) 2 Complexes. crystal structures of the spin-crossover species Fe (trans-stpy) 4 (NCS) 2 and of the high-spin species Fe (cis-stpy) 4 (NCS) 2. *Inorganic Chemistry*, 33(10), 2273-2279.

- [17] Ksenofontov, V., Gaspar, A. B., Levchenko, G., Fitzsimmons, B., & Gülich, P. (2004). Pressure effect on spin crossover in [Fe(phen)₂(NCS)₂] and [CrI₂(depe)₂]. *The Journal of Physical Chemistry B*, 108(23), 7723-7727.
- [18] Bousseksou, A., Molnár, G., Salmon, L., & Nicolazzi, W. (2011). Molecular spin crossover phenomenon: recent achievements and prospects. *Chemical Society Reviews*, 40(6), 3313-3335.
- [19] Vef, A., Manthe, U., Gülich, P., & Hauser, A. (1994). Intersystem crossing dynamics in the spin-crossover systems [M: Fe(pic)₃]Cl₂·Sol (M= Mn or Zn, Sol= MeOH or EtOH). *The Journal of chemical physics*, 101(11), 9326-9332.
- [20] Guionneau, P. (2014). Crystallography and spin-crossover. A view of breathing materials. *Dalton Transactions*, 43(2), 382-393.
- [21] Tuchagues, J. P., Bousseksou, A., Molnár, G., McGarvey, J. J., & Varret, F. (2004). The role of molecular vibrations in the spin crossover phenomenon. *Spin Crossover in Transition Metal Compounds III*, 84-103.
- [22] Kumar, K. S., & Ruben, M. (2017). Emerging trends in spin crossover (SCO) based functional materials and devices. *Coordination Chemistry Reviews*, 346, 176-205.
- [23] Molnár, G., Rat, S., Salmon, L., Nicolazzi, W., & Bousseksou, A. (2018). Spin crossover nanomaterials: from fundamental concepts to devices. *Advanced Materials*, 30(5), 1703862.
- [24] Kipgen, L., Bernien, M., Tuzek, F., & Kuch, W. (2021). Spin - Crossover Molecules on Surfaces: From Isolated Molecules to Ultrathin Films. *Advanced Materials*, 2008141.
- [25] Salmon, Lionel, and Laure Catala. "Spin-crossover nanoparticles and nanocomposite materials." *Comptes Rendus Chimie* 21.12 (2018): 1230-1269.
- [26] Soyer, H., et al. "Spin Crossover of a Langmuir–Blodgett Film Based on an Amphiphilic Iron (II) Complex." *Langmuir* 14.20 (1998): 5890-5895.
- [27] Cobo, Saioa, et al. "Multilayer sequential assembly of thin films that display room - temperature spin crossover with hysteresis." *Angewandte Chemie* 118.35 (2006): 5918-5921.
- [28] Rat, Sylvain, et al. "Coupling mechanical and electrical properties in spin crossover polymer composites." *Advanced Materials* 30.8 (2018): 1705275.
- [29] Matsuda, Masaki, and Hiroyuki Tajima. "Thin film of a spin crossover complex [Fe(dpp)₂](BF₄)₂." *Chemistry Letters* 36.6 (2007): 700-701.
- [30] Manrique - Juárez, María D., et al. "Micromachining - Compatible, Facile Fabrication of Polymer Nanocomposite Spin Crossover Actuators." *Advanced Functional Materials* 28.29 (2018): 1801970.
- [31] Benchohra, Amina. Magnetic molecular switches: from their synthesis to their integration into hybrid (nano) materials. Diss. Sorbonne université, 2019.
- [32] Piedrahita-Bello, Mario, et al. "Mechano-electric coupling in P(VDF-TrFE)/spin crossover composites." *Journal of Materials Chemistry C* 8.18 (2020): 6042-6051.
- [33] Mallah, Talal, and Massimiliano Cavallini. "Surfaces, thin films and patterning of spin crossover compounds." *Comptes Rendus Chimie* 21.12 (2018): 1270-1286.
- [34] Villalva, Julia, et al. "Spin-state-dependent electrical conductivity in single-walled carbon nanotubes encapsulating spin-crossover molecules." *Nature communications* 12.1 (2021): 1-8.
- [35] Miyamachi, Toshio, et al. "Robust spin crossover and memristance across a single molecule." *Nature communications* 3.1 (2012): 1-6.

- [36] Gopakumar, Thiruvancheril G., et al. "Electron - induced spin crossover of single molecules in a bilayer on gold." *Angewandte Chemie International Edition* 51.25 (2012): 6262-6266.
- [37] Harzmann, Gero D., et al. "Single - molecule spin switch based on voltage - triggered distortion of the coordination sphere." *Angewandte Chemie International Edition* 54.45 (2015): 13425-13430.
- [38] Bairagi, Kaushik, et al. "Molecular-scale dynamics of light-induced spin cross-over in a two-dimensional layer." *Nature communications* 7.1 (2016): 1-7.
- [39] Frisenda, Riccardo, et al. "Stretching-induced conductance increase in a spin-crossover molecule." *Nano letters* 16.8 (2016): 4733-4737.
- [40] Aragonès, Albert C., et al. "Large conductance switching in a single-molecule device through room temperature spin-dependent transport." *Nano letters* 16.1 (2016): 218-226.
- [41] Burzurí, Enrique, et al. "Spin-state dependent conductance switching in single molecule-graphene junctions." *Nanoscale* 10.17 (2018): 7905-7911.
- [42] Bellec, Amandine, Jérôme Lagoute, and Vincent Repain. "Molecular electronics: Scanning tunneling microscopy and single-molecule devices." *Comptes Rendus Chimie* 21.12 (2018): 1287-1299.
- [43] Gruber, Manuel, and Richard Berndt. "Spin-crossover complexes in direct contact with surfaces." *Magnetochemistry* 6.3 (2020): 35.
- [44] Salmon, L., & Catala, L. (2018). Spin-crossover nanoparticles and nanocomposite materials. *Comptes Rendus Chimie*, 21(12), 1230-1269.
- [45] Orava, J., Kohoutek, T., & Wagner, T. (2014). Deposition techniques for chalcogenide thin films. In *Chalcogenide glasses* (pp. 265-309). Woodhead Publishing.
- [46] Kumar, K. S., & Ruben, M. (2021). Sublimable Spin - Crossover Complexes: From Spin - State Switching to Molecular Devices. *Angewandte Chemie International Edition*, 60(14), 7502-7521.
- [47] Shi, S., Schmerber, G., Arabski, J., Beaufrand, J. B., Kim, D. J., Boukari, S., ... & Ruch, D. (2009). Study of molecular spin-crossover complex Fe (phen) 2 (NCS) 2 thin films. *Applied Physics Letters*, 95(4), 202.
- [48] Palamarciuc, T., Oberg, J. C., El Hallak, F., Hirjibehedin, C. F., Serri, M., Heutz, S., ... & Rosa, P. (2012). Spin crossover materials evaporated under clean high vacuum and ultra-high vacuum conditions: from thin films to single molecules. *Journal of Materials Chemistry*, 22(19), 9690-9695.
- [49] Naggert, H., Bannwarth, A., Chemnitz, S., von Hofe, T., Quandt, E., & Tuczek, F. (2011). First observation of light-induced spin change in vacuum deposited thin films of iron spin crossover complexes. *Dalton Transactions*, 40(24), 6364-6366.
- [50] Ossinger, S., Naggert, H., Kipgen, L., Jasper-Toennies, T., Rai, A., Rudnik, J., ... & Tuczek, F. (2017). Vacuum-evaporable spin-crossover complexes in direct contact with a solid surface: Bismuth versus gold. *The Journal of Physical Chemistry C*, 121(2), 1210-1219.
- [51] Poggini, L., Milek, M., Londi, G., Naim, A., Poneti, G., Squillantini, L., ... & Mannini, M. (2018). Room temperature control of spin states in a thin film of a photochromic iron (II) complex. *Materials Horizons*, 5(3), 506-513.
- [52] Schleicher, F., Studniarek, M., Kumar, K. S., Urbain, E., Katcko, K., Chen, J., ... & Bowen, M. (2018). Linking electronic transport through a spin crossover thin film to the molecular spin state using x-ray absorption spectroscopy operando techniques. *ACS applied materials & interfaces*, 10(37), 31580-31585.

- [53] Kumar, K. S., Studniarek, M., Heinrich, B., Arabski, J., Schmerber, G., Bowen, M., ... & Ruben, M. (2018). Engineering On - Surface Spin Crossover: Spin - State Switching in a Self - Assembled Film of Vacuum - Sublimable Functional Molecule. *Advanced Materials*, 30(11), 1705416.
- [54] Bernien, M., Wiedemann, D., Hermanns, C. F., Krüger, A., Rolf, D., Kroener, W., ... & Kuch, W. (2012). Spin crossover in a vacuum-deposited submonolayer of a molecular iron (II) complex. *The journal of physical chemistry letters*, 3(23), 3431-3434.
- [55] Salmon, L., Molnár, G., Cobo, S., Oulié, P., Etienne, M., Mahfoud, T., ... & Bousseksou, A. (2009). Re-investigation of the spin crossover phenomenon in the ferrous complex [Fe (HB (pz) 3) 2]. *New Journal of Chemistry*, 33(6), 1283-1289.
- [56] Mahfoud, T., Molnár, G., Cobo, S., Salmon, L., Thibault, C., Vieu, C., ... & Bousseksou, A. (2011). Electrical properties and non-volatile memory effect of the [Fe (HB (pz) 3) 2] spin crossover complex integrated in a microelectrode device. *Applied Physics Letters*, 99(5), 157.
- [57] Rat, S., Ridier, K., Vendier, L., Molnár, G., Salmon, L., & Bousseksou, A. (2017). Solvatomorphism and structural-spin crossover property relationship in bis [hydrotris (1, 2, 4-triazol-1-yl) borate] iron (II). *CrystEngComm*, 19(24), 3271-3280.
- [58] Shalabaeva, V., Rat, S., Manrique-Juarez, M. D., Bas, A. C., Vendier, L., Salmon, L., ... & Bousseksou, A. (2017). Vacuum deposition of high-quality thin films displaying spin transition near room temperature. *Journal of Materials Chemistry C*, 5(18), 4419-4425.
- [59] Iasco, O., Boillot, M. L., Bellec, A., Guillot, R., Rivière, E., Mazerat, S., ... & Mallah, T. (2017). The disentangling of hysteretic spin transition, polymorphism and metastability in bistable thin films formed by sublimation of bis (scorpionate) Fe (II) molecules. *Journal of Materials Chemistry C*, 5(42), 11067-11075.
- [60] Atzori, M., Poggini, L., Squillantini, L., Cortigiani, B., Gonidec, M., Bencok, P., ... & Mannini, M. (2018). Thermal and light-induced spin transition in a nanometric film of a new high-vacuum processable spin crossover complex. *Journal of Materials Chemistry C*, 6(33), 8885-8889.
- [61] Rohlf, S., Gruber, M., Flöser, B. M., Grunwald, J., Jarausch, S., Diekmann, F., ... & Rosnagel, K. (2018). Light-induced spin crossover in an Fe (II) low-spin complex enabled by surface adsorption. *The journal of physical chemistry letters*, 9(7), 1491-1496.
- [62] Jasper-Tönnies, T., Gruber, M., Karan, S., Jacob, H., Tuczek, F., & Berndt, R. (2017). Deposition of a cationic FeIII spin-crossover complex on Au (111): impact of the counter ion. *The journal of physical chemistry letters*, 8(7), 1569-1573.
- [63] Bas, A. C., Shalabaeva, V., Thompson, X., Vendier, L., Salmon, L., Thibault, C., ... & Bousseksou, A. (2019). Effects of solvent vapor annealing on the crystallinity and spin crossover properties of thin films of [Fe (HB (tz) 3) 2]. *Comptes Rendus Chimie*, 22(6-7), 525-533.
- [64] Prins, F., Monrabal - Capilla, M., Osorio, E. A., Coronado, E., & van der Zant, H. S. (2011). Room - temperature electrical addressing of a bistable spin - crossover molecular system. *Advanced Materials*, 23(13), 1545-1549.
- [65] Rotaru, A., Dugay, J., Tan, R. P., Guralskiy, I. A., Salmon, L., Demont, P., ... & Bousseksou, A. (2013). Nano - electromanipulation of Spin Crossover Nanorods: Towards Switchable Nanoelectronic Devices. *Advanced Materials*, 25(12), 1745-1749.

- [66] Dugay, J., Giménez - Marqués, M., Kozlova, T., Zandbergen, H. W., Coronado, E., & van der Zant, H. S. (2015). Spin Switching in Electronic Devices Based on 2D Assemblies of Spin - Crossover Nanoparticles. *Advanced Materials*, 27(7), 1288-1293.
- [67] Etrillard, C., Faramarzi, V., Dayen, J. F., Letard, J. F., & Doudin, B. (2011). Photoconduction in [Fe (Htrz) 2 (trz)](BF 4)· H 2 O nanocrystals. *Chemical Communications*, 47(34), 9663-9665.
- [68] Torres-Cavanillas, R., Sanchis-Gual, R., Dugay, J., Coronado-Puchau, M., Giménez-Marqués, M., & Coronado, E. (2019). Design of Bistable Gold@ Spin-Crossover Core–Shell Nanoparticles Showing Large Electrical Responses for the Spin Switching. *Advanced Materials*, 31(27), 1900039.
- [69] Hao, G., Mosey, A., Jiang, X., Yost, A. J., Sapkota, K. R., Wang, G. T., ... & Dowben, P. A. (2019). Nonvolatile voltage controlled molecular spin state switching. *Applied Physics Letters*, 114(3), 032901.
- [70] Matsuda, M., Isozaki, H., & Tajima, H. (2008). Electroluminescence quenching caused by a spin-crossover transition. *Chemistry letters*, 37(3), 374-375.
- [71] Matsuda, M., Isozaki, H., & Tajima, H. (2008). Reproducible on–off switching of the light emission from the electroluminescent device containing a spin crossover complex. *Thin Solid Films*, 517(4), 1465-1467.
- [72] Matsuda, M., Kiyoshima, K., Uchida, R., Kinoshita, N., & Tajima, H. (2013). Characteristics of organic light-emitting devices consisting of dye-doped spin crossover complex films. *Thin Solid Films*, 531, 451-453.
- [73] Lefter, C., Rat, S., Costa, J. S., Manrique - Juárez, M. D., Quintero, C. M., Salmon, L., ... & Bousseksou, A. (2016). Current Switching Coupled to Molecular Spin - States in Large - Area Junctions. *Advanced Materials*, 28(34), 7508-7514.
- [74] Shalabaeva, V., Ridier, K., Rat, S., Manrique-Juarez, M. D., Salmon, L., Séguy, I., ... & Bousseksou, A. (2018). Room temperature current modulation in large area electronic junctions of spin crossover thin films. *Applied Physics Letters*, 112(1), 013301.
- [75] Poggini, L., Gonidec, M., Balasubramanyam, R. K. C., Squillantini, L., Pecastaings, G., Caneschi, A., & Rosa, P. (2019). Temperature-induced transport changes in molecular junctions based on a spin crossover complex. *Journal of Materials Chemistry C*, 7(18), 5343-5347.
- [76] Poggini, L., Gonidec, M., González - Estefan, J. H., Pecastaings, G., Gobaut, B., & Rosa, P. (2018). Vertical tunnel junction embedding a spin crossover molecular film. *Advanced Electronic Materials*, 4(12), 1800204.
- [77] Cucinotta, G., Poggini, L., Giaconi, N., Cini, A., Gonidec, M., Atzori, M., ... & Mannini, M. (2020). Space charge-limited current transport mechanism in crossbar junction embedding molecular spin crossovers. *ACS applied materials & interfaces*, 12(28), 31696-31705.
- [78] Karuppanan, S. K., Martín-Rodríguez, A., Ruiz, E., Harding, P., Harding, D. J., Yu, X., ... & Nijhuis, C. A. (2021). Room temperature conductance switching in a molecular iron (III) spin crossover junction. *Chemical Science*, 12(7), 2381-2388.
- [79] Dugay, J., Aarts, M., Giménez-Marqués, M., Kozlova, T., Zandbergen, H. W., Coronado, E., & Van Der Zant, H. S. J. (2017). Phase transitions in spin-crossover thin films probed by graphene transport measurements. *Nano letters*, 17(1), 186-193.

- [80] van Geest, E. P., Shakouri, K., Fu, W., Robert, V., Tudor, V., Bonnet, S., & Schneider, G. F. (2020). Contactless Spin Switch Sensing by Chemo - Electric Gating of Graphene. *Advanced Materials*, 32(10), 1903575.
- [81] Holovchenko, Anastasia, et al. "Near room - temperature memory devices based on hybrid spin - crossover@ SiO₂ nanoparticles coupled to single - layer graphene nanoelectrodes." *Advanced Materials* 28.33 (2016): 7228-7233.
- [82] Konstantinov, N., Tauzin, A., Noubé, U. N., Dragoe, D., Kundys, B., Majjad, H., ... & Dayen, J. F. (2021). Electrical read-out of light-induced spin transition in thin film spin crossover/graphene heterostructures. *Journal of Materials Chemistry C*, 9(8), 2712-2720.
- [83] Dayen, Jean Francois, et al. "Room temperature optoelectronic device operating with spin crossover nanoparticles." *Materials Horizons* (2021).
- [84] Mosey, A., Dale, A. S., Hao, G., N'Diaye, A., Dowben, P. A., & Cheng, R. (2020). Quantitative Study of the Energy Changes in Voltage-Controlled Spin Crossover Molecular Thin Films. *The Journal of Physical Chemistry Letters*, 11(19), 8231-8237.
- [85] Ekanayaka, Thilini K., et al. "Nonvolatile Voltage Controlled Molecular Spin-State Switching for Memory Applications." *Magnetochemistry* 7.3 (2021): 37.
- [86] Rat, Sylvain. Synthèses et caractérisations de films et de nanocomposites de matériaux à transition de spin pour des applications dans des dispositifs électroniques et mécaniques. Diss. Université Paul Sabatier-Toulouse III, 2017.
- [87] Janod, Etienne, et al. "Resistive switching in Mott insulators and correlated systems." *Advanced Functional Materials* 25.40 (2015): 6287-6305.
- [88] Sawa, Akihito. "Resistive switching in transition metal oxides." *Materials today* 11.6 (2008): 28-36.
- [89] del Valle, Javier, et al. "Challenges in materials and devices for resistive-switching-based neuromorphic computing." *Journal of Applied Physics* 124.21 (2018): 211101.
- [90] Lee, Jae Sung, Shinbuhm Lee, and Tae Won Noh. "Resistive switching phenomena: A review of statistical physics approaches." *Applied Physics Reviews* 2.3 (2015): 031303.
- [91] Feng, P. A. N., et al. "Nonvolatile resistive switching memories-characteristics, mechanisms and challenges." *Progress in Natural Science: Materials International* 20 (2010): 1-15.
- [92] Manrique - Juarez, Maria D., et al. "A Bistable Microelectromechanical System Actuated by Spin - Crossover Molecules." *Angewandte Chemie* 129.28 (2017): 8186-8190.
- [93] Bas, A. C., Shalabaeva, V., Thompson, X., Vendier, L., Salmon, L., Thibault, C., ... & Bousseksou, A. (2019). Effects of solvent vapor annealing on the crystallinity and spin crossover properties of thin films of [Fe (HB (tz) 3) 2]. *Comptes Rendus Chimie*, 22(6-7), 525-533.
- [94] Glatthaar, Markus, et al. "Efficiency limiting factors of organic bulk heterojunction solar cells identified by electrical impedance spectroscopy." *Solar energy materials and solar cells* 91.5 (2007): 390-393.
- [95] Reese, Matthew O., et al. "Photoinduced degradation of polymer and polymer–fullerene active layers: experiment and theory." *Advanced Functional Materials* 20.20 (2010): 3476-3483.
- [96] Schafferhans, Julia, et al. "Oxygen doping of P3HT: PCBM blends: Influence on trap states, charge carrier mobility and solar cell performance." *Organic Electronics* 11.10 (2010): 1693-1700.

- [97] Zhan, Xiaowei, et al. "A high-mobility electron-transport polymer with broad absorption and its use in field-effect transistors and all-polymer solar cells." *Journal of the American Chemical Society* 129.23 (2007): 7246-7247.
- [98] Yadav, Pankaj, et al. "Intrinsic and interfacial kinetics of perovskite solar cells under photo and bias-induced degradation and recovery." *Journal of Materials Chemistry C* 5.31 (2017): 7799-7805.
- [99] McCreery, Richard L., Haijun Yan, and Adam Johan Bergren. "A critical perspective on molecular electronic junctions: there is plenty of room in the middle." *Physical Chemistry Chemical Physics* 15.4 (2013): 1065-1081.
- [100] Rotaru, Aurelian, et al. "Spin state dependence of electrical conductivity of spin crossover materials." *Chemical Communications* 48.35 (2012): 4163-4165.
- [101] Rotaru, Aurelian, et al. "Nano - electromanipulation of Spin Crossover Nanorods: Towards Switchable Nanoelectronic Devices." *Advanced Materials* 25.12 (2013): 1745-1749.
- [102] Molnár, Gábor, et al. "Interplay between the charge transport phenomena and the charge-transfer phase transition in $Rb_x Mn [Fe (CN)_6]_y \cdot z H_2O$." *The Journal of Physical Chemistry C* 113.6 (2009): 2586-2593.
- [103] Gheorghe, Andrei-Cristian, et al. "Anomalous Pressure Effects on the Electrical Conductivity of the Spin Crossover Complex $[Fe (pyrazine)_2 Au (CN)_2]_2$." *Magnetochemistry* 6.3 (2020): 31.
- [104] Jasper-Tönnies, Torben, et al. "Deposition of a cationic FeIII spin-crossover complex on Au (111): impact of the counter ion." *The journal of physical chemistry letters* 8.7 (2017): 1569-1573.
- [105] Jasper-Toennies, Torben, et al. "Robust and selective switching of an FeIII spin-crossover compound on Cu₂N/Cu (100) with memristance behavior." *Nano letters* 17.11 (2017): 6613-6619.
- [106] Ossinger, Sascha, et al. "Effect of ligand methylation on the spin-switching properties of surface-supported spin-crossover molecules." *Journal of Physics: Condensed Matter* 32.11 (2019): 114003.
- [107] Miyamachi, Toshio, et al. "Robust spin crossover and memristance across a single molecule." *Nature communications* 3.1 (2012): 1-6.
- [108] Aragonès, Albert C., et al. "Large conductance switching in a single-molecule device through room temperature spin-dependent transport." *Nano letters* 16.1 (2016): 218-226.
- [109] Aragonès, Albert C., et al. "Control over near-ballistic electron transport through formation of parallel pathways in a single-molecule wire." *Journal of the American Chemical Society* 141.1 (2018): 240-250.
- [110] Aravena, Daniel, and Eliseo Ruiz. "Coherent transport through spin-crossover single molecules." *Journal of the American Chemical Society* 134.2 (2012): 777-779.
- [111] Bairagi, Kaushik, et al. "Molecular-scale dynamics of light-induced spin cross-over in a two-dimensional layer." *Nature communications* 7.1 (2016): 1-7.
- [112] Gopakumar, Thiruvancheril G., et al. "Electron - induced spin crossover of single molecules in a bilayer on gold." *Angewandte Chemie International Edition* 51.25 (2012): 6262-6266.
- [113] Gruber, Manuel, et al. "Spin state of spin-crossover complexes: From single molecules to ultrathin films." *Physical Review B* 89.19 (2014): 195415.

- [114] Zhang, Luqiong, et al. "Anomalous light - induced spin - state switching for iron (II) spin - crossover molecules in direct contact with metal surfaces." *Angewandte Chemie International Edition* 59.32 (2020): 13341-13346.
- [115] Akai-Kasaya, M., et al. "Coulomb blockade in a two-dimensional conductive polymer monolayer." *Physical review letters* 115.19 (2015): 196801.
- [116] Poggini, L., Gonidec, M., González - Estefan, J. H., Pecastaings, G., Gobaut, B., & Rosa, P. (2018). Vertical tunnel junction embedding a spin crossover molecular film. *Advanced Electronic Materials*, 4(12), 1800204.
- [117] Dixon, Isabelle M., et al. "On the spin-state dependence of redox potentials of spin crossover complexes." *Inorganic Chemistry* 59.24 (2020): 18402-18406.
- [118] Bokdam, Menno, Deniz Çakır, and Geert Brocks. "Fermi level pinning by integer charge transfer at electrode-organic semiconductor interfaces." *Applied physics letters* 98.11 (2011): 59.
- [119] Gregg, J. F., et al. "Giant magnetoresistive effects in a single element magnetic thin film." *Physical Review Letters* 77.8 (1996): 1580.
- [120] Wolf, Stuart A., Almadena Yu Chtchelkanova, and Daryl M. Treger. "Spintronics—A retrospective and perspective." *IBM journal of research and development* 50.1 (2006): 101-110.
- [121] Dediu, V., et al. "Room temperature spin polarized injection in organic semiconductor." *Solid State Communications* 122.3-4 (2002): 181-184.
- [122] Naber, W. J. M., et al. "Controlled tunnel-coupled ferromagnetic electrodes for spin injection in organic single-crystal transistors." *Organic electronics* 11.5 (2010): 743-747.
- [123] Cinchetti, Mirko, V. Alek Dediu, and Luis E. Hueso. "Activating the molecular spinterface." *Nature materials* 16.5 (2017): 507-515.
- [124] Sun, Meifang, and Wenbo Mi. "Progress in organic molecular/ferromagnet spinterfaces: towards molecular spintronics." *Journal of Materials Chemistry C* 6.25 (2018): 6619-6636.
- [125] Barraud, Clément, et al. "Unravelling the role of the interface for spin injection into organic semiconductors." *Nature Physics* 6.8 (2010): 615-620.
- [126] Yamashita, Yoshiro. "Organic semiconductors for organic field-effect transistors." *Science and technology of advanced materials* 10.2 (2009): 024313.
- [127] Perrin, Mickael L., Enrique Burzurí, and Herre SJ van der Zant. "Single-molecule transistors." *Chemical Society Reviews* 44.4 (2015): 902-919.
- [128] Huitema, H. Edzer A., et al. "Active - Matrix Displays Driven by Solution - Processed Polymeric Transistors." *Advanced Materials* 14.17 (2002): 1201-1204.
- [129] Di, Chong - an, Fengjiao Zhang, and Daoben Zhu. "Multi - functional integration of organic field - effect transistors (OFETs): advances and perspectives." *Advanced Materials* 25.3 (2013): 313-330.
- [130] Wakayama, Yutaka, et al. "Photochromism for optically functionalized organic field-effect transistors: a comprehensive review." *Journal of Materials Chemistry C* 8.32 (2020): 10956-10974.

- [131] Lefter, Constantin, et al. "Dielectric and charge transport properties of the spin crossover complex $[\text{Fe}(\text{Htrz})_2(\text{trz})](\text{BF}_4)$." *physica status solidi (RRL)–Rapid Research Letters* 8.2 (2014): 191-193.
- [132] Bousseksou, Azzedine, et al. "Observation of a thermal hysteresis loop in the dielectric constant of spin crossover complexes: towards molecular memory devices." *Journal of Materials Chemistry* 13.9 (2003): 2069-2071.
- [133] Dugay, J., Aarts, M., Giménez-Marqués, M., Kozlova, T., Zandbergen, H. W., Coronado, E., & Van Der Zant, H. S. J. (2017). Phase transitions in spin-crossover thin films probed by graphene transport measurements. *Nano letters*, 17(1), 186-193.
- [134] van Geest, E. P., Shakouri, K., Fu, W., Robert, V., Tudor, V., Bonnet, S., & Schneider, G. F. (2020). Contactless Spin Switch Sensing by Chemo - Electric Gating of Graphene. *Advanced Materials*, 32(10), 1903575.
- [135] Konstantinov, N., Tauzin, A., Noubé, U. N., Dragoie, D., Kundys, B., Majjad, H., ... & Dayen, J. F. (2021). Electrical read-out of light-induced spin transition in thin film spin crossover/graphene heterostructures. *Journal of Materials Chemistry C*, 9(8), 2712-2720.
- [136] Dayen, Jean Francois, et al. "Room temperature optoelectronic device operating with spin crossover nanoparticles." *Materials Horizons* (2021).
- [137] Hao, G., Mosey, A., Jiang, X., Yost, A. J., Sapkota, K. R., Wang, G. T., ... & Dowben, P. A. (2019). Nonvolatile voltage controlled molecular spin state switching. *Applied Physics Letters*, 114(3), 032901.
- [138] Mosey, A., Dale, A. S., Hao, G., N'Diaye, A., Dowben, P. A., & Cheng, R. (2020). Quantitative Study of the Energy Changes in Voltage-Controlled Spin Crossover Molecular Thin Films. *The Journal of Physical Chemistry Letters*, 11(19), 8231-8237.
- [139] Faddoul, Rita. Printing processes dedicated for the mass production of ceramic based microelectronic devices. Diss. Institut National Polytechnique de Grenoble-INPG, 2012.
- [140] Horowitz, G., R. Hajlaoui, and F. Kouki. "An analytical model for the organic field-effect transistor in the depletion mode. Application to sexithiophene films and single crystals." *The European Physical Journal-Applied Physics* 1.3 (1998): 361-367.
- [141] Ostroverkhova, Oksana, ed. *Handbook of Organic Materials for Electronic and Photonic Devices*. Woodhead Publishing, 2018.
- [142] Haddad, Clara. Fabrication, caractérisation électrique et fiabilité des OTFTs imprimés sur substrat plastique. Diss. Université Grenoble Alpes (ComUE), 2018.

- [143] Mathijssen, Simon GJ, et al. "Dynamics of threshold voltage shifts in organic and amorphous silicon field - effect transistors." *Advanced Materials* 19.19 (2007): 2785-2789.
- [144] Qiu, Ya-Ru, et al. "Enhanced dielectricity coupled to spin-crossover in a one-dimensional polymer iron (ii) incorporating tetrathiafulvalene." *Chemical science* 11.24 (2020): 6229-6235.
- [145] Pingel, P., and Dieter Neher. "Comprehensive picture of p-type doping of P3HT with the molecular acceptor F 4 TCNQ." *Physical Review B* 87.11 (2013): 115209.
- [146] Yuan, Yongbo, et al. "Ultra-high mobility transparent organic thin film transistors grown by an off-centre spin-coating method." *Nature communications* 5.1 (2014): 1-9.
- [147] Park, Joon Seok, et al. "Review of recent developments in amorphous oxide semiconductor thin-film transistor devices." *Thin solid films* 520.6 (2012): 1679-1693.
- [148] Blaise, G., and C. Le Gressus. "Charging and flashover induced by surface polarization relaxation process." *Journal of Applied Physics* 69.9 (1991): 6334-6339.
- [149] Pannemann, Ch, T. Diekmann, and U. Hilleringmann. "Degradation of organic field-effect transistors made of pentacene." *Journal of Materials Research* 19.7 (2004): 1999-2002.
- [150] Häusermann, Roger, and Bertram Batlogg. "Gate bias stress in pentacene field-effect-transistors: Charge trapping in the dielectric or semiconductor." *Applied Physics Letters* 99.8 (2011): 175.
- [151] Miller, Kevin J., Richard F. Haglund, and Sharon M. Weiss. "Optical phase change materials in integrated silicon photonic devices." *Optical Materials Express* 8.8 (2018): 2415-2429.
- [152] Yang, Zheng, and Shriram Ramanathan. "Breakthroughs in photonics 2014: phase change materials for photonics." *IEEE Photonics Journal* 7.3 (2015): 1-5.
- [153] Raoux, Simone. "Phase change materials." *Annual Review of Materials Research* 39 (2009): 25-48.
- [154] Wuttig, Matthias, Harish Bhaskaran, and Thomas Taubner. "Phase-change materials for non-volatile photonic applications." *Nature Photonics* 11.8 (2017): 465-476.
- [155] Raoux, Simone, Wojciech Welnic, and Daniele Ielmini. "Phase change materials and their application to nonvolatile memories." *Chemical reviews* 110.1 (2010): 240-267.
- [156] Liu, Hongwei, Junpeng Lu, and Xiao Renshaw Wang. "Metamaterials based on the phase transition of VO₂." *Nanotechnology* 29.2 (2017): 024002.

- [157] Yang, Zheng, Changhyun Ko, and Shriram Ramanathan. "Oxide electronics utilizing ultrafast metal-insulator transitions." *Annual Review of Materials Research* 41 (2011): 337-367.
- [158] Beeckman, Jeroen, Kristiaan Neyts, and Pieter JM Vanbrabant. "Liquid-crystal photonic applications." *Optical Engineering* 50.8 (2011): 081202.
- [159] Kahn, Olivier, Jonas Kröber, and Charlotte Jay. "Spin transition molecular materials for displays and data recording." *Advanced Materials* 4.11 (1992): 718-728.
- [160] Kahn, Olivier, and C. Jay Martinez. "Spin-transition polymers: from molecular materials toward memory devices." *Science* 279.5347 (1998): 44-48.
- [161] Quintero, Carlos, et al. "Detection of molecular spin-state changes in ultrathin films by photonic methods." *Journal of Nanophotonics* 6.1 (2012): 063517.
- [162] Hauser, Andreas. "Four-wave-mixing in the Fe (II) spin-crossover system [Zn_{1-x}Fe_x(ptz)₆](BF₄)₂ (ptz= 1-propyltetrazole)." *Chemical physics letters* 202.1-2 (1993): 173-178.
- [163] Félix, Gautier, et al. "Surface plasmons reveal spin crossover in nanometric layers." *Journal of the American Chemical Society* 133.39 (2011): 15342-15345.
- [164] Halcrow, Malcolm A., ed. *Spin-crossover materials: properties and applications*. John Wiley & Sons, 2013.
- [165] Bertoni, Roman, et al. "Ultrafast light-induced spin-state trapping photophysics investigated in Fe (phen)₂ (NCS)₂ spin-crossover crystal." *Accounts of chemical research* 48.3 (2015): 774-781.
- [166] Hauser, A. "Spin crossover in transition metal compounds II." *Topics in Current Chemistry* 234 (2004): 155-198.
- [167] Dong, Weiling, et al. "Wide bandgap phase change material tuned visible photonics." *Advanced Functional Materials* 29.6 (2019): 1806181.
- [168] Mounaix, Patrick, et al. "One-dimensional tunable photonic crystals with spin crossover material for the terahertz range." *Applied physics letters* 89.17 (2006): 174105.
- [169] Bartual-Murgui, Carlos, et al. "Spin-crossover metal-organic frameworks: promising materials for designing gas sensors." *Journal of Materials Chemistry C* 3.6 (2015): 1277-1285.
- [170] Akou, Amal, et al. "Soft lithographic patterning of spin crossover complexes. Part 2: stimuli-responsive diffraction grating properties." *Journal of Materials Chemistry* 22.9 (2012): 3752-3757.

- [171] Abdul-Kader, Khaldoun, et al. "Synergistic switching of plasmonic resonances and molecular spin states." *Nanoscale* 5.12 (2013): 5288-5293.
- [172] Palluel, Marlène, et al. "The Interplay between Surface Plasmon Resonance and Switching Properties in Gold@ Spin Crossover Nanocomposites." *Advanced Functional Materials* 30.17 (2020): 2000447.
- [173] Suzuki, Senichi, Kazuhiro Oda, and Yoshinori Hibino. "Integrated-optic double-ring resonators with a wide free spectral range of 100 GHz." *Journal of lightwave technology* 13.8 (1995): 1766-1771.
- [174] Heebner, John E., Robert W. Boyd, and Q-Han Park. "Slow light, induced dispersion, enhanced nonlinearity, and optical solitons in a resonator-array waveguide." *Physical Review E* 65.3 (2002): 036619.
- [175] Allan, William R., et al. "Multiplexed fiber Bragg grating interrogation system using a microelectromechanical Fabry–Perot tunable filter." *IEEE Sensors Journal* 9.8 (2009): 936-943.
- [176] Jones, Robert, Catherine Wykes, and Jones Wykes. *Holographic and speckle interferometry*. No. 6. Cambridge university press, 1989.
- [177] Ridier, Karl, et al. "Finite Size Effects on the Switching Dynamics of Spin - Crossover Thin Films Photoexcited by a Femtosecond Laser Pulse." *Advanced Materials* 31.25 (2019): 1901361.
- [178] Windt, David L. "IMD—Software for modeling the optical properties of multilayer films." *Computers in physics* 12.4 (1998): 360-370.
- [179] Wiley, Benjamin J., et al. "Maneuvering the surface plasmon resonance of silver nanostructures through shape-controlled synthesis." (2006): 15666-15675.
- [180] Ridier, Karl, et al. "Unprecedented switching endurance affords for high-resolution surface temperature mapping using a spin-crossover film." *Nature communications* 11.1 (2020): 1-9.

Annexes

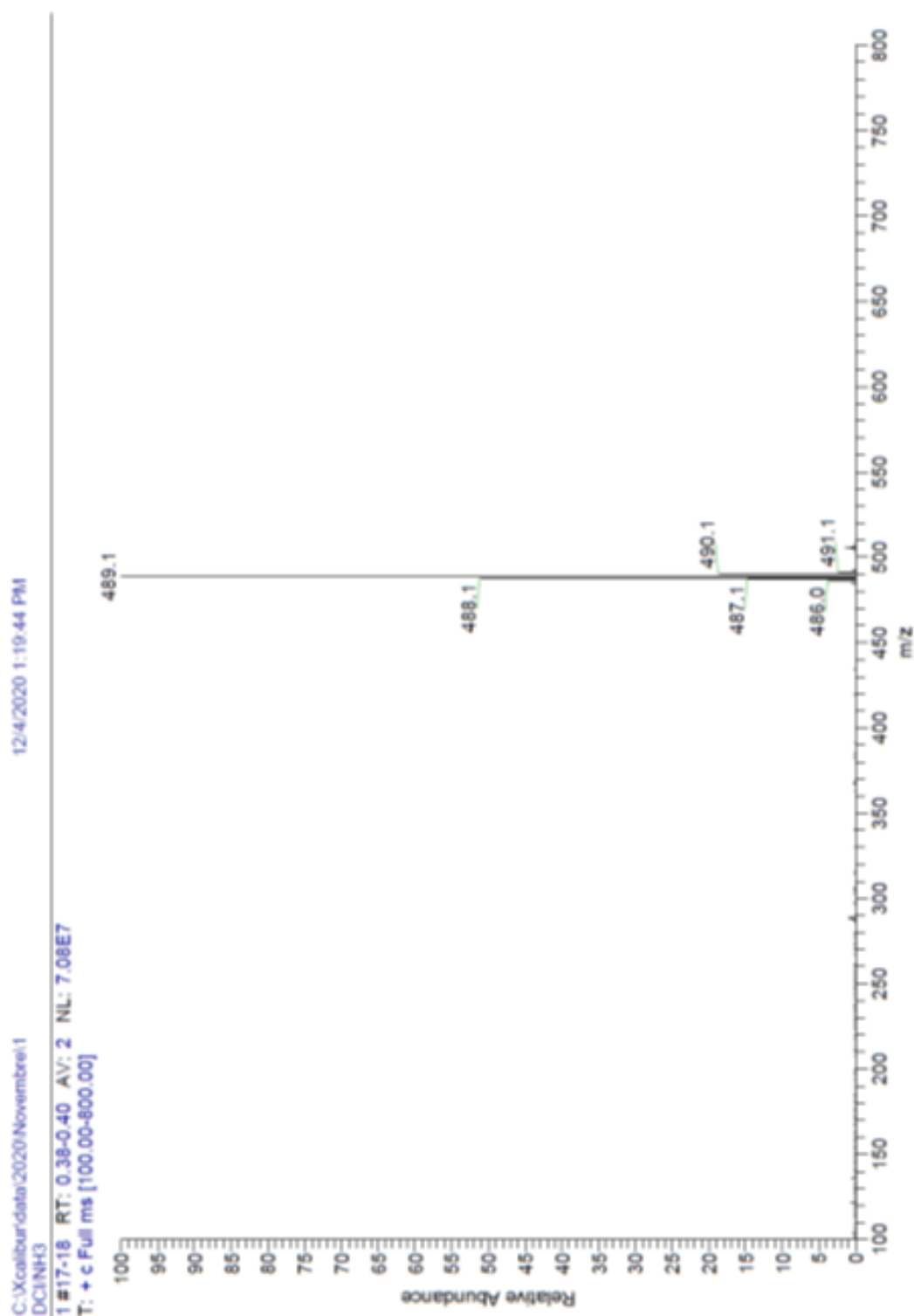
Table of contents

A2.1 Characterizations of as-synthesized $[\text{Fe}(\text{HB}(\text{tz})_3)_2]$ complex.....	139
A2.1.1 Mass spectrum of $[\text{Fe}(\text{HB}(\text{tz})_3)_2]$ complex.....	139
A2.1.2 IR spectrum of $[\text{Fe}(\text{HB}(\text{tz})_3)_2]$ complex.....	140
A2.1.3 Synthesis and purification of $[\text{Fe}(\text{HB}(\text{tz})_3)_2]$ complex.....	141
A2.1.4 Variable-temperature optical reflectivity spectrum of $[\text{Fe}(\text{HB}(\text{tz})_3)_2]$ complex of different batch of samples.....	144
A2.2 Characterizations of thin films.....	145
A2.2.1 Thickness characterizations by AFM, representative results of $[\text{Fe}(\text{HB}(\text{tz})_3)_2]$ thin film (<i>ca.</i> 99 nm) and thick film (<i>ca.</i> 667 nm).....	145
A2.2.2 Thickness characterizations by Filmetrics, representative results of thin film (<i>ca.</i> 100 nm) and thick film (<i>ca.</i> 900 nm).....	146
A2.2.3 GIXRD (with the glazing incident of 0° , 5° and 7°) of as-deposited $[\text{Fe}(\text{HB}(\text{tz})_3)_2]$ thin films on the fused silica substrates.....	147
A2.2.4 UV-Vis absorption spectrum of the $[\text{Zn}(\text{HB}(\text{tz})_3)_2]$ thin films.....	147
A2.2.5 Surface morphologies (AFM graphs) of annealed $[\text{Fe}(\text{HB}(\text{tz})_3)_2]$ thin films.....	148
A2.2.6 Surface morphologies (optical microscope graphs) of annealed $[\text{Fe}(\text{HB}(\text{tz})_3)_2]$ thin films.....	150
A2.2.7 UV-vis spectra of annealed $[\text{Fe}(\text{HB}(\text{tz})_3)_2]$ thin films by different batch.....	152
A2.2.8 Characterizations of other thin films.....	154
A2.2.8.1 Raman spectra of $[\text{Zn}(\text{HB}(\text{tz})_3)_2]$ thin films (water annealed and without water annealed).....	154
A2.2.8.2 Thickness and morphology of thermal evaporated spiropyran thin films.....	154
A2.3 Characterizations of multilayer two-terminal devices.....	157
A2.3.1 Characterizations of $[\text{Zn}(\text{HB}(\text{tz})_3)_2]$ -based two-terminal devices. (5V, $5^\circ\text{C}/\text{min}$).....	157
A2.3.2 Characterizations of “1-year aged” non-encapsulated ITO/100 nm $[\text{Fe}(\text{HB}(\text{tz})_3)_2]$ /Al junction at 2V.....	157

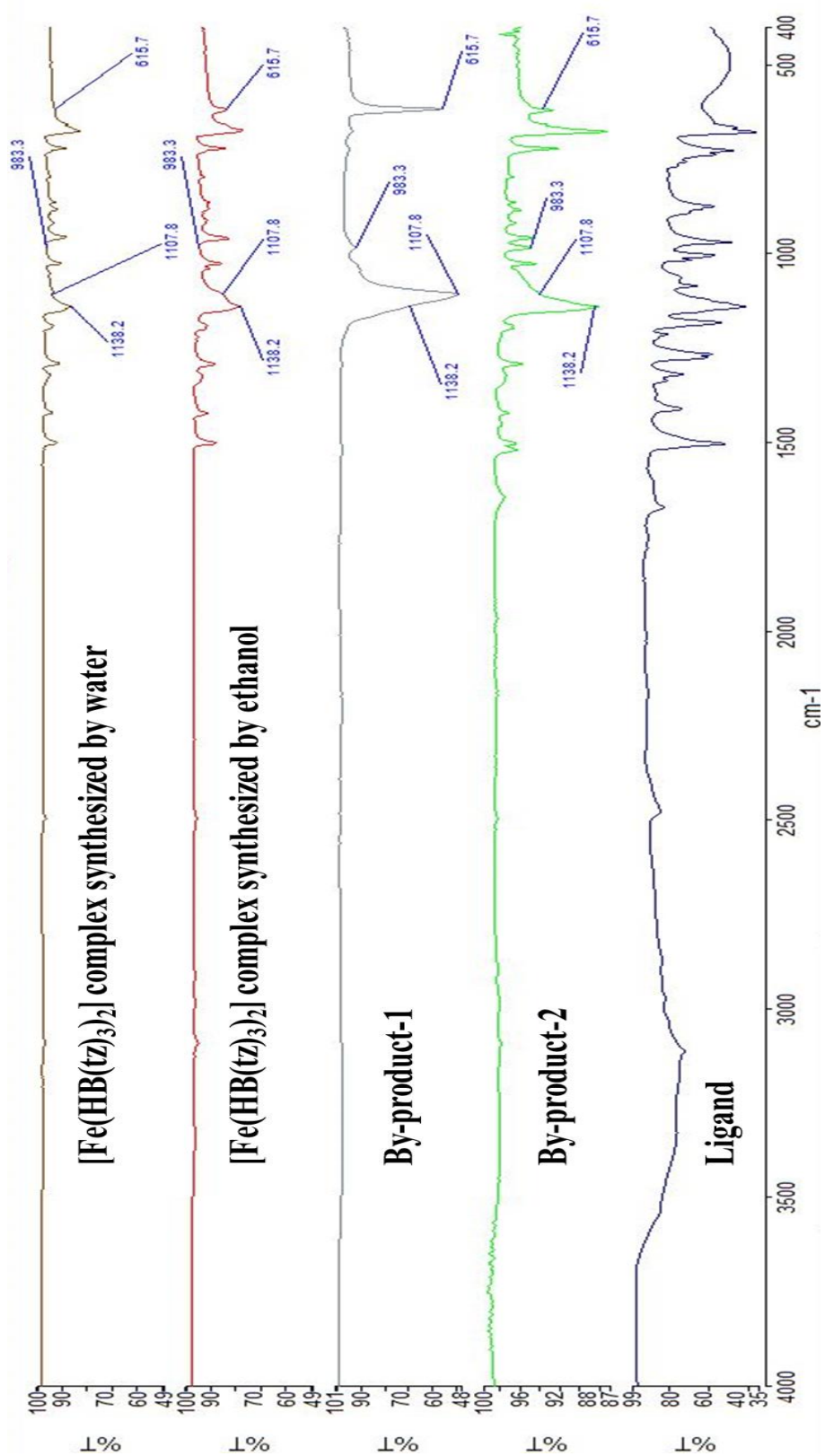
A2.3.3 Characterizations of other [Fe(HB(tz) ₃) ₂]-based two-terminal devices.....	158
A3.1 Output characteristics of Device A (without SCO).....	161
A3.2 OFETs degradation tests under vacuum.....	161
A3.3 Output and transfer characteristics in different temperatures of different OFETs.....	162
A3.4 Temperature accelerated degradation of OFETs.....	176
A4.1 Representative SEM graphs of a high-resolution shadow mask.	177
A4.2 Representative OM graphs of a high-resolution shadow mask.	178
A4.3 Representative SEM graphs of patterned 100 nm thick Al deposited on glass substrate.	179
A4.4 Representative OM graphs of patterned 100 nm thick Al deposited on glass substrate.	179
A4.5 Representative AFM graphs of patterned 100 nm thick Al deposited on glass substrate.	180
A4.6 Representative OM graphs of 100 nm thick Al deposited on the top of 100 nm thick SCO layer.	181

A2.1 Characterizations of as-synthesized $[\text{Fe}(\text{HB}(\text{tz})_3)_2]$ complex.

A2.1.1 Mass spectrum of $[\text{Fe}(\text{HB}(\text{tz})_3)_2]$ complex.



A2.1.2 IR spectrum of $[\text{Fe}(\text{HB}(\text{tz})_3)_2]$ complex.



A2.1.3 Synthesis and purification of [Fe(HB(tz)₃)₂] complex.

The synthesis of [Fe(HB(tz)₃)₂] complex follow the equation as below:



Usually, as-received [Fe(HB(tz)₃)₂] powder synthesized in ethanol contained some ‘white’ powder, and according to the synthesis route and post-synthesis treatment, we thought it was K₂SO₄, however, the fact is more complicated. The reasons are listed as below:

(i) Purification (thermal evaporation) of as-synthesized powder (synthesized in ethanol).

Similar as the mechanism of the tube furnace to purify the compounds, for our sublimator, we set several temperatures (150 °C, 200 °C and 250 °C) and collected powder at the fixed temperatures. Figure below is the photo of the sublimator after operated in 250 °C. Obviously, there are some white powder sublimated together with the purple powder, and they are not ligand or salt (because of the sublimation temperature range and IR spectrum).



(ii) Follow the normal stoichiometric condition (ligand:salt = 2:1), but change the solvent from ethanol to water, and do 3 times of centrifugation (in water) after synthesis. According to the solubility of the compounds, ligand and salt should be removed after this kind of post-synthesis treatment (centrifugation by water).

[Solubility data: Iron salt FeSO_4 25.6 g/100 ml (20 °C)

Potassium salt K_2SO_4 11.1 g/100 ml (20 °C)

Ligand $\text{KHB}(\text{tz})_3 > 20$ g/100 ml (20 °C)]

Nevertheless, we still observed the mixture of white and purple powder. This indicates that unlike the ligand and salt, the white powder has bad solubility in water.

Based on these results above, we propose a hypothesis about the origin of the white powder:

Maybe because what we synthesised of ligand, is not that pure. Another possibility is the minor mistake in weighing the compounds ($\text{KHB}(\text{tz})_3 + \text{FeSO}_4$).

$[\text{Fe}(\text{HB}(\text{tz})_3)_{2x}(\text{SO}_4)_y]$ ($2X+y=2$), when x took the majority, it would be very similar to triazolyl complex.

$[\text{Fe}(\text{HB}(\text{tz})_3)_{2x}(\text{SO}_4)_y]$ ($2X+y=2$), when y took the majority, it is more different from the triazolyl complex, from pink to white/grey, but still low solubility in water.

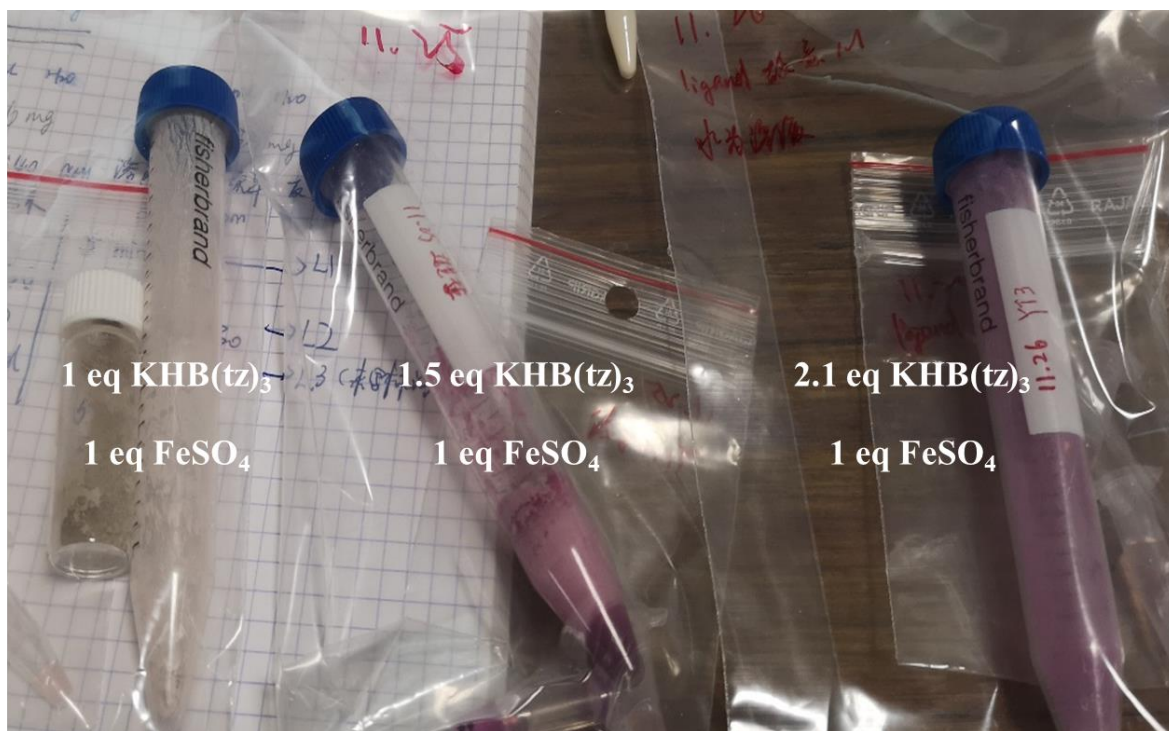
To verify this hypothesis, I did several synthesis with different stoichiometric conditions. (note that the synthesis was done in water and the product was washed by water by centrifugation several times).

1 eq $\text{KHB}(\text{tz})_3$ and 1 eq FeSO_4 gave a total grey product.

1.5 eq $\text{KHB}(\text{tz})_3$ and 1 eq FeSO_4 gave a mixture of purple/white product.

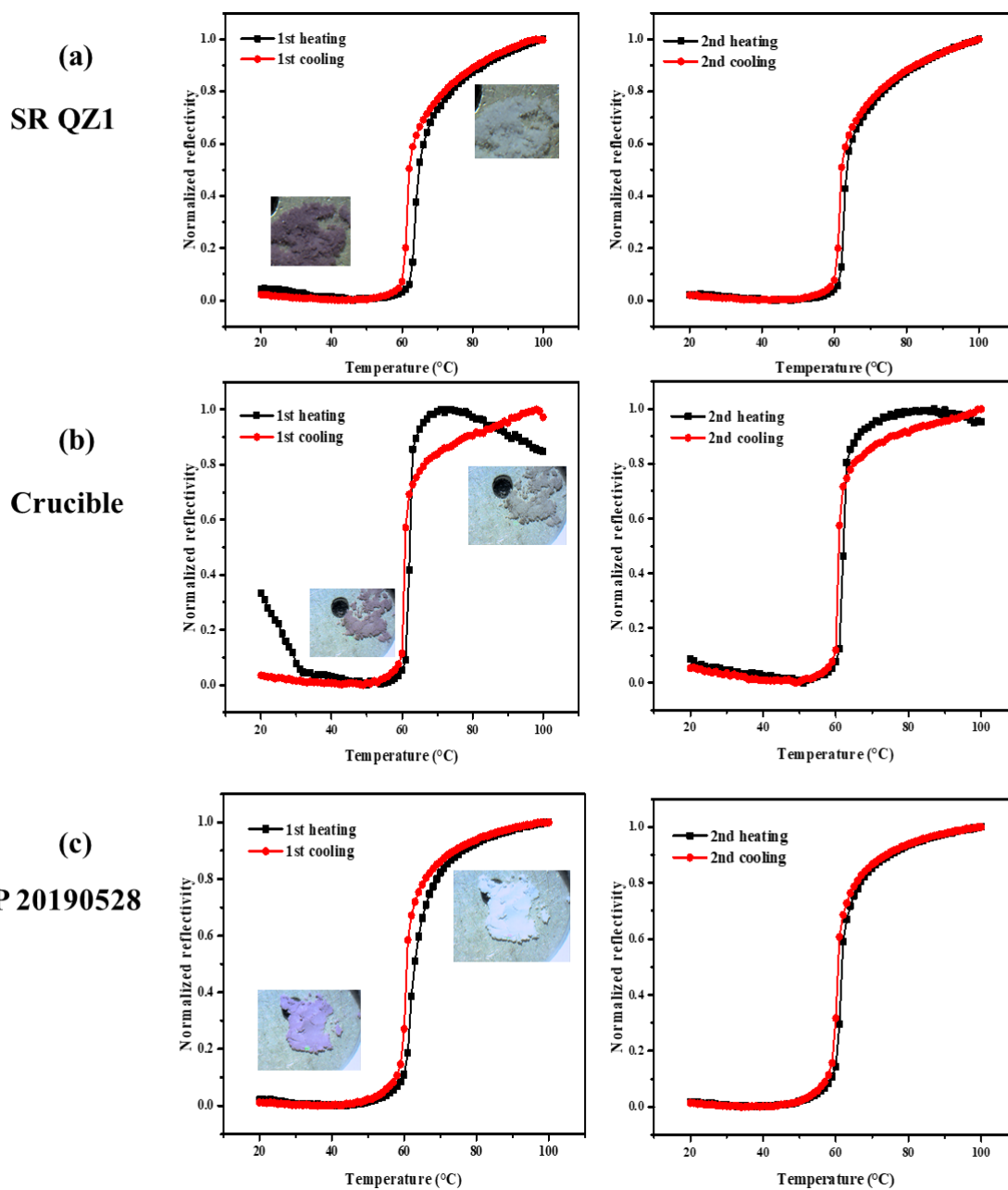
2.1 eq $\text{KHB}(\text{tz})_3$ and 1 eq FeSO_4 gave a purple product.

The photo of the result of different stoichiometric conditions is shown as below:



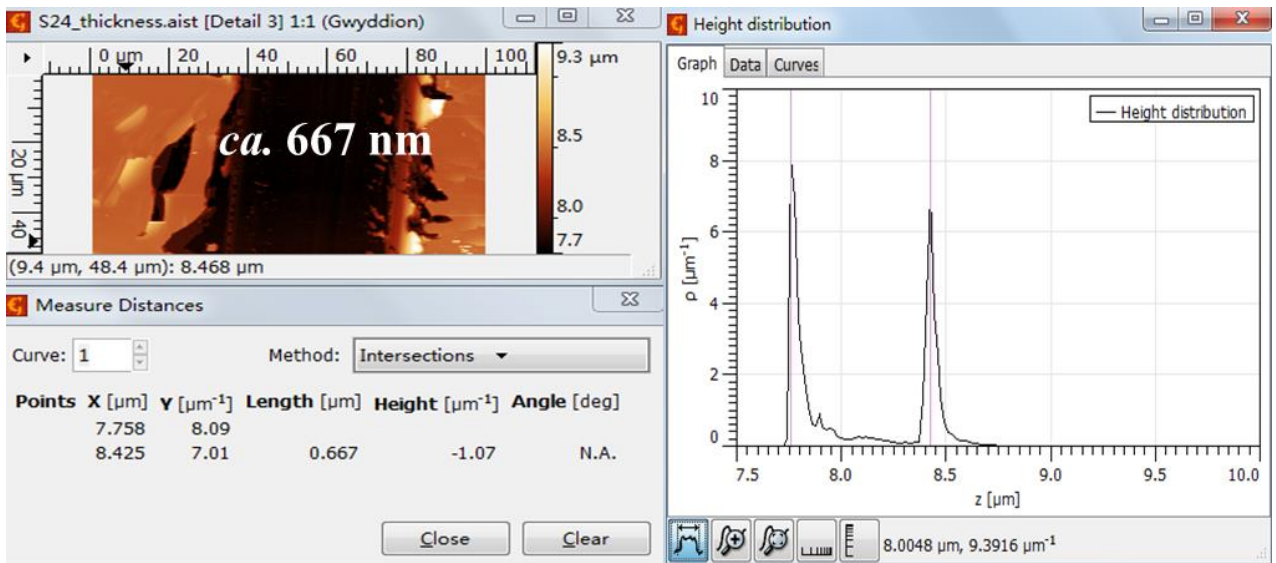
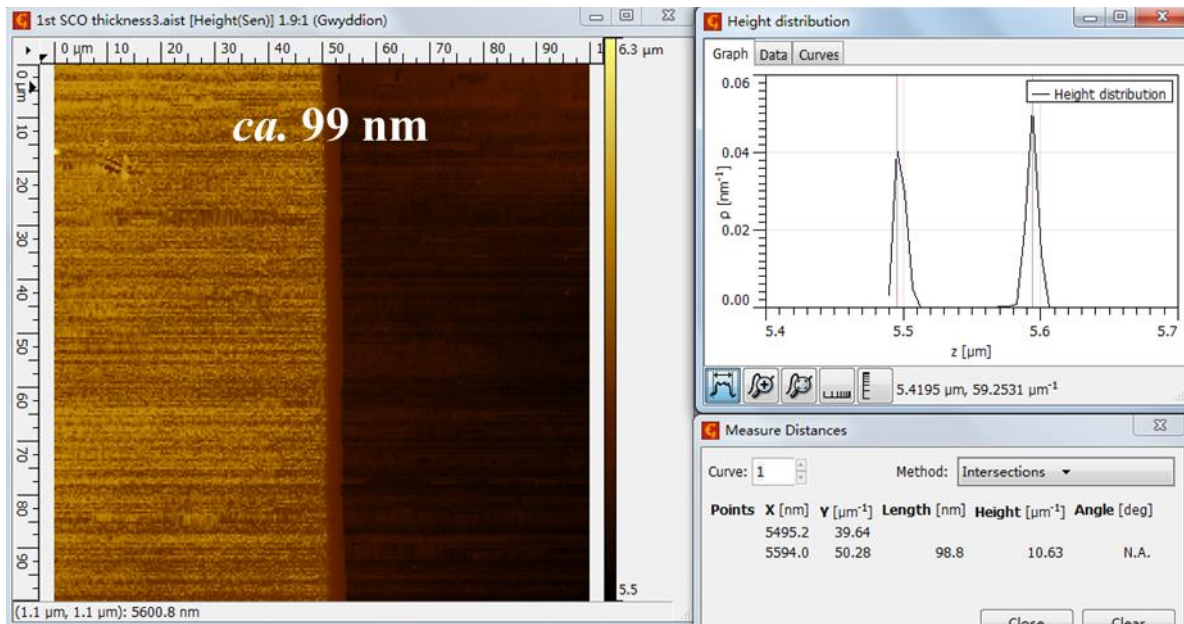
Therefore, in my opinion, using non-stoichiometric condition (ligand:salt >2:1) and washed by water would be one of the solutions to increase the purity of $[\text{Fe}(\text{HB}(\text{tz})_3)_2]$, which had been verified by mass spectrum and IR spectrum.

A2.1.4 Variable-temperature optical reflectivity spectrum of $[\text{Fe}(\text{HB}(\text{tz})_3)_2]$ complex of different batch of samples.

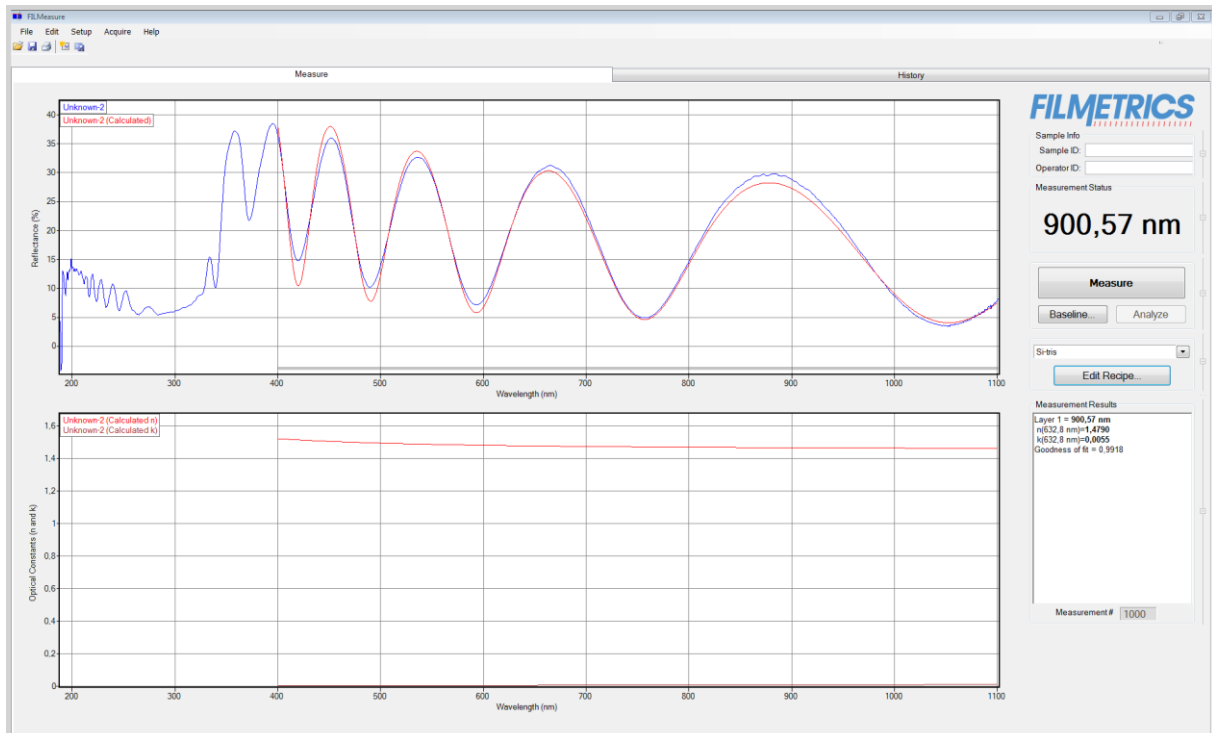
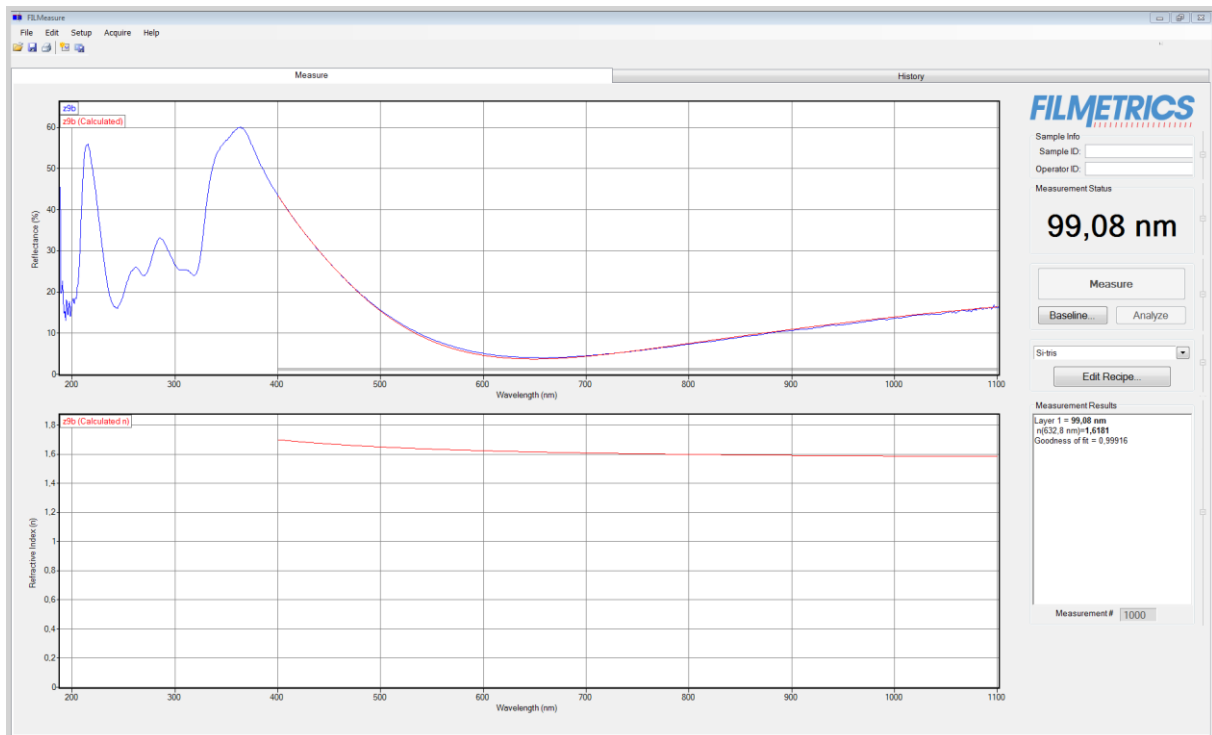


A2.2 Characterizations of thin films.

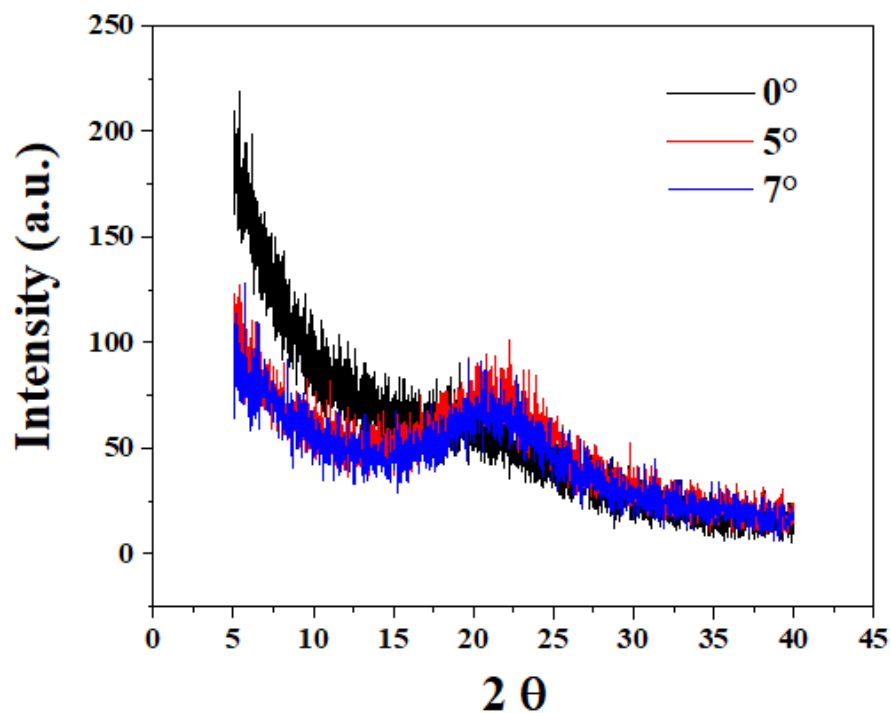
A2.2.1 Thickness characterizations by AFM, representative results of $[\text{Fe}(\text{HB}(\text{tz})_3)_2]$ thin film (ca. 99 nm) and thick film (ca. 667 nm).



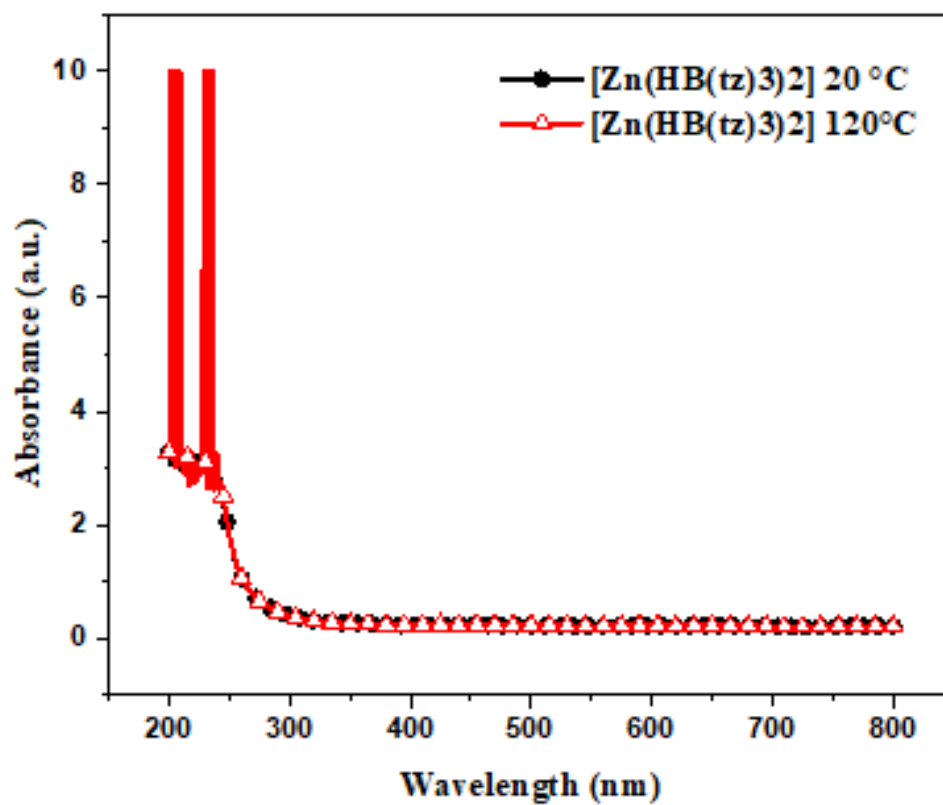
A2.2.2 Thickness characterizations by Filmetrics, representative results of thin film (ca. 100 nm) and thick film (ca. 900 nm).



A2.2.3 GIXRD (with the glazing incident of 0° , 5° and 7°) of as-deposited $[\text{Fe}(\text{HB}(\text{tz})_3)_2]$ thin films on the fused silica substrates.



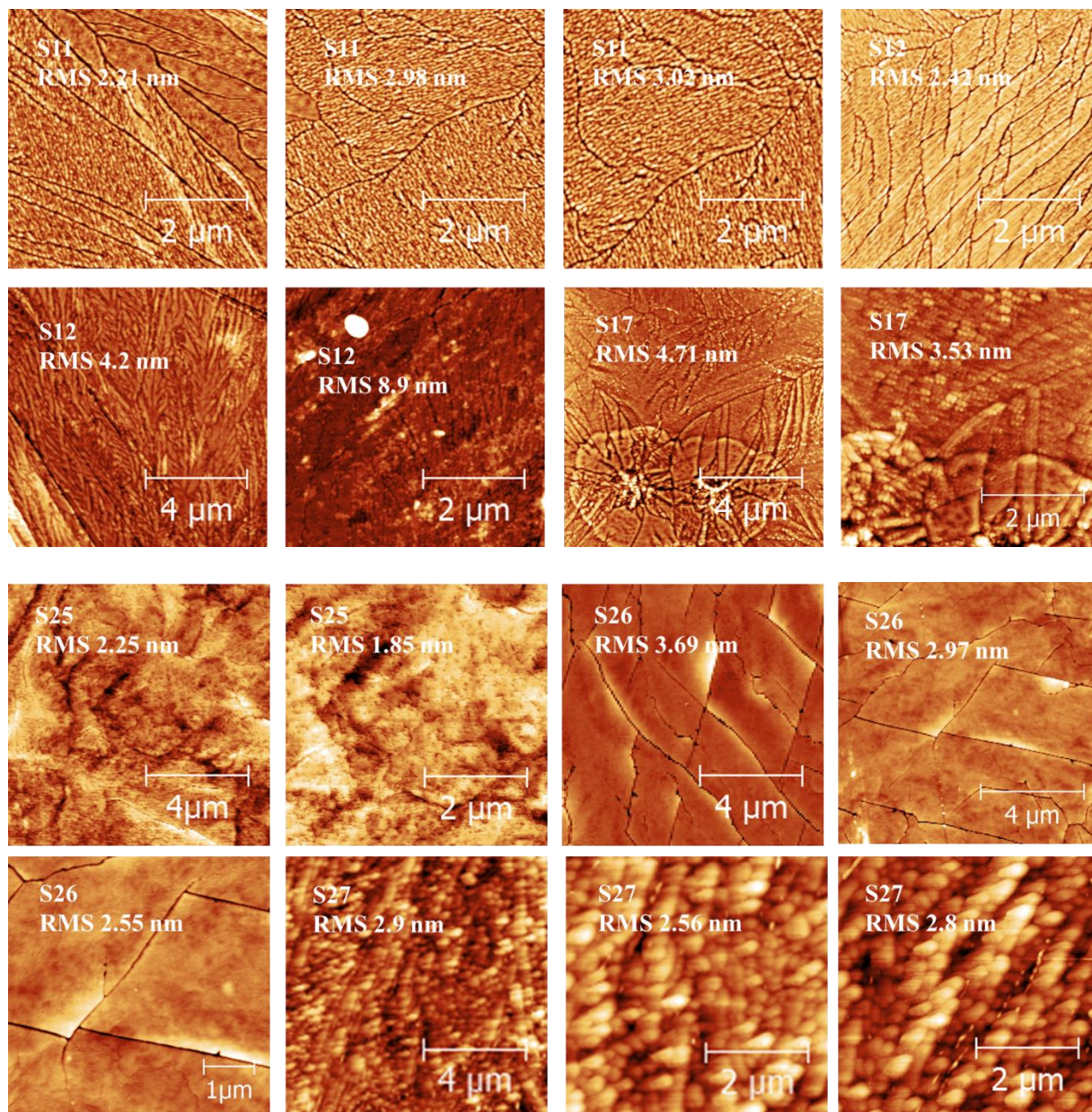
A2.2.4 UV-Vis absorption spectrum of the $[\text{Zn}(\text{HB}(\text{tz})_3)_2]$ thin films.

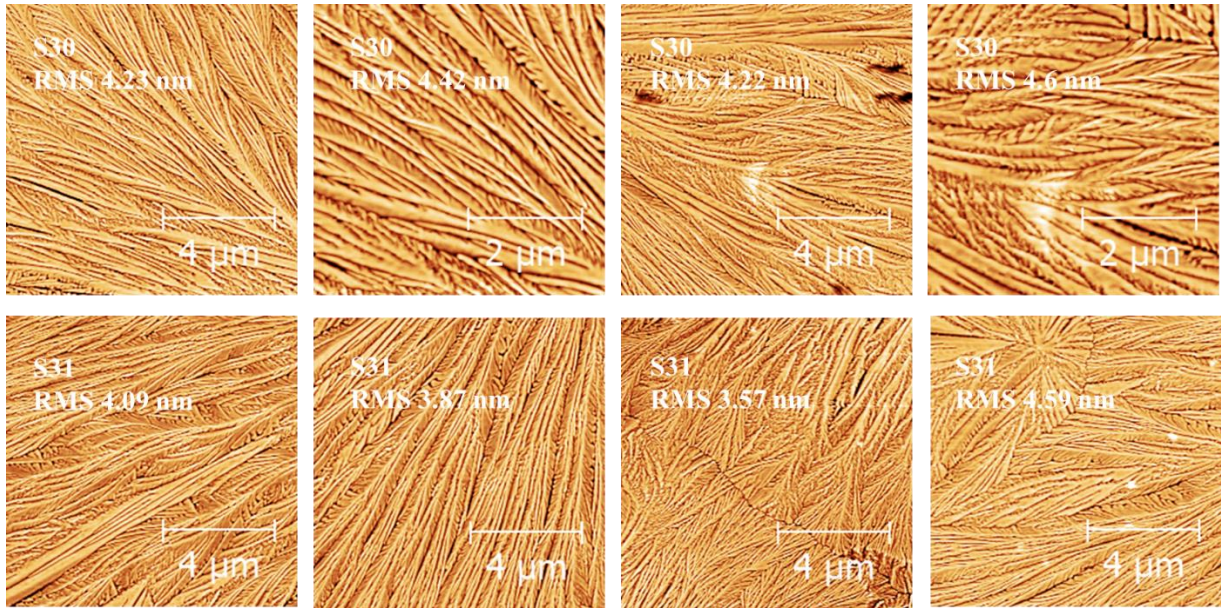


A2.2.5 Surface morphologies (AFM graphs) of annealed $[\text{Fe}(\text{HB}(\text{tz})_3)_2]$ thin films.

Samples prepared by PREVAC thermal evaporation system:

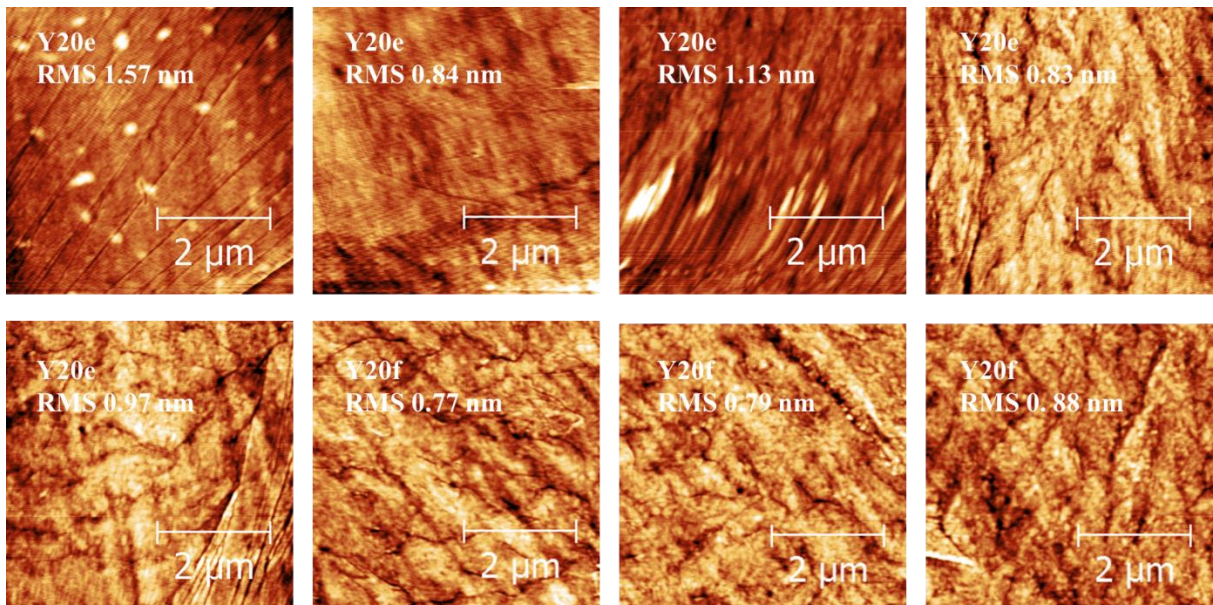
(Note that the samples were deposited in different batches, the substrates were washed by acetone and ethanol for 5 minutes, respectively)

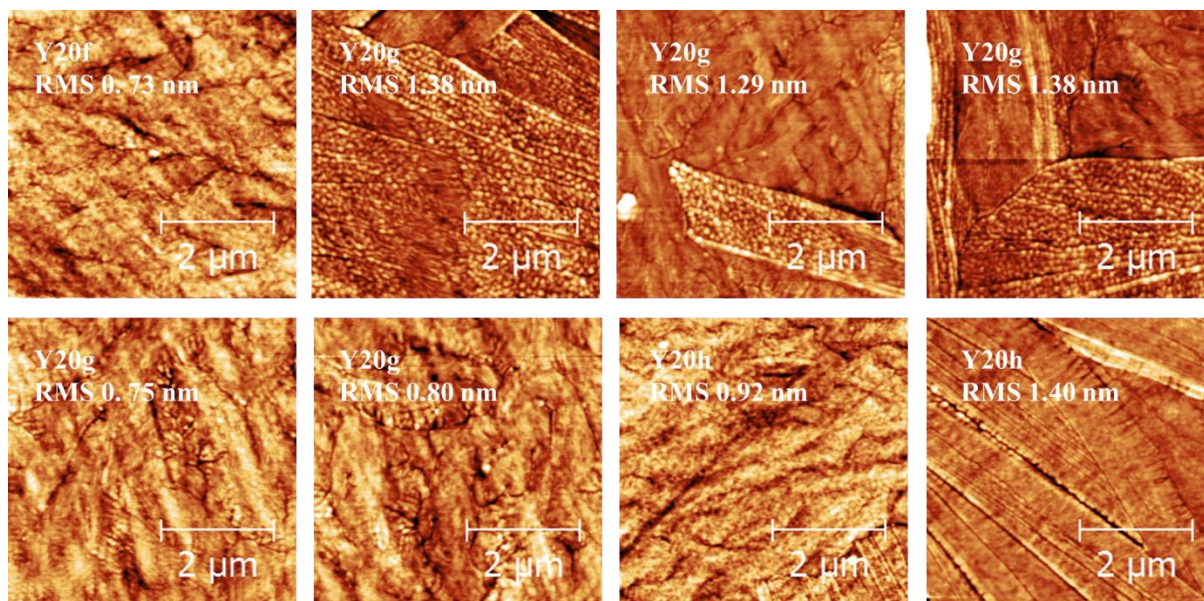




Samples prepared by PLASSYS thermal evaporation system:

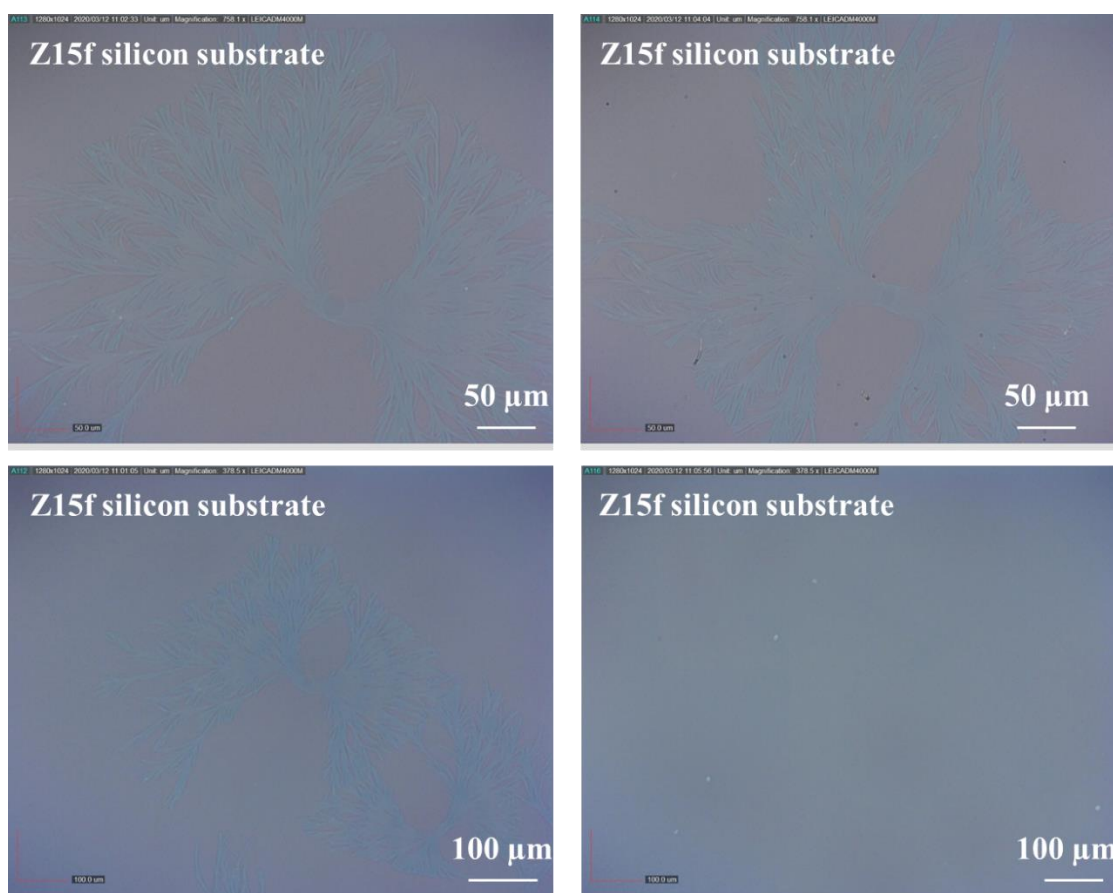
(Note that the samples were deposited in different batches, the substrates were rinsed successively by acetone (VLSI, 99.5%) and ethanol (VLSI, 99.9%) for 5 minutes under sonication. The substrates were dried by a nitrogen gas flow and followed by UV/O₃ treatment for 10 minutes.)

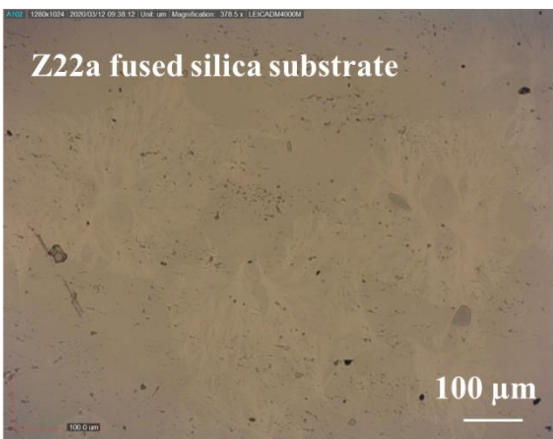
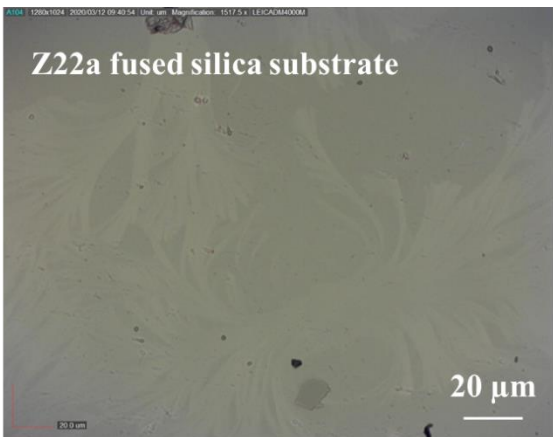
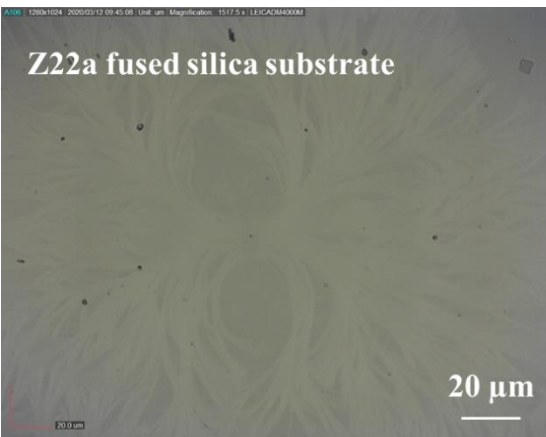
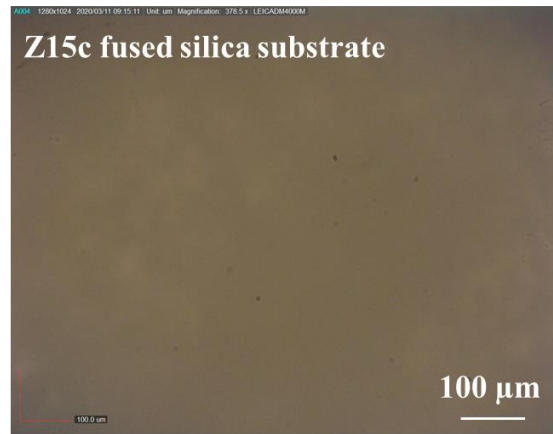
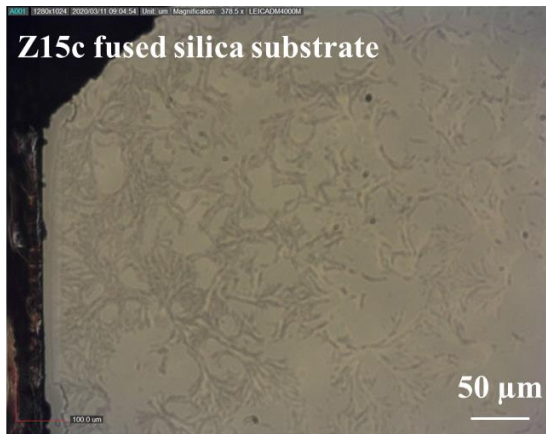
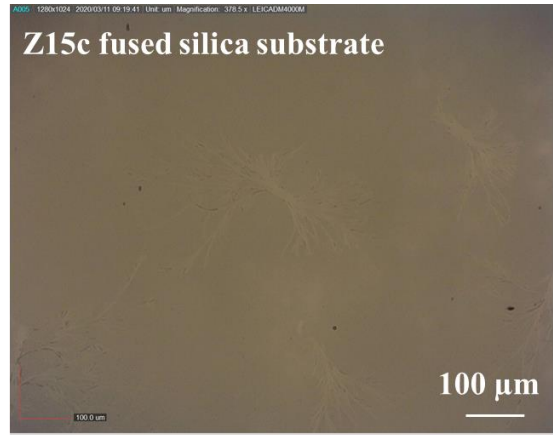
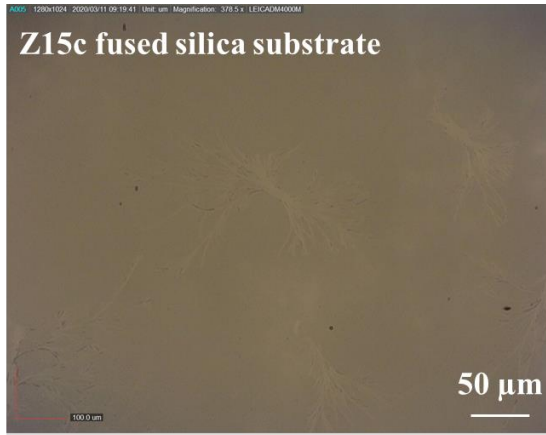




A2.2.6 Surface morphologies (optical microscope graphs) of annealed $[\text{Fe}(\text{HB}(\text{tz})_3)_2]$ thin films.

(Note that the samples were deposited in different batches, the substrates were rinsed successively by acetone and ethanol for 5 minutes under sonication. The substrates were dried by a nitrogen gas flow and followed by UV/O₃ treatment for 10 minutes.)





A2.2.7 UV-vis spectra of annealed [Fe(HB(tz)₃)₂] thin films by different batch.

Sample (Z7a is 80 nm, the rest samples are 100 nm)	SVA treatment	Δ_{abs} (318 nm)	$T_{1/2} \uparrow$	$T_{1/2} \downarrow$
Z7a	74-77% for 1h	0.21	65 °C	65 °C
Z9a	72-77% for 1h	0.31	65 °C	64 °C
Z10a	75-79% for 1h	0.31	66 °C	61 °C
Z11a	72-77% for 40 min	0.30	67 °C	66 °C
Z12a	72-80 for 40 min	0.32	66 °C	64 °C
Z13a	64-74% for 40 min, during this, above 73% for 10 min	0.33	65 °C	64 °C

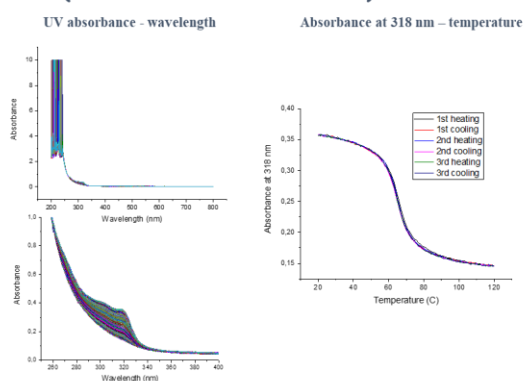
Description:

Z7a, 9a, 10a, 11a, 12a and 13a are quartz witness sample,

SVA treatment condition :

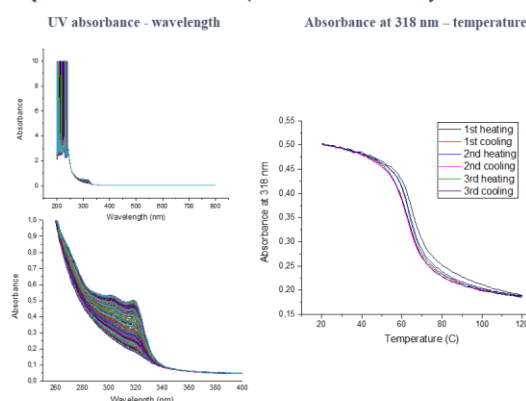
Z7: 16:55(74%) 17:00(74%) 17:05(75%) 17:10(76%) 17:15(77%) 17:20(77%) 17:25(77%)
17:30(76%) 17:35(77%) 17:40(76%) 17:45(76%) 17:50(77%) 17:55(77%)
Z8: 11:52(75%) 11:57(72%) 12:02(73%) 12:07(74%) 12:12(75%) 12:17(75%) 12:22(76%)
12:27(75%) 12:32(76%) 12:37(76%) 12:42(76%) 12:47(76%) 12:52(77%)
Z9: 11:50(78%) 11:55(75%) 12:00(76%) 12:05(77%) 12:10(79%) 12:15(79%) 12:20(78%)
12:25(78%) 12:35(79%) 12:40(77%) 12:45(78%) 12:50(79%)
Z10: 11:15(73%) 11:20(72%) 11:25(73%) 11:30(75%) 11:35(75%) 11:40(75%) 11:45(75%)
11:50(75%) 11:55(76%)
Z11: 15:57(73%) 15:59(71%) 16:06(72%) 16:09 (73%) 16:12(74%) 16:17(75%) 16:22(75%)
Z12: 10:35(78%) 10:43(72%) 10:46(78%) 11:05(79%)
Z13: 11:12(70%) 11:18(64%) 11:23(66%) 11:26(67%) 11:28(68%) 11:37(71%) 11:41(73%)
11:41(73%) 11:44(74%) 11:49(74%) 11:51(73%)

Z7a (witness for 80 nm on MEMS)



Sample	Δ_{abs} (318 nm)	$T_{1/2} \uparrow$	$T_{1/2} \downarrow$
Z7a	0.21	65 °C	65 °C

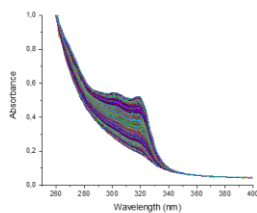
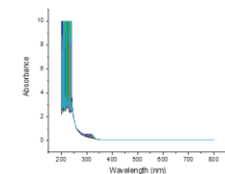
Z9a (Witness for 100 nm, also 710a-Z13a)



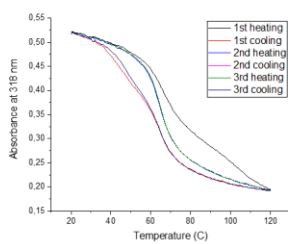
Sample	Δ_{abs} (318 nm)	$T_{1/2} \uparrow$	$T_{1/2} \downarrow$
Z9a 1st	0.31	66 °C	63 °C
Z9a 2nd	0.31	65 °C	63 °C
Z9a 3rd	0.31	65 °C	64 °C

Z10a

UV absorbance - wavelength



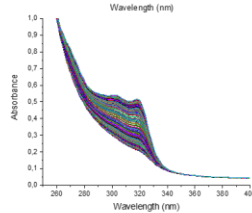
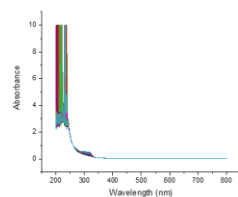
Absorbance at 318 nm - temperature



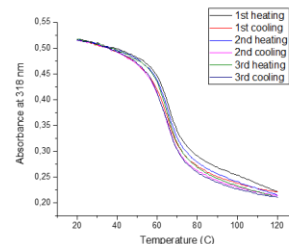
Sample	Δ abs (318 nm)	$T_{1/2} \uparrow$	$T_{1/2} \downarrow$
Z10a 1st	0.31	72 °C	61 °C
Z10a 2nd	0.31	66 °C	61 °C
Z10a 3rd	0.31	66 °C	61 °C

Z11a

UV absorbance - wavelength



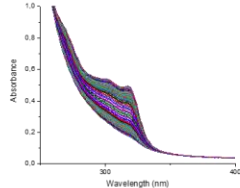
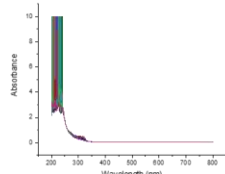
Absorbance at 318 nm - temperature



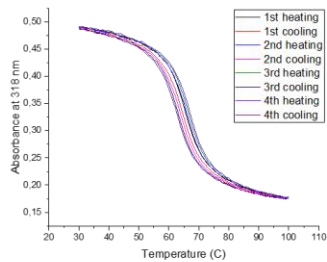
Sample	Δ abs (318 nm)	$T_{1/2} \uparrow$	$T_{1/2} \downarrow$
Z11a 1st	0.29	67 °C	65 °C
Z11a 2nd	0.30	67 °C	65 °C
Z11a 3rd	0.30	67 °C	66 °C

Z12a

UV absorbance - wavelength



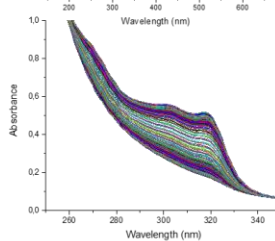
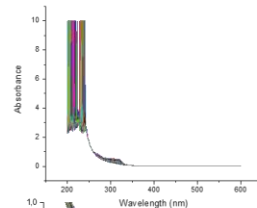
Absorbance at 318 nm - temperature



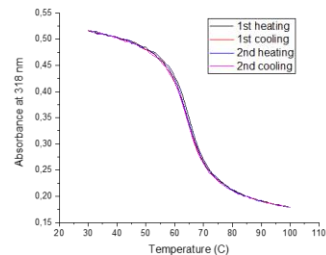
Sample	Δ abs (318 nm)	$T_{1/2} \uparrow$	$T_{1/2} \downarrow$
Z12a 1st	0.32	65 °C	64 °C
Z12a 2nd	0.32	66 °C	64 °C
Z12a 3rd	0.32	66 °C	64 °C
Z12a 4th	0.32	67 °C	63 °C

Z13a

UV absorbance - wavelength



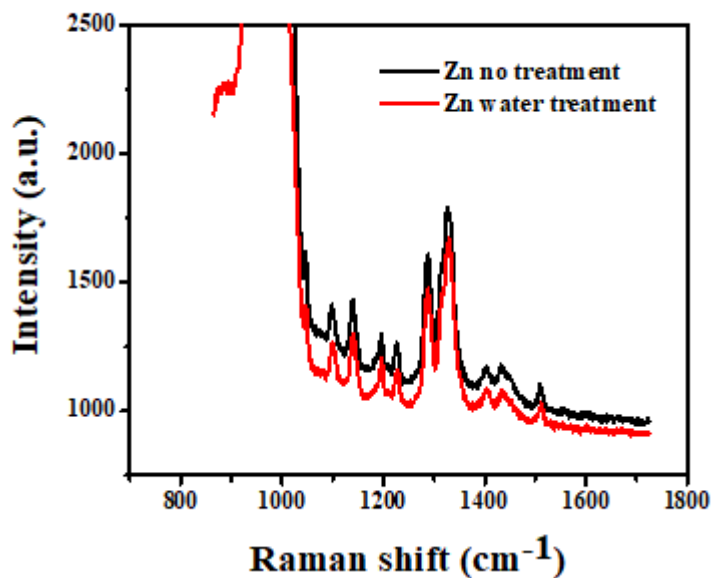
Absorbance at 318 nm - temperature



Sample	Δ abs (318 nm)	$T_{1/2} \uparrow$	$T_{1/2} \downarrow$
Z13a 1st	0.33	65 °C	64 °C
Z13a 2nd	0.33	65 °C	64 °C

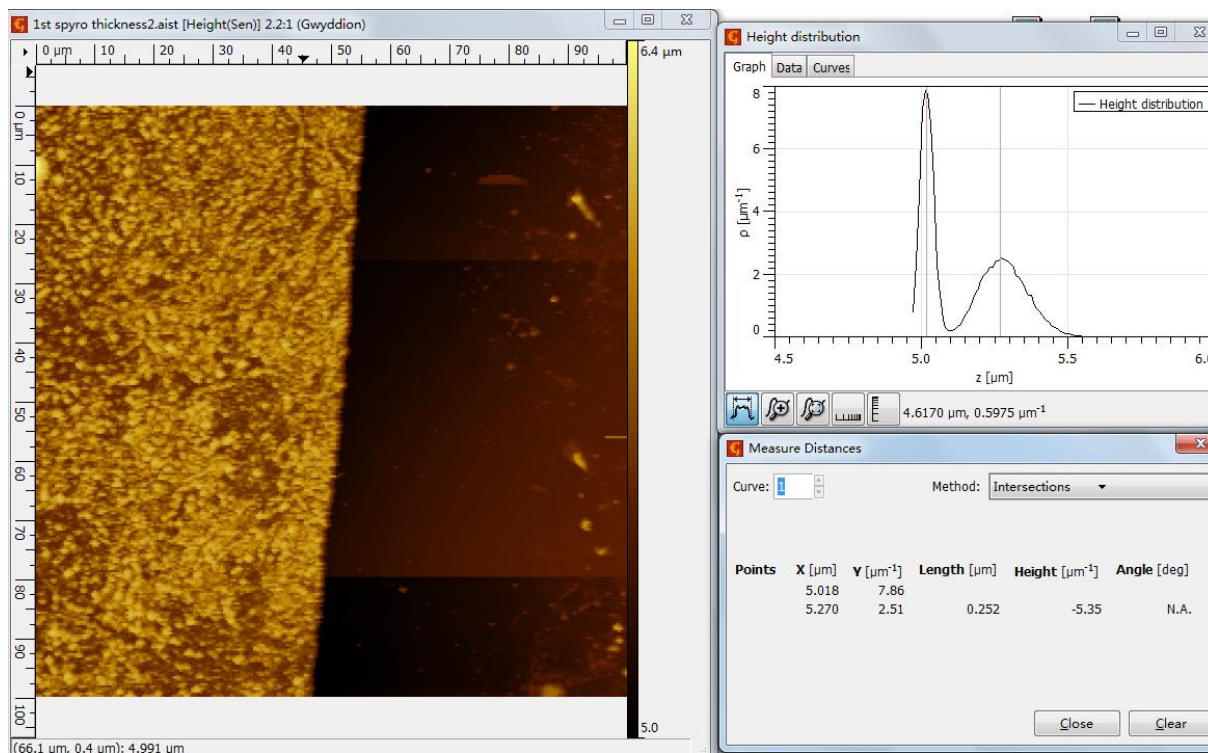
A2.2.8 Characterizations of other thin films.

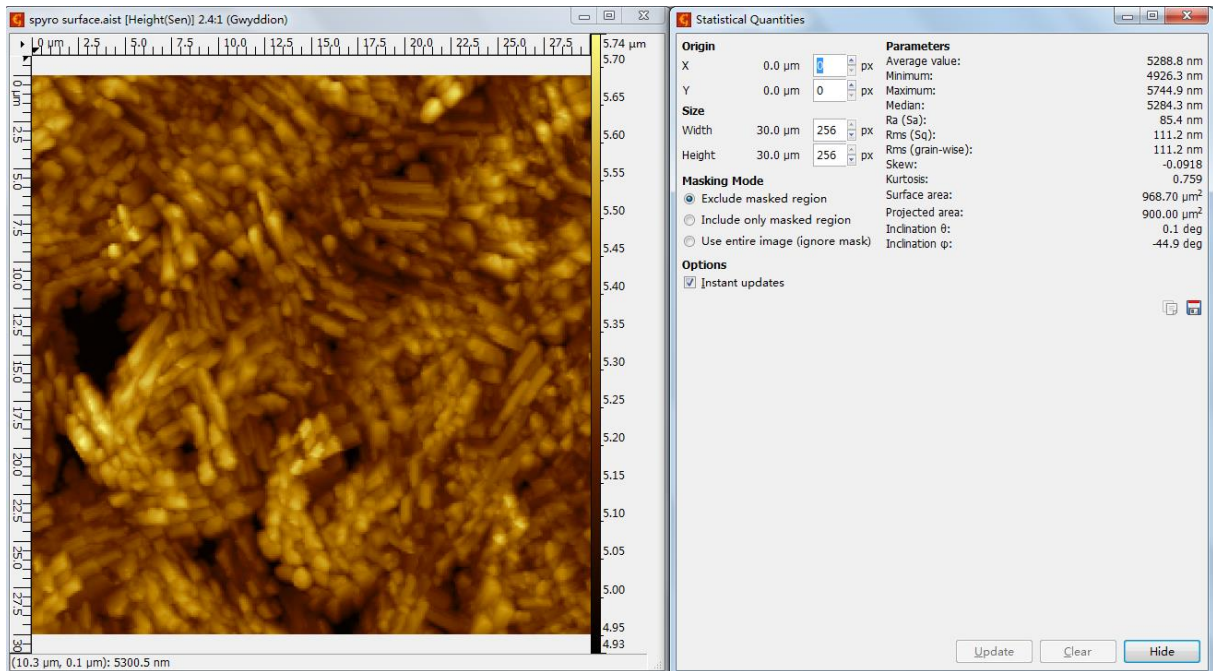
A2.2.8.1 Raman spectra of $[\text{Zn}(\text{HB}(\text{tz})_3)_2]$ thin films (water annealed and without water annealed).



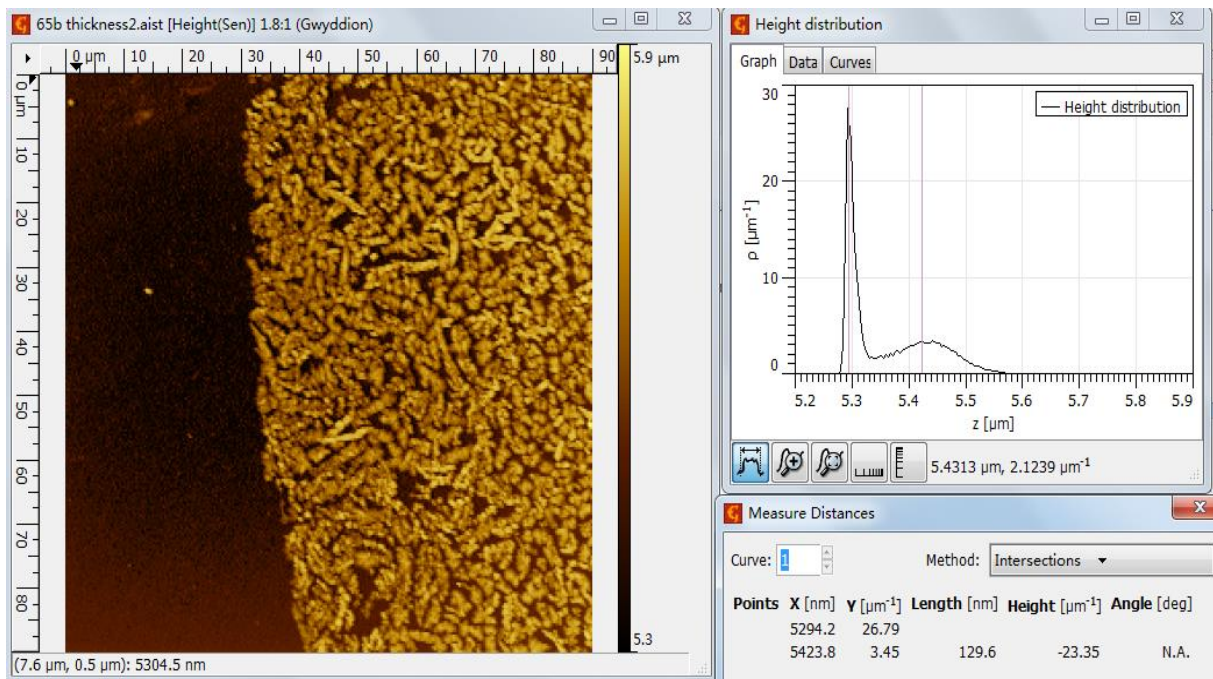
A2.2.8.2 Thickness and morphology of thermal evaporated spiropyran thin films.

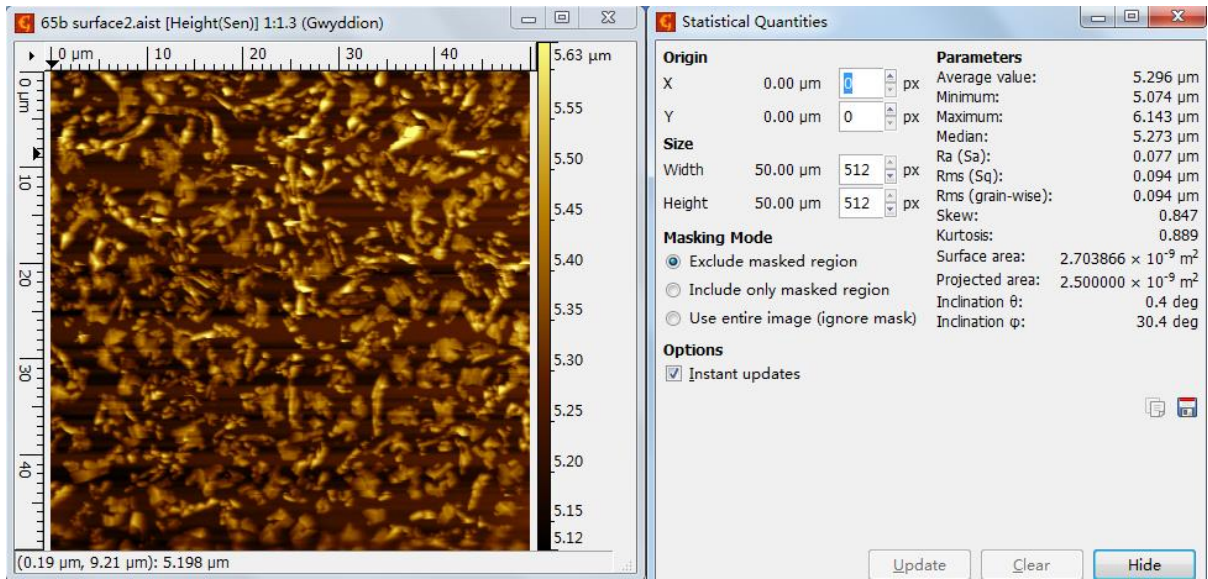
Ca. 252 nm thick film:



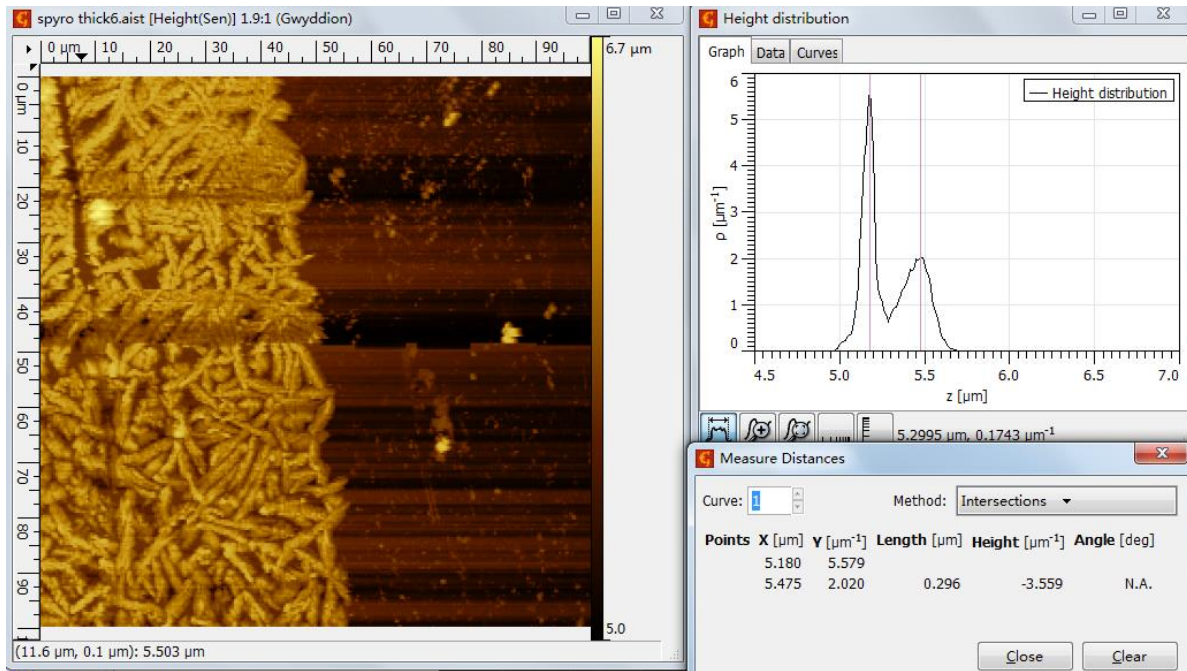


Ca. 130 nm thick film:



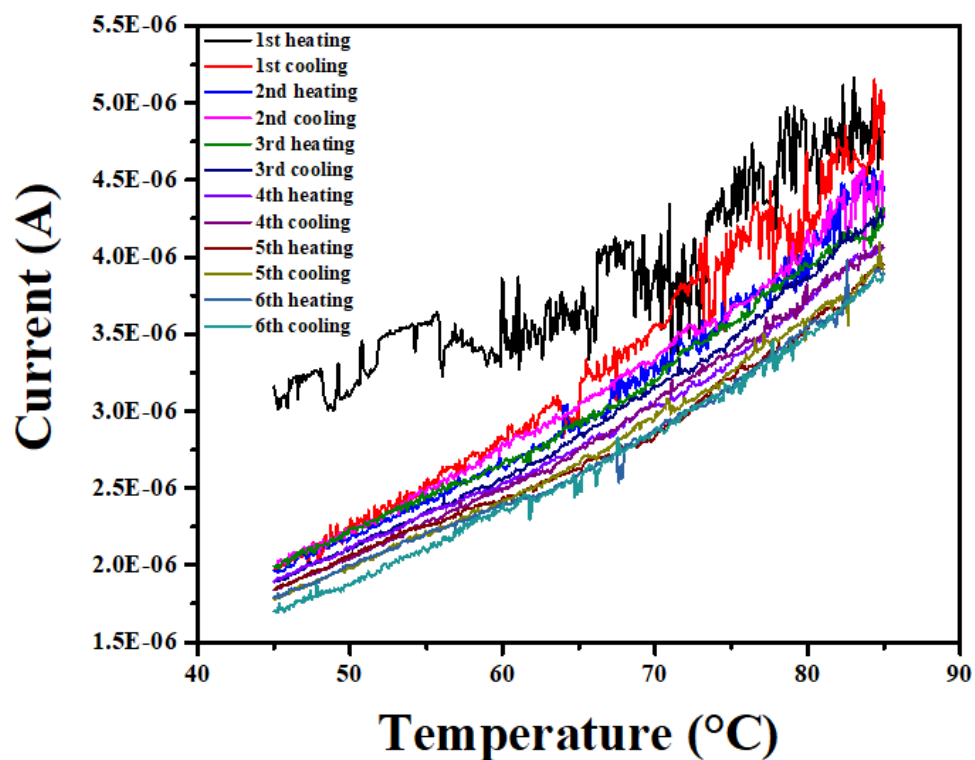


Ca. 296 nm thick film:

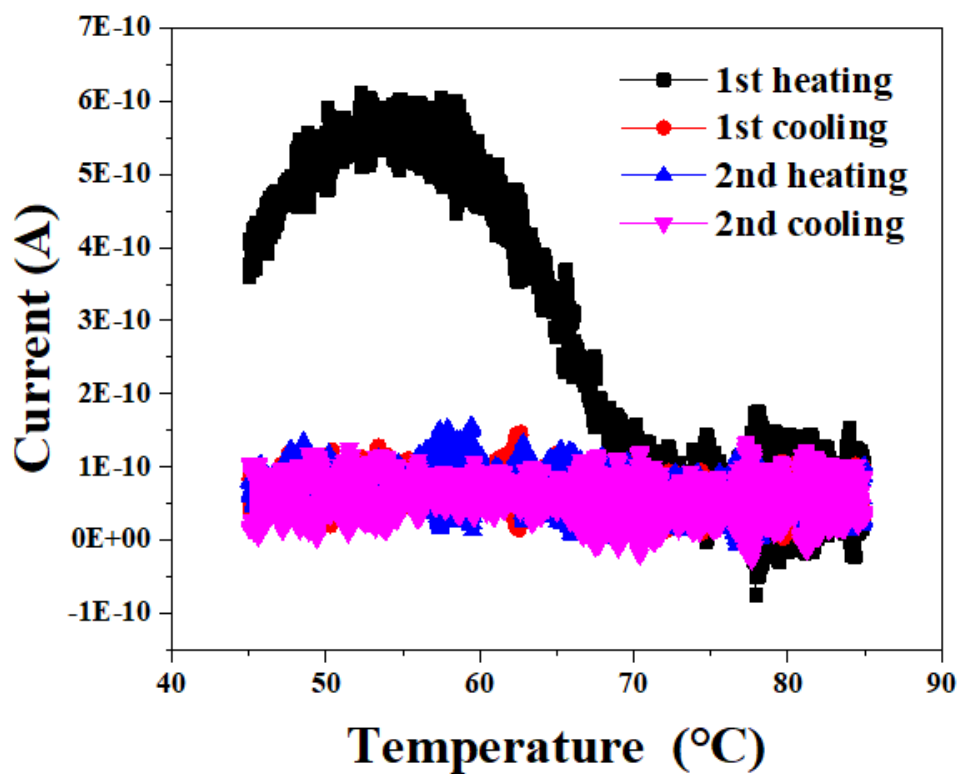


A2.3 Characterizations of multilayer two-terminal devices.

A2.3.1 Characterizations of [Zn(HB(tz)₃)₂]-based two-terminal devices. (5V, 5°C/min)



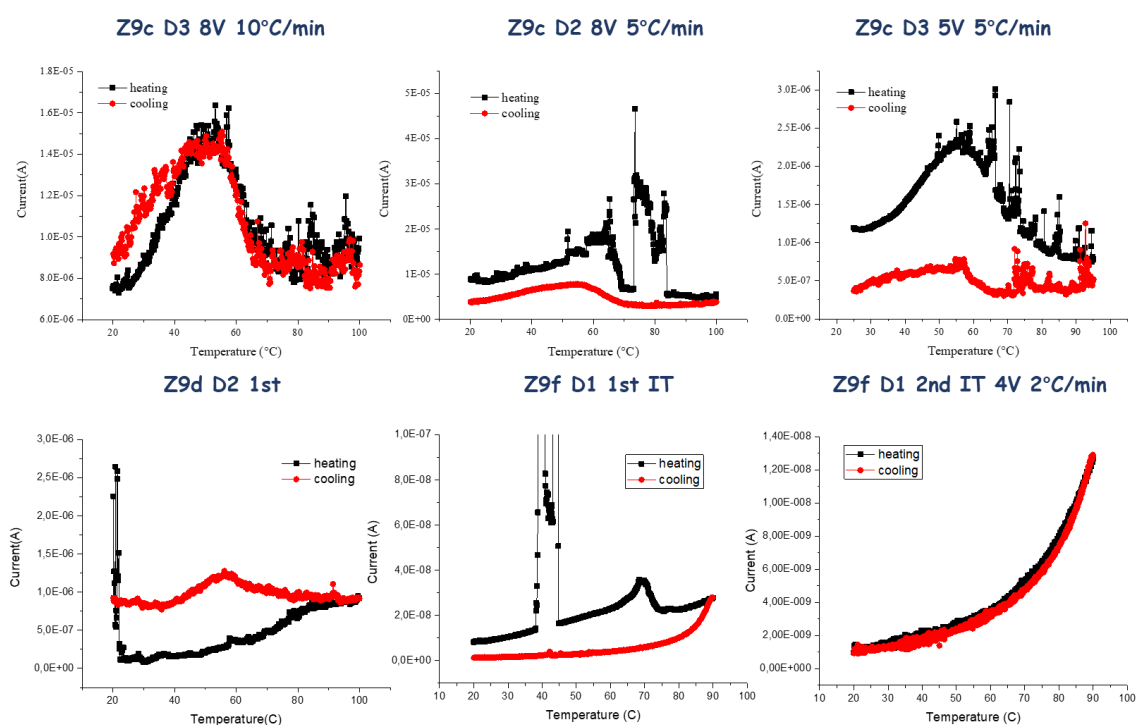
A2.3.2 Characterizations of “1-year aged” non-encapsulated ITO/100 nm [Fe(HB(tz)₃)₂]/Al junction at 2V.

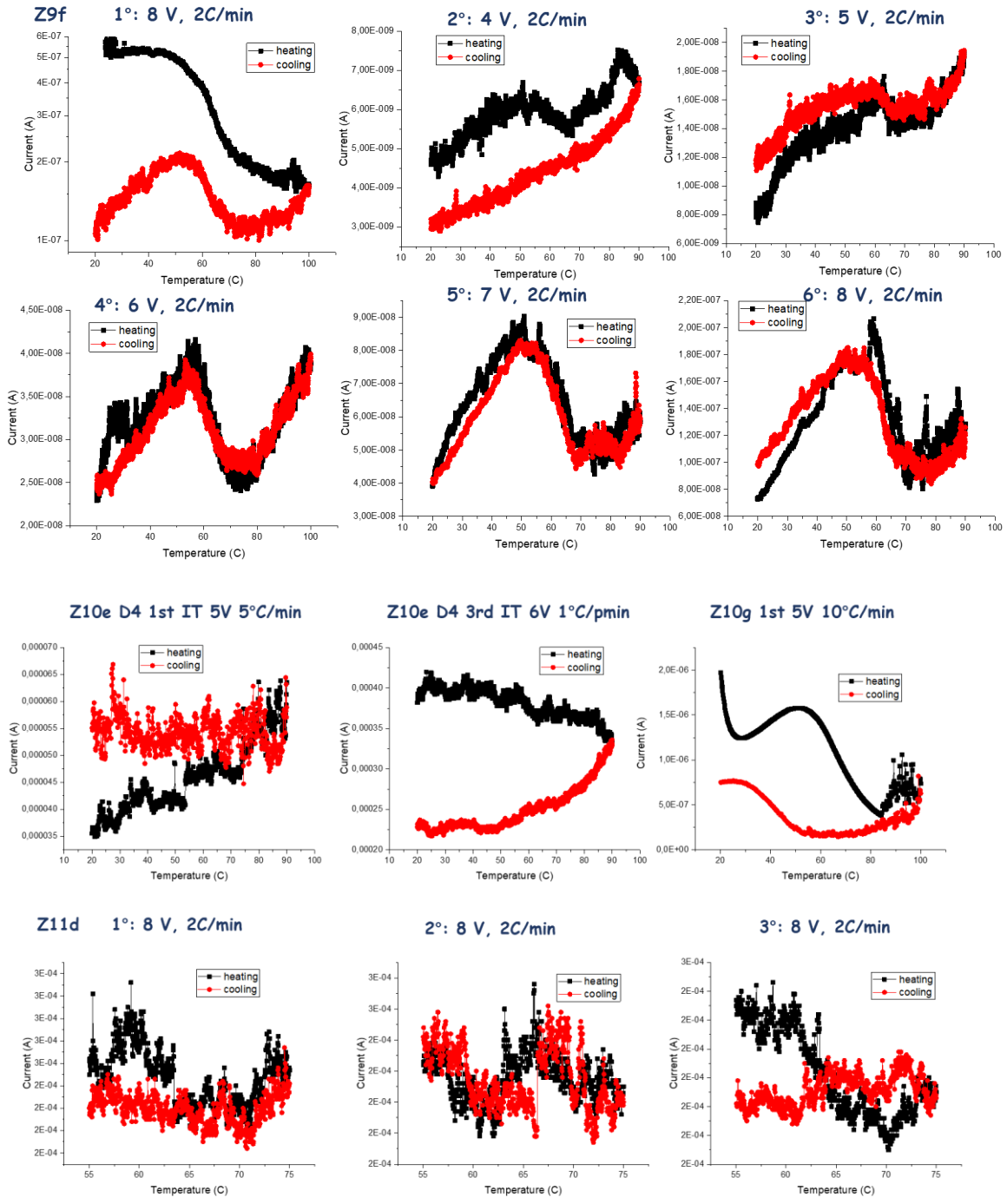


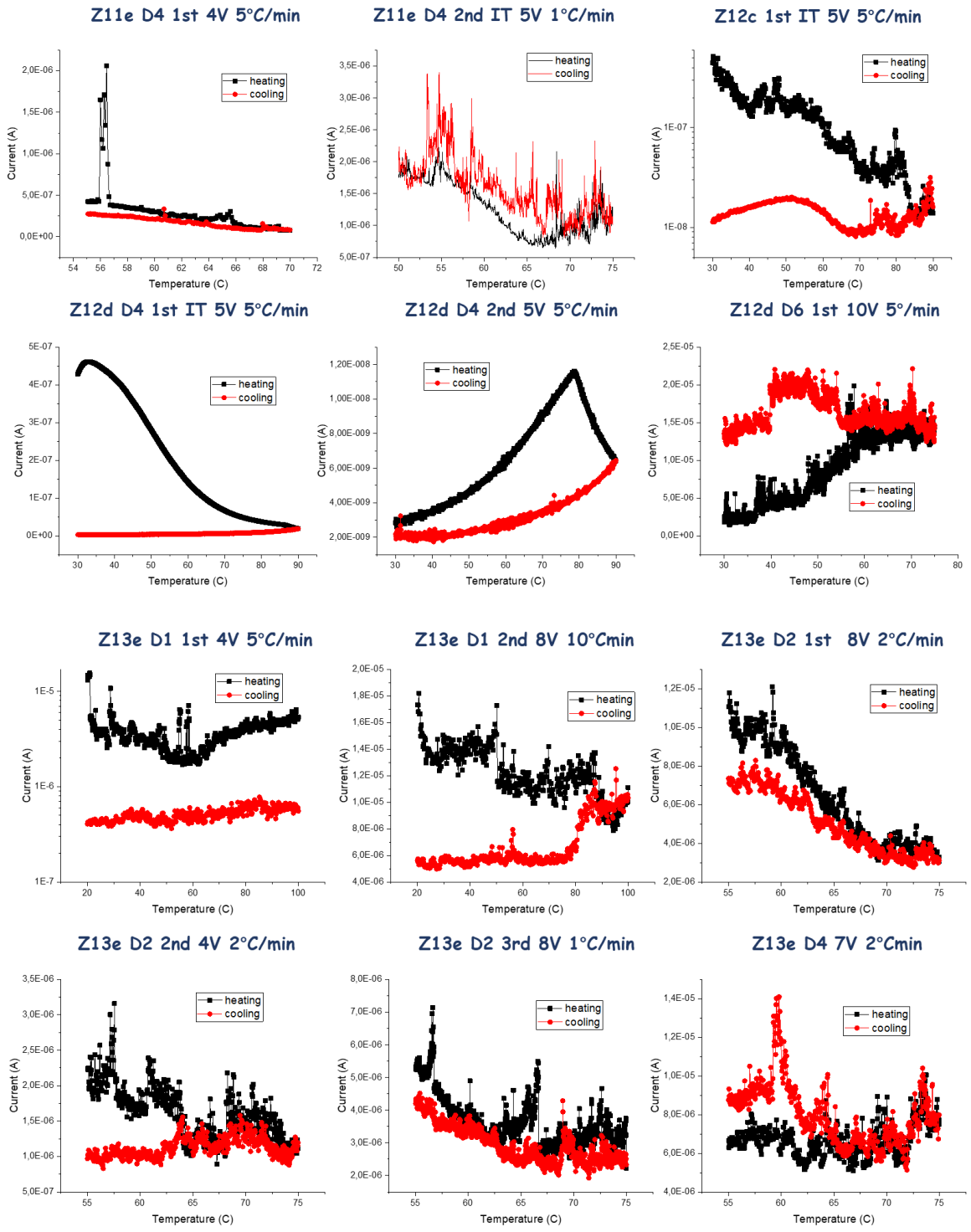
A2.3.3 Characterizations of other [Fe(HB(tz)₃)₂]-based two-terminal devices.

Device	Structure
Z9c (S14)	ITO/100 nm SCO/Al, encapsulated
Z9d (S19)	ITO/100 nm SCO/2 nm Liq/Al, encapsulated
Z9e (S16)	ITO/7 nm HAT-CN/100 nm SCO/Al, without encapsulated
Z9f (S23)	ITO/7 nm HAT-CN/100 nm SCO/2 nm Liq/Al, encapsulated
Z10d (S12)	ITO/100 nm SCO/Al, WVA, thermal annealing after SCO deposition, encapsulated
Z10e (S17)	ITO/100 nm SCO/Al, EVA, thermal annealing after SCO deposition, encapsulated
Z10f (S29)	ITO/100 nm SCO/Al, EVA, encapsulated
Z10g (S18)	ITO/100 nm SCO/Al, EVA, without encapsulation
Z11c (S12)	ITO/100 nm SCO/Al, encapsulated
Z11d (S20)	ITO/100 nm SCO/Al, plasma treated. encapsulated
Z11e (S25)	ITO/100 nm SCO/Al, plasma treated, without encapsulation
Z11f (S26)	ITO/100 nm SCO/2 nm Liq/ Al, encapsulation
Z12c (S11)	ITO/100 nm SCO/Al, encapsulated
Z12d (S02)	ITO/pedot/100 nm SCO/Al, encapsulated
Z12e (S26)	ITO/ 100 nm SCO/Liq/Al, encapsulated
Z12f (S09)	ITO/pedot/100 nm SCO/2 nm Liq/ Al, encapsulated
Z13e (S16)	ITO/100 nm SCO/Al, thermal annealing, encapsulated
Z13f (S17)	ITO/100 nm SCO/Al, encapsulated
Z13g (S18)	ITO/PEDOT/100 nm SCO/ Al, encapsulated
Z13h (S20)	ITO/PEDOT/100 nm SCO/Al, thermal annealing, encapsulated

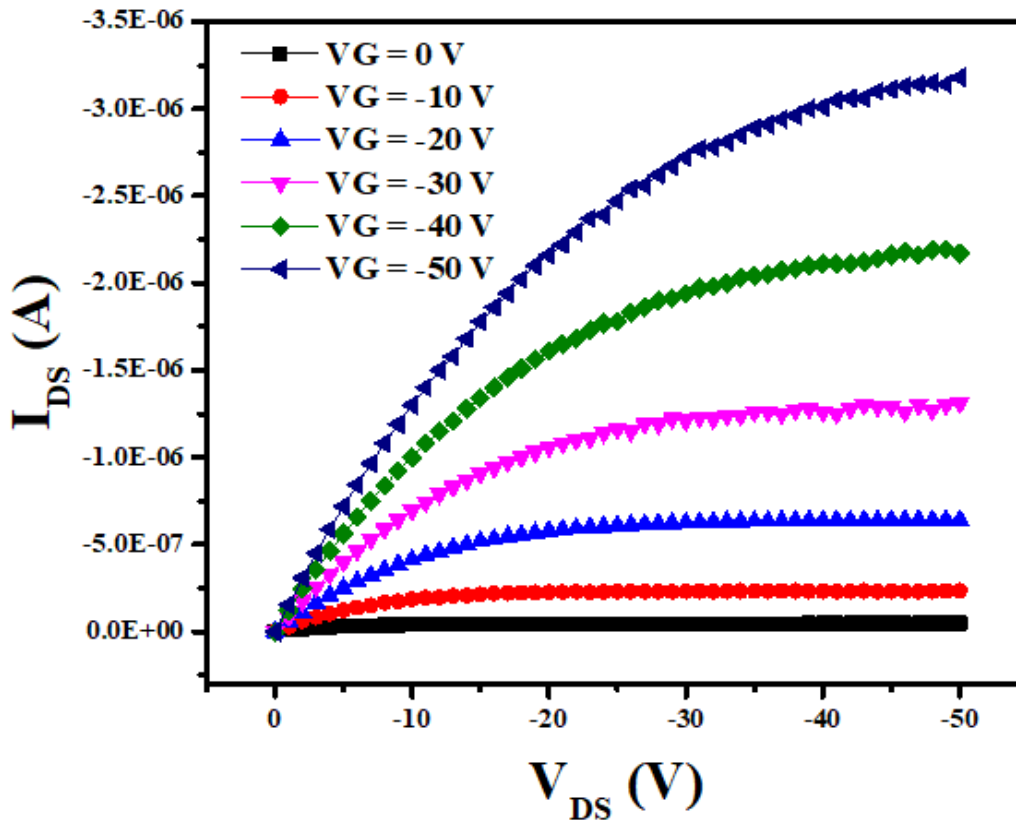
Representative I-T characteristics (even the ‘standard device’ did not show the expected characteristics):







A3.1 Output characteristics of Device A (without SCO)



A3.2 OFETs degradation tests under vacuum.

To better understand temperature's effect on the OFETs, we carried out another four successive temperature dependent current characterization on a standard device. These data was recorded under a vacuum of 1×10^{-3} mbar to remove doubts of water / oxygen of the ambient environment that may influence the aging test, even though the device had been encapsulated. The details of another four successive temperature dependent current characterization is listed in Table 3.1.

Table 3.1: Parameters of another four successive temperature dependent current characterization on a standard device.

Thermal cycles	Measurements (1×10^{-3} mbar vacuum)
1 st (45-85-45 °C)	I-T characteristic ($V_G = -30$ V, $V_{DS} = -10$ V), temperature interval = 1 °C, 20 °C/min
2 nd (45-85-45 °C)	I-T characteristic ($V_G = -30$ V, $V_{DS} = -10$ V), temperature interval = 1 °C, 20 °C/min
3 rd (35-55-35 °C)	I-T characteristic ($V_G = -30$ V, $V_{DS} = -10$ V), temperature interval = 1 °C, 10 °C/min
4 th (35-55-35 °C)	I-T characteristic ($V_G = -30$ V, $V_{DS} = -10$ V), temperature interval = 1 °C, 10 °C/min

I-T characteristics of these four thermal cycles is shown in Figure 3.2.

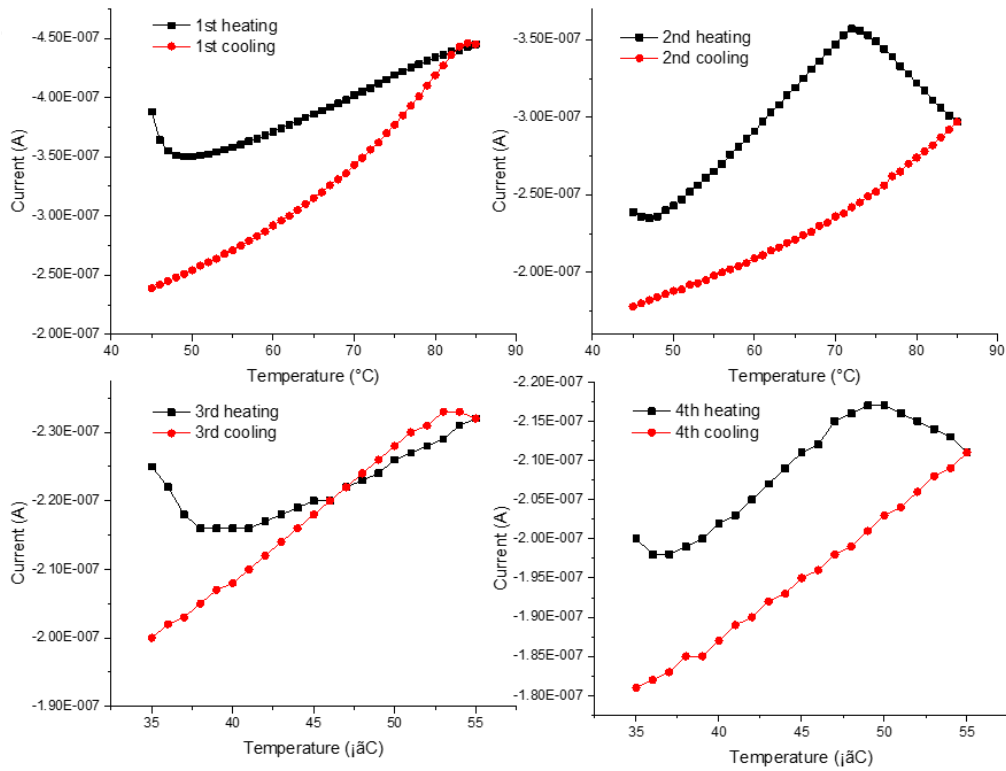
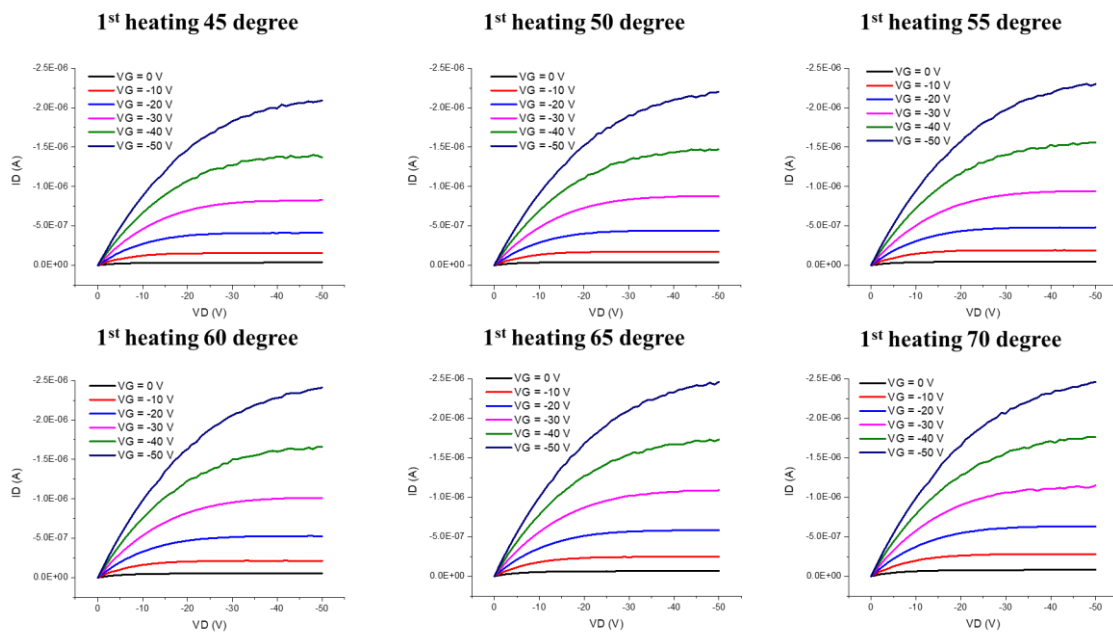


Figure 3.2: (a) Current-temperature (I-T) characteristics.

A3.3 Output and transfer characteristics in different temperatures of different OFETs.

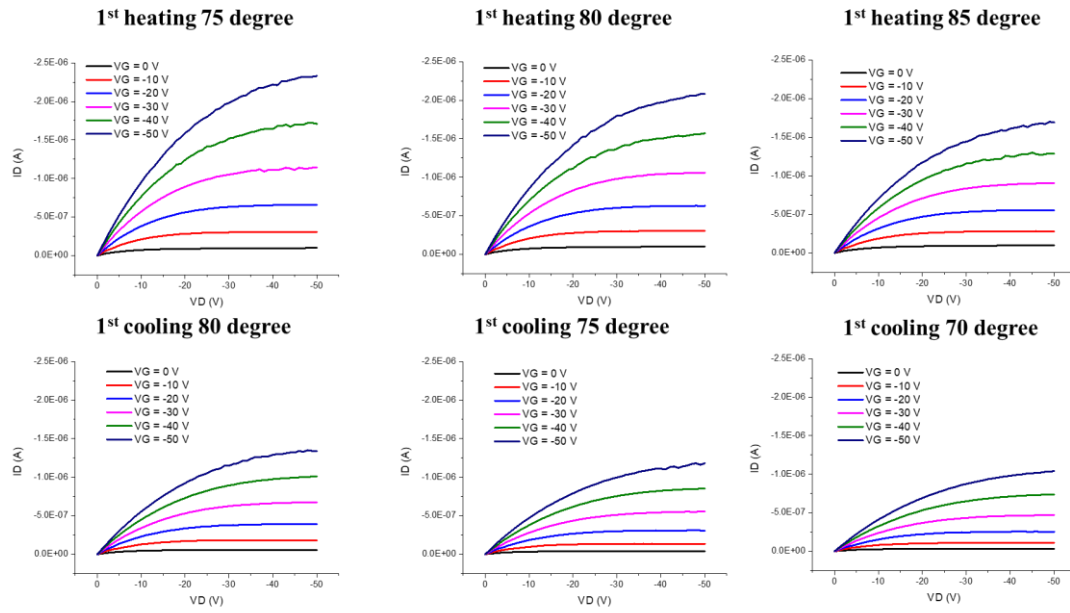
Output characteristics Bottom gate/bottom contact, without SCO, $W = 70 \mu\text{m}$, $L = 1000 \mu\text{m}$

TB4



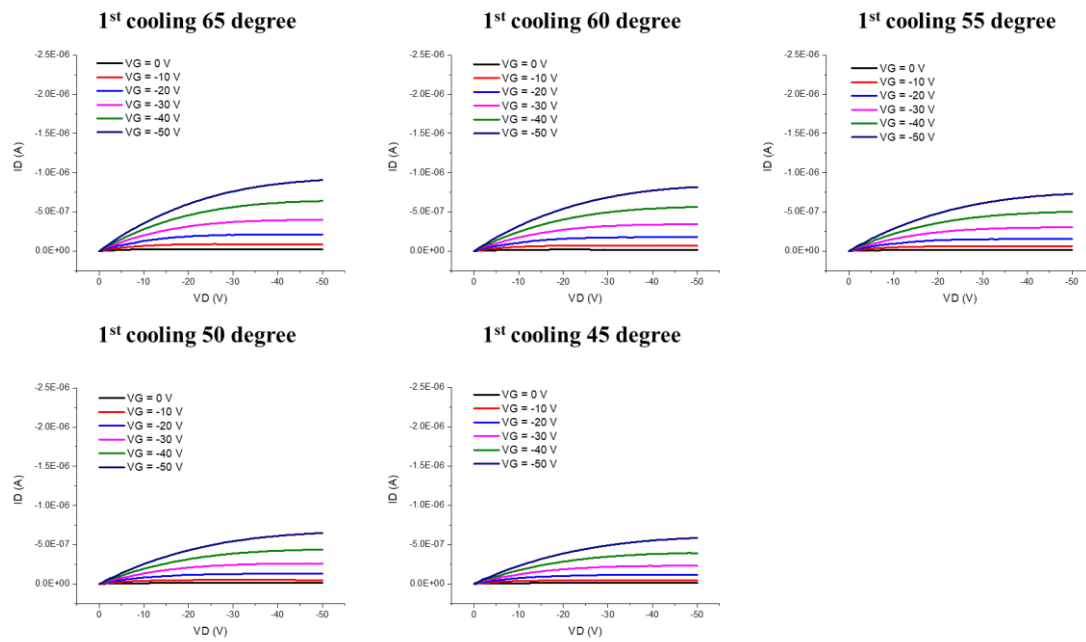
Output characteristics Bottom gate/bottom contact, without SCO, $W = 70 \mu\text{m}$, $L = 1000 \mu\text{m}$

TB4



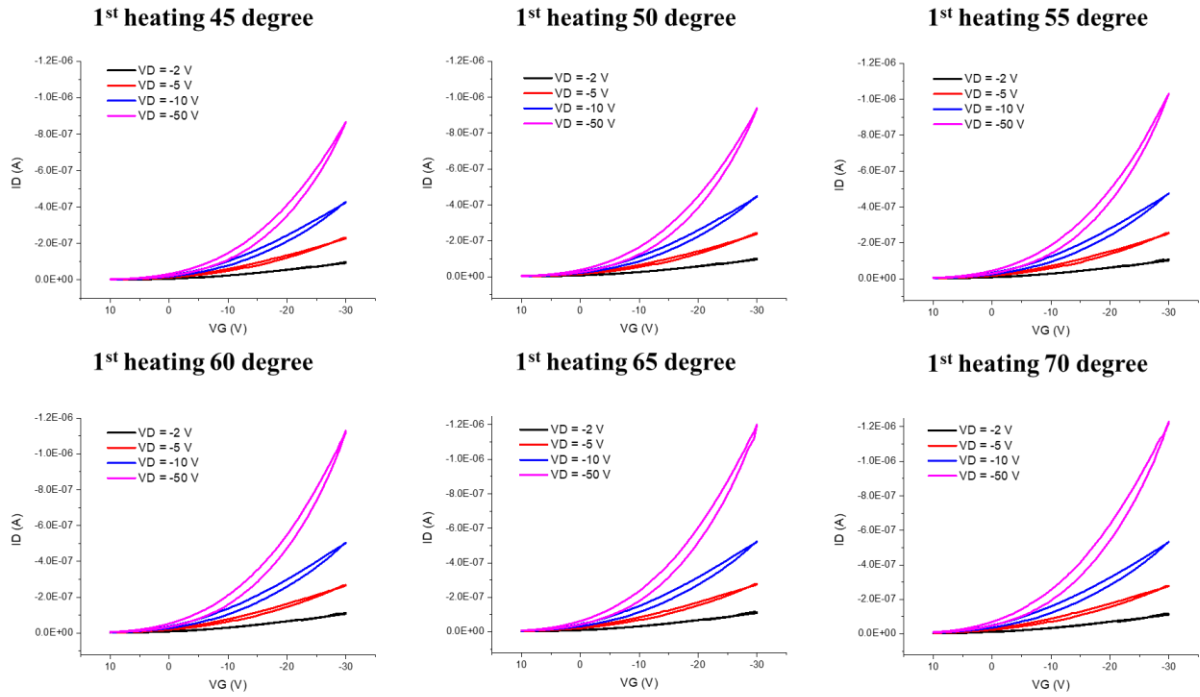
Output characteristics Bottom gate/bottom contact, without SCO, $W = 70 \mu\text{m}$, $L = 1000 \mu\text{m}$

TB4



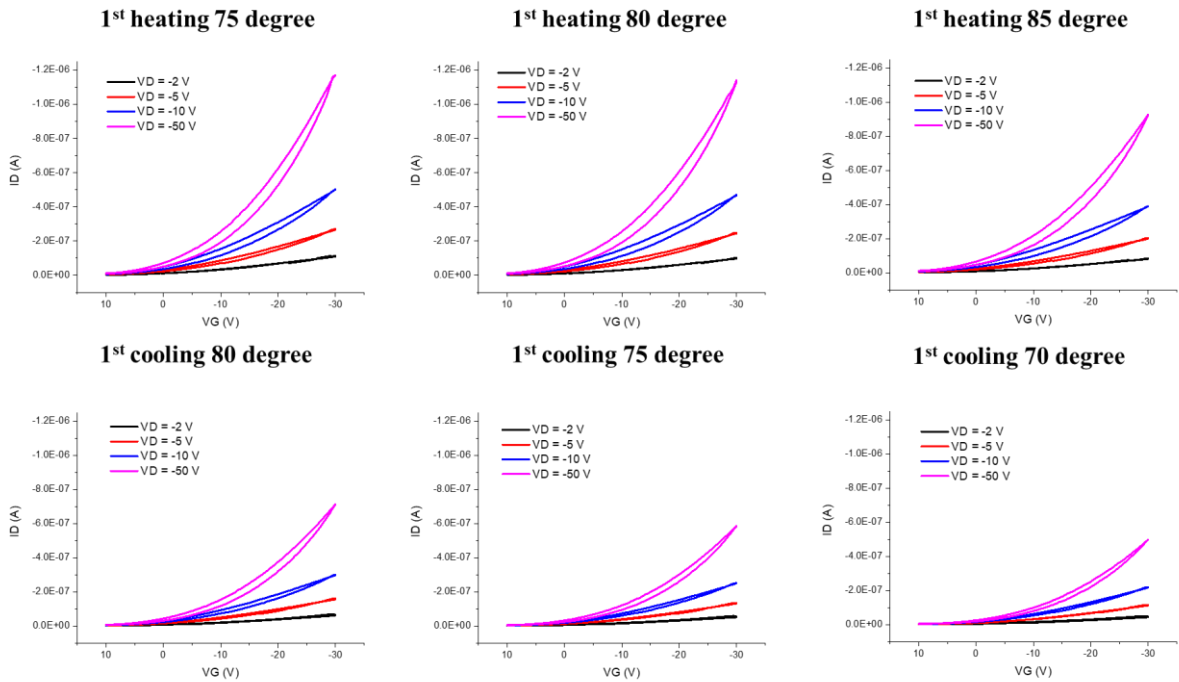
Transfer characteristics Bottom gate/bottom contact, without SCO, W = 70 μm, L = 1000 μm

TB4



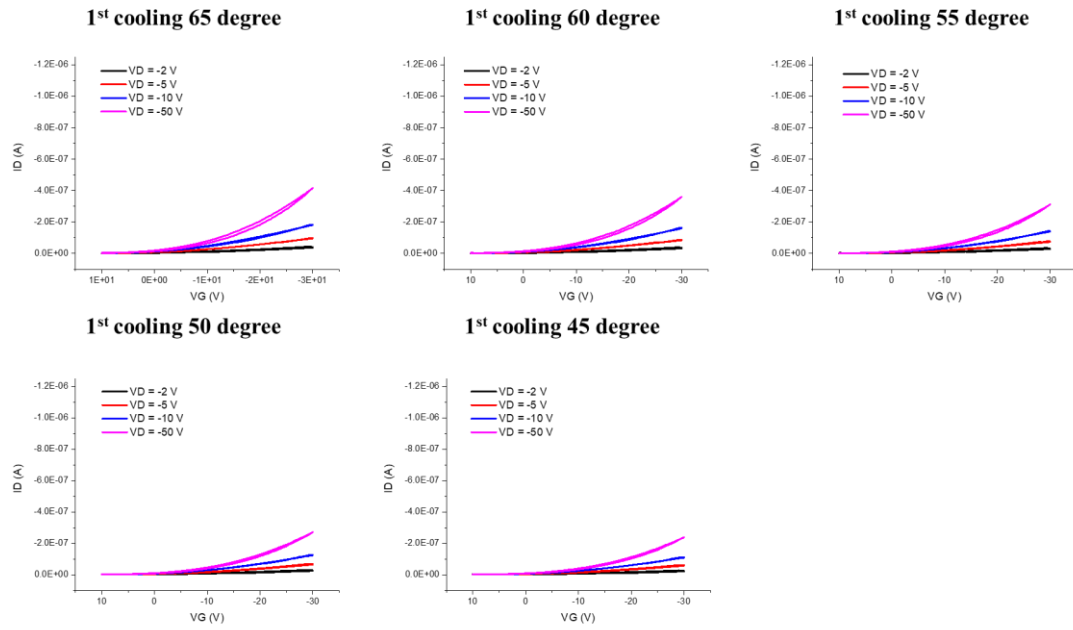
Transfer characteristics Bottom gate/bottom contact, without SCO, W = 70 μm, L = 1000 μm

TB4



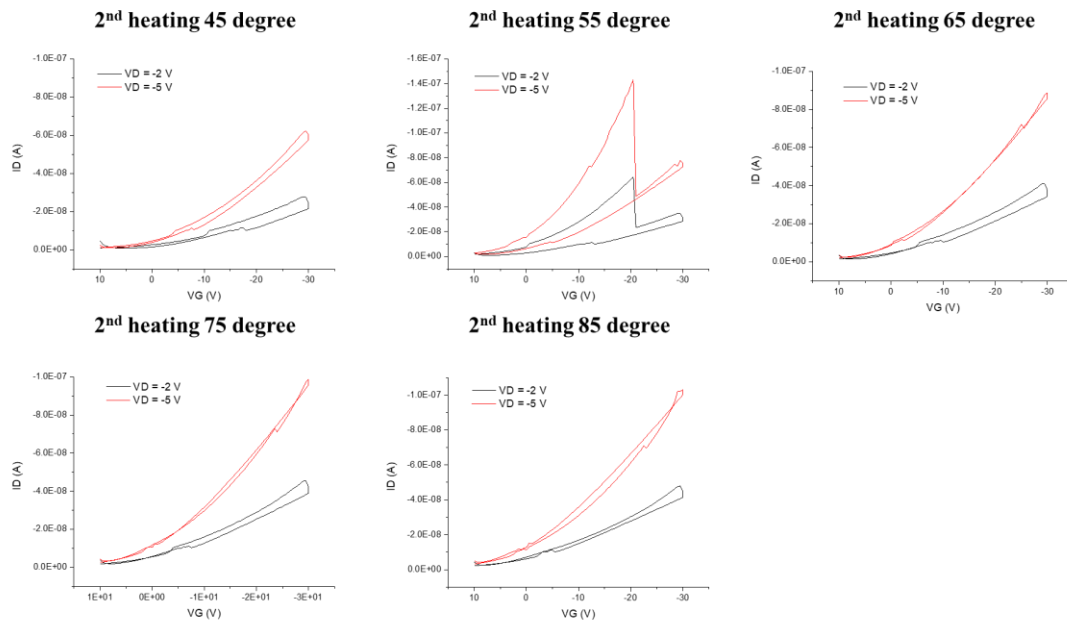
Transfer characteristics Bottom gate/bottom contact, without SCO, W = 70 μm, L = 1000 μm

TB4



Transfer characteristics Bottom gate/bottom contact, without SCO, W = 70 μm, L = 1000 μm

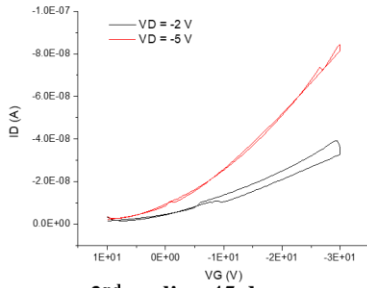
TB4



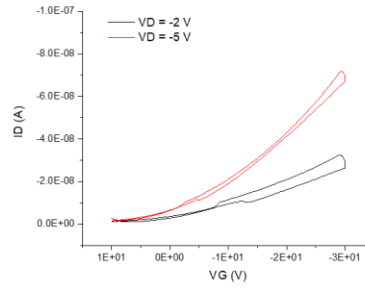
Transfer characteristics Bottom gate/bottom contact, without SCO, W = 70 μm, L = 1000 μm

TB4

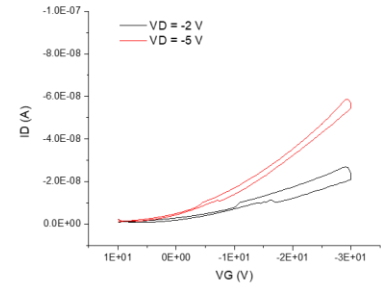
2nd cooling 75 degree



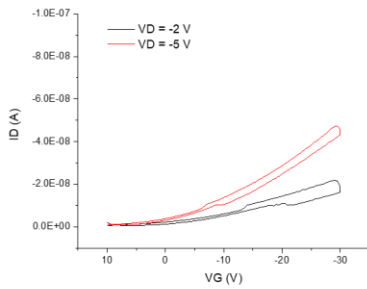
2nd cooling 65 degree



2nd cooling 55 degree



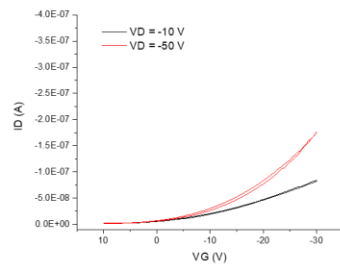
2nd cooling 45 degree



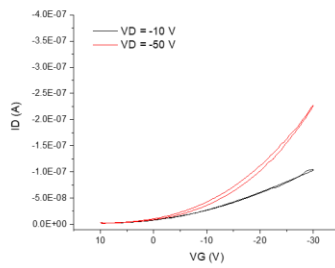
Transfer characteristics Bottom gate/bottom contact, without SCO, W = 70 μm, L = 1000 μm

TB4

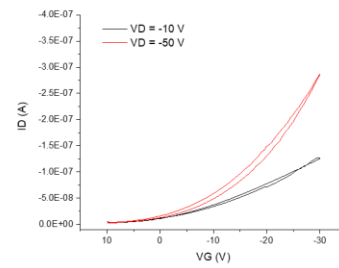
3rd heating 45 degree



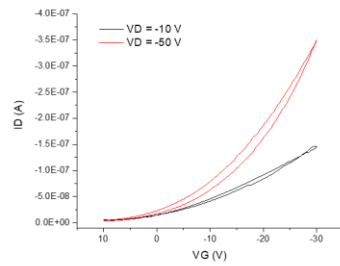
3rd heating 55 degree



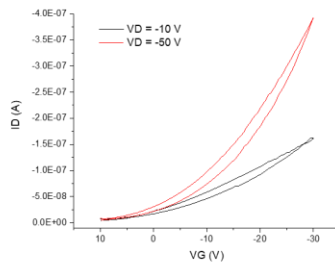
3rd heating 65 degree



3rd heating 75 degree

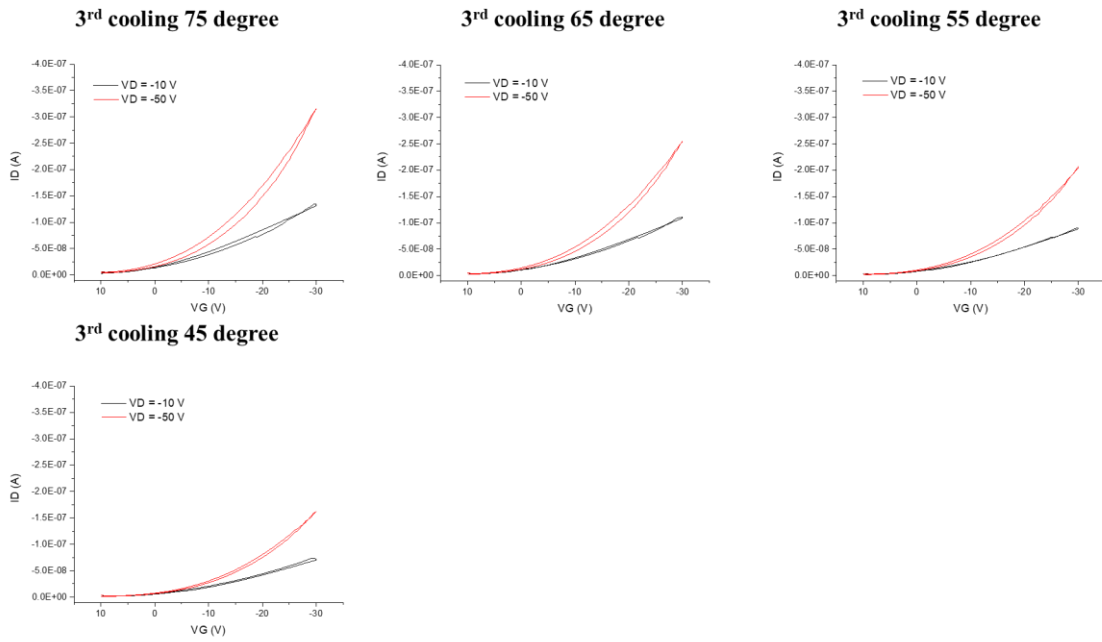


3rd heating 85 degree



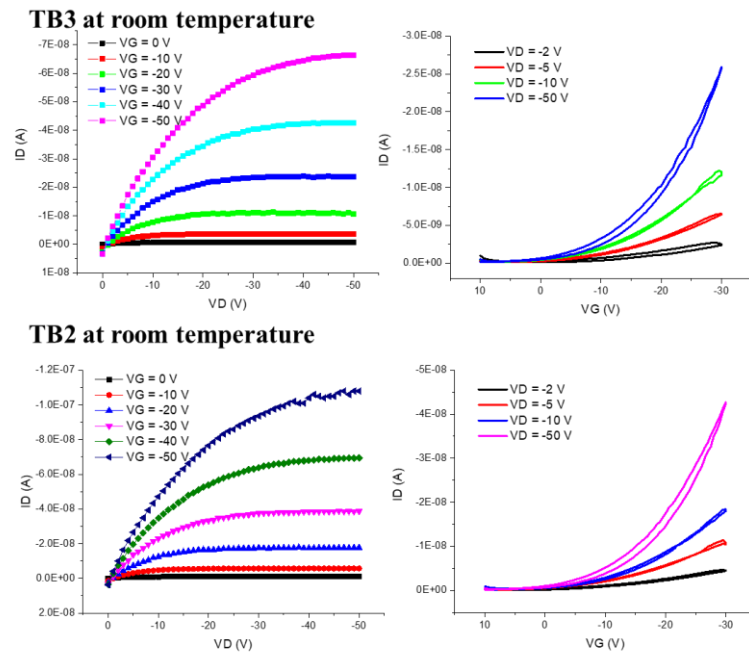
Transfer characteristics Bottom gate/bottom contact, without SCO, W = 70 μm , L = 1000 μm

TB4



The other transistors on the same substrate with TB4

TB



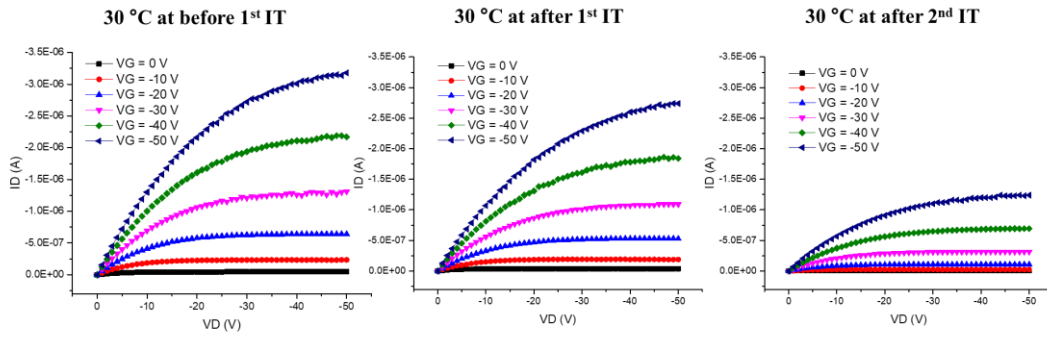
TB3 and TB2 didn't experience any measurements before, but their maximum current of no matter output/transfer characteristics is 1-2 orders of magnitude less than it should be.

TB3: Bottom gate/bottom contact, without SCO, W = 50 μm , L = 1000 μm

TB2: Bottom gate/bottom contact, without SCO, W = 30 μm , L = 1000 μm

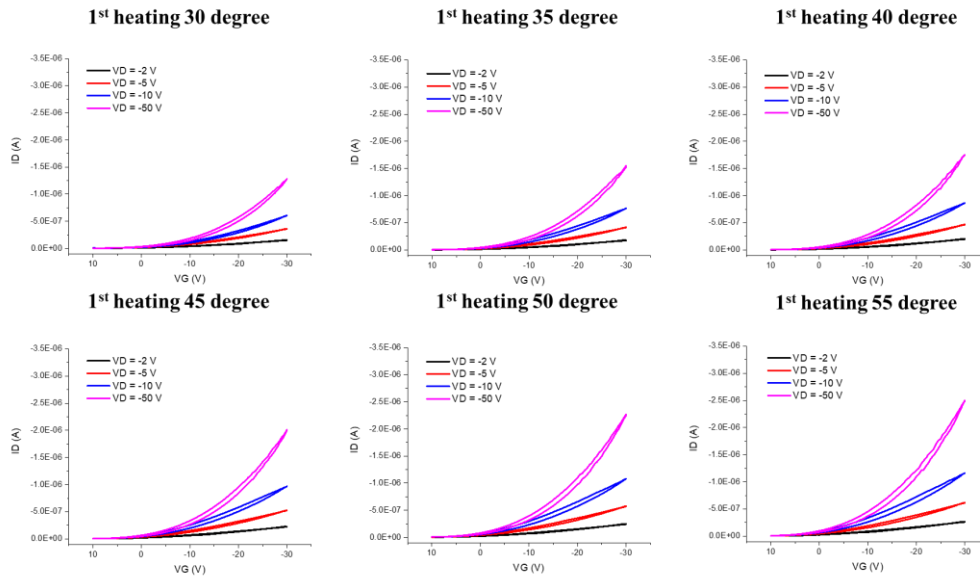
Output characteristics Bottom gate/top contact, without SCO, $W = 50 \mu\text{m}$, $L = 1500 \mu\text{m}$

RB3



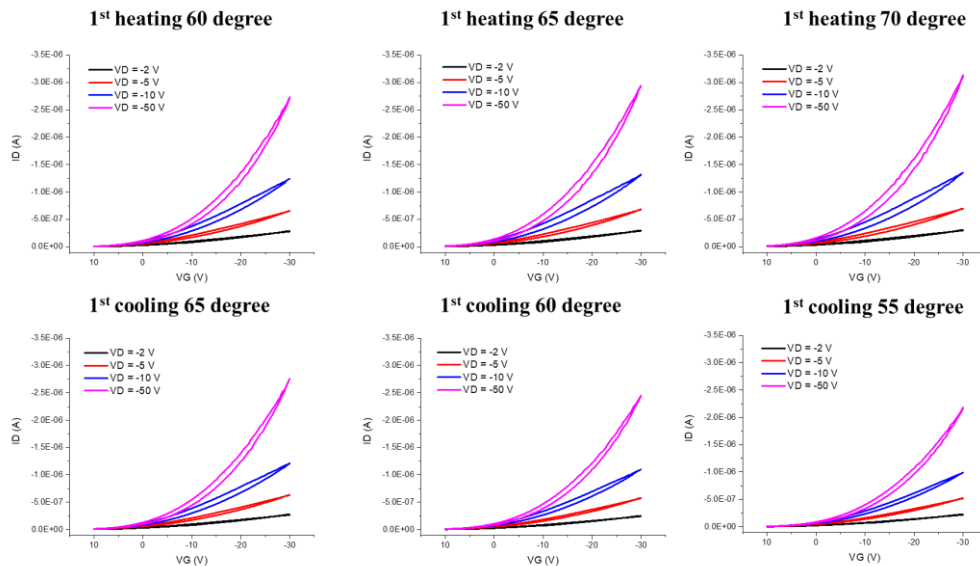
Transfer characteristics Bottom gate/top contact, without SCO, $W = 50 \mu\text{m}$, $L = 1500 \mu\text{m}$

RB3



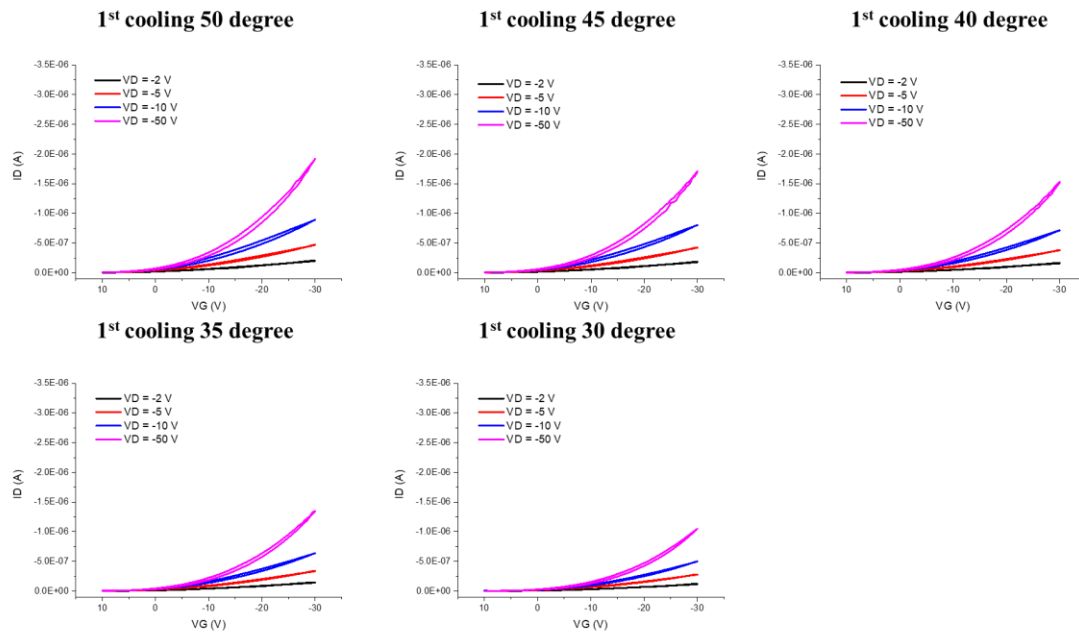
Transfer characteristics Bottom gate/top contact, without SCO, $W = 50 \mu\text{m}$, $L = 1500 \mu\text{m}$

RB3



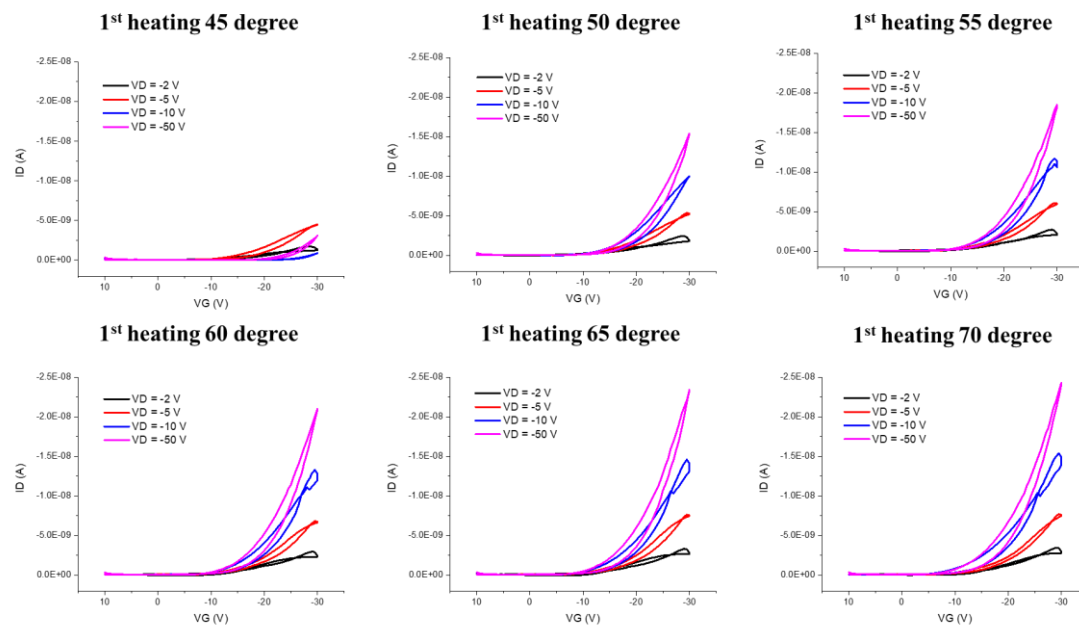
Transfer characteristics Bottom gate/top contact, without SCO, W = 50 μm , L = 1500 μm

RB3



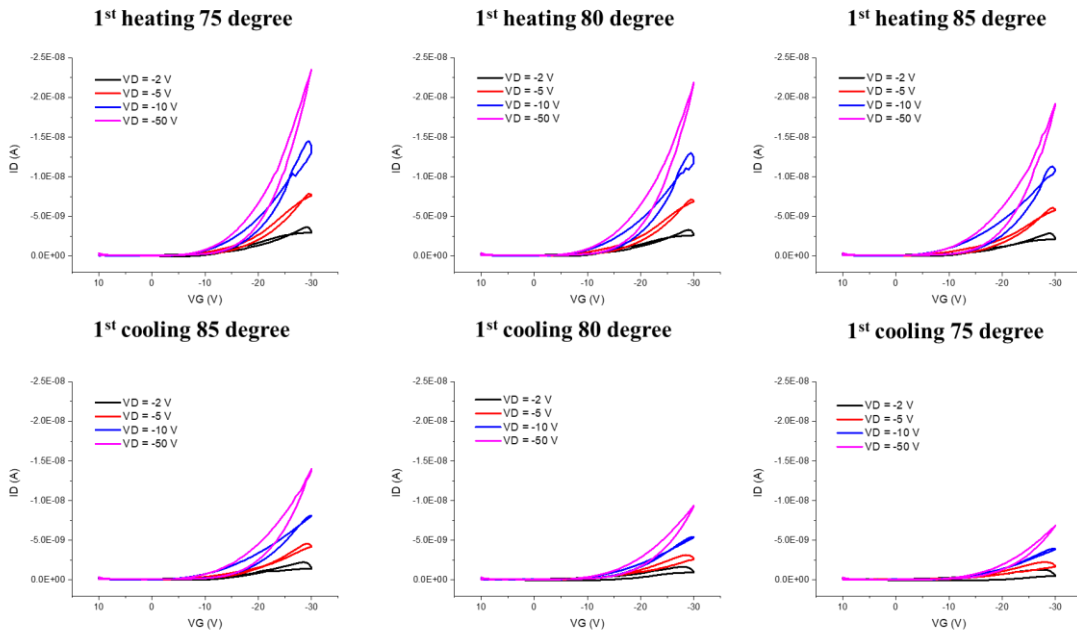
Transfer characteristics Bottom gate/top contact, with SCO, W = 110 μm , L = 1000 μm

QB5



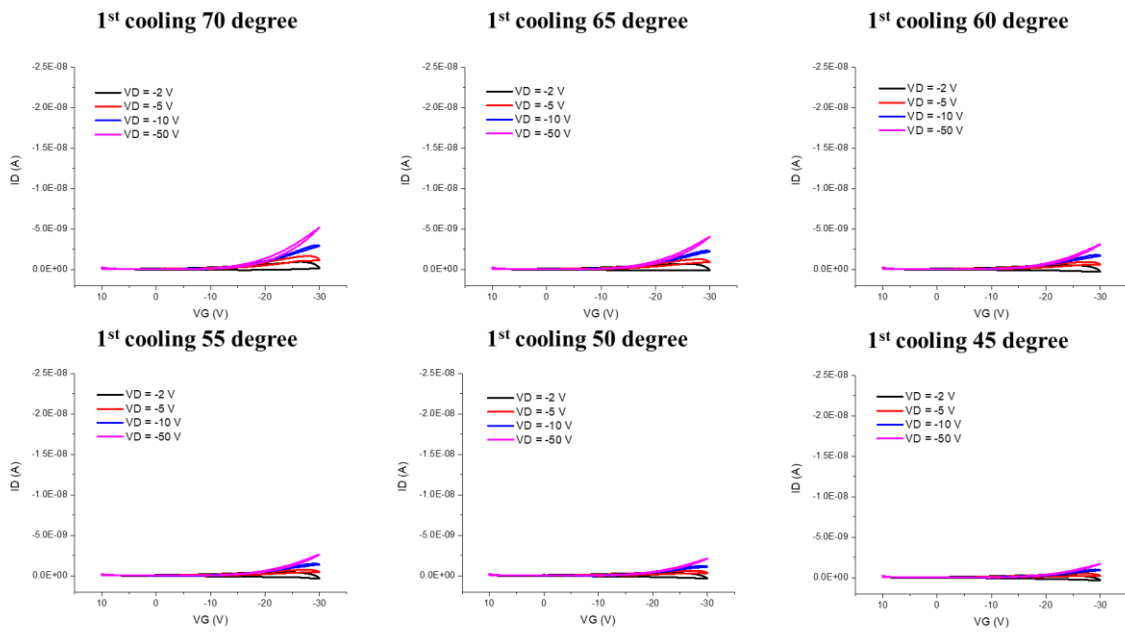
Transfer characteristics Bottom gate/top contact, with SCO, W = 110 μm , L = 1000 μm

QB5



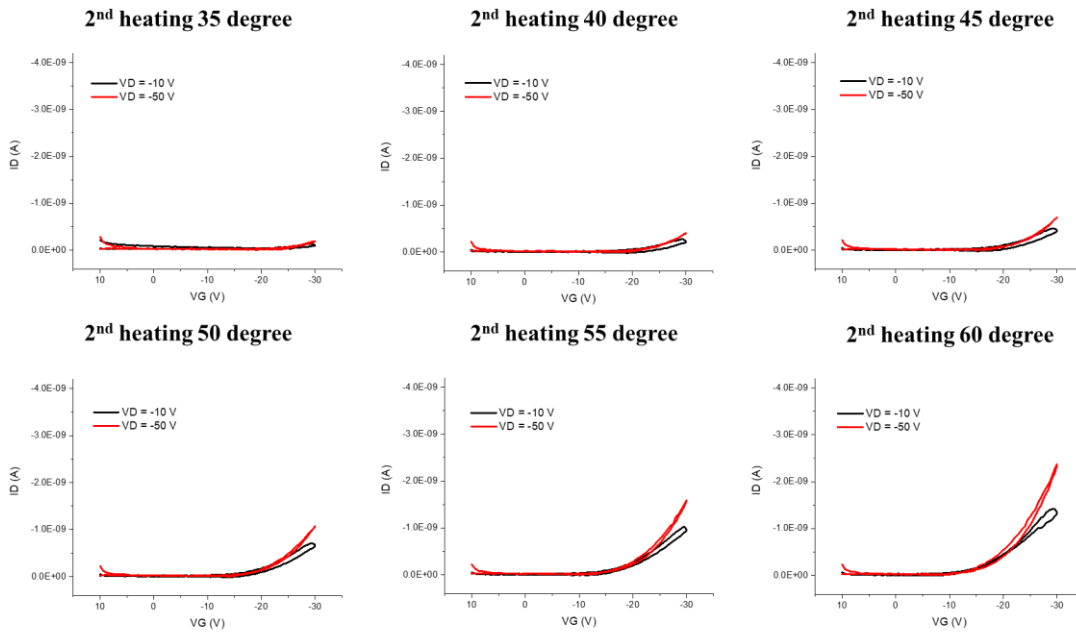
Transfer characteristics Bottom gate/top contact, with SCO, W = 110 μm , L = 1000 μm

QB5



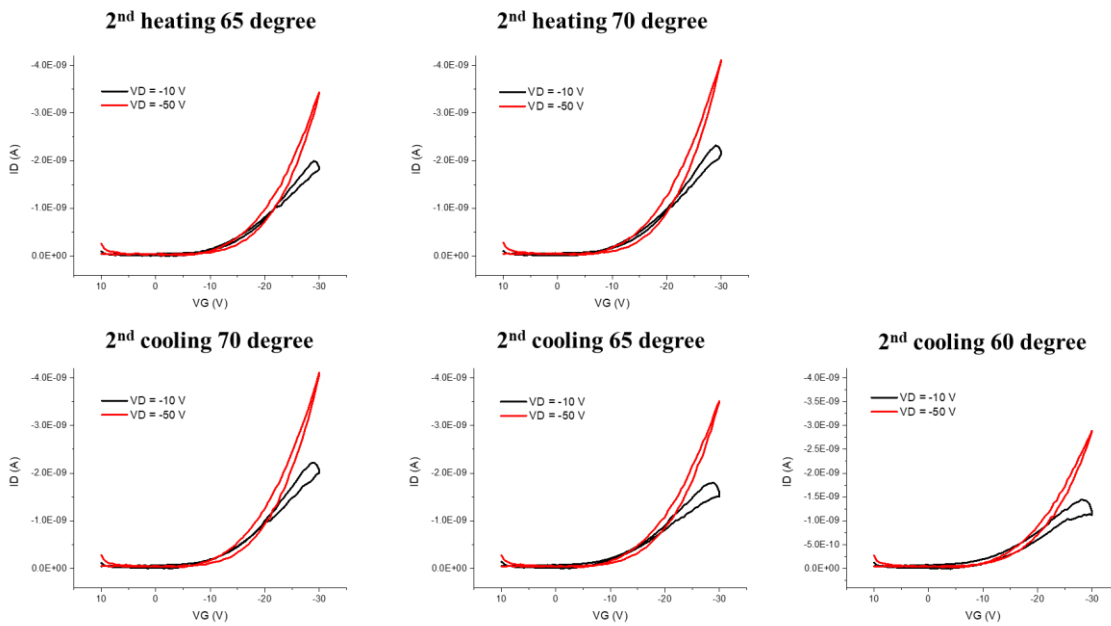
Transfer characteristics Bottom gate/top contact, with SCO, W = 110 μm, L = 1000 μm

QB5



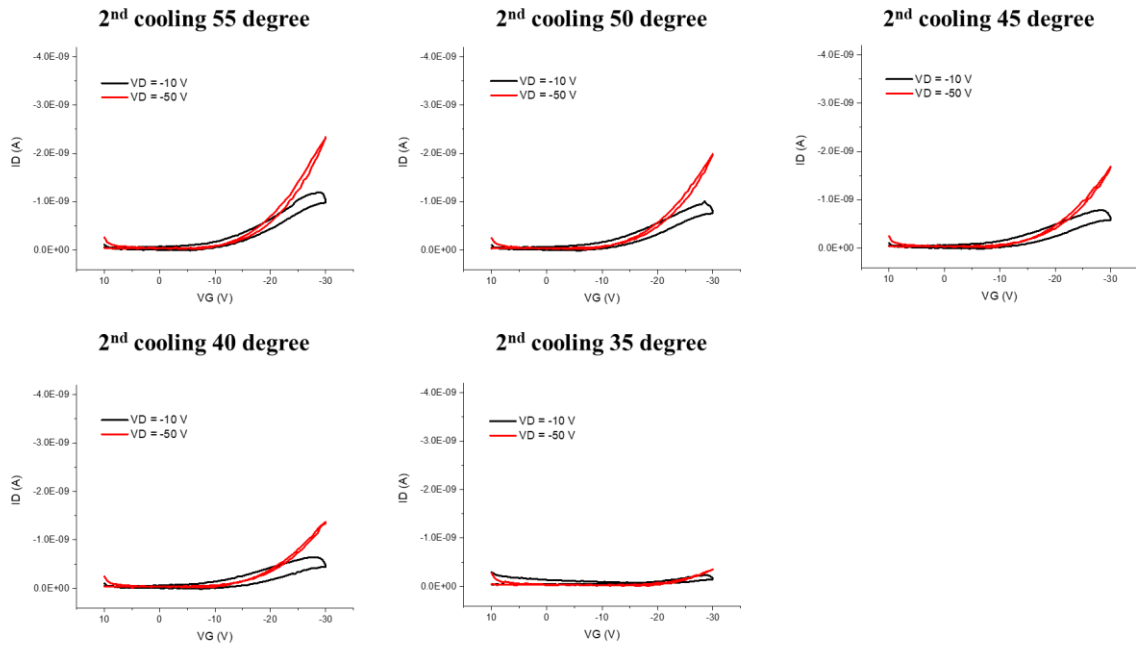
Transfer characteristics Bottom gate/top contact, with SCO, W = 110 μm, L = 1000 μm

QB5



Transfer characteristics Bottom gate/top contact, without SCO, W = 110 μm , L = 1000 μm

QB5



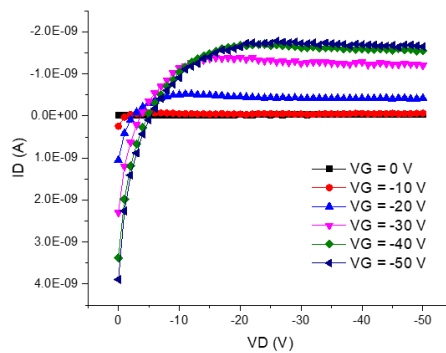
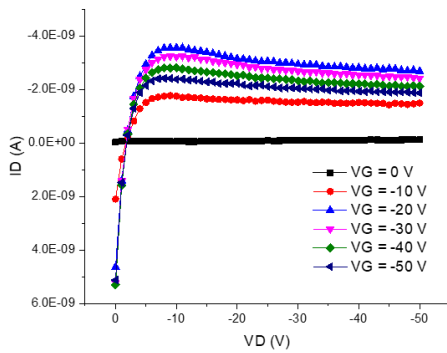
Output characteristics

QB5

Bottom gate/top contact, with SCO, W = 110 μm , L = 1000 μm

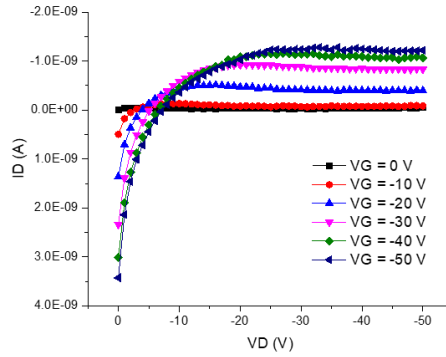
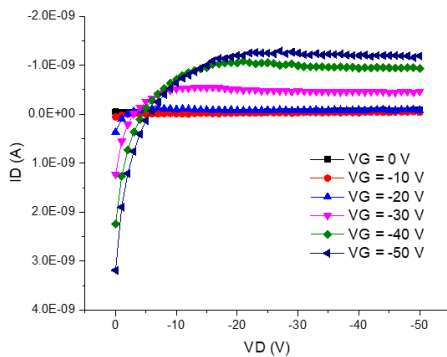
1st heating 45 degree

1st cooling 45 degree



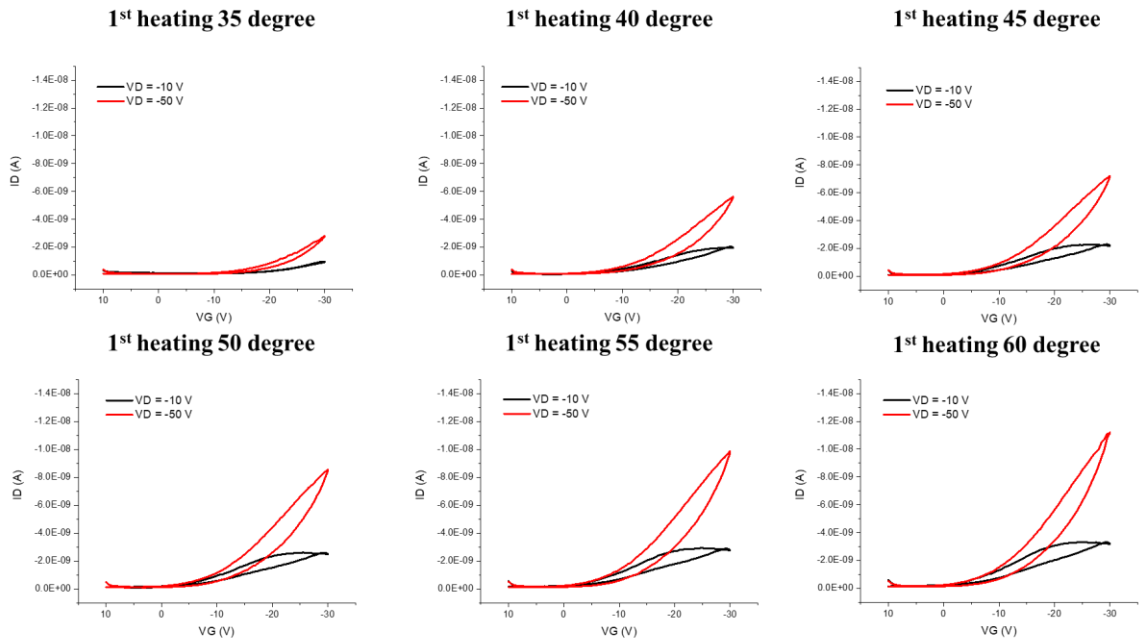
2nd heating 35 degree

2nd cooling 35 degree



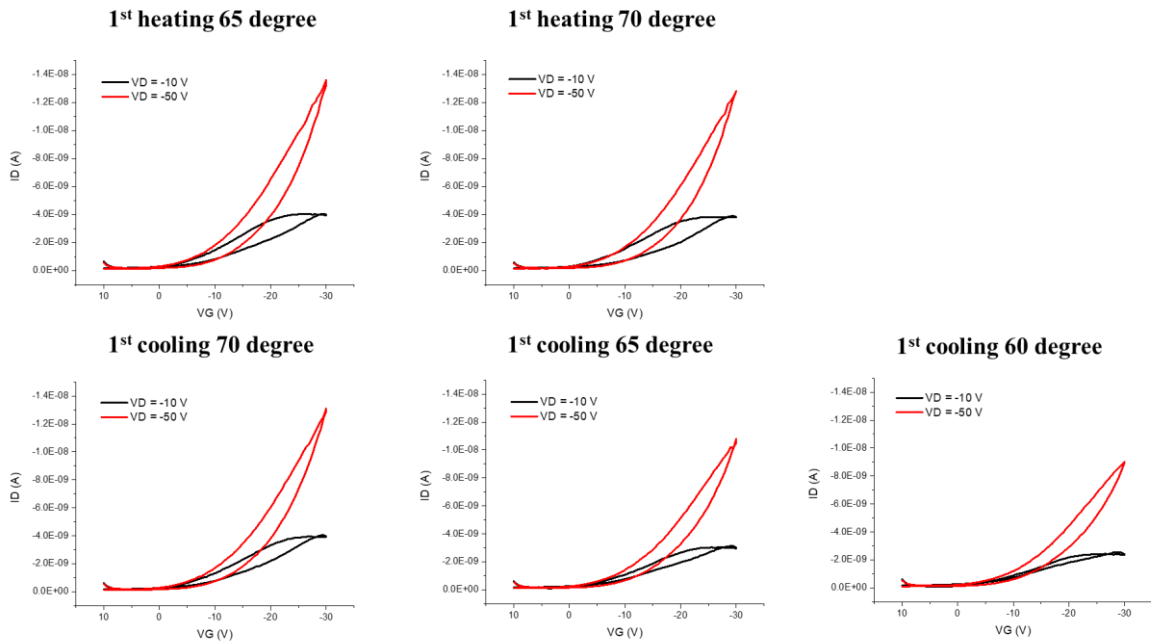
Transfer characteristics Bottom gate/top contact, with SCO, W = 50 μm , L = 1000 μm

QB3



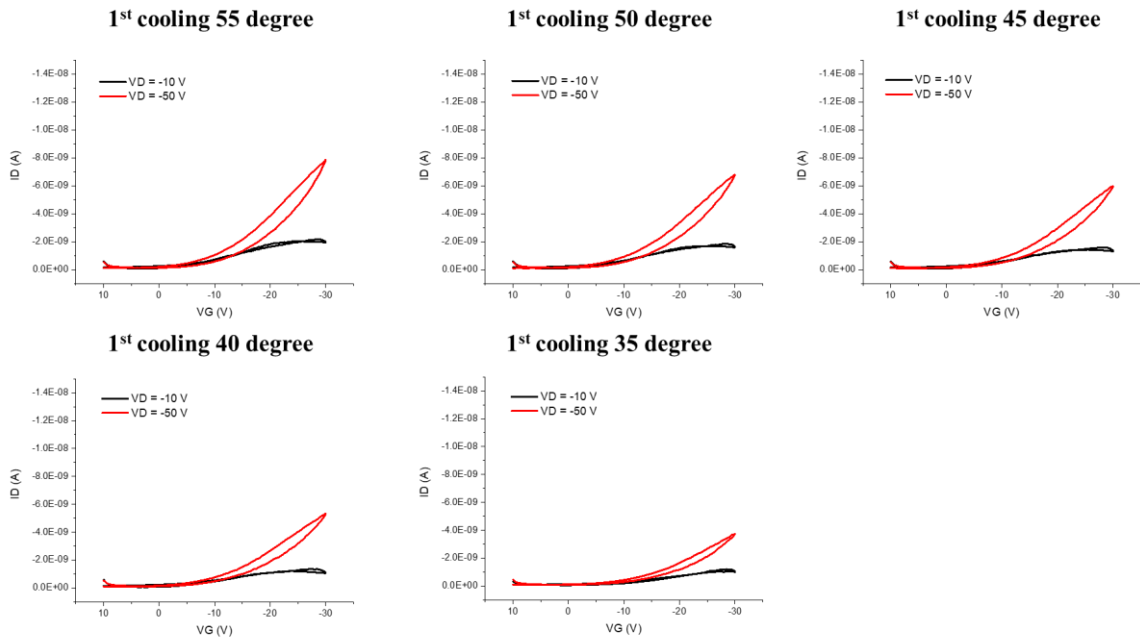
Transfer characteristics Bottom gate/top contact, with SCO, W = 50 μm , L = 1000 μm

QB3



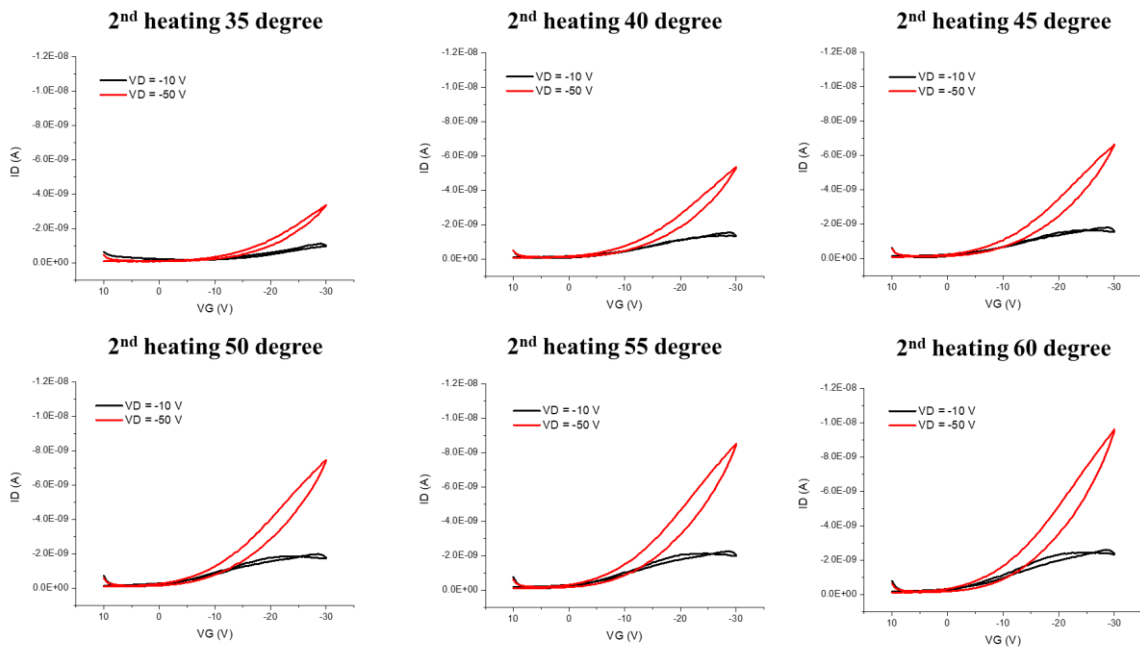
Transfer characteristics Bottom gate/top contact, with SCO, W = 50 μm , L = 1000 μm

QB3



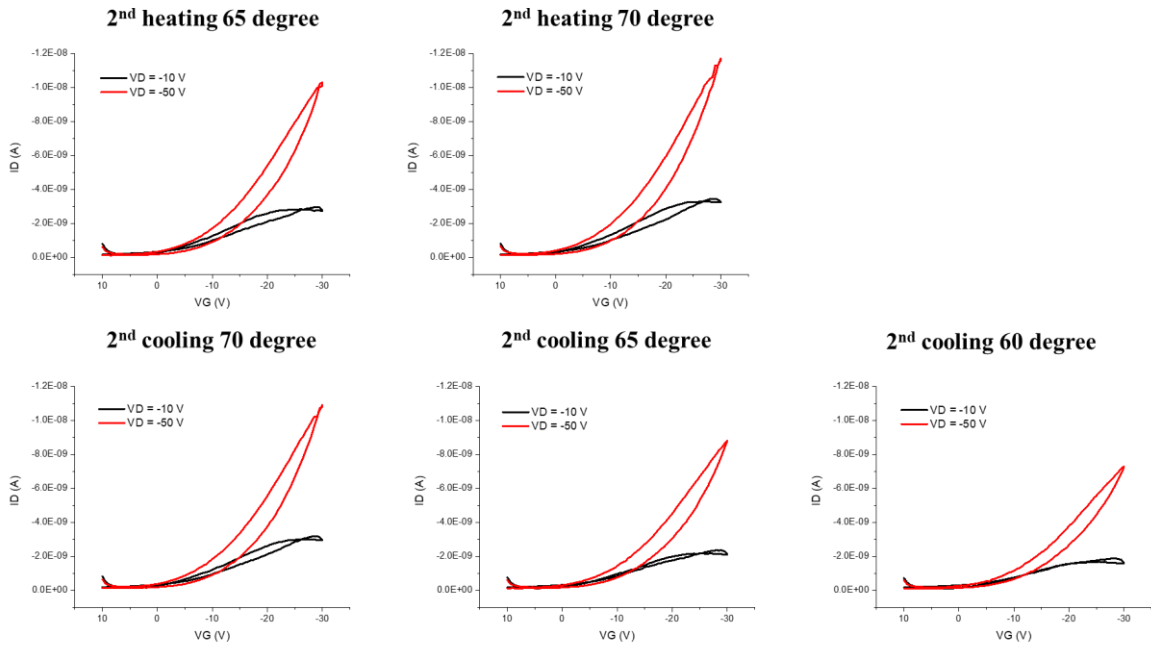
Transfer characteristics Bottom gate/top contact, with SCO, W = 50 μm , L = 1000 μm

QB3



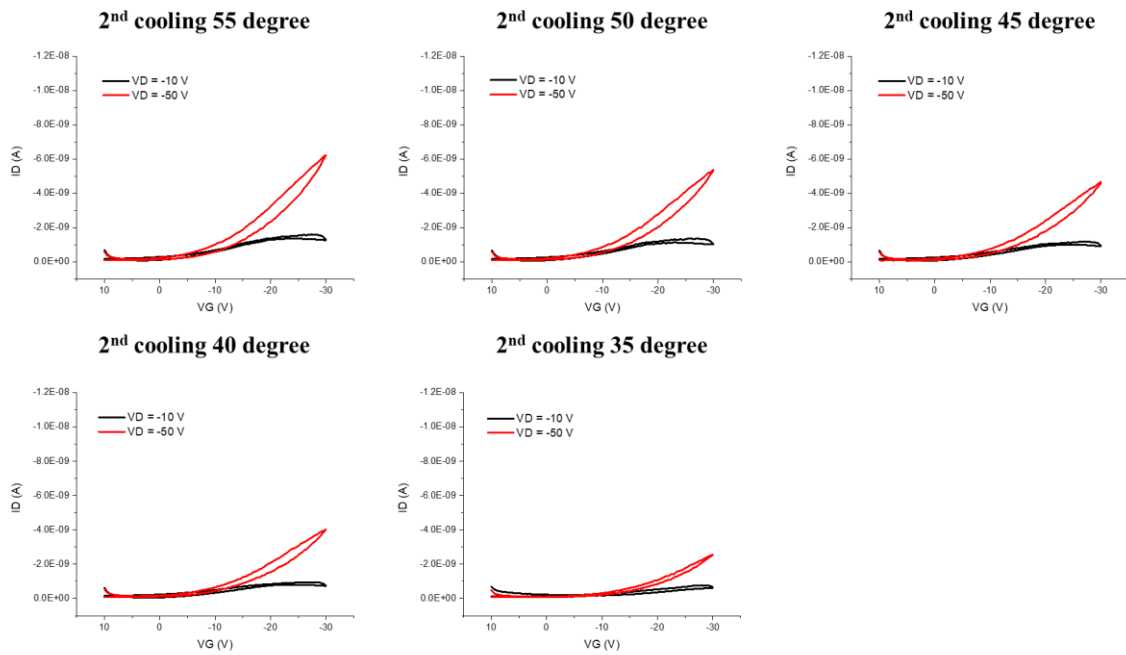
Transfer characteristics Bottom gate/top contact, with SCO, W = 50 μm , L = 1000 μm

QB3



Transfer characteristics Bottom gate/top contact, with SCO, W = 50 μm , L = 1000 μm

QB3



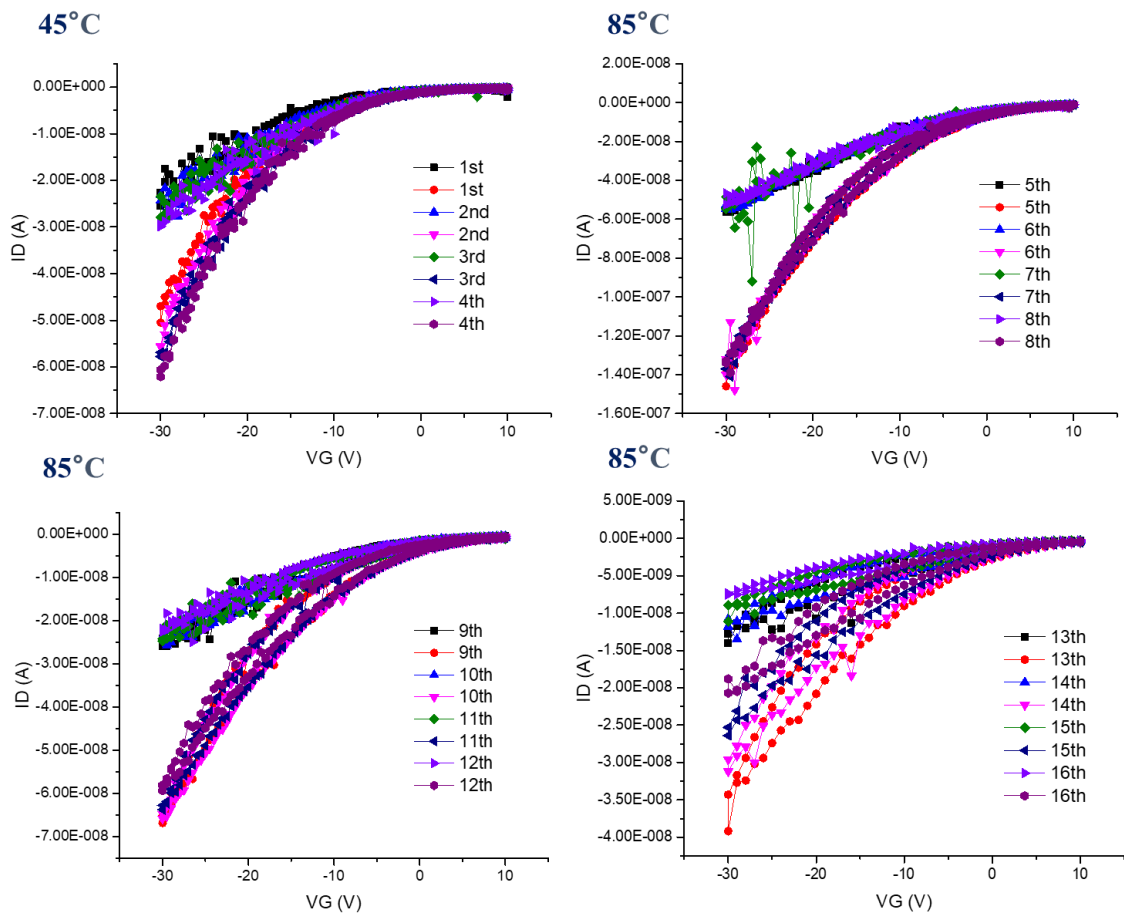
A3.4 Temperature accelerated degradation of OFETs.

N. Of Measurements	Details
1 st -4 th	Measured every 0.5 V/ Hold time for every point=0/ Delay time for every point=0/ T=45°C
5 th -8 th	Measured every 0.5 V/ Hold time for every point=0/ Delay time for every point=0/ T=85°C
8 th -12 th	Measured every 0.5 V/ Hold time for every point=0.5 s/ Delay time for every point=0.1 s/ T=85°C
13 th -16 th	Measured every 1 V/ Hold time for every point=1 s/ Delay time for every point=1 s/ T=85°C

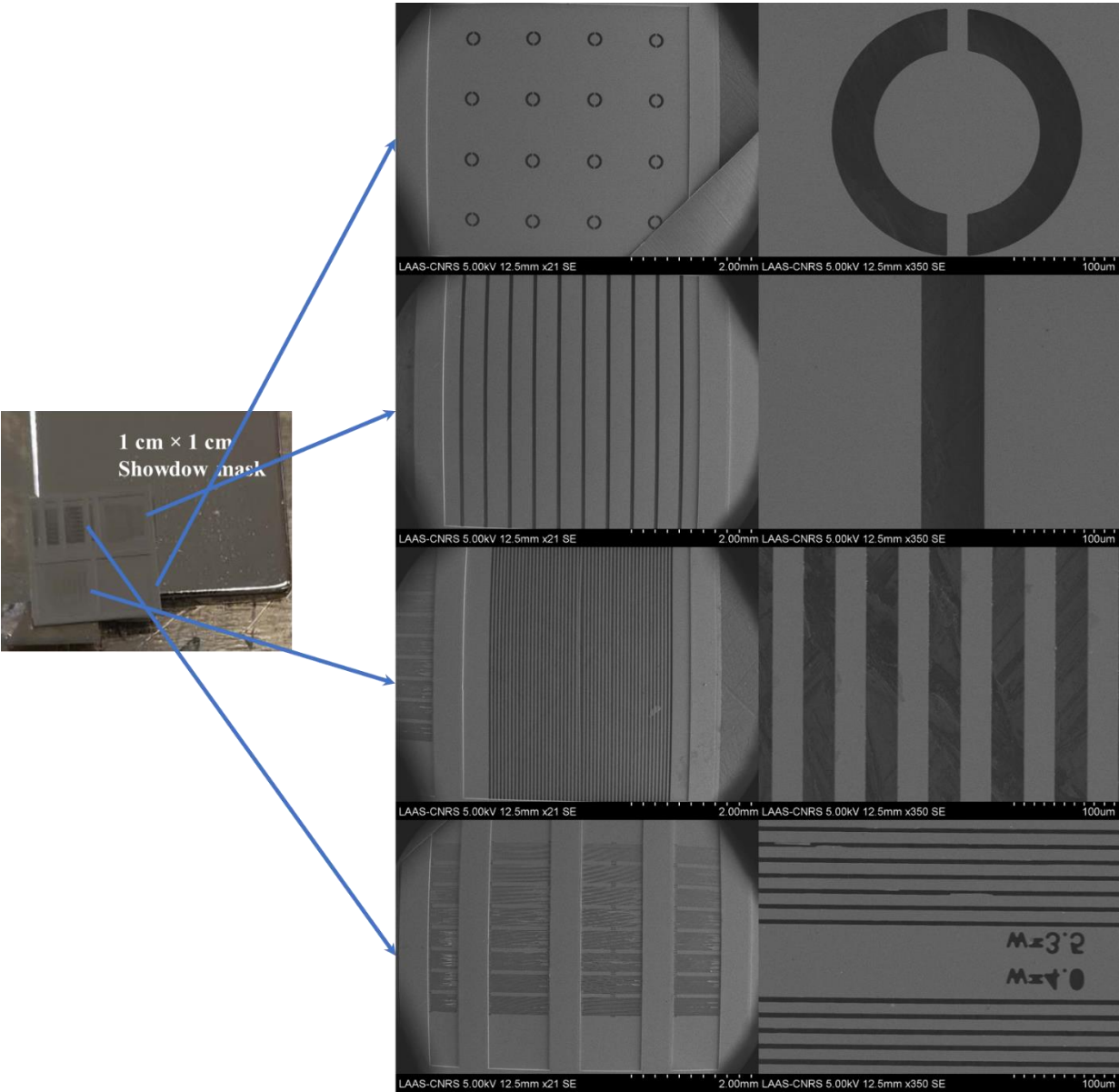
Because the Hold/Delay setting, time consuming for each measurement is different from 1st-4th, 5th-8th, 8th-12th and 13th-16th. Transfer characteristics measurement costs 1-2 mins, 1-2mins, 2-3 mins and 5 mins, respectively.

Transfer properties were measured at VG from 10 to -30V, VDS= -10V/-50V for each measurement.

Holding/Delay = 0 is default setting.



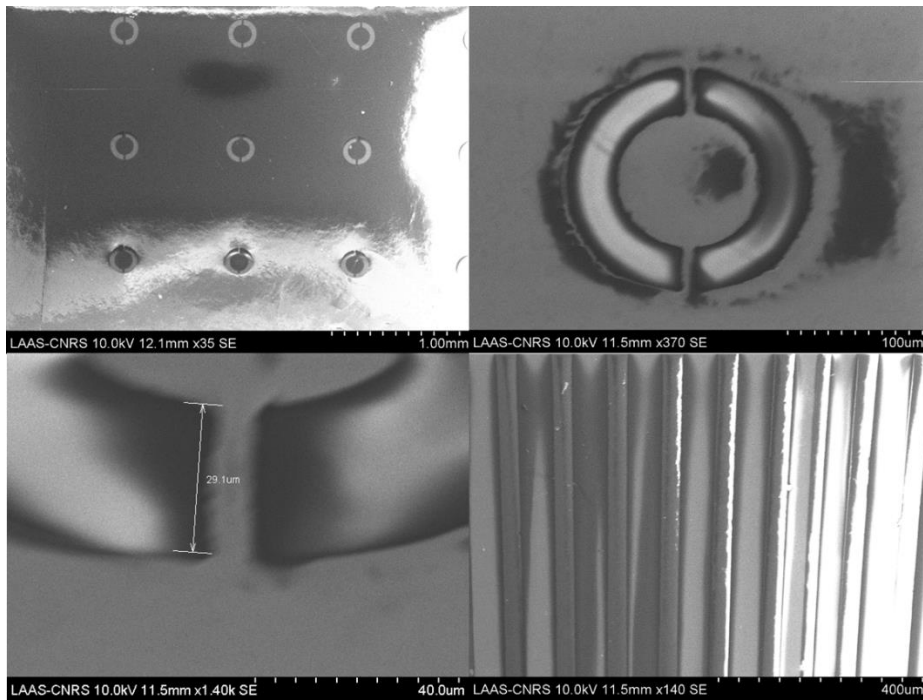
A4.1 Representative SEM graphs of a high-resolution shadow mask.



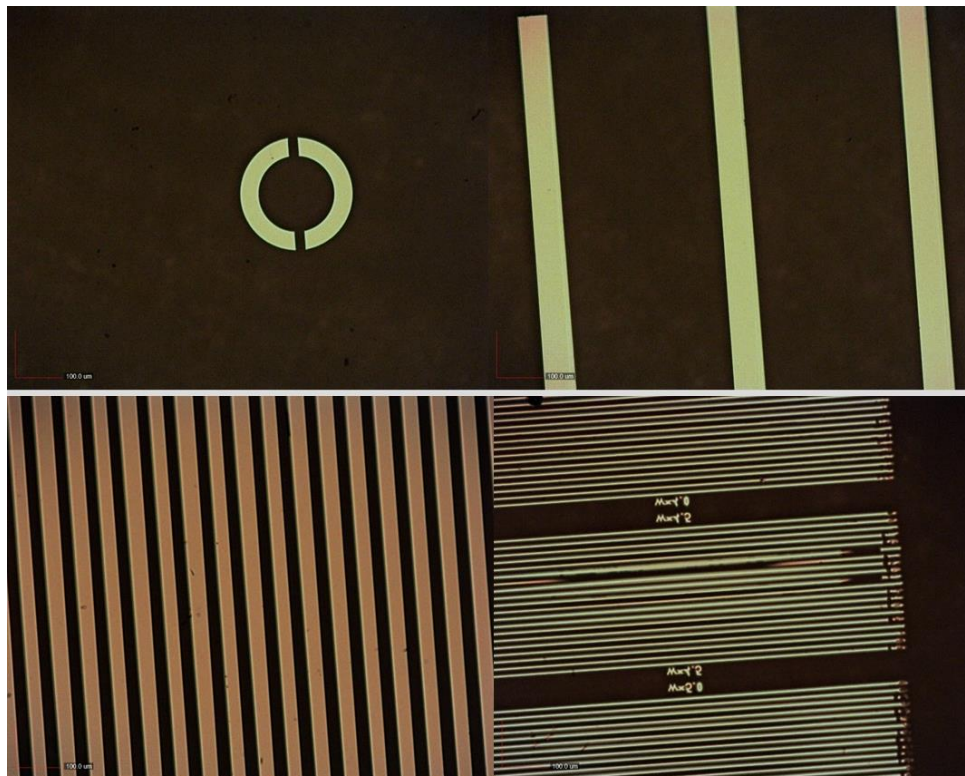
A4.2 Representative OM graphs of a high-resolution shadow mask.



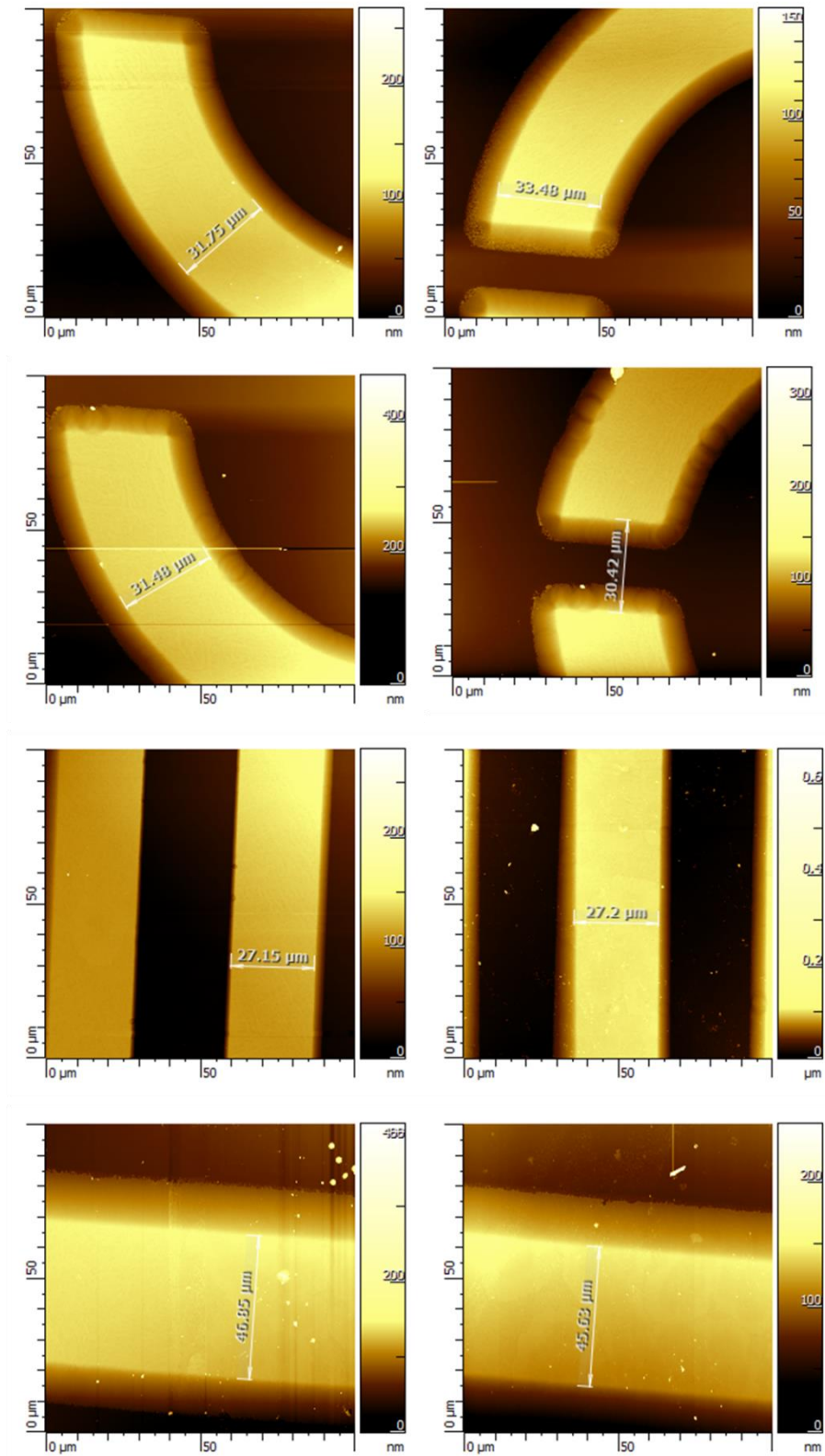
A4.3 Representative SEM graphs of patterned 100 nm thick Al deposited on glass substrate.



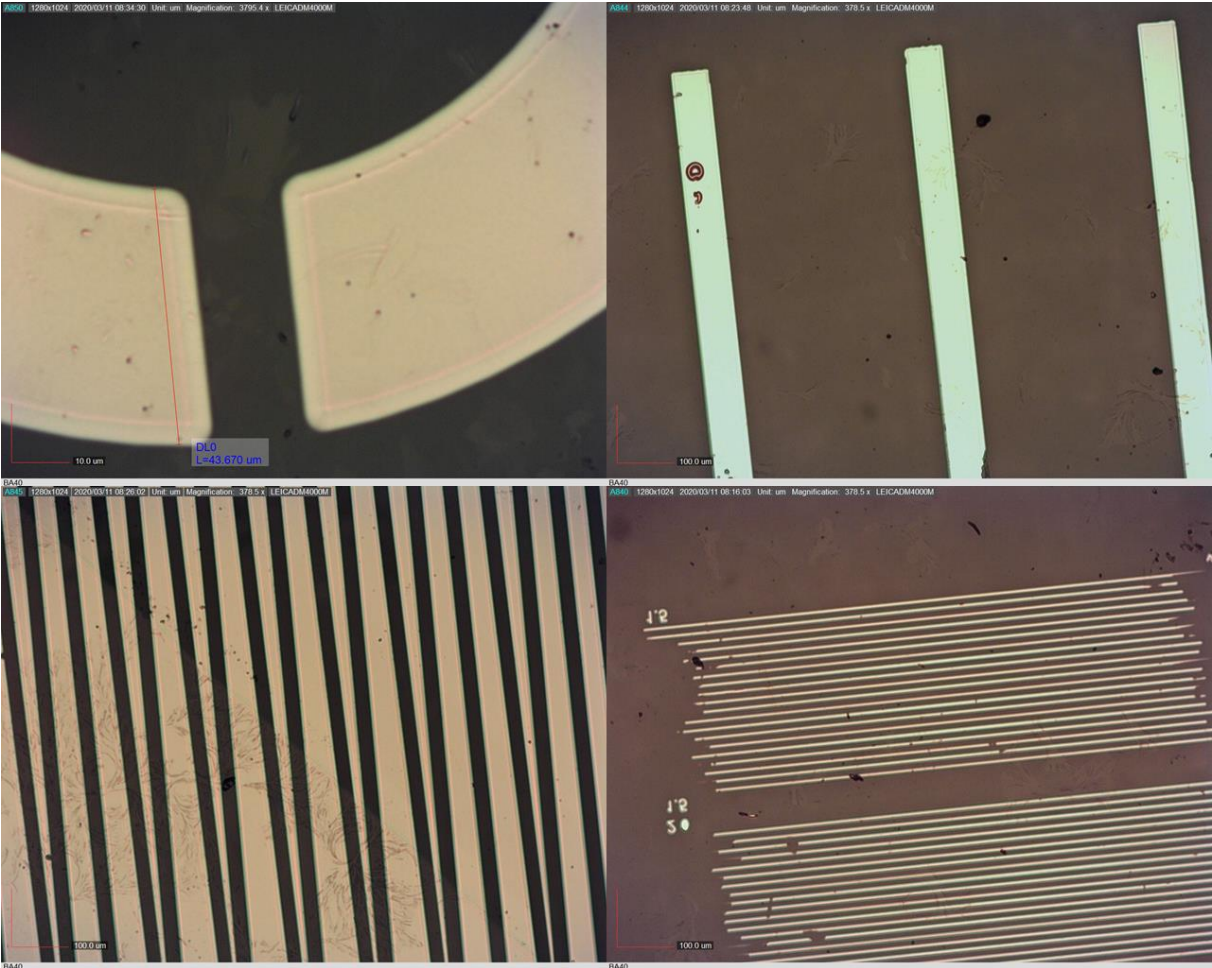
A4.4 Representative OM graphs of patterned 100 nm thick Al deposited on glass substrate.



A4.5 Representative AFM graphs of patterned 100 nm thick Al deposited on glass substrate.



A4.6 Representative OM graphs of 100 nm thick Al deposited on the top of 100 nm thick SCO layer.



Introduction générale

Au cours des dernières décennies, les matériaux moléculaires ont été de plus en plus envisagés pour des applications technologiques car la miniaturisation des dispositifs conventionnels à base de silicium s'approche de diverses limites technologiques et physiques. Dans ce contexte, les sciences moléculaires peuvent apporter de nouvelles solutions avec la synthèse et l'intégration de molécules fonctionnelles dans des dispositifs. Parmi ces molécules fonctionnelles, les complexes à transition de spin (SCO) de certains ions de métaux de transition de troisième rang présentent une commutation réversible entre leurs configurations électroniques de bas spin (LS) et de haut spin (HS). La commutation entre ces deux états peut être déclenchée par divers stimuli externes tels que la température, la pression, la lumière, les champs magnétiques intenses ou l'inclusion de molécules « invitées ». Les composés SCO dans les deux états de spin présentent des propriétés physiques différentes, notamment des propriétés magnétiques, diélectriques, optiques, mécaniques et thermiques. Certains des matériaux SCO présentent même une commutation à température ambiante (ou au-dessus de la température ambiante), ce qui est évidemment un atout essentiel pour toute application. Une autre caractéristique importante des complexes SCO est que l'état de spin moléculaire peut être commuté par irradiation lumineuse sur une échelle de temps sub-ps, ce qui rend possible un fonctionnement rapide. Ces propriétés attrayantes des composés SCO ont suscité un intérêt pour l'étude de leurs propriétés électriques dans le contexte des dispositifs électroniques et spintroniques. En effet, la nature moléculaire de ces matériaux offre des fonctions inédites, qui restent à explorer. L'idée générale est d'étudier les différentes possibilités offertes par les molécules SCO pour moduler les caractéristiques des dispositifs électroniques. Notamment, les matériaux SCO entraînent une variation considérable du gap électronique HOMO-LUMO, du moment magnétique, de la densité massique, de la permittivité diélectrique complexe (dans une large gamme de fréquences, allant des fréquences quasi-statiques aux fréquences optiques), etc. On peut donc s'attendre à un effet substantiel de la transition de spin sur diverses propriétés du dispositif (résistance, magnétorésistance, capacité et caractéristiques optiques). Le défi est, cependant, de trouver un moyen d'utiliser ces atouts remarquables dans un dispositif électronique technologiquement pertinent.

Dans ce contexte, ce travail de thèse tire profit du développement récent dans notre équipe de films minces cristallins de grande qualité du complexe SCO $[\text{Fe}(\text{HB}(\text{tz})_3)_2]$ ($\text{tz} = 1,2,4\text{-triazol-1-yl}$), présentant une transition de spin robuste (sans fatigue), au-dessus de la température ambiante⁰. Ce complexe moléculaire peut être déposé par évaporation thermique sous vide, ce

qui a permis de l'intégrer dans différentes configurations de dispositifs fondamentaux, notamment des jonctions de commutation par résistance multicouches à deux bornes et des transistors à effet de champ à trois bornes.

Au cours de ce travail, nous avons fabriqué diverses structures multicouches métal/SCO/métal et nous avons constaté que ces structures présentent également des fonctionnalités photoniques remarquables, en plus de leurs propriétés électriques.

Ceci a conduit à un résultat inattendu, qui consiste à développer des résonateurs optiques accordables, basés sur le phénomène de la transition de spin. La thèse est organisée en quatre chapitres :

Le chapitre 1 commence par une brève introduction générale au phénomène de la transition de spin (SCO), incluant des considérations sur le champ de ligands et la description de différents stimuli pour déclencher le phénomène ainsi que les techniques expérimentales pour le caractériser. Ensuite, nous passons en revue l'état de l'art des films minces SCO évaporables ainsi que des dispositifs électroniques basés sur des films minces SCO, classés en dispositifs à deux ou trois bornes.

Le chapitre 2 est focalisé sur l'intégration de films minces de $[\text{Fe}(\text{HB}(\text{tz})_3)_2]$ dans des dispositifs électroniques multicouches à deux terminaux et de grande surface, destinés à la commutation de résistance. La pureté du produit de départ, les qualités des films minces, les conditions de fabrication et de fonctionnement du dispositif ont été prises en compte pour explorer et optimiser les performances du dispositif (rapports de commutation ON/OFF, endurance du cycle, ...). Le mécanisme de transport de charge associé à la commutation par résistance est également discuté. Enfin, nous présentons la fabrication et la caractérisation des premières jonctions SCO multicouches à électrodes magnétiques.

Le chapitre 3 est consacré à l'intégration de couches minces de $[\text{Fe}(\text{HB}(\text{tz})_3)_2]$ dans des transistors à effet de champ organiques (OFET) à trois bornes. Différentes configurations de dispositifs sont comparées (grille inférieure - contact inférieur, grille inférieure - contact supérieur, ...), visant l'utilisation du phénomène SCO pour moduler les caractéristiques de transfert/sortie des transistors.

Le chapitre 4 s'appuie sur l'expertise acquise lors du développement d'empilements multicouches métal/ $[\text{Fe}(\text{HB}(\text{tz})_3)_2]$ /métal. Contrairement aux chapitres précédents, l'accent est mis ici sur les propriétés optiques de ces structures multicouches. En particulier, la conception

et les propriétés des cavités Fabry Pérot sont présentées et la modulation de la résonance de la cavité due au phénomène SCO est démontré.

La thèse se termine par des conclusions générales et des perspectives.

Chapitre 1 Introduction

Selon la théorie du champ cristallin, dans un champ de ligand octaédrique, les cinq orbitales d dégénérées (dans le cas de l'ion métallique libre) subissent une séparation énergétique en deux niveaux : un niveau de faible énergie t_{2g} et un niveau d'énergie plus élevé e_g . Pour un complexe octaédrique avec un ion de métal de transition $3d^4-3d^7$, selon l'intensité du champ de ligands autour de l'ion métallique, son état de spin peut être soit de haut spin (HS), soit de bas spin (LS). Dans un champ ligand faible, l'énergie de division du champ cristallin $10Dq$ est inférieure à l'énergie d'appariement des électrons P , ce qui permet aux électrons d d'occuper à la fois les niveaux d'énergie t_{2g} et e_g , c'est-à-dire un état de spin élevé avec une multiplicité de spin maximale. Inversement, dans un champ de ligand fort, l'énergie de division du champ cristallin $10Dq$ est supérieure à l'énergie d'appariement des électrons P , et les électrons d occupent entièrement le niveau d'énergie t_{2g} avant d'occuper les orbitales e_g de haute énergie, c'est-à-dire un état à faible spin avec une multiplicité de spin minimale. Parmi les complexes de métaux de transition avec des configurations électroniques $3d^4-3d^7$, le Fe(II) a été le plus étudié, bien que le phénomène SCO ait également été rapporté pour les complexes de Fe(III), Co(II), Co(III), Cr(II), Mn(II) et Mn(III).

Dans cette thèse, nous avons travaillé exclusivement avec des complexes à transition de spin, qui ont un ion central Fe(II) ($3d^6$). La figure 1.1 montre les configurations électroniques HS et LS d'un complexe ferreux octaédrique. Dans l'état de spin faible, le complexe est diamagnétique ($S=0$), alors que dans l'état de spin élevé, il est paramagnétique ($S=2$).

Lorsque l'écart d'énergie (ΔE_{0HL}) entre les puits de potentiel à haut et bas spin est suffisamment faible (comparable à l'énergie thermique), différents stimuli externes (température, lumière, pression, etc.) peuvent induire un changement d'état de spin (Fig. 1.1).

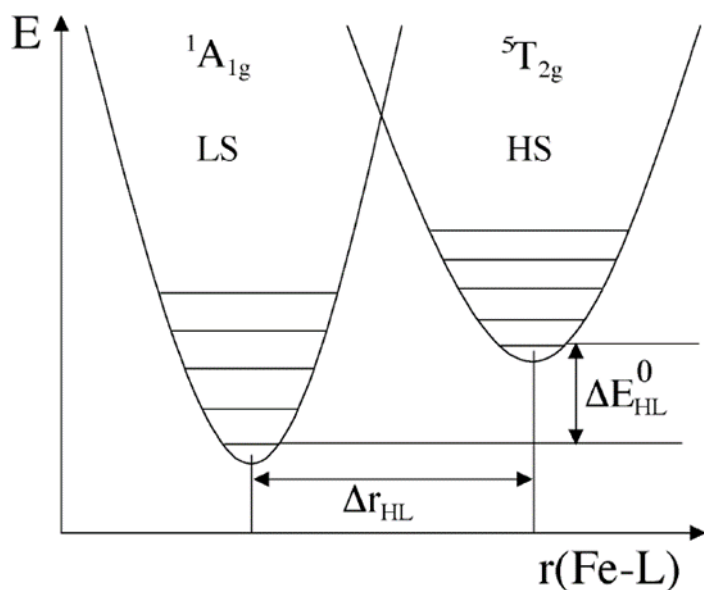


Figure 1.1 : Diagramme de configuration simplifié des deux états de spin moléculaires (HS et LS) pour un complexe Fe(II) octaédrique.

Nous appelons ce phénomène transition de spin de l'anglais "Spin Crossover". En raison de ce phénomène, les propriétés physiques (magnétiques, optiques, électriques, mécaniques, etc.) du complexe à l'état solide changent donc. Le passage d'un état de spin à l'autre peut être déclenché par divers stimuli externes, tels que la température, l'irradiation lumineuse, la pression, un champ magnétique intense, etc. Parmi ces facteurs, la façon la plus habituelle de changer l'état de spin est de changer la température, qui est également la méthode appliquée dans cette thèse pour détecter la transition de spin.

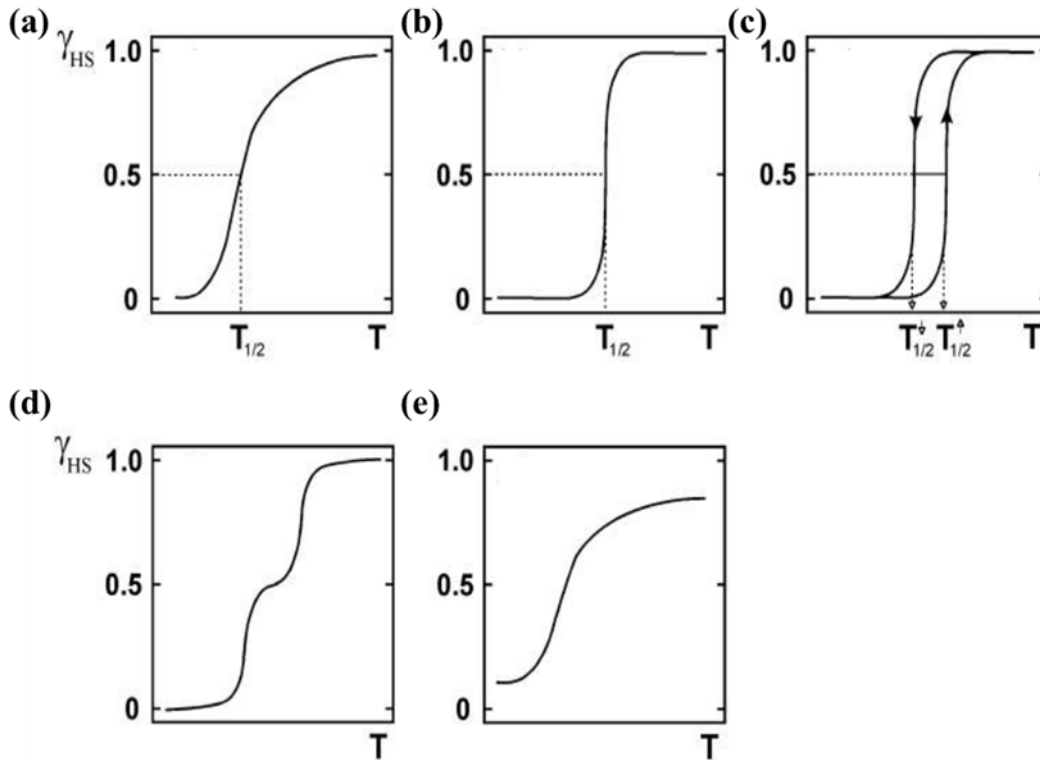


Figure 1.2 : Représentation des courbes de transition thermique de spin (a) graduelle, (b) abrupte, (c) à hystérésis, (d) en deux étapes et (e) incomplète.

Pour utiliser les matériaux SCO dans des applications "réelles", il est nécessaire de les utiliser sous forme de film mince. Cependant, la fragilité du phénomène SCO et la possibilité de traitement relativement faible des matériaux SCO ont limité leur développement pour des applications technologiques. Récemment, de grands progrès ont été réalisés dans la croissance de films minces de SCO et la fabrication de nanostructures de SCO. Parmi ces techniques, l'évaporation thermique sous vide s'avère être une méthode privilégiée pour déposer des films minces de SCO de grande surface, de haute qualité, continus et peu rugueux avec une épaisseur inférieure au micromètre.

Le tableau 1.1 présente une liste (qui se veut exhaustive) et quelques caractéristiques de base des molécules de SCO thermo-évaporables rapportées. Malgré les nombreux efforts de différentes équipes de recherche, la liste est plutôt courte, en raison des exigences générales imposées aux complexes à évaporer (charge neutre, faible poids moléculaire, thermiquement stable, sans solvant, etc.) Dans la plupart des cas, les complexes SCO thermiquement

évaporables sont des complexes de Fe(II) de la famille des complexes de « *scorpionate* », c'est-à-dire des dérivés de pyrazolyl et triazolyl-borate.

Tableau 1.1 : Liste des complexes SCO sublimables rapportés dans la littérature.

Molecule	$T_{1/2}/\Delta T$ (K, bulk)	Thickness of thin film (nm)	$T_{1/2}/\Delta T$ (K, thin film)	T_{sub} (K) $/P_{\text{sub}}$ (mbar)	Ref
[Fe(phen) ₂ (NCS) ₂]	176/ \approx 1	280	175	453/10 ⁻⁸	Shi 2009
[Fe(H ₂ B(pz) ₂) ₂ (phen)]	163.7/ \approx 4	355	151/6	435/10 ⁻²	Rosa 2012
[Fe(H ₂ B(pz) ₂) ₂ (bipy)]	160	564	153/4	433/10 ⁻²	Rosa 2012
[Fe(H ₂ B(pz) ₂) ₂ L ¹]	141	>100	148	448/3×10 ⁻⁸	Ossinger 2016
[Fe(H ₂ B(pz) ₂) ₂ L ²]	140	5		425/1×10 ⁻¹⁰	Poggini 2018
[Fe(H ₂ B(pz) ₂) ₂ L ³]	154	230	\approx 150	/4.3 × 10 ⁻⁸	Bowen2019
[Fe(H ₂ B(pz) ₂) ₂ L ⁴]	197	10	176.5	423/	Kumar2018
[Fe(dpepd)(NCS) ₂]	\approx 251	0.8 monolayer	235(6)	510/5×10 ⁻⁹	Bernien 2012
[Fe(HB(pz) ₃) ₂]	393			463/ \approx 10 ⁻⁵	Mahfoud2011
[Fe(HB(tz) ₃) ₂]	333/ \approx 1	100	336	523/ \approx 2×10 ⁻⁷	Shalabaieva2017
[Fe(HB(3,5-(CH ₃) ₂ (pz) ₃) ₂)]	190/31	130	152/17	393- 413/10 ⁻⁸	Iasco 2017

[Fe(qnal) ₂].xCH ₂ Cl ₂	220 (x=1) and 260 (x=0)	50	210	490/10 ⁻⁷	Atzori 2018
[Fe(pypyr(CF ₃) ₂) ₂ (phen)]	390	40	330	433/5×10 ⁻⁹	Rohlf 2018 monolayer
[Fe(pap) ₂]ClO ₄ .H ₂ O	172.5/15			~363/ 1×10 ⁻⁹	Tönnies 2017

Certains des films existants ont pu être intégrés avec succès dans des dispositifs électroniques présentant différentes configurations : à 2 ou 3 bornes, planaires ou verticales. Les configurations et les principales propriétés des dispositifs électroniques à base de SCO sont résumées dans le tableau 1.2 ci-dessous :

Tableau 1.2 : Propriétés de commutation de courant rapportées pour diverses jonctions SCO

SCO compound	Device structure	Current LS (A)	Current HS (A)	ON/OFF ratio	Ref.
[Fe(H ₂ B(pz) ₂) ₂ (phen)] film	ITO/SCO/Al	2.0×10 ⁻⁹	1.0×10 ⁻⁹	↓ 2	Lefter2016
[Fe(HB(tz) ₃) ₂] film	ITO/SCO/Al	5.0×10 ⁻⁶	5.0×10 ⁻⁷	↓ 8	Shalabaeva 2018
[Fe(H ₂ B(pz) ₂) ₂ (phen)] film	^{TS} Au/SCO/EGa In	3×10 ⁻¹⁰	3×10 ⁻⁹	↑ 10	Poggiini2019
[Fe(HB(tz) ₃) ₂] film	^{TS} Au/SCO/EGa In	3×10 ⁻⁸	3×10 ⁻⁶	↑ 100	Poggiini2018
[Fe(H ₂ B(pz) ₂) ₂ (NH ₂ -phen)] film	Au/SCO/Au	8×10 ⁻⁸	8×10 ⁻⁶	↑ 100	Bowen2018

[Fe(Htz)₂(tz)](BF₄) nanorods	Au/ SCO/Au	2.6×10 ⁻⁸	1.5×10 ⁻⁸	↓ 1.7	Rotaru2013
[Fe(Htz)₂(tz)](BF₄) nanoparticles	Au/ SCO/Au	1×10 ⁻⁹	3×10 ⁻¹²	↓ 300	Dugay2015
Au@[Fe(Htz)₂(tz)](BF₄) nanoparticles	Au/ SCO/Au	6×10 ⁻⁹	4×10 ⁻¹²	↓ 1500	Torres2019
[Fe(tz)₃](BF₄)₂ NPs	Au/ SCO/Au	0.26	0.88	↑ 3	Prins2011
[Fe(tz)₃](BF₄)₂ NPs	G/SCO/G			2	Dugay2016
[Fe(tz)₃](BF₄)₂ NPs	Au/G+SCO/Au	3×10 ⁻¹⁰	3×10 ⁻¹¹	↓ 10	Holovchenko2016
[FeIII(qsal-I)₂]NTf₂ thin film	Cu/SLG/SCO/ GaOx/EGaIn	-3.6 (Log J)	-2.6 (Log J)	↑ 10	Nijhuis2020

Chapitre 2 Intégration du complexe [Fe(HB(tz)₃)₂] à transition de spin dans des dispositifs de commutation par résistance à deux bornes

Dans ce chapitre, nous décrivons d'abord la synthèse et la caractérisation du complexe sous forme de poudre et de films minces. Après avoir décrit les propriétés des films minces, nous discutons de la fabrication et des propriétés des jonctions à deux terminaux, multicouches et de grande surface, basées sur ces films.

L'architecture “*crossbar*” est universellement utilisée dans les applications de commutation par résistance, dans lesquelles chaque point de croisement présente une configuration de type condensateur, comme le montre la figure 2.1. Jusqu'à présent, un grand nombre de matériaux isolants (oxydes, nitrures, chalcogénures, polymères, matériaux organiques, etc.) ont été rapportés dans les applications de commutation par résistance. Récemment, les matériaux SCO ont également été intégrés dans des dispositifs similaires de type “*crossbar*”.

En raison des propriétés physiques bistables des composés SCO, ces dispositifs peuvent potentiellement permettre un comportement de commutation par résistance.

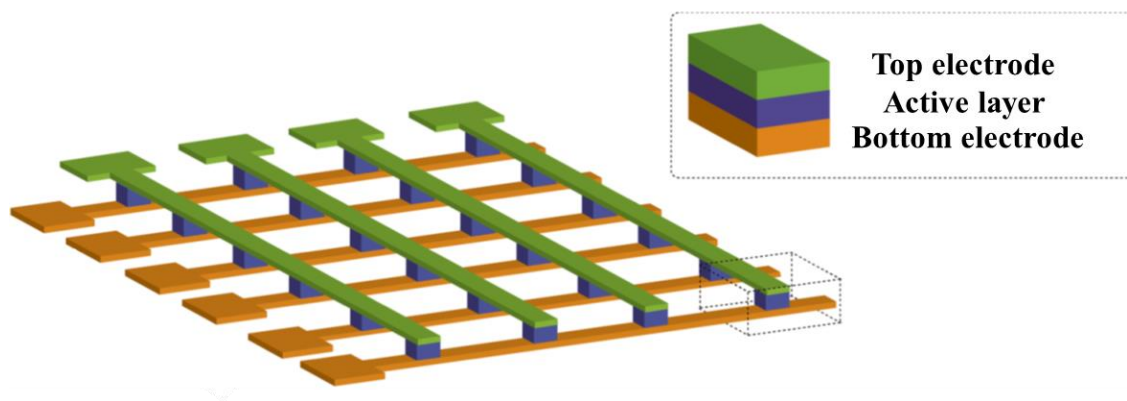
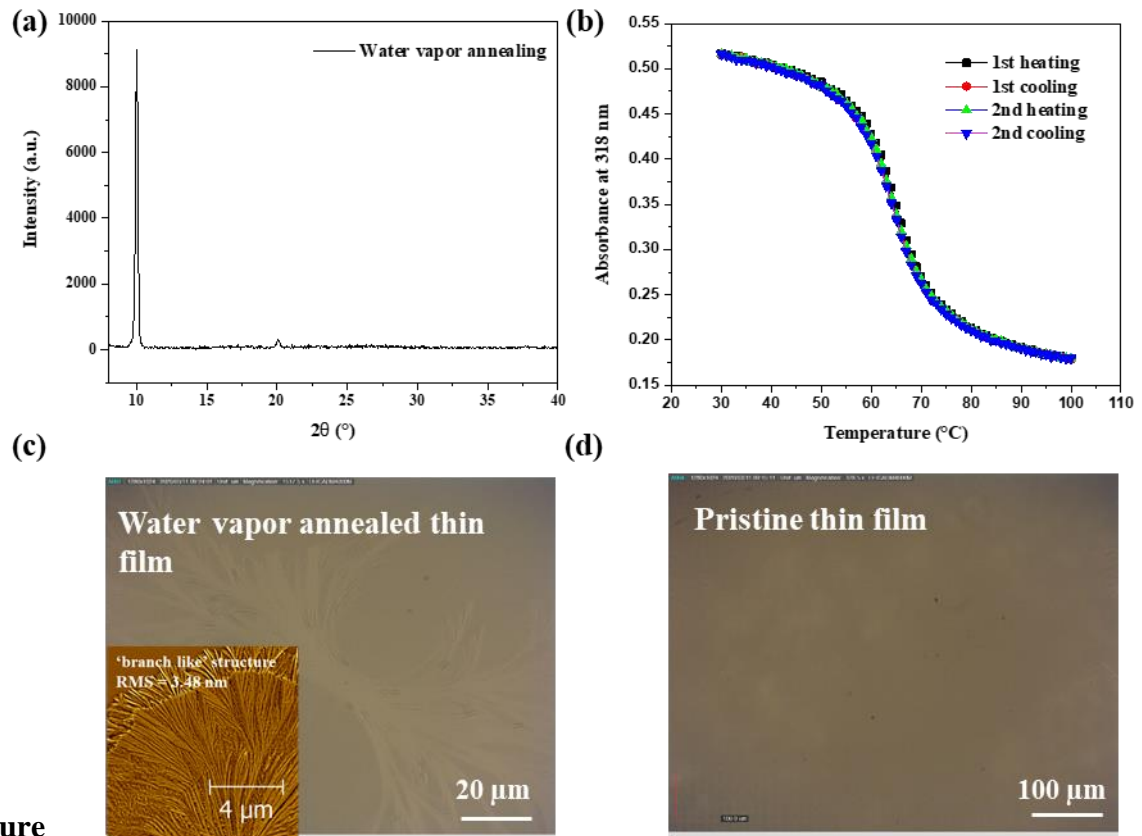


Figure 2.1 : Architecture “*crossbar*” typique utilisée dans les applications de commutation résistive.

La synthèse du complexe $[\text{Fe}(\text{HB}(\text{tz})_3)_2]$ a été réalisée selon le mode opératoire de nos précédents travaux. Les films minces de $[\text{Fe}(\text{HB}(\text{tz})_3)_2]$ ont ensuite été fabriqués par évaporation thermique sous vide. Grâce à un traitement facile, appelé recuit à la vapeur de solvant, les films minces deviennent cristallins avec une orientation préférentielle. Les films minces recuits ont été caractérisés par GIXRD, UV-Vis, AFM et Mesures optiques. Comme le montre la figure 2.2a, le diagramme de diffraction du film mince de $[\text{Fe}(\text{HB}(\text{tz})_3)_2]$ recuit à la vapeur d'eau présente un pic unique et intense à $2\theta = 10,02^\circ$ indiquant une orientation cristallographique hautement préférentielle. La dépendance en température de l'absorbance à 318 nm le long de deux cycles de chauffage-refroidissement du film mince de $[\text{Fe}(\text{HB}(\text{tz})_3)_2]$ recuit à la vapeur d'eau est présentée dans la Figure 2.2b. On peut y voir une chute abrupte autour de 65°C avec presque aucune hystérésis due au phénomène SCO. Comme nous pouvons le voir sur les images de la Mesure Optique des figures 2.2c-d, le recuit à la vapeur d'eau peut induire une structure dendritique "ramifiée" dans le film mince, qui peut atteindre des centaines de μm . A Noter qu'à l'exception de la zone présentant des structures de type "branche", le reste

de la surface semble lisse et homogène, tout comme le film mince vierge (sans recuit à la vapeur de solvant).



Figure

2.2 : (a) Spectre GIXRD du film mince de $[\text{Fe}(\text{HB}(\text{tz})_3)_2]$ recuit à la vapeur d'eau. (b) Dépendance en température de l'absorbance à 318 nm d'un film mince recuit à la vapeur d'eau (ca. 100 nm) le long de deux cycles de chauffage-refroidissement. Images de microscopie optique (MO) de (c) films minces recuits à la vapeur d'eau (insert : image AFM) et (d) films minces vierges.

Les films minces de $[\text{Fe}(\text{HB}(\text{tz})_3)_2]$ recuits ont ensuite été intégrés dans des dispositifs à deux bornes. Les jonctions ITO/ $[\text{Fe}(\text{HB}(\text{tz})_3)_2]$ /Al ont d'abord été fabriquées et caractérisées. La procédure de fabrication des jonctions transversales ITO/SCO/Al est illustrée sur la figure 2.3 ci-dessous :

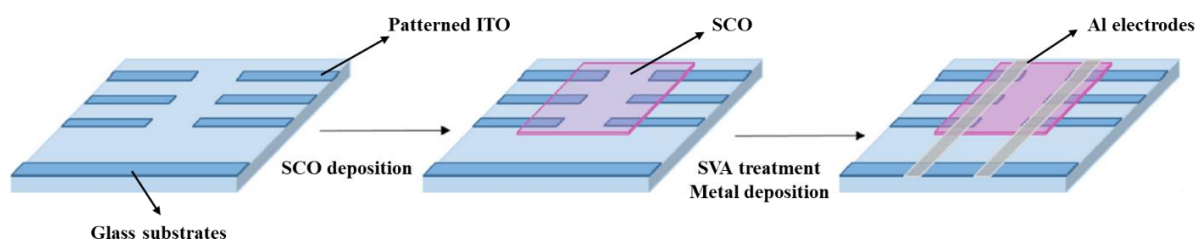


Figure 2.3 : Procédure de fabrication des jonctions ITO/[Fe(HB(tz)3)2]/Al.

Les résistances des jonctions ITO/[Fe(HB(tz)3)2]/Al ont d'abord été caractérisées à température ambiante. Aucune des jonctions n'a été court-circuitée et la valeur moyenne globale de résistance de $3,0 \pm 0,4 \text{ M}\Omega$ est bien reproduite d'un dispositif à l'autre.

Tableau 2.1 : Comparaison de la résistance électrique à température ambiante d'un lot de jonctions ITO/100 nm [Fe(HB(tz)3)2]/Al.

La figure 2.4 illustre les caractéristiques I-V et I-T en fonction de la température d'une jonction ITO/[Fe(HB(tz)3)2]/Al. Les courbes I-T montrent une faible activation thermique et un changement substantiel d'un état de haute conductance à un état de basse conductance se produit à environ $65 \text{ }^\circ\text{C}$ pendant le chauffage. Contrairement au rapport ON/OFF de 8 rapporté précédemment (c'est-à-dire une commutation d'un ordre de grandeur), dans les expériences actuelles, les changements de résistance atteignent 2 à 3 ordres de grandeur dans plusieurs dispositifs, avec des rapports ON/OFF allant jusqu'à 400. Nous pensons que cette amélioration spectaculaire des rapports de commutation ON/OFF, par rapport aux dispositifs rapportés précédemment, est probablement liée à une manipulation plus prudente des dispositifs en termes d'exposition à l'air, aux hautes tensions et aux hautes températures.

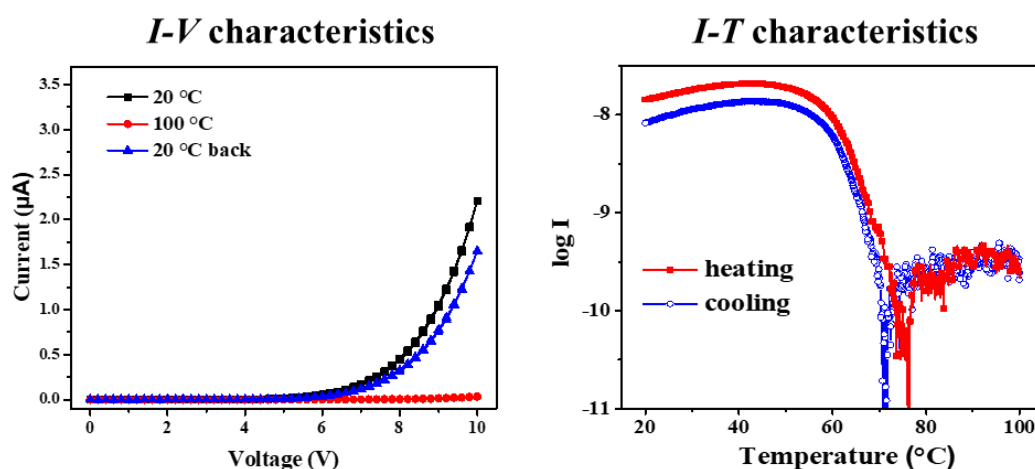


Figure 2.4 : Caractéristiques électriques d'une jonction ITO/100 nm [Fe(HB(tz)₃)₂]/Al. À gauche : courbes I-V enregistrées à 20 °C et 100 °C, puis à nouveau à 20 °C à des vitesses de ±100 mV/s. À droite : courbes log I- T enregistrées avec une polarisation appliquée de 5 V.

L'amélioration de la stabilité à long terme et de l'endurance de commutation des dispositifs électroniques à base de SCO est essentielle au déploiement de cette technologie. Nous avons étudié la résistance aux cycles de la jonction ITO/100 nm [Fe(HB(tz)₃)₂]/Al non encapsulée, âgée d'un an, lors de cycles thermiques sous une tension de polarisation constante de 3 V.

Étonnamment, nous avons enregistré plus de 10 000 cycles de commutation de résistance entre les états de spin moléculaire élevé (faible intensité de courant) et faible (forte intensité de courant) dans la jonction (figure 2.5).

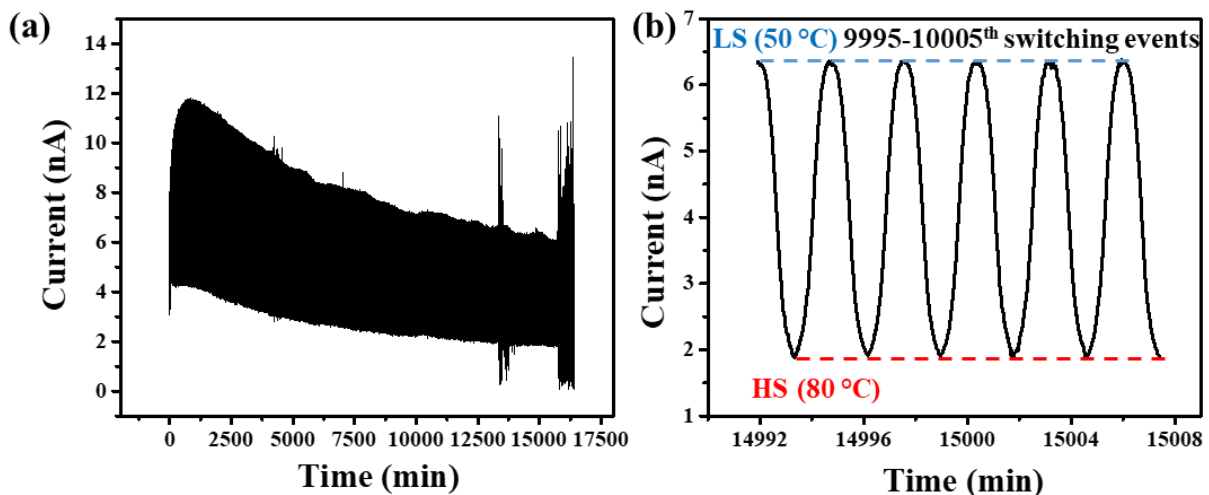


Figure 2.5 : (a) Cycles de commutation actuels entre le HS et le LS dans la jonction pendant >10.000 commutations. Des zooms sont également montrés sur les 9995ème - 10005ème (b) événements de commutation.

Afin de mieux comprendre le rôle des interfaces molécule-électrode dans la propriété de commutation de résistance des jonctions, nous avons conçu et caractérisé des jonctions ITO/100 nm [Fe(HB(tz)₃)₂]/Ca. Le rapport de courant ON/OFF atteint une valeur de 50 (Fig. 2.6), ce qui est comparable en magnitude aux dispositifs fabriqués avec une cathode en Al.

Ce résultat semble corroborer notre hypothèse selon laquelle le phénomène de commutation de résistance est lié au transport de saut de charges dans le film de SCO.

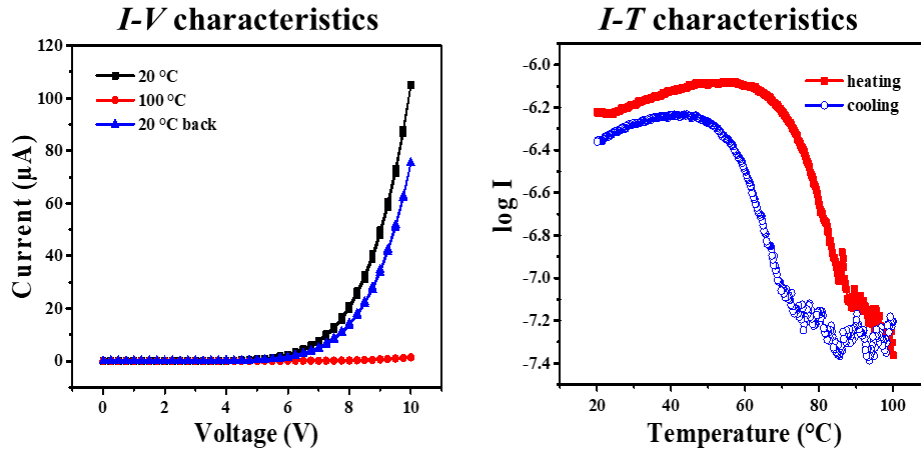


Figure 2.6: Electrical characteristics of an ITO/100 nm [Fe(HB(tz)₃)₂]/Ca junction. Left: *I-V* curves. Right: log *I* - *T* curves recorded with an applied bias of 5 V.

De plus, nous avons fabriqué un dispositif à valve de spin dans lequel la couche SCO est prise en sandwich entre deux électrodes magnétiques. Nous avons réussi à fabriquer des jonctions NiFe/[Fe(HB(tz)₃)₂]/Co avec une épaisseur de couche de SCO d'environ 100 nm, qui présentaient les caractéristiques I-V et magnétiques attendues. Cependant, à ce stade, nous n'avons pas encore pu mettre en évidence une quelconque propriété de magnétorésistance ni un effet clair de la SCO sur les propriétés électriques du dispositif.

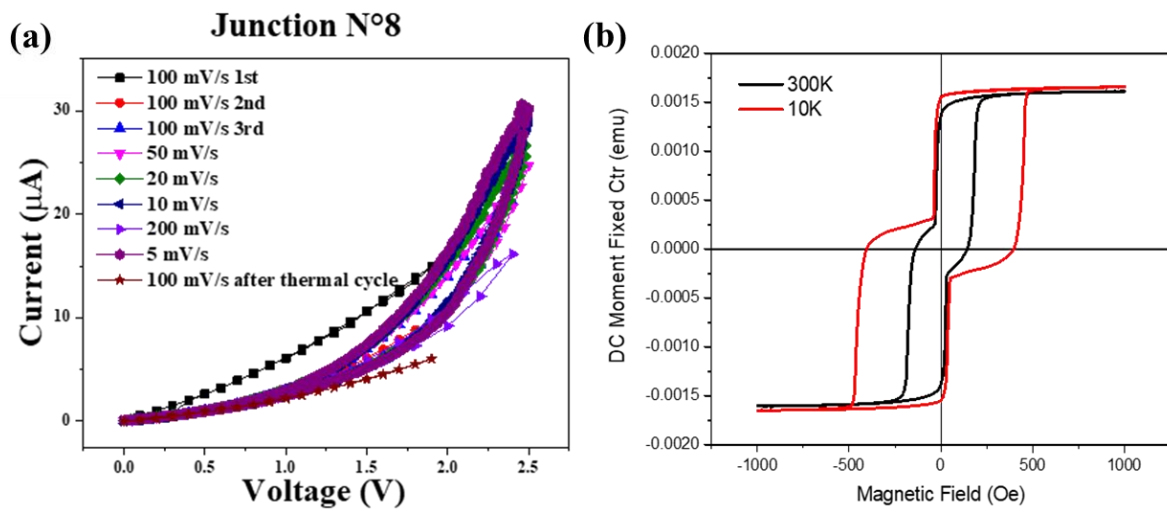


Figure 2.7 : Caractéristiques I-V (a) et magnétiques (b) de jonctions NiFe/[Fe(HB(tz)₃)₂]/Co.

Chapitre 3 Intégration du complexe à transition de spin $[\text{Fe}(\text{HB}(\text{tz})_3)_2]$ dans des dispositifs électroniques à trois bornes

Ce chapitre est consacré à l'étude de la possibilité d'intégrer les molécules SCO dans des dispositifs de transistors à effet de champ organiques (OFET) afin de moduler les caractéristiques du dispositif via le phénomène SCO. Trois dispositifs OFET différents ont été conçus et fabriqués dans des configurations grille inférieure - contact inférieur ou grille inférieure - contact supérieur. Les structures de ces dispositifs sont présentées à la figure 3.1 ci-dessous :

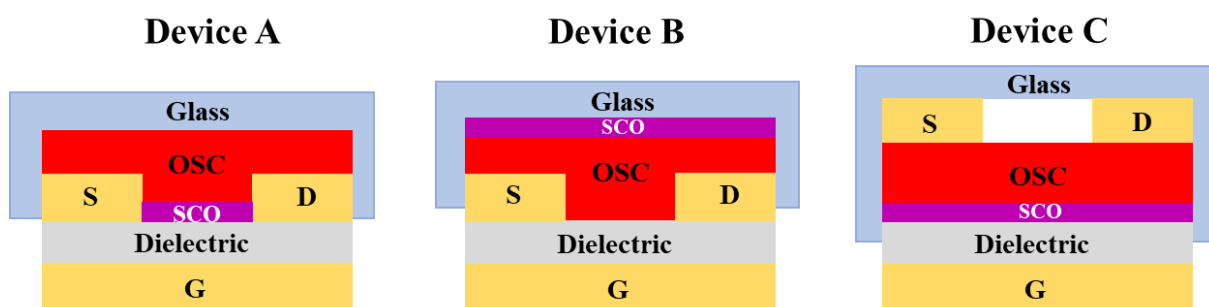


Figure 3.1 : Configurations du dispositif A, du dispositif B et du dispositif C.

En particulier, une photo représentative du dispositif C est présentée à la figure 3.2. Chaque puce contient cinq transistors. Pour les mesures électriques, trois pointes de tungstène recouvertes d'or ont été placées en contact avec le prolongement des électrodes de drain/source/grille, la puce étant placée sur un étage de chauffage-refroidissement.

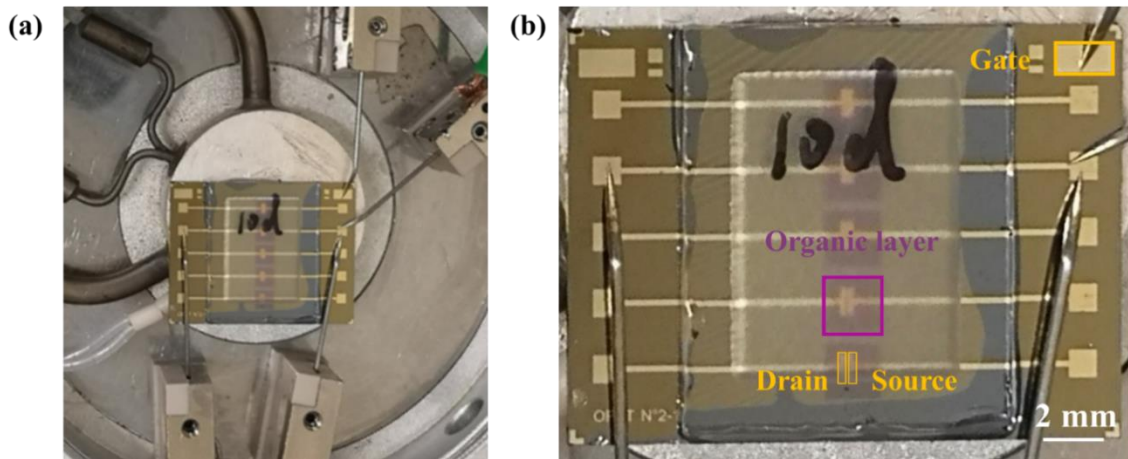


Figure 3.2 : Photos de (a) une puce avec cinq transistors sur l'étage de chauffage-refroidissement et (b) un zoom sur la puce. On peut également y voir les sondes utilisées pour les mesures.

Les caractéristiques de sortie ou les caractéristiques de transfert ont été aussi mesurées pour évaluer les performances des OFET. La figure 3.3 illustre une caractéristique de sortie représentative (a) et une caractéristique de transfert (b) d'un dispositif A avec une épaisseur de SCO de 30 nm. À partir de la courbe de sortie, nous pouvons voir que le courant source-drain est très faible ($<10^{-10}$ A), ce qui indique que le canal n'est pas conducteur. Nous pensons que l'échec du dispositif A est lié à la présence d'une " intercouche " de SCO entre les électrodes source/drain et le semi-conducteur organique.

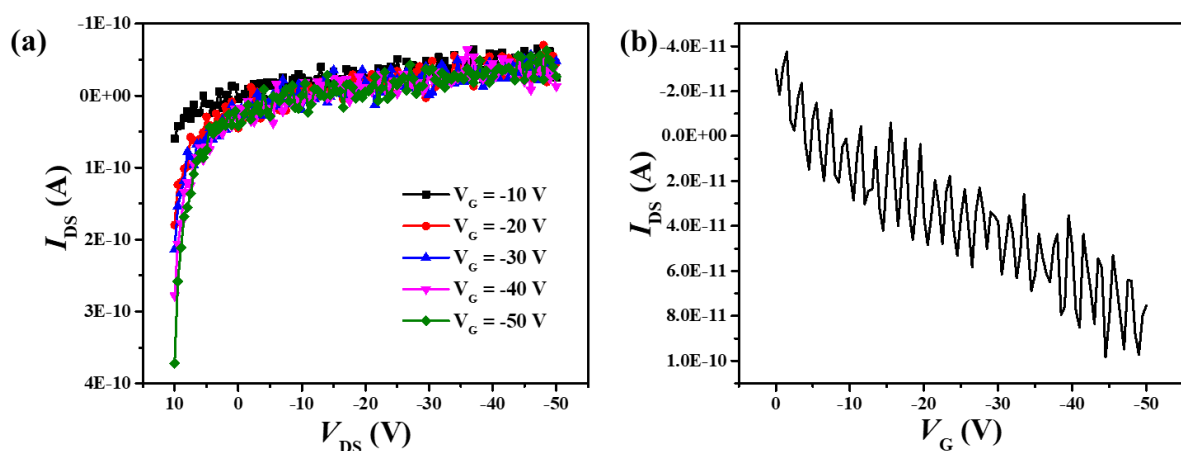


Figure 3.3 : Caractéristiques représentatives (a) de sortie et (b) de transfert du dispositif A. $W = 50 \mu\text{m}$, $L = 1500 \mu\text{m}$.

Nous avons également examiné les caractéristiques électriques du dispositif B. Dans cette configuration, un film de tétracène de 75 nm d'épaisseur a d'abord été déposé sur le substrat propre fonctionnalisé par SAM, puis un film de $[\text{Fe}(\text{HB}(\text{tz})_3)_2]$ de 150 nm d'épaisseur a été déposé lors de la dernière étape de la fabrication du dispositif. La figure 3.4 illustre une caractéristique de sortie représentative (a) et une caractéristique de transfert (b) d'un dispositif B. On peut voir sur la courbe caractéristique de sortie que le courant drain-source (I_{DS}) est de l'ordre de 10^{-6} A avec un effet de champ significatif, ce qui indique que le transistor fonctionne.

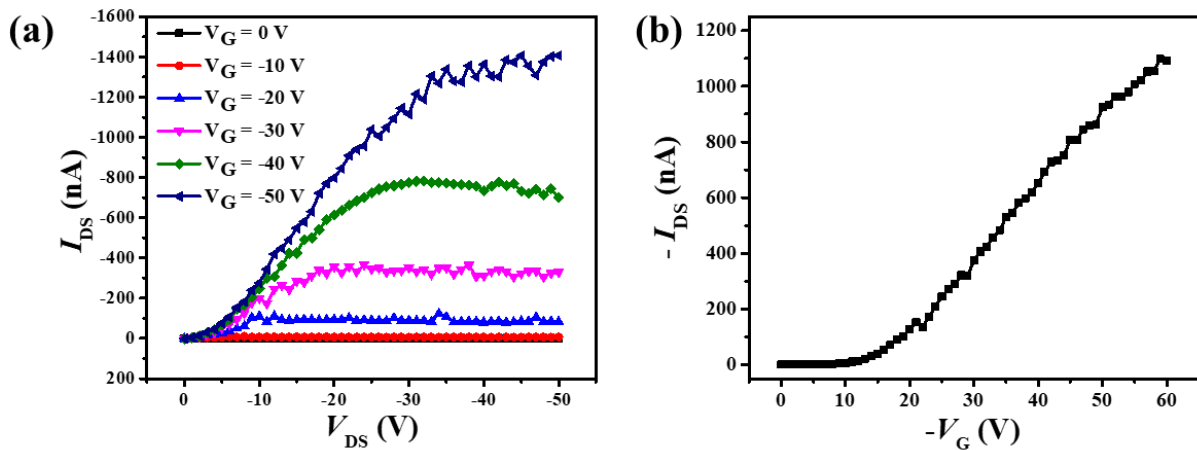


Figure 3.4 : Caractéristiques représentatives (a) de sortie et (b) de transfert du dispositif B. $W = 50 \mu\text{m}$, $L = 1000 \mu\text{m}$.

La variation de l'intensité du courant était souvent bruyante et peu reproductible. Plus important encore, aucun signe clair pour les changements liés au phénomène SCO n'a pu être déduit. Pour cette raison, notre attention s'est portée sur l'optimisation du dispositif C à la fois en termes de processus de fabrication et de protocoles de caractérisation, permettant une meilleure stabilité du dispositif. Les caractéristiques de sortie et de transfert du dispositif C à $45 \text{ }^\circ\text{C}$ sont présentées à la figure 3.5. La courbe caractéristique de sortie du dispositif C montre un effet de champ clair : le courant drain-source peut être réglé par la tension de grille et les régions linéaires/saturation peuvent être clairement distinguées. À notre connaissance, il s'agit du premier OFET fonctionnel incorporant un matériau à transition spin dans la couche diélectrique. Le courant de fuite (c'est-à-dire le courant à l'état OFF) est de plusieurs dizaines de pA, alors

que le courant à l'état ON peut atteindre plusieurs nA. On peut également noter une hystérésis dans les caractéristiques de transfert dénotant la présence de pièges à charge.

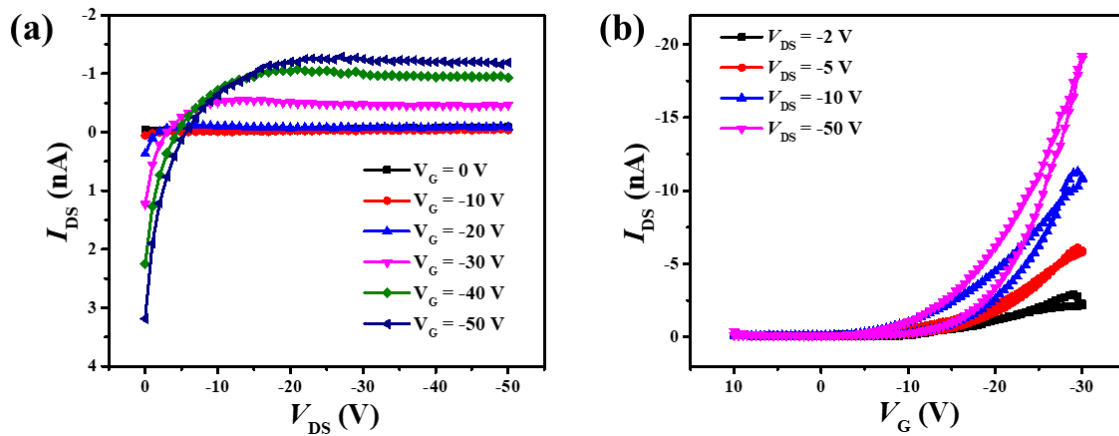


Figure 3.5 : (a) Caractéristiques de sortie et (b) caractéristiques de transfert d'un dispositif C mesurées à 45 °C. $W = 110 \mu\text{m}$, $L = 1000 \mu\text{m}$.

Des mesures dépendantes de la température ont été effectuées à la fois sur le 'dispositif standard' (dispositif à grille inférieure/contact supérieur sans SCO) et sur le dispositif C. Nous avons extrait des courbes de transfert du dispositif C et d'un 'dispositif standard' la dépendance en température du courant drain-source à des valeurs fixes de V_{DS} et V_G . Ces résultats sont résumés dans la Fig. 3.6. La comparaison de ces données obtenues en présence ou en l'absence du film SCO a révélé des différences faibles, mais significatives. Des travaux ultérieurs devraient confirmer dans quelle mesure ces différences pourraient être liées au phénomène SCO.

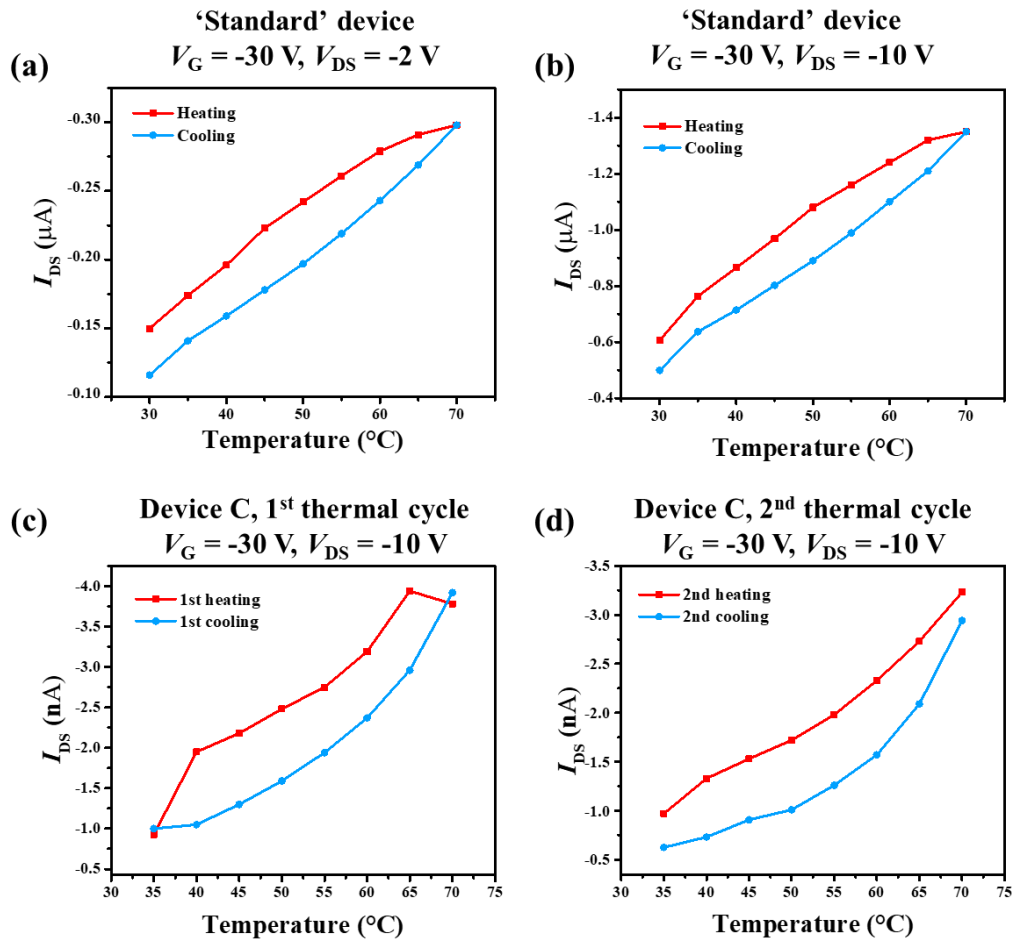


Figure 3.6 : Caractéristiques représentatives du courant drain-source dépendant de la température d'un " dispositif standard " (panneau supérieur) et du dispositif C (panneau inférieur). $W = 50 \text{ }\mu\text{m}$, $L = 1000 \text{ }\mu\text{m}$.

Chapitre 4 Intégration du complexe à transition de Spin $[\text{Fe}(\text{HB}(\text{tz})_3)_2]$ dans des cavités optiques

Dans ce chapitre, nous décrivons la conception, la fabrication et les propriétés optiques de cavités Fabry-Perot multicouches $\text{Ag}/[\text{Fe}(\text{HB}(\text{tz})_3)_2]/\text{Ag}$. Ces dispositifs utilisent la remarquable commutation de l'indice de réfraction ($n = 0,04 - 0,2$) entre les états à bas et haut spin dans le film $[\text{Fe}(\text{HB}(\text{tz})_3)_2]$ pour réaliser la modulation de la résonance de la cavité.

La dépendance en température de l'indice de réfraction n et de l'épaisseur du film L est représentée sur les figures 4.1(a) et (b), respectivement. Ces courbes montrent une corrélation convaincante. Loin de la transition de spin, n et t sont faiblement dépendants de la température, en accord avec le coefficient de dilatation thermique presque nul de $[\text{Fe}(\text{HB}(\text{tz})_3)_2]$. Autour de

la température de transition de spin (65 °C), l'épaisseur du film augmente brusquement de 4,6(4) %, de 91,2(3) dans l'état LS à 95,4(2) nm dans l'état HS.

Cette variation est en accord raisonnable avec l'expansion de 5,4(8) % de l'axe c orthorhombique de la cellule unitaire lors de la SCO révélé par la diffraction des rayons X sur monocristal. (N.B. Rappelons que le film est orienté avec l'axe c normal au substrat). D'autre part, la valeur de n diminue concomitamment d'environ 0,2-0,04 (selon la longueur d'onde) à la transition LS vers SH. En particulier, à 500 nm, nous avons extrait un changement de $n=1,62$ à 1,56 lors du passage de l'état LS à l'état HS.

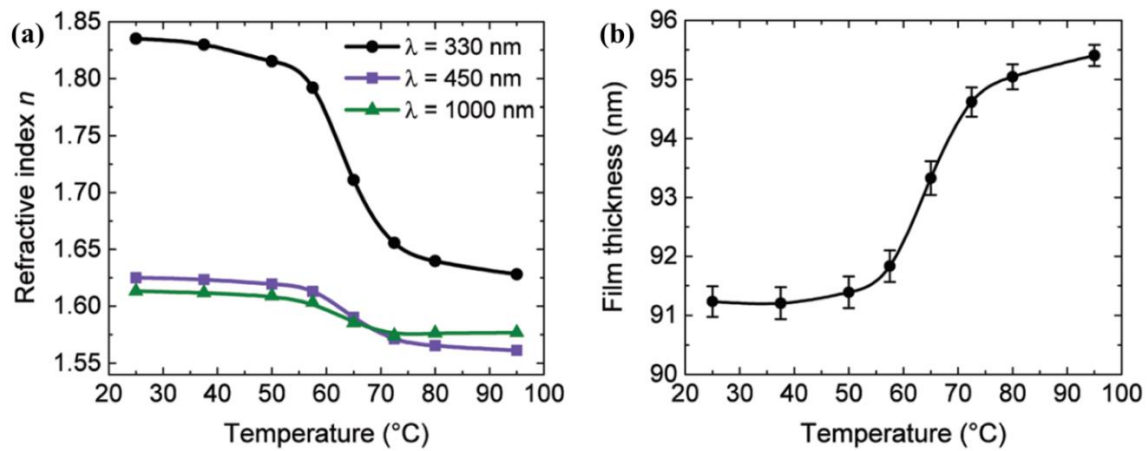


Figure 4.1 : Caractérisation ellipsométrique d'un film de [Fe(HB(tz)3)2] d'une épaisseur nominale de 100 nm. (a) Dépendance en température de l'indice de réfraction n à certaines longueurs d'onde (mode chauffage). (b) Variation de l'épaisseur du film L en fonction de la température (mode chauffage).

La figure 4.2 montre la profondeur de modulation induite par la commutation entre les états LS et HS (définis en réflexion comme $|RHS-RLS|$) pour un empilement Ag/115 nm SCO/Ag à incidence normale. Ces types de tracés peuvent être utilisés pour rechercher les conditions optimales où le SCO permet la plus grande variation possible de la réflectance (ou de la transmittance) de la cavité.

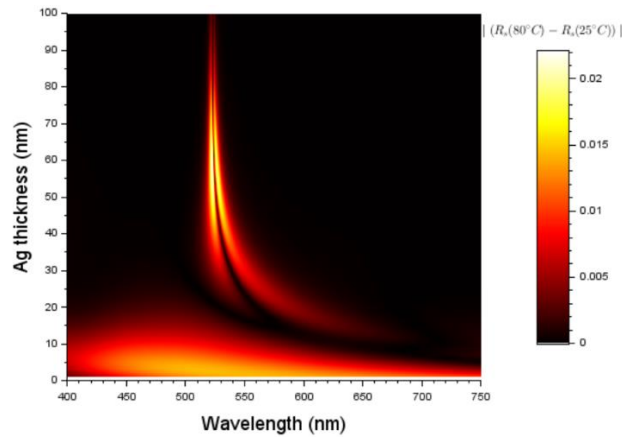


Figure 4.2 : Profondeur de modulation $|R_{HS}-R_{LS}|$ pour un empilement Ag/115 nm SCO/Ag à $AOI=0^\circ$.

D'après les simulations, le premier dispositif Fabry-Perot à base de SCO a été conçu pour être 50 nm Ag/115 nm SCO/50 nm Ag. La figure 4.3a montre des spectres de réflectance représentatifs des cavités enregistrés dans les états LS (25 °C) et HS (80 °C) à des angles d'incidence sélectionnés sous un éclairage polarisé TE. D'autre part, la figure 4.3b compare la réflectance des cavités pour les polarisations TE et TM à un AOI fixe (60°). Comme prévu dans les simulations, la structure multicouche Ag/SCO/Ag présente des résonances prononcées avec une dépendance significative à la fois de l'AOI et de l'état de polarisation de l'onde lumineuse incidente. Cet effet combiné de l'AOI et de la polarisation est plus clairement illustré dans la courbe de dispersion de la cavité présentée à la figure 4.3c. Là encore, nous notons la bonne correspondance avec les résultats de la simulation. Il est important de noter que les pics de résonance présentent un décalage vers le bleu lors du passage de l'état LS à l'état HS. Ce décalage peut être mieux apprécié sur la figure 4.3d, qui montre un balayage détaillé de la température (pour $AOI=45^\circ$ et une polarisation TE). Le plus grand décalage que nous avons pu observer à l'OCS était d'environ 8 nm pour $AOI 60^\circ$ à la polarisation TE. Comme le montre la figure 4.3b, ce décalage de longueur d'onde se traduit par une modulation de la réflectance de la cavité d'environ 30 %.

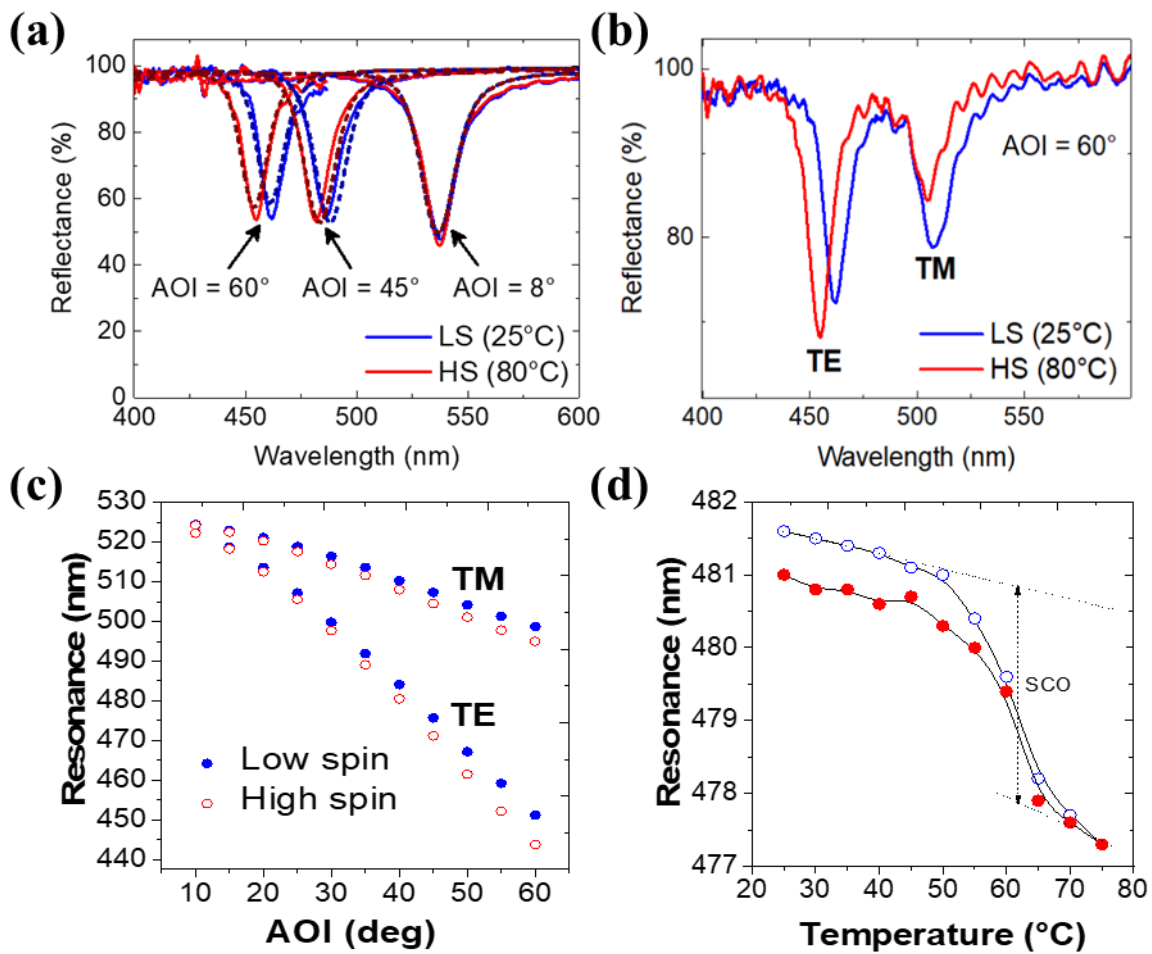


Figure 4.3 : Propriétés optiques des cavités Fabry-Perot multicouches Ag (50 nm)/SCO (115 nm)/Ag (50 nm). (a) Spectres de réflectance à des valeurs AOI sélectionnées dans les deux états de spin pour la polarisation TE. (b) Spectres de réflectance à une AOI fixe de 60° dans les deux états de spin pour les polarisations TE et TM. (c) Courbes de dispersion dans les deux états de spin pour les polarisations TE et TM. (d) Résonance de la cavité (polarisation TE, AOI = 45°) en fonction de la température pour un cycle complet de chauffage - refroidissement.

Conclusions générales et perspectives

Plusieurs décennies se sont écoulées depuis qu'Olivier Kahn a proposé et prévu l'intégration potentielle des molécules à transition de spin dans les dispositifs électroniques. En effet, les matériaux à transition de spin présentent des atouts intéressants pour les applications technologiques en raison de leurs propriétés physiques bistables (optiques, magnétiques, électriques, ...) et du fait que le changement d'état de spin peut être déclenché par divers stimuli externes, tels que la température, la pression, l'irradiation par la lumière et les rayons X, les

champs magnétiques intenses, ou l'inclusion de molécules solvantées ou invitées (c'est-à-dire des stimuli chimiques). Ces propriétés, ainsi que la vitesse de commutation rapide et la polyvalence de ces matériaux (plusieurs centaines de composés SCO connus), les rendent attrayants pour différentes applications, notamment les commutateurs, les mémoires, les écrans, les capteurs, les actionneurs, etc. Notamment, plusieurs équipes de recherche ont travaillé au cours des dernières décennies à l'incorporation de matériaux SCO dans des dispositifs électroniques et plusieurs résultats remarquables ont été obtenus. Cependant, il est juste d'admettre que nous n'en sommes encore qu'au stade initial du transfert des propriétés des SCO dans différentes formes de dispositifs ainsi que de la compréhension des mécanismes physiques pertinents. De plus, la durée de vie des dispositifs est de plus en plus considérée comme une question importante du point de vue des applications du " monde réel". Partant de ces motivations, la thèse a été construite dans le but d'intégrer des matériaux SCO sous forme de films minces dans différents dispositifs (configurations), d'établir la corrélation entre le phénomène SCO et les caractéristiques du dispositif, d'étudier les facteurs qui influencent la durée de vie des dispositifs électroniques basés sur SCO et de creuser les protocoles avec une compréhension globale des points ci-dessus pour améliorer la performance générale des dispositifs.

Grâce aux progrès récents de notre équipe en matière de films minces cristallins de haute qualité du complexe SCO $[\text{Fe}(\text{HB}(\text{tz})_3)_2]$, présentant une SCO robuste, au-dessus de la température ambiante, nous avons intégré avec succès ces films minces par évaporation thermique sous vide dans différentes configurations de dispositifs fondamentaux, qui ont été mis en œuvre en collaboration avec la plateforme microélectronique du LAAS-CNRS-Toulouse.

Pour la première étape expérimentale, nous avons construit des jonctions électroniques multicouches ITO/SCO/Al à deux bornes, de grande surface, pour étudier leur fonctionnalité de commutation de résistance. Nous avons examiné divers détails, notamment la voie de synthèse, les méthodes de purification, la préparation des substrats, le dépôt de la couche mince, les traitements post-dépôt, l'encapsulation du dispositif, les protocoles de caractérisation, etc. afin d'obtenir les meilleures performances du dispositif.

En conséquence, nous avons pu observer une commutation de résistance due au phénomène SCO, jusqu'à trois ordres de grandeur, dans les dispositifs avec une couche SCO de 100 nm d'épaisseur.

De façon remarquable, les jonctions sont assez robustes et nous avons montré que la propriété de commutation de résistance peut être préservée même après un stockage dans l'environnement ambiant pendant un an sans encapsulation. Ces jonctions ont montré une grande résistance à la fatigue (grande endurance aux cycles de température), avec un rapport de commutation par résistance ON/OFF considérable et stable pendant plus de 10 000 événements de commutation. Nous avons découvert que les paramètres clés pour atteindre cette stabilité de commutation sont la plage de température de travail réduite ($< \sim 80^{\circ}\text{C}$) et une tension de polarisation constante.

Nous avons également donné un aperçu du mécanisme de transport des dispositifs en remplaçant le matériau de la cathode. Malgré le fait que les fonctions de travail de l'Al et du Ca sont très différentes (fournissant ainsi des barrières d'injection d'électrons très différentes), la performance de la jonction semble assez similaire avec des rapports de commutation de résistance ON/OFF comparables, ce qui indique que le transport limité par le volume est le mécanisme dominant dans nos dispositifs.

Une perspective intéressante de ce travail serait de corréler les propriétés de transport de charge avec l'orientation cristalline des films. Une autre perspective importante serait l'étude de jonctions multicouches avec différentes épaisseurs de film, jusqu'à quelques nanomètres, afin d'atteindre un régime de transport de charge qui ne soit pas dominé par les propriétés de transport de masse du film SCO.

Nous avons également intégré des films minces de $[\text{Fe}(\text{HB}(\text{tz})_3)_2]$ dans une configuration de dispositif à valve de spin avec deux électrodes magnétiques. Au stade actuel de nos travaux, nous n'avons pas encore pu mettre en évidence une quelconque propriété de magnétorésistance, ni un effet clair du SCO sur les propriétés électriques du dispositif.

Néanmoins, nous pensons que ces dispositifs représentent une plateforme prometteuse pour des travaux ultérieurs sur de nouvelles combinaisons de matériaux et de fonctionnalités spintroniques.

Dans l'étape suivante de nos expériences, les matériaux SCO ont été intégrés dans des OFETs fonctionnels. Ce type de dispositifs à trois terminaux représente un sujet d'inspiration avec une augmentation de la liberté de conception par rapport aux simples configurations de diodes à deux terminaux. En effet, dans nos expériences, nous avons pu étudier différentes configurations d'OFET. Pour les OFETs à contact inférieur, nous avons rencontré un problème technique pour insérer le film de SCO entre l'OSC et les couches diélectriques sans déposer les molécules de SCO sur les électrodes de drain/source, laissant le dispositif résultant plutôt isolant.

Néanmoins, nous avons imaginé que ce problème pourrait être résolu ultérieurement en déposant les électrodes de drain/source après le dépôt de SCO ou en utilisant un masque d'ombre. Dans notre travail, pour éviter ce problème, nous avons choisi de travailler avec des OFETs à contact supérieur et à grille inférieure. Nous avons effectué une étude approfondie de la stabilité du dispositif et nous avons pu établir des protocoles de mesure, qui nous ont permis de minimiser la dégradation du dispositif à un niveau acceptable. La comparaison de la dépendance en température du courant drain-source et de la tension de seuil en présence ou en l'absence du film SCO a révélé des différences faibles, mais significatives. Des travaux supplémentaires devraient confirmer dans quelle mesure ces différences pourraient être liées au phénomène SCO. Les perspectives d'avenir incluent l'utilisation de semi-conducteurs organiques plus robustes en conjonction avec l'utilisation de matériaux SCO, qui présentent une transition de spin à température ambiante avec hystérésis ainsi qu'un changement important de sa permittivité diélectrique. Ces propriétés pourraient donner lieu non seulement à une meilleure stabilité des dispositifs, mais aussi à une possibilité d'application très utile, à savoir un effet de mémoire non volatile.

En capitalisant sur l'expertise acquise lors du développement des empilements multicouches métal/[Fe(HB(tz)₃)₂]/métal, nous avons également développé des cavités optiques à base de SCO qui présentent des propriétés optiques commutables. Premièrement, nous avons montré que les films de [Fe(HB(tz)₃)₂] présentent un changement substantiel de leur indice de réfraction lors de la transition de spin, alors qu'ils conservent leur bonne transparence pour les longueurs d'onde VIS-NIR. En utilisant les constantes optiques mesurées, nous avons effectué des calculs pour simuler et prédire les caractéristiques des cavités Fabry-Perot métal/[Fe(HB(tz)₃)₂]/métal. Sur la base de ces calculs, la configuration du dispositif a été fixée à 50 nm Ag/115 nm SCO/50 nm Ag avec une résonance située dans le domaine spectral visible et associée à une transmittance et un facteur Q raisonnablement élevés. Les cavités fabriquées présentaient des résonances spectralement accordables (jusqu'à 8 nm de décalage) lors de la transition de spin, qui pouvaient être attribuées à l'indice de réfraction et aux changements d'épaisseur du film associés au SCO. Ce travail ouvre des perspectives pour une multitude d'applications reconfigurables et auto-adaptatives, y compris des modulateurs de lumière spatiaux, des circuits intégrés photoniques et des composants optiques accordables - avec une pertinence particulière pour la gamme de longueurs d'onde visibles où d'autres familles de matériaux optiques actifs sont moins performants. Dans nos futurs travaux, nous cherchons à

construire des guides d'ondes optiques, des réseaux de résonance à mode guidé et d'autres dispositifs photoniques incorporant une fine couche de composés SCO évaporables.

Pour conclure, nous avons réussi à incorporer des matériaux à transition de spin (SCO) dans des dispositifs électroniques et photoniques à deux/trois bornes. En tant que tel, ce travail fournit une petite brique aux différents efforts visant à transformer les composés SCO d'une curiosité scientifique en de vrais matériaux pour l'ingénierie.

Bien qu'il reste une myriade d'inconnues à explorer dans ces domaines, nous pouvons prédire une large fenêtre pour les technologies basées sur les SCO. En particulier, nos résultats ont révélé que certains des dispositifs à base de SCO présentent des performances entièrement prévisibles (par exemple, les cavités Fabry-Perot) ainsi qu'une endurance considérable en mode opérationnel (par exemple, les jonctions à commutation de résistance), ce qui constitue sans aucun doute des problèmes importants pour toute application dans le monde réel.

Nous pensons que dans un avenir proche, grâce aux efforts continus et aux recherches approfondies des physiciens, des chimistes et des ingénieurs, les molécules SCO sortiront du monde académique vers de réelles innovation technologiques.

Titre: Dispositifs électroniques et optiques à base de complexe à transition de spin [Fe(HB(1,2,4-triazol-1-yl)₃)₂]

Mots-clés: transition de spin, couches minces, dispositifs électroniques, cavités optiques.

Résumé: L'objectif central de cette thèse est l'exploration des applications potentielles des complexes moléculaires à transition de spin dans les dispositifs électroniques et photoniques. Dans ce but, des films minces cristallins de haute qualité, déposés thermiquement sous vide, du complexe [Fe(HB(tz)₃)₂] (tz = (1,2,4-triazol-1-yl), présentant une bistabilité robuste à température ambiante, ont été incorporés dans des dispositifs à deux et trois bornes. Des jonctions verticales de grande surface ont été formées par des empilements ITO/[Fe(HB(tz)₃)₂]/Al. Ces jonctions ont présenté une chute de résistance allant jusqu'à trois ordres de grandeur lors du passage de l'état bas spin à l'état haut spin. Elles ont également révélé une grande résistance à la fatigue lors du stockage (> 1 an) et lors de commutations répétées (>10 000) à l'air ambiant. Le mécanisme de commutation de résistance pourrait être lié au transport de charge intrinsèque au film de complexe à transition de spin. Des jonctions multicouches similaires avec des électrodes magnétiques ont également été fabriquées pour la première fois. Des films de [Fe(HB(tz)₃)₂] ont été par la suite incorporés dans des transistors organiques à effet de champ. Différentes configurations ont été réalisées (grille inférieure/contact inférieur, grille inférieure/contact supérieur) - dans le but d'utiliser le phénomène de transition de spin pour moduler les propriétés des transistors. Malgré des difficultés considérables pour obtenir des caractérisations reproductibles en fonction de la température, nous avons pu mettre en évidence de modifications de différentes caractéristiques en fonction de la température, qui pourraient être liées à la transition de spin. En parallèle, des cavités multicouches Ag/[Fe(HB(tz)₃)₂]/Ag de type Fabry-Perot ont également été fabriquées. Ces dispositifs utilisent la commutation remarquable de l'indice de réfraction (n = 0,04 - 0,2) entre les états bas spin et haut spin dans le film [Fe(HB(tz)₃)₂] pour réaliser la modulation de la résonance de la cavité. Cette possibilité d'ajustement de la longueur d'onde centrale est associée à de faibles pertes d'absorption dans les domaines spectraux du visible et du proche infrarouge, ce qui ouvre la voie au développement des dispositifs photoniques reconfigurables et auto-adaptatives.

Title: Electronic and optical devices integrating thin films of the spin crossover complex [Fe(HB(1,2,4-triazol-1-yl)₃)₂]

Keywords: spin crossover, thin films, electronic devices, optical cavities.

Abstract: The central aim of this thesis is the exploration of potential applications of molecular spin crossover complexes in electronic and photonic devices. To this aim vacuum thermal deposited, high quality, crystalline thin films of the complex [Fe(HB(tz)₃)₂] (tz = (1,2,4-triazol-1-yl), displaying robust, above-room-temperature spin crossover, were incorporated into two- and three-terminal device configurations. Large-area, vertical junctions were formed by ITO/[Fe(HB(tz)₃)₂]/Al stacks. The junctions exhibited up to three orders of magnitude resistance drop when switching from the low-spin to the high-spin state. They revealed also high resistance to fatigue both on storage (> 1 year) and on repeated switching (>10,000) in ambient air. The resistance switching mechanism could be linked to the intrinsic charge transport in the spin crossover film. Similar multilayer junctions with magnetic electrodes were also fabricated for the first time. [Fe(HB(tz)₃)₂] films were then incorporated into organic field-effect transistors. Different device configurations were created (bottom gate/bottom contact, bottom gate/top contact) - aiming for the use of the spin crossover phenomenon to modulate the transfer/output characteristics of the transistors. Despite considerable difficulties in achieving reproducible temperature-dependent characterizations, we could evidence changes of the device characteristics, which may be related to the spin crossover phenomenon. In parallel, multilayer Ag/[Fe(HB(tz)₃)₂]/Ag Fabry-Perot cavities were also fabricated. These devices use the remarkable refractive index switching ($\Delta n = 0.04 - 0.2$) between the low-spin and high-spin states in the [Fe(HB(tz)₃)₂] film to achieve modulation of the cavity resonance. This wavelength tuneability is coupled with low absorption losses in the visible and near infrared spectral ranges, providing scope for reconfigurable and self-adaptive photonics applications.